ISBN 978-82-471-1215-1 (printed ver.)
ISBN 978-82-471-1216-8 (electronic ver.)
ISSN 1503-8181

NTNU
Norwegian University of
Science and Technology

Doctoral Theses at NTNU, 2008:260

Vagesh D. Narasimhamurthy

Wake dynamics of flow past tapered bluff bodies

NTNU
Norwegian University of
Science and Technology

Thesis for the degree of
philosophiae doctor

Faculty of Engineering Science and Technology
Department of Energy and Process Engineering

Vagesh D. Narasimhamurthy

Doctoral Thesis

Theses at NTNU, 2008:260

NTNU

Vagesh D. Narasimhamurthy

Wake dynamics of flow past tapered bluff bodies

Thesis for the degree of philosophiae doctor

Trondheim, September 2008

Norwegian University of
Science and Technology
Faculty of Engineering Science and Technology
Department of Energy and Process Engineering

NTNU
Norwegian University of
Science and Technology

NTNU
Norwegian University of Science and Technology

Thesis for the degree of philosophiae doctor

Faculty of Engineering Science and Technology
Department of Energy and Process Engineering

ISBN 978-82-471-1215-1 (printed ver.)
ISBN 978-82-471-1216-8 (electronic ver.)
ISSN 1503-8181

Theses at NTNU, 2008:260

Printed by Tapir Uttrykk

Abstract

The present doctoral thesis concerns the wake dynamics from uniform and tapered bluff bodies. Bluff body configurations characterized by both arbitrary separation points and fixed separation points were considered, i.e. both the circular cylinder configuration and the normal flat plate configuration were used. Different flow regimes, from steady laminar wakes to transitional and turbulent wakes were explored. In all the cases, Direct Numerical Simulations were performed to solve the incompressible Navier-Stokes equations for an isothermal and Newtonian flow. Some results from the in-house PIV measurements were also presented. The characteristic features of the flow were investigated by means of frequency (both Fourier and Wavelet) analysis, three-dimensional flow visualizations and two-point correlations. Variations of the velocity and the pressure fields were also explored. The impact of the base pressure on the vortex formation process was elaborated. Reynolds-averaged statistical quantities were presented and the underlying flow physics were discussed.

List of articles

ARTICLE 1: Narasimhamurthy, V. D., Schwertfirm, F., Andersson, H. I. & Pettersen, B. 2006 Simulation of unsteady flow past tapered circular cylinders using an immersed boundary method. In *Proc. ECCOMAS European Conference on Computational Fluid Dynamics, Egmond aan Zee, The Netherlands* (ed. P. Wesseling, E. Oñate & J. Périaux), TU Delft.

ARTICLE 2: Narasimhamurthy, V. D., Andersson, H. I. & Pettersen, B. Steady viscous flow past a tapered cylinder. Accepted for publication in *Acta Mechanica*.

ARTICLE 3: Narasimhamurthy, V. D., Andersson, H. I. & Pettersen, B. 2007 Direct numerical simulation of vortex shedding behind a linearly tapered circular cylinder. In *Proc. IUTAM Symposium on Unsteady Separated Flows and their Control, Corfu, Greece* (ed. M. Braza & K. Hourigan), To be published by Springer.

ARTICLE 4: Narasimhamurthy, V. D., Visscher, J., Andersson, H. I. & Pettersen, B. 2007 DNS and PIV study of the 3D wake behind tapered circular cylinders. In *Proc. Fifth International Symposium on Turbulence and Shear Flow Phenomena, Munich, Germany*, pp. 667-672.

ARTICLE 5: Narasimhamurthy, V. D., Andersson, H. I. & Pettersen, B. Cellular vortex shedding behind a tapered circular cylinder. Submitted to *Physics of Fluids*.

ARTICLE 6: Huang, Z., Narasimhamurthy, V. D., Andersson, H. I. & Cui, W. Asymmetries in the wake behind a circular cylinder in planar shear flow. Manuscript to be submitted.

ARTICLE 7: Narasimhamurthy, V. D., Andersson, H. I. & Pettersen, B. Cellular vortex shedding in the wake of a tapered plate. Accepted for publication in *Journal of Fluid Mechanics*.

ARTICLE 8: Narasimhamurthy, V. D. & Andersson, H. I. Turbulent wake behind a normal flat plate. Submitted to *International Journal of Heat and Fluid Flow*.

ARTICLE 9: Khaledi, H. A., Narasimhamurthy, V. D., & Andersson, H. I. Cellular vortex shedding in the wake of a tapered plate at low Reynolds numbers. Submitted to *Physics of Fluids*.

Acknowledgments

I would like to express my deepest regards to my supervisor, Prof. Helge I. Andersson for all his support and guidance through out these three and a half years. Special thanks to him for teaching me how to write good scientific articles. I am very grateful to him for always helping me out, both on the professional front and also on the personal front, especially while i was suffering from wrist injury.

I wish to thank my co-supervisor, Prof. Bjørnar Pettersen for all the help and encouragement i received from him. I am also very grateful to him for giving me an opportunity to work on this project.

A very special thanks to Prof. Ian P. Castro, at School of Engineering Sciences, University of Southampton, for providing some helpful suggestions and constructive comments. I would also like to thank Prof. Mike Gaster, at Department of Engineering, Queen Mary, University of London, for his constructive comments and suggestion for improvements.

I wish to thank my colleagues, especially Dr. Peter S. Johansson for helping me in the beginning of the project and Jan Visscher for providing the PIV data. Special thanks to Asso. Prof. Reidar Kristoffersen and Florian Schwertfirm for their kind help.

Finally, I would like to thank my family for their love and support through out these years.

Nomenclature

Upper-case Roman

2D	Two-dimensional
3D	Three-dimensional
C_p	Pressure co-efficient
$\overline{C_p}$	Mean pressure co-efficient
L1	Creeping flow or non-separation regime
L2	Steady separation or closed near-wake regime
L3	Unsteady separation or periodic laminar wake regime
L_x, L_y, L_z	Length of the computational domain in each coordinate direction
L_w	Length of the steady recirculation bubble
N_x, N_y, N_z	Number of grid points in each coordinate direction
P	Instantaneous pressure
Re	Reynolds number based on the diameter of the cylinder or the width of the plate
Re_{local}	Local Reynolds number based on the local diameter of the cylinder or the local width of the plate
R_T	Taper ratio
S_{ij}	Strain rate tensor
St	Strouhal number
St_{local}	Local Strouhal number
TrW	Transition in wake regime
TrSL	Transition in shear layers or Subcritical state
TrBL	Transition in boundary layers or Critical state
U_i	Cartesian components of velocity vector
U	Streamwise velocity component
V	Spanwise velocity component
W	Cross-streamwise velocity component
X_i	Cartesian coordinate vector component

Lower-case Roman

d	diameter of the cylinder or width of the plate

d_{local}	local diameter of the cylinder or local width of the plate
d_m	mean diameter of the cylinder or mean width of the plate
f	shedding frequency
k	fluctuating kinetic energy
l	length of the cylinder or plate
t	time

Upper-case Greek

Δt	Time step
ΔX_i	Grid spacing along each coordinate direction
Ω_{ij}	Rotation rate tensor

Lower-case Greek

δ	Boundary layer thickness
δ_{ij}	Kronecker delta
ε	Dissipation rate of fluctuating kinetic energy
η	Kolmogorov micro scale
λ_2	second largest eigenvalue of the symmetric tensor $S_{ij}S_{ij} + \Omega_{ij}\Omega_{ij}$
μ	Dynamic viscosity
ν	Kinematic viscosity, $\nu = \mu/\rho$
ρ	Density
$T_{ij}^{(v)}$	Viscous stress tensor
ω_i	Vorticity vector
$\lvert\omega\rvert$	Vorticity magnitude

Subscripts

∞	free stream or ambient conditions

Superscripts

$\prime$	Turbulent fluctuation
$\prime\prime$	Unsteady fluctuation

Symbols

$\overline{(\dots)}$	Time averaged quantity

Abbreviations

AR	Aspect Ratio
CFD	Computational Fluid Dynamics
CFL	Courant-Friedrichs-Lewy
CWT	Continuous Wavelet Transform
DNS	Direct Numerical Simulation
FFT	Fast Fourier Transform
FVM	Finite Volume Method
IBM	Immersed Boundary Method
PIV	Particle Image Velocimetry
SIP	Strongly Implicit Procedure

Contents

Chapter 1

Introduction

Flow past immersed bodies is arguably one of the most studied research topics in fluid mechanics. The knowledge gained after over a century of research work by academicians and engineers is impressive but confines mostly to two-dimensional flows and around simplified objects. In reality, though, complex three-dimensional flows occur behind 3D bodies in nature. Such complex 3D flows in nature can only be realized (to some extent) by means of laboratory experiments or numerical simulations and is still (unfortunately) beyond the reach of theoretical fluid mechanics.

1.1 Bluff body wakes

If we now proceed to classify the bodies based on the nature of the flow field they produce, two broad classifications can be observed in the literature (Roshko (1993); Zdravkovich (1997); Buresti (2000)). If the boundary layers are completely attached to the body surface and the wakes are thin and usually steady then the bodies are considered as "*aerodynamic bodies*". Conversely, "*bluff-bodies*" are characterized by a premature separation of boundary layers from their surface and the wakes produced by them are wide and generally unsteady (see figure 1.1). The above definition implies that aerodynamic bodies are generally elongated in the direction of the primary flow and have sharp trailing edges to avoid boundary layer separation. Thus the shape of a body is a crucial parameter while deciding the *degree of bluffness*. However, it should be noted that the nature of the flow field around the body not only depends on the shape of the body but also on the orientation of the body with respect to the primary flow (oncoming stream) direction. Thus any aerodynamic body may become a bluff-body for certain degree of orientation (e.g. stalled aerofoils at high angle of incidence). Another important characteristic feature of the bluff bodies is that they normally have substantially higher drag coefficients (an order of magnitude larger) than the aerodynamic bodies. This is due to the remarkable increase in *pressure drag* deriving from

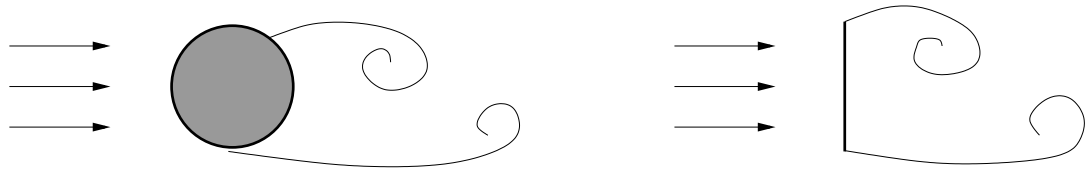

Figure 1.1: Sample bluff body configurations

the boundary layer separation. It should be noted that pressure drag in the case of bluff bodies is normally much higher than the *viscous or friction drag*. In contrast, the main contribution to the drag of an aerodynamic body stems from the friction drag.

As already discussed bluff bodies are associated with separated wakes. Based on the location of the separation points, bluff bodies can be further classified into two groups. For certain bluff bodies with sharp edges on their circumferences, such as flat plates, triangular, rectangular, and polygonal cylinders, flow separation is usually fixed by the sharp edges. On the contrary, the point of separation can take arbitrary positions for bodies with rounded corners (e.g. circular, elliptical, and arbitrary oval cylinders). Flow separation point for such rounded bodies depend on all the parameters influencing boundary layer transition (Reynolds number, surface roughness, free-stream turbulence, etc). Two special configurations (circular cylinders and normal flat plates) and the regions of disturbed flow they produce under the influence of Reynolds number variations will be discussed in the following sub-section.

1.1.1 Uniform circular cylinders

Flow past circular cylinders is perhaps the most studied bluff-body configuration during the past century. The amount of information available in the existing literature is quite exhaustive (Williamson (1996); Zdravkovich (1997, 2002)). At very low Reynolds numbers, i.e. in the *creeping flow* regime, boundary layers are completely attached to the cylinder surface. With the increase in Reynolds number, flow separation initiates at $Re = 4 - 5$ (Coutanceau & Defaye (1991); Zdravkovich (1997)). The separated boundary layers continue to develop downstream as free shear layers and eventually reattach along the wake centerline, thus forming a steady, symmetric, and closed near-wake region. The length of this closed near-wake (steady recirculation bubble) is already known to increase monotonically with Reynolds number (Coutanceau & Bouard (1977); Fornberg (1980)). (See article 2 for more references)

On further increasing the Reynolds number, $Re > 47$, the separated near-wake undergoes a *Hopf* bifurcation, i.e. transition from a steady state to an unsteady state. A sinusoidal oscillation of shear layers commences at the reattachment point and the amplitude of oscillation increases with rising Re

and eventually shear layers roll up and vortex shedding occurs. The Strouhal number, $St = fd/U_\infty$, where f is the vortex shedding frequency, is known to vary inversely with the $\sqrt{Re}$. Various formulations for the relationship between St and Re exists in the literature. Of all, the two most popular formulations are deduced by Williamson & Brown (1998) and Fey *et al.* (1998). Flow in this laminar vortex shedding regime ($47 < Re < 189$) is two-dimensional, i.e. spanwise vortex filaments are shed parallel to the axis of the cylinder. This, however, may not be the case in experiments, where end effects are known to cause "*oblique vortex shedding*", i.e. spanwise vortex filaments are shed at an angle to the cylinder axis (see Williamson (1996) for a detailed review).

A second transition, also known as spatial transition, which renders the flow three-dimensional (and eventually turbulent) occurs at $Re > 189$ (Barkley & Henderson (1996)). This flow regime is popularly called transition-in-wake or simply TrW regime (Zdravkovich (1997)). It should be noted that these three-dimensionalities are intrinsically induced and are not associated with end effects. Low-frequency modulations, a typical feature that occurs during this laminar-turbulent transition, were first observed by Roshko (1954). Later Bloor (1964) suggested that these low-frequency irregularities reflect the presence of three-dimensionalities that would render the flow turbulent as it travels downstream. However, it was Williamson (1992) who attributed these low-frequency irregularities in TrW regime to the presence of large-scale spot-like *vortex dislocations*. (More references can be found in article 3, article 4, and article 5).

With the further increase in Re, the transition point moves upstream. The development of *Kelvin-Helmholtz* instability at $Re > 1200$ in the shear layers trigger another transition (TrSL). The boundary layer, though, still remains laminar. At $Re \approx 10^5$, a sudden burst to turbulence occurs in the free shear layers near the side of the cylinder, which causes base suction and drag to decrease at a spectacular rate. With the occurance of $K - H$ waves in the boundary layer ($Re \approx 10^6$), base suction and drag reaches a minimum value. These high Reynolds number flows are beyond the scope of the present doctoral thesis and hence won't be elaborated further. For more details please refer Roshko (1993) and Zdravkovich (1997).

1.1.2 Normal flat plates

In contrast to the circular cylinders, normal flat plate configurations has received less attention from the research community. This is perhaps due to the fact that flow separation is fixed by the edges of the plate and is independent of the Reynolds number and free-stream turbulence effects. Another reason could be that it has less industrial applications when compared to circular cylinders. Nevertheless, the disturbed flow around all bluff bodies have some

similarities, despite differences in shape and the presence or absence of sharp edges. A detailed literature review of flow past normal flat plates is documented in article 8. However, some highlights of the wake flow features will be presented here.

The critical Reynolds number at which separation first occurs was predicted by Imai (1957). He reported that there exists a standing vortex pair of vanishing thickness at vanishing Reynolds number. Later Hudson & Dennis (1985) observed that the flow separation occurs as early as $Re = 0.1$. Dennis *et al.* (1993) found that the separated near-wake was symmetrical and steady for $Re \leq 20$. Recently, Saha (2007) reported that the separated near-wake of a normal flat plate undergoes a Hopf bifurcation at a Reynolds number that lies in between 30 and 35. With the further increase in Reynolds number, transition-in-wake occurs at $Re = 105 - 110$ (Thompson *et al.* (2006)). The critical Reynolds number at which transition occurs in the free shear layers is still unknown, though, Wu *et al.* (2005) claim that their Reynolds number range ($1.8 \times 10^3 - 2.7 \times 10^4$) was in the TrSL regime. There is no further information in the literature about the high Reynolds number flows.

1.2 Motivation

It is evident from the preceding section that the flow past uniform circular cylinders and (to some extent) uniform flat plates have been extensively studied in detail. In contrast, the three-dimensionalities, extrinsically induced by the tapered bluff-bodies (e.g. tapered circular cylinders, tapered flat plates) are least explored.

The credit for studying such a complex flow case for the first time goes to Gaster (1969). In his famous experimental study on slender cones Gaster (1969) found that even a small linear variation of the diameter along the span could induce complex three-dimensionalities in the wake. Such linear variations of the local diameter imply a linear variation of the local Reynolds number along the span. Further Gaster (1969) observed that the spanwise vortex filaments were shedding at an angle to the axis of the cone and were experiencing vortex dislocations. Since then, some experimental and numerical studies have been carried out in this field (see article 5 for all the references). However, almost all the previous studies on the flow past linearly tapered circular cylinders are either in the laminar vortex shedding regime or in the turbulent flow regime. It is therefore not clear at this stage how the flow responds in both the steady separation regime and also in the transition-in-wake regime.

Following the successful findings of "*cellular vortex shedding*" in the wake of cones, Gaster & Ponsford (1984) went on to investigate the wake of tapered flat plates at high Reynolds numbers. Their hot-wire measurements, how-

ever, failed to capture any cellular vortex shedding. On the contrary, Castro & Rogers (2002) and Castro & Watson (2004) performed similar hot-wire measurements in the wake of tapered flat plates and they have observed cellular vortex shedding. The disagreement between the two experimental findings therefore adds more confusion and there is no further evidence in the literature to prove (or disprove) that cellular vortex shedding also occurs in the wake of tapered flat plates.

An in-depth and comprehensive study of the wake behind tapered circular cylinders and tapered flat plates is therefore awaited. The above issues will be addressed for the first time in the present doctoral thesis.

Chapter 2

Numerical Simulation

2.1 Governing equations of fluid motion

All fluid motions of Newtonian fluids (where the continuum approximation is valid) are governed by a system of dynamical equations, namely the *Navier-Stokes* equations,

$$\left[\frac{\partial \rho}{\partial t} + U_j \frac{\partial \rho}{\partial x_j}\right] + \rho \frac{\partial U_j}{\partial x_j} = 0 \tag{2.1}$$

$$\rho \left[\frac{\partial U_i}{\partial t} + U_j \frac{\partial U_i}{\partial x_j}\right] = -\frac{\partial P}{\partial x_i} + \frac{\partial {T_{ij}}^{(v)}}{\partial x_j} \tag{2.2}$$

where, $U_i = U_i(\vec{x}, t)$, is a function of space $\vec{x}$ and time t and ρ denotes the density of the fluid. $T_{ij}^{(v)}(\vec{x}, t)$ is the viscous stress tensor and $P(\vec{x}, t)$ is the pressure.
The Newtonian closure for the viscous stress tensor relates it to the fluid motion using a property of fluid, molecular viscosity (μ).

$$T_{ij}^{(v)} = 2\mu \left(S_{ij} - \frac{1}{3} S_{kk} \delta_{ij}\right) \tag{2.3}$$

where, S_{ij} is the instantaneous strain rate tensor given by,

$$S_{ij} = \frac{1}{2}\left(\frac{\partial U_i}{\partial x_j} + \frac{\partial U_j}{\partial x_i}\right) \tag{2.4}$$

In the present thesis, it is always assumed that the flow is incompressible and isothermal. Thus, equation (2.1) and (2.2) reduces to,

$$\frac{\partial U_j}{\partial x_j} = 0 \tag{2.5}$$

$$\left[\frac{\partial U_i}{\partial t} + U_j \frac{\partial U_i}{\partial x_j}\right] = -\frac{1}{\rho}\frac{\partial P}{\partial x_i} + \nu \frac{\partial^2 U_i}{\partial x_j \partial x_j} \tag{2.6}$$

2.2 Numerical solution to the Navier-Stokes equations

A complete description of a three-dimensional flow of a Newtonian fluid, where the flow variables are a function of space and time can only be obtained by solving the Navier-Stokes equations numerically. This numerical approach, when applied to solve transitional and turbulent flows is popularly called Direct Numerical Simulation (see Moin & Mahesh (1998) and Sandham (2002) for detailed reviews). For laminar flows, though, it would be appropriate to call it just Navier-Stokes solution (by convention). Conceptually, DNS is rather an easy approach to solve flow problems, since it involves no modeling of transition or turbulence. In practice, however, DNS demands high performance computational resources. This is because in DNS the governing equations are discretized and integrated such that all physically relevant scales are resolved in time and space. In order to achieve this massive parallel computers are required. And even with such facilities available one is restricted to low Reynolds number flow cases which are mostly of academic interest.

The code MGLET

In the present thesis, the incompressible Navier-Stokes equations (2.5, 2.6) were solved in 3D space and time using a Finite Volume code called MGLET (Manhart *et al.* (2001); Manhart (2004)). The history of MGLET dates back to early 1990s when Werner (1991) began the work on an efficient finite volume code for Large Eddy Simulations and Direct Numerical Simulations of turbulent flows. In those days MGLET was a single processor code with second-order accuracy in time and space. Since then the code has steadily been developed into today's version which, among other things, offers various numerical schemes for spatial and temporal discretization, parallelization using Message Passing Interface, zonal grid refinement and the possibility to implement arbitrary shaped bodies in the Cartesian grid (Tremblay *et al.* (2001); Tremblay (2001); Peller *et al.* (2006)). (some recent publications in which MGLET has been used to solve other complex flow cases: Neumann & Wengle (2004); Krogstad *et al.* (2005); Schwertfirm *et al.* (2007); Breuer *et al.* (2008)).

Numerical schemes, the solver and the grid

In all the computations, staggered Cartesian grid arrangement was used. Spatial discretization of the convective and diffusive fluxes was carried out using a 2^{nd} order central-differencing scheme. The momentum equations are advanced in time by a fractional time stepping using a 3^{rd} order explicit Runge-Kutta scheme (Williamson (1980); Ferziger & Peric (1996)). For the

Poisson equation, Stone's incomplete LU decomposition method (Strongly Implicit Procedure) was used (Stone (1968); Ferziger & Peric (1996)).

The time-step chosen in each of the cases was such that it satisfies the CFL condition. In grid generation care was taken to have a sufficient number of grid points upstream of the bluff-bodies, in order to capture the Hiemenz-like boundary layer (Panton (1997)) at the stagnation point. For more information regarding the computational domain, grid, etc see individual articles.

Boundary conditions

At solid boundaries, Dirichlet boundary condition was used for the velocities and Neumann boundary condition for the pressure. These boundary conditions were implemented by using a direct forcing Immersed Boundary Method (see article 1 and article 7). The detailed derivation, validation and implementation of this method in MGLET were explained in Peller *et al.* (2006). For other boundary and initial conditions see individual articles.

Chapter 3

Summary of Articles

In this chapter a brief summary of each of the nine articles attached will be presented. The first six papers concern the wake dynamics from uniform and tapered cylinders. The last three papers focus on wake dynamics from uniform and tapered plates. The flow regimes investigated in general varied from steady laminar wakes to turbulent wakes. The results documented in all the nine articles were obtained from three-dimensional numerical calculations. In article 4, however, some results from the in-house PIV measurements were presented.

3.1 Article 1

Simulation of unsteady flow past tapered circular cylinders using an immersed boundary method

This is the first simulation performed during the present doctoral thesis work and hence the results are preliminary in nature. The main objective was to study the numerical aspects of the code and estimate the performance of the Immersed Boundary Method. Both steady laminar wake and unsteady laminar wake behind a linearly tapered circular cylinder was investigated. The results from both the simulations were qualitatively in good agreement with the previous studies. However, owing to the coarse grid resolutions adopted, quantitative deviations were observed. The overall computational performance of the Immersed Boundary Method was found to be very promising when compared to the boundary fitted or unstructured grid solvers.
Part of this work was initially presented at the *Sixth Euromech Fluid Mechanics Conference, Stockholm, Sweden, 2006*.

3.2 Article 2

Steady viscous flow past a tapered cylinder

In the preceding paper, numerical oscillations were observed in the steady laminar flow case due to the coarse grid resolution adopted close to the cylinder body. This issue was resolved in the present article, where a high-definition grid was used to study the same steady flow case. The geometrical and flow parameters were the same as in the preceding article. Pressure-driven secondary flow along the span of the cylinder was observed, both in the front stagnation zone and also in the wake of the cylinder. In spite of this secondary motion, the primary flow in planes perpendicular to the cylinder axis was found to be practically indistinguishable from the two-dimensional flow past a uniform circular cylinder.

3.3 Article 3

Direct numerical simulation of vortex shedding behind a linearly tapered circular cylinder

After studying the unsteady laminar wake in article 1 and the steady laminar wake in article 2, the transitional wake behind a tapered circular cylinder was investigated in the present article. The taper ratio of the cylinder was intentionally chosen to be same as that in the preceding two articles (article 1 and article 2). The local Reynolds number variation along the span was such that both the laminar and the transitional flow regimes co-existed along the span. The results were preliminary in nature, in the sense that the total sampling time adopted for performing frequency analysis was modest and some limited results were extracted during the post-processing.

3.4 Article 4

DNS and PIV study of the 3D wake behind tapered circular cylinders

In this article the DNS results from article 3 was compared with the in-house PIV measurements carried out at higher Reynolds numbers. Due to practical issues in the laboratory the Reynolds number in the experiments could not be matched with the DNS case. The taper ratio, though, was same in both the cases. Therefore, the objective was not to have a one-to-one quantitative comparison between the numerical and the experimental data but rather to study the qualitative features in common.

3.5 Article 5

Cellular vortex shedding behind a tapered circular cylinder

This paper is an extension of article 3. A very long time sampling was adopted for the statistics to be fully converged to a stationary state. In addition to frequency (both Fourier and Wavelet) analysis a more detailed investigation of the spanwise two-point correlations, instantaneous vortical structures and the Reynolds-averaged statistics were carried out. The spanwise variations of the velocity and the pressure fields were also studied. A complex secondary flow pattern was observed in the wake of the cylinder, whose behaviour was attributed to the intrinsic secondary instabilities. Upstream the cylinder, however, the secondary flow was driven by a spanwise pressure gradient.

3.6 Article 6

Asymmetries in the wake behind a circular cylinder in planar shear flow

In this article planar shear flow past a uniform circular cylinder was investigated in the transition-in-wake regime and the results were compared with an uniform inflow case. Except the inflow condition, the geometrical and flow parameters were the same in both the cases. On comparing the results, it was observed that the Strouhal number, mean separation angle and the wavelength of mode B surprisingly match in both the cases. In the planar shear flow case, the vortices shed from either side of the cylinder seems to merge further downstream and may eventually lead to complete suppression of the vortex shedding. This, however, has to be further verified.

3.7 Article 7

Cellular vortex shedding in the wake of a tapered plate

In the present article both steady laminar wake and the turbulent wake behind a tapered plate was investigated. Pressure-driven spanwise secondary motion was observed in both the flow regimes. The length of the recirculation bubble in the steady laminar case was found to be in good agreement with non-tapered (i.e. uniform) plate data. Thus the flow field in planes perpendicular to the plate axis can be considered as quasi-two-dimensional in the steady laminar flow regime. In the turbulent flow case, however, it was observed that a tapered plate creates longer formation length coupled with

higher base pressure than compared to non-tapered (i.e. uniform) plates. A significant base pressure reduction towards the narrow end of the plate, which results in a corresponding increase in Strouhal number, was also noticed.
Parts of the results presented as a poster at the *International Symposium Fluids Days, Bangalore, India, 2007*.

3.8 Article 8

Turbulent wake behind a normal flat plate

In this article the turbulent wake behind a uniform flat plate placed perpendicular to an oncoming stream have been examined. In addition to frequency analysis and vortical structure information, a detailed analysis of Reynolds averaged statistical quantities were presented. The coupling between the base pressure and the vortex formation process was explored in the present study. It was observed that the reduction in base pressure causes a surge in the shedding frequency and hence produces a shorter recirculation bubble.

3.9 Article 9

Cellular vortex shedding in the wake of a tapered plate at low Reynolds numbers

Vortex shedding from uniform and tapered plates in the laminar flow regime was analysed in the present article. Except the Reynolds number, the flow configuration remains same as in article 7. Three different flow regimes were observed along the span of the tapered plate. The wake flow was steady behind the narrow end of the plate. Vortex shedding occured along the mid-span. Towards the wide end of the plate complex streamwise vortical structures were noticed. In spite of this, the spanwise secondary motion observed was driven by a pressure-gradient. The impact of the base pressure on the shedding frequency and the vortex formation process was also explored.

Bibliography

BARKLEY, D. & HENDERSON, R. D. 1996 Three-dimensional Floquet stability analysis of the wake of a circular cylinder. *J. Fluid Mech.* **322**, 215–241.

BLOOR, M. S. 1964 The transition to turbulence in the wake of a circular cylinder. *J. Fluid Mech.* **19**, 290–304.

BREUER, M., PELLER, N., RAPP, CH. & MANHART, M. 2008 Flow over periodic hills−numerical and experimental study in a wide range of reynolds numbers. *Computers & Fluids* **(in press)**.

BURESTI, G. 2000 Bluff-body aerodynamics. In *Proc. International Advance School on Wind Excited and Aeroelastic Vibrations of Structures* (ed. G. Solari).

CASTRO, I. P. & ROGERS, P. 2002 Vortex shedding from tapered plates. *Exp. Fluids* **33**, 66–74.

CASTRO, I. P. & WATSON, L. 2004 Vortex shedding from tapered, triangular plates: taper and aspect ratio effects. *Exp. Fluids* **37**, 159–167.

COUTANCEAU, M. & BOUARD, R. 1977 Experimental determination of the main features of the viscous flow in the wake of a circular cylinder in uniform translation. part 1. steady flow. *J. Fluid Mech.* **79**, 231–256.

COUTANCEAU, M. & DEFAYE, J.-R. 1991 Circular cylinder wake configurations: a flow visualization survey. *Appl. Mech. Rev.* **44**, 255–305.

DENNIS, S. C. R., WANG QIANG, COUTANCEAU, M. & LAUNAY, J. L. 1993 Viscous flow normal to a flat plate at moderate reynolds numbers. *J. Fluid Mech.* **248**, 605–635.

FERZIGER, J. H. & PERIC, M. 1996 *Computational Methods for Fluid Dynamics*. Springer.

FEY, U., KÖNIG, M. & ECKELMANN, H. 1998 A new Strouhal-Reynolds number relationship for the circular cylinder in the range $47 < \mathrm{R}e < 2 \times 10^5$. *Phys. Fluids* **10**, 1547–1549.

FORNBERG, B. 1980 A numerical study of steady viscous flow past a circular cylinder. *J. Fluid Mech.* **98**, 819–855.

GASTER, M. 1969 Vortex shedding from slender cones at low reynolds numbers. *J. Fluid Mech.* **38**, 565–576.

GASTER, M. & PONSFORD, P. J. 1984 The flows over tapered flat plates normal to the stream. *Aeronautical J.* **88**, 206–212.

HUDSON, J. D. & DENNIS, S. C. R. 1985 The flow of a viscous incompressible fluid past a normal flat plate at low and intermediate reynolds numbers: the wake. *J. Fluid Mech.* **160**, 369–383.

IMAI, I. 1957 *Univ. Maryland Inst. Fluid Dyn. Appl. Maths. Tech. Rep.* 104.

KROGSTAD, P.-Å., ANDERSSON, H. I., BAKKEN, O. M. & ASHRAFIAN, A. 2005 An experimental and numerical study of channel flow with rough walls. *J. Fluid Mech.* **530**, 327–352.

MANHART, M. 2004 A zonal grid algorithm for DNS of turbulent boundary layers. *Computers & Fluids* **33**, 435–461.

MANHART, M., TREMBLAY, F. & FRIEDRICH, R. 2001 MGLET: a parallel code for efficient DNS and LES of complex geometries. In *Parallel Computational Fluid Dynamics 2000* (ed. Jensen et al.), pp. 449–456. Elsevier Science B. V.

MOIN, P. & MAHESH, K. 1998 Direct numerical simulation: A tool in turbulence research. *Annu. Rev. Fluid Mech.* **30**, 539–578.

NEUMANN, J. & WENGLE, H. 2004 Coherent structures in controlled separated flow over sharp-edged and rounded steps. *J. Turbulence* **5**, No. 22.

PANTON, R. L. 1997 *Incompressible flow*. Wiley-Inderscience.

PELLER, N., LE DUC, A., TREMBLAY, F. & MANHART, M. 2006 High-order stable interpolations for immersed boundary methods. *Int. J. Numer. Meth. Fluids* **52**, 1175–1193.

ROSHKO, A. 1954 On the development of turbulent wakes from vortex streets. *Tech. Rep.* 1191. NACA.

ROSHKO, A. 1993 Perspectives on bluff body aerodynamics. *J. Wind Eng. and Industrial Aerodyn.* **49**, 79–100.

SAHA, A. K. 2007 Far-wake characteristics of two-dimensional flow past a normal flat plate. *Phys. Fluids* **19**, 128110.

SANDHAM, N. D. 2002 Introduction to direct numerical simulation. In *Closure Strategies for Turbulent and Transitional Flows* (ed. B. E. Launder & N. D. Sandham), pp. 248–266. Cambridge University Press.

SCHWERTFIRM, F., GRADL, J., SCHWARZER, H. C., PEUKERT, W. & MANHART, M. 2007 The low reynolds number turbulent flow and mixing in a confined impinging jet reactor. *Int. J. Heat Fluid Flow* **28**, 1429–1442.

STONE, H. L. 1968 Iterative solution of implicit approximations of multidimensional partial differential equations. *SIAM J. Numer. Anal.* **5**, 530–558.

THOMPSON, M. C., HOURIGAN, K., RYAN, K. & SHEARD, G. J. 2006 Wake transition of two-dimensional cylinders and axisymmetric bluff bodies. *J. Fluids Struct.* **22**, 793–806.

TREMBLAY, F. 2001 Direct and large-eddy simulation of flow around a circular cylinder at subcritical Reynolds numbers. PhD thesis, Technische Universität München, Munich, Germany.

TREMBLAY, F., MANHART, M. & FRIEDRICH, R. 2001 DNS and LES of flow around a circular cylinder at a subcritical reynolds number with cartesian grids. In *LES of Complex Transitional and Turbulent Flows* (ed. R. Friedrich & W. Rodi), pp. 133–150. Kluwer Academic Publishers.

WERNER, H. 1991 Grobstruktursimulation der turbulenten strömung über eine querliegende rippe in einem plattenkanal bei hoher reynoldszahl. PhD thesis, Universität der Bundeswehr München, Neubiberg, Germany.

WILLIAMSON, C. H. K. 1992 The natural and forced formation of spot-like dislocations in the transition of a wake. *J. Fluid Mech.* **243**, 393–441.

WILLIAMSON, C. H. K. 1996 Vortex dynamics in the cylinder wake. *Annu. Rev. Fluid Mech.* **28**, 477–539.

WILLIAMSON, C. H. K. & BROWN, G. L. 1998 A series in $1/\sqrt{Re}$ to represent the Strouhal-Reynolds number relationship of the cylinder wake. *J. Fluids Struct.* **12**, 1073–1085.

WILLIAMSON, J. H. 1980 Low−storage Runge−Kutta schemes. *J. Comput. Phys.* **35**, 48–56.

WU, S. J., MIAU, J. J., HU, C. C. & CHOU, J. H. 2005 On low-frequency modulations and three-dimensionality in vortex shedding behind a normal plate. *J. Fluid Mech.* **526**, 117–146.

ZDRAVKOVICH, M. M. 1997 *Flow around Circular Cylinders. Volume 1: Fundamentals*. Oxford Univ. Press.

ZDRAVKOVICH, M. M. 2002 *Flow around Circular Cylinders. Volume 2: Applications*. Oxford Univ. Press.

Article 1

Simulation of unsteady flow past tapered circular cylinders using an immersed boundary method

Narasimhamurthy, V. D., Schwertfirm, F., Andersson, H. I. & Pettersen, B.

In *Proc. ECCOMAS European Conference on Computational Fluid Dynamics, Egmond aan Zee, The Netherlands*, TU Delft, 2006.

European Conference on Computational Fluid Dynamics
ECCOMAS CFD 2006
P. Wesseling, E. Oñate and J. Périaux (Eds)

SIMULATION OF UNSTEADY FLOW PAST TAPERED CIRCULAR CYLINDERS USING AN IMMERSED BOUNDARY METHOD

Vagesh D. Narasimhamurthy[†], Florian Schwertfirm[‖], Helge I. Andersson[†] and Bjørnar Pettersen[§]

[†]Norwegian University of Science and Technology (NTNU), Dept. of Energy and Process Engineering, NO-7491 Trondheim, Norway
e-mail: vagesh.d.narasimhamurthy@ntnu.no

[‖]Technische Universität München, Fachgebiet Hydromechanik, 80333 Munich, Germany

[§]Norwegian University of Science and Technology (NTNU), Dept. of Marine Technology, NO-7491 Trondheim, Norway

Key words: Cellular vortex shedding, Tapered cylinder, Immersed Boundary Method, Oblique vortex shedding

Abstract. *Three-dimensional numerical calculations of laminar vortex shedding behind a linearly tapered circular cylinder with taper ratio 75:1 have been carried out at a Reynolds number 131 (based on the large diameter and the uniform inflow velocity) using a Finite Volume code. Computations were performed on a staggered-Cartesian grid and a direct forcing Immersed Boundary Method (IBM) was used to transform the boundary condition at the solid surface into internal boundary conditions at the nodes of the Cartesian grid. Results showed a pattern of discrete oblique shedding cells, which included both vortex dislocation and vortex splitting. The local Strouhal number versus local Reynolds number curve showed excellent qualitative agreement with the experimental results reported by Piccirillo and Van Atta in 1993. However, quantitative deviations exist between the two techniques. Numerical noise (oscillations) was observed along the span in the steady flow calculation with Reynolds number 40, the reason for which has to be further investigated. The overall computational performance of the IBM proved to be very promising when compared to the boundary fitted or unstructured grid solvers.*

1 INTRODUCTION

Three-dimensional (3-D) vortex shedding may occur in the wake of a circular cylinder for three fundamentally different reasons: i) the vortex dynamics in the wake may be intrinsically three-dimensional, ii) the inflow may be non-uniform, and iii) the cylinder geometry may itself be non-uniform. In the present paper we focus on the latter category,

i.e. on the three-dimensionalisation induced by a spanwise variation of the cylinder diameter. Tapered cylinders are basically truncated cones and are of great practical relevance (e.g., oil-platform legs, chimneys and light houses). They offer a geometrically simple configuration with complex flow physics in the near wake. Depending on the taper ratio ($R_T = l/(d_2 - d_1)$; where l is the length of the circular cylinder and d_2 and d_1 denote the diameter of its wide and narrow ends, respectively) the variation of local Reynolds number along the span of the cylinder may produce a range of distinct flow-regimes (e.g., steady wake, laminar unsteady wake and turbulent wake) exist side by side in the same geometry.

Until recently, the majority of numerical calculations of the flow over tapered cylinders were performed using boundary-fitted grids (Jespersen & Levit[1] and Vallès et al.[2] have performed calculations in the laminar unsteady wake regime) but solvers for curvilinear or unstructured grids are less efficient than Cartesian solvers in terms of computational time and memory requirements[11]. Recently Parnaudeau et al.[3,4] have performed turbulent flow calculations using a direct forcing Immersed Boundary Method (IBM). However their Reynolds number Re_2 (based on the large diameter d_2 and the uniform inflow velocity U) was in another range compared to the present investigation. Vallès et al.[2] have carried out flow calculations for two different R_T (75:1 and 100:1) and in the Re_2 range 131-178. They found that the numerical results compared surprisingly well with the extensive laboratory experiments reported by Piccirillo & Van Atta[5]. However, the predicted variation of local Strouhal number ($St_{local} = f_s d_{local}/U$; where f_s is the shedding frequency) versus local Reynolds number ($Re_{local} = U d_{local}/\nu$) did not match the curve fit $St = 0.195 - 5.0/Re$ deduced from the laboratory experiments[5]. In the present study we used a direct forcing IBM[6,7] to clarify some deviations between the simulations and the experiments. A detailed investigation of numerical noise level and its origin was carried out by studying steady-flow over the cylinder at $Re_2 = 40$.

2 FLOW CONFIGURATION AND PARAMETERS

The computational domain was as shown in figure 1. All dimensions were normalised by the diameter at the wide end ($d_2 = 1$). The normalised diameter at the narrow end was $d_1 = 0.556$ and the length of the cylinder was $l = 33.461$. The taper ratio of the cylinder was defined as,

$$R_T = \frac{l}{(d_2 - d_1)} = 75 : 1 \tag{1}$$

and was the same in both cases considered. The Reynolds number based on the uniform inflow velocity ($U = 1$) and the diameters at wide, narrow and center-span ($d_{cs} = 0.778$) of the cylinder for both laminar unsteady wake and steady wake flow were as shown in Table 1. The kinematic viscosity was therefore different in the two cases. The Reynolds numbers were well below 190 at which the intrinsic 'mode A' instability is known to occur in otherwise two-dimensional configurations.

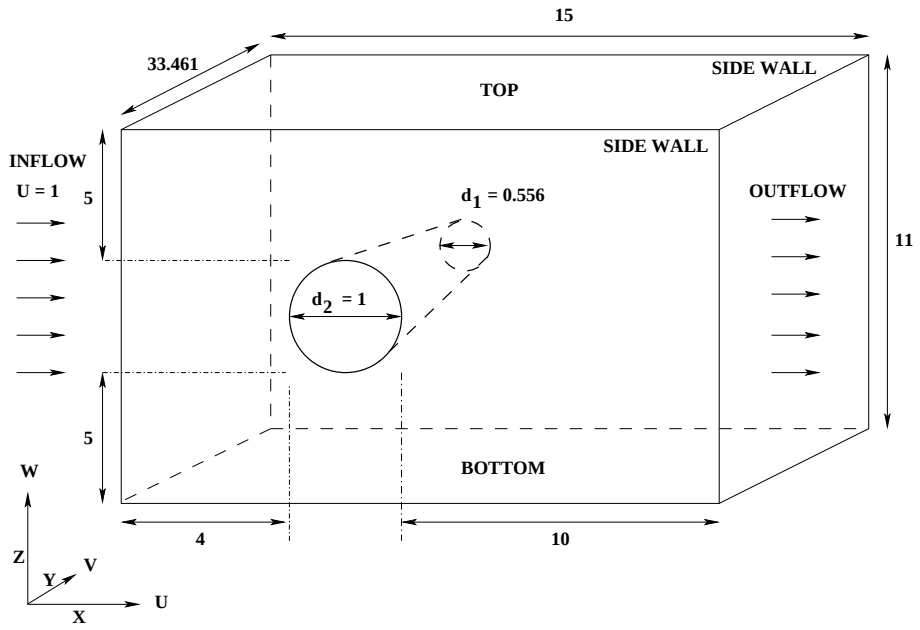

Figure 1: Computational domain (not to scale)

Case	$\mathbf{Re_2}$	$\mathbf{Re_1}$	$\mathbf{Re_{cs}}$
Laminar unsteady wake	131	72.83	101.91
Steady wake	40	22.24	31.12

Table 1: Reynolds number

3 NUMERICAL METHOD

3.1 Instantaneous equations of motion

All fluid motions of Newtonian fluids (where the continuum approximation is valid) are governed by a system of dynamical equations, namely the Navier Stokes (N-S) equations. For incompressible flows, the N-S equations reduce to,

$$\frac{\partial \tilde{u}_j}{\partial \tilde{x}_j} = 0 \tag{2}$$

$$\left[\frac{\partial \tilde{u}_i}{\partial t} + \tilde{u}_j \frac{\partial \tilde{u}_i}{\partial x_j}\right] = -\frac{1}{\rho}\frac{\partial \tilde{p}}{\partial x_i} + \nu \frac{\partial^2 \tilde{u}_i}{\partial x_j \partial x_j} \tag{3}$$

where, $\tilde{u}_i = \tilde{u}_i(\vec{x}, t)$, is a function of space $\vec{x}$ and time t and ν and ρ denote the kinematic viscosity and the density of the fluid.

3.2 Numerical schemes, the solver and the grid

The governing equations were solved in 3-D space and time using a Finite Volume code[8,9]. The code uses staggered Cartesian grid arrangement. Time marching was carried

out using a 3^{rd} order explicit Runge-Kutta scheme for the momentum equations and an iterative SIP (Strongly Implicit Procedure) solver[10] for the Poisson equation. Spatial discretization was carried out using a 2^{nd} order central-differencing scheme. In all the computations we employed non-equidistant Cartesian grids in X-Z plane. Equidistant grid points were used in Y-direction. As an example a fine mesh of 3.3x10^6 grid points is shown in Figure 2. In grid generation care was taken to have a sufficient number of grid points upstream of the cylinder, in order to capture the Hiemenz-like boundary layer[14] at the stagnation point. The boundary layer thickness δ was given by,

$$\delta = \frac{1.2d}{\sqrt{Re_d}} \tag{4}$$

where, d is the local diameter at any span-wise position and Re_d is the Reynolds number based on d. The boundary layer thickness δ for both unsteady and steady cases was estimated as shown in Table 2.

Case	δ_2	δ_1
Laminar unsteady wake	0.10484	0.07808
Steady wake	0.18973	0.14147

Table 2: Hiemenz boundary layer thickness in the stagnation zone

3.3 Boundary conditions

Boundary conditions were as shown in Table 3. A uniform inflow velocity profile $U = 1$ was fixed at the inlet. Convective and diffusive fluxes were set to zero on both sides and top and bottom (see figure 1). At the outflow, Neumann boundary condition was used for velocities and pressure was set to zero. The no-slip boundary condition on the cylinder body was implemented by using a direct forcing IBM which will be discussed in the following section.

Face	**Boundary condition**
Inflow	$U = 1; V = W = 0; \partial P/\partial X = 0$
Side walls	$V = 0; \partial U/\partial Y = \partial W/\partial Y = \partial P/\partial Y = 0$
Top and Bottom walls	$W = 0; \partial U/\partial Z = \partial V/\partial Z = \partial P/\partial Z = 0$
Outflow	$\partial U/\partial X = \partial V/\partial X = \partial W/\partial X = 0; P = 0$

Table 3: Boundary conditions

4 IMMERSED BOUNDARY METHOD

In the present computation we used a *direct forcing* IBM[6,7] to transform the boundary condition at the solid cylindrical surface into internal boundary conditions at the nodes of the Cartesian grid. The forcing is called *direct* because the boundary condition remains

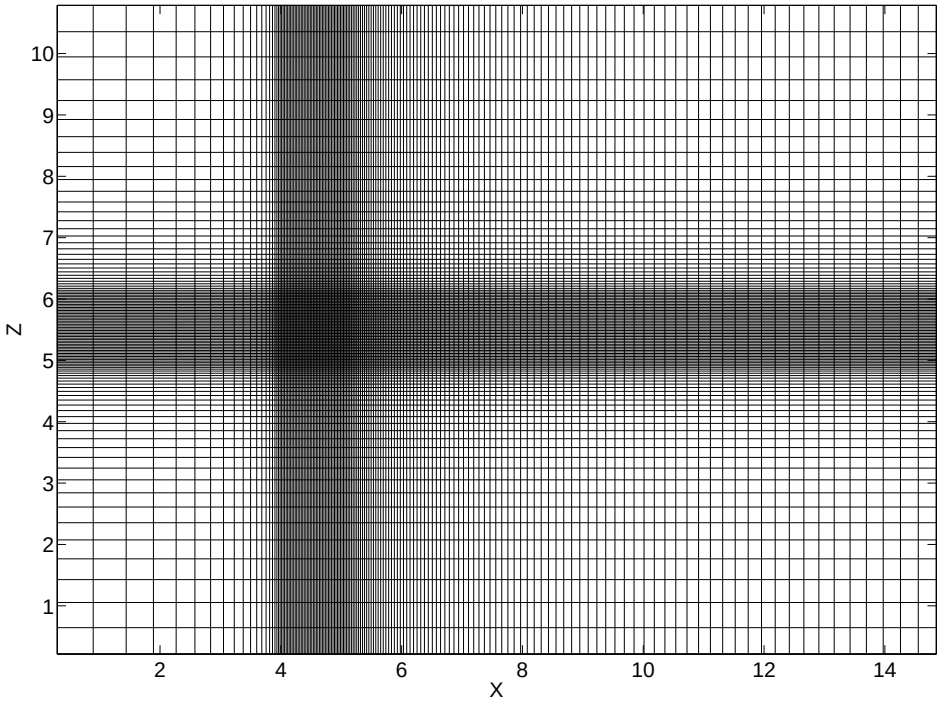

Figure 2: Mesh in X-Z plane: 3.3x10^6 grid points in total ([N_X x N_Y x N_Z] = [150 x 200 x 110])

the same at each time step regardless of the characteristic frequencies of the flow (see Iaccarino & Verzicco[12] and Mittal & Iaccarino[13] for an extensive review of different IBMs). Direct forcing is practically the same as enforcing the boundary condition within the flow. When the boundary does not coincide with Cartesian grid points, an interpolation is required. Thus the accuracy of IBM depends on the interpolation technique, the order of interpolation and the direction of interpolation. In this section we discuss the blocking algorithm and the interpolation technique used.

4.1 Blocking algorithm

The cylinder surface to be immersed in the Cartesian mesh was represented by a mesh consisting of triangles. The blocking of the Cartesian cells intersected by these triangles was carried out as follows:
i) The intersection points of triangle surface and the coordinate line passing through the pressure cell center were identified. The pressure cells containing those intersection points were blocked, as shown in Figure 3.
ii) In the second sweep all the pressure cells within the blocked surface were blocked.
iii) Finally all the velocity cells corresponding to blocked pressure cells were blocked.

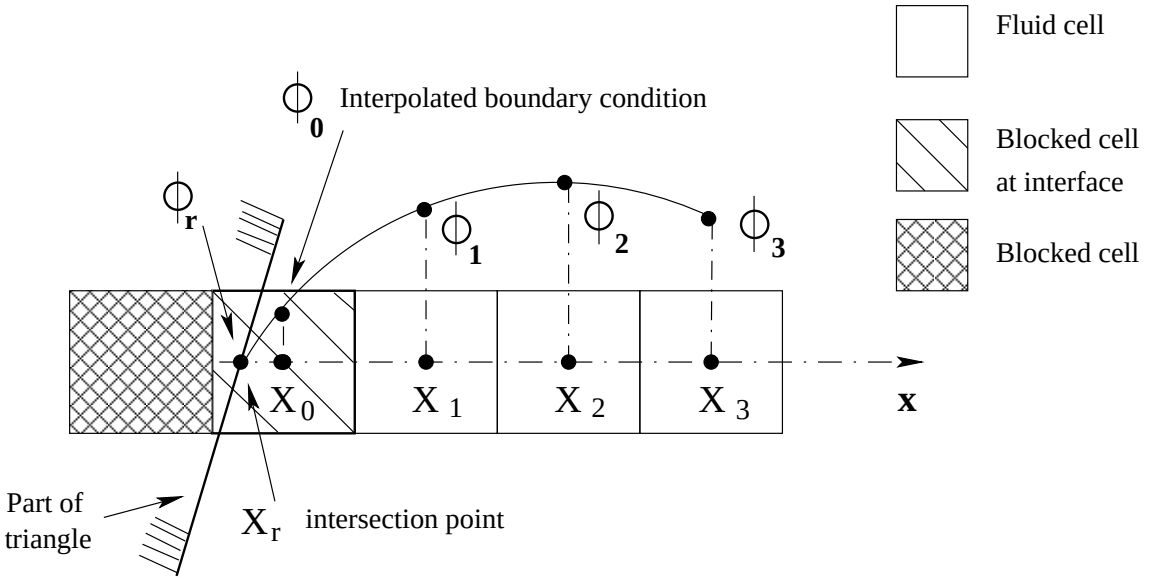

Figure 3: 1-Dimensional stencil configuration for interpolation in x-direction

All these blocked cells were marked inactive and were excluded from certain steps in the time-marching algorithm (e.g., convergence check).

4.2 Interpolation technique

In Figure 3, ϕ_0 is the internal boundary condition value to be determined by interpolation. X_r is the intersection point between the triangle and the coordinate line. ϕ_r is the value at X_r which is known (the value on the wall). Thus by considering the neighbouring variables ϕ_i ($\phi_1, \phi_2, \phi_3, etc$) the stencils are formed. A general stencil formulation for ϕ_0 looks like,

$$\phi_0 = (\sum_{i=1}^{N} \alpha_i.\phi_i) + \alpha_r.\phi_r \tag{5}$$

where, N is the number of neighbouring cells involved in the interpolation. The interpolation coefficients α_i and α_r depend on the interpolation technique and geometry only and therefore were computed in a preprocessing step.

In the present simulation we used *least squares* interpolation of 3^{rd} order. The detailed derivation of this technique was explained in Peller et al.[6]. Using matrix stability analysis they studied the numerical stability of higher-order *Lagrange* and *least squares* interpolation and concluded that *least squares* interpolation of 3^{rd} order is very robust and numerically stable. Higher-order interpolation may indeed avoid strong grid-clustering in the wall vicinity but may not increase the accuracy of the solver (the spatial accuracy of the solver was 2^{nd} order as discussed in previous section). The stencil in each direction was 1-dimensional but Tremblay et al.[7] have employed *weighting* to account for three

dimensionality.

5 RESULTS AND DISCUSSION

5.1 Laminar unsteady flow

The unsteady flow calculations were carried out with two different grid resolutions. Table 4 illustrates the mesh parameters. N_X, N_Y, and N_Z correspond to the number of grid points in X, Y, and Z directions, respectively. Similarly N_{US} and N_{DS} correspond to the number of grid points upstream the cylinder and downstream the cylinder. Δ_{cyl} represents the grid cell size close to the cylinder in both X and Z directions.

Case	**Nodes**	$\mathbf{N_X}$	$\mathbf{N_Y}$	$\mathbf{N_Z}$	$\mathbf{N_{US}}$	$\mathbf{N_{DS}}$	$\mathbf{\Delta_{cyl}}$
Coarse mesh	1.2x10^6	120	100	100	20	80	0.05
Fine mesh	3.3x10^6	150	200	110	20	90	0.025

Table 4: Grid parameters

The time step $\Delta t = 0.005$ was found to assure stability and appropriate both with respect to the CFL condition and von Neumann analysis. The coarse-mesh computations were performed on a single processor Linux-PC (Intel P4-3.2GHz with 1GB RAM) and the fine-mesh on 15 processors of SGI Origin 3800. A detailed comparison of computational performance of the present simulations and that of Vallès et al.[2] is shown in Table 5. A noteworthy distinction is that Vallès et al.[2] used an implicit time-stepping.

Case	**Computer**	**Nodes**	$\mathbf{\Delta t}$	**Iterations/Δt**	**cpu$\frac{\mathbf{S}}{\mathbf{\Delta t}}$**
Coarse mesh	Linux PC	1.2x10^6	0.005 d_2/U	15	3.9
Fine mesh	SGI Origin 3800	3.3x10^6	0.005 d_2/U	15	5
Vallès et al.[2]	Cray T3E	0.256x10^6	0.1 d_2/U	20	3060

Table 5: Computational performance

Flow visualization of 3-D vortex shedding could be carried out in many ways. In figure 4 and figure 5 the time evolution of the pressure along the span for both coarse mesh and fine mesh has been plotted. The instantaneous pressure was sampled along a line parallel to the axis of the cylinder located $2d_{cs}$ downstream the axis in X-direction and $1d_{cs}$ offset in Z-direction. The offset in Z-direction was carried out to detect only one side of the vortex street. An initial comparison between the two figures itself indicate the complex flow structure and vortex splitting. Both figures show a nearly periodic occurence of vortex splitting around the center span of the cylinder. However, this phenomenon of periodic occurence of vortex cells was more evident in the coarse mesh simulation. This could be due to the inability of the coarse mesh to capture the instabilities along the span. It should also be noted that the vortex shedding was more oblique in the fine mesh than on the coarse mesh. This point was further justified in figure 6, where iso-pressure contours for the fine mesh clearly indicate the larger shedding angle compared to the coarse mesh.

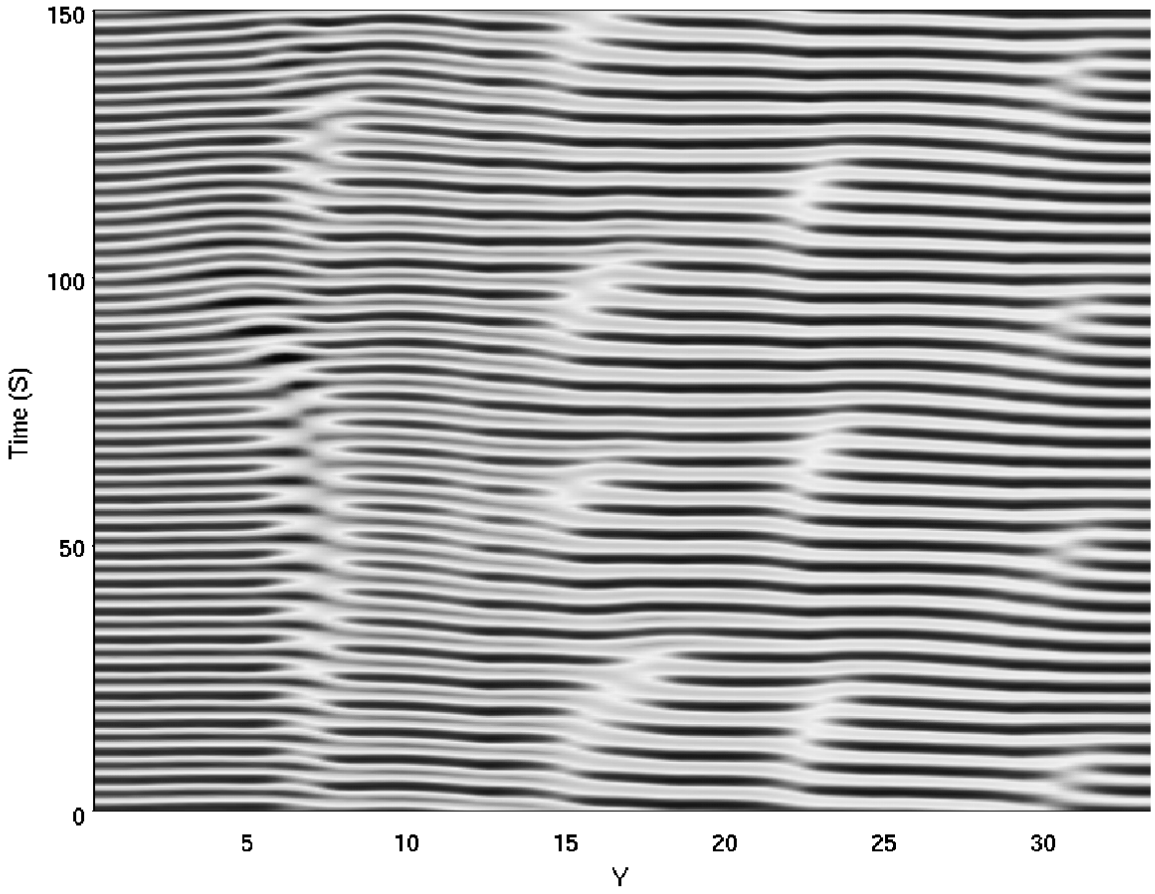

Figure 4: Time evolution of the pressure along the entire span: Coarse mesh

However further qualitative investigations were carried out by spectral analysis of pressure time traces.

Our primary objective was to investigate the significant deviations in the St_{local} versus Re_{local} curve between simulations[2] and experiments[5] and therefore the power spectrum of pressure time traces were investigated. In figure 7 Piccirillo & Van Atta's[5] curve-fit $St = 0.195 - 5.0/Re$ along with Williamson & Brown's[15] universal *St-Re* curve for straight uniform circular cylinders given by,

$$St = A + \frac{B}{\sqrt{Re}} + \frac{C}{Re} \tag{6}$$

where, $A = 0.2850, B = -1.3897$ and $C = 1.8061$, were plotted together with numerical results. (Note: In Vallès et al.[2] the present case corresponds to their *Case B* , which accidentally was mis-labelled as *Case C* in their *St-Re* figure) Both our coarse and fine

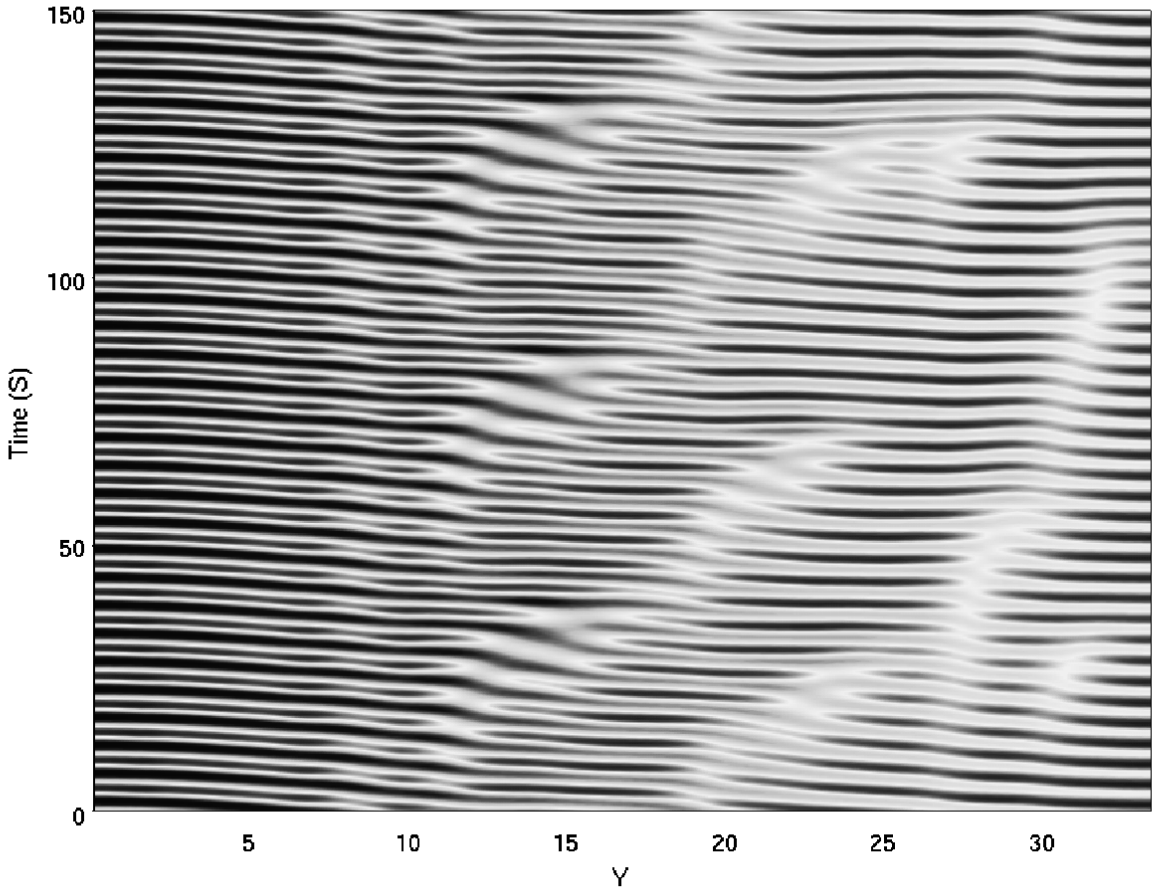

Figure 5: Time evolution of the pressure along the entire span: Fine mesh

mesh simulations clearly captured the distinct shedding cells with constant shedding frequency and fine splitting. It should be worth to mention here that our *St-Re* curve was very sensitive to the sampling time and we sampled the instantaneous pressure for nearly 300 d_2/U to get reliable statistics. Even though our simulations qualitatively reproduced what have been observed in the laboratory there still exists quantitative deviations both from the experiments[5] and the earlier simulation[2]. However, the trend of all computer simulations is similar. It should be noted that the experimental curve-fit was based on the Strouhal number values at the centre of each shedding cell (cell-center Strouhal number), whereas all the numerical results were based on a truly local Strouhal number for each spanwise location. In figure 8 shedding cell mid-point locations were compared with both experiment and other numerical results. Here also significant quantitative deviations exist between the different techniques. One possible reason could be the difference in boundary conditions in the laboratory set-up and computer calculations. However a further step

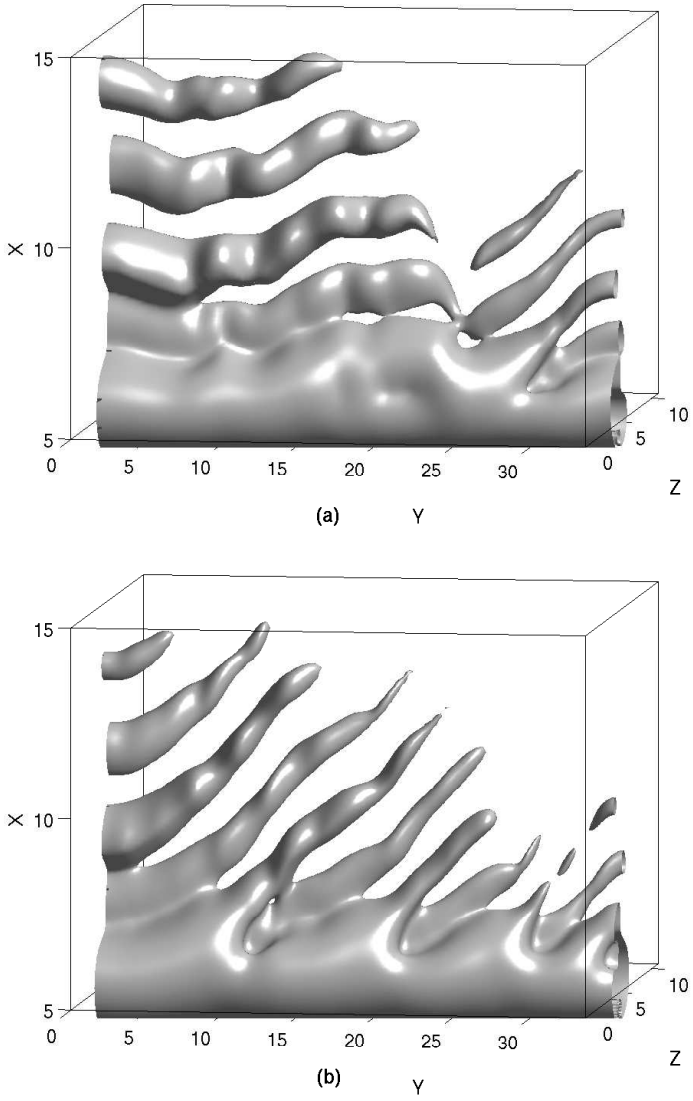

Figure 6: 3-dimensional iso-pressure contours. Contour level $\tilde{p}$ = - 0.1. (a)coarse mesh; (b)fine mesh. The flow direction is from bottom to top.

was taken to investigate the accuracy of our present approach by simulating a steady flow over the same configuration.

5.2 Steady flow

Steady flow calculations were performed with the same computational configuration as above by reducing Re_2 to 40. The flow was simulated only with the fine mesh. The objective was to avoid the unsteady effects and focus only on the numerical noise (if any). The spanwise numerical oscillations (if any) were studied by comparing the non-

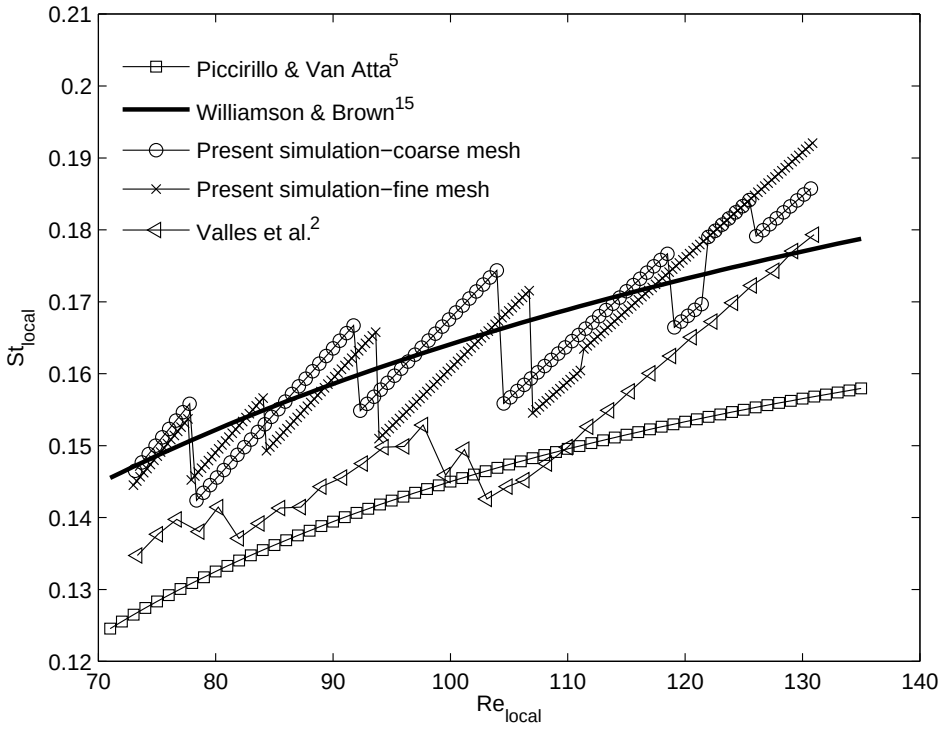

Figure 7: St_{local} versus Re_{local}

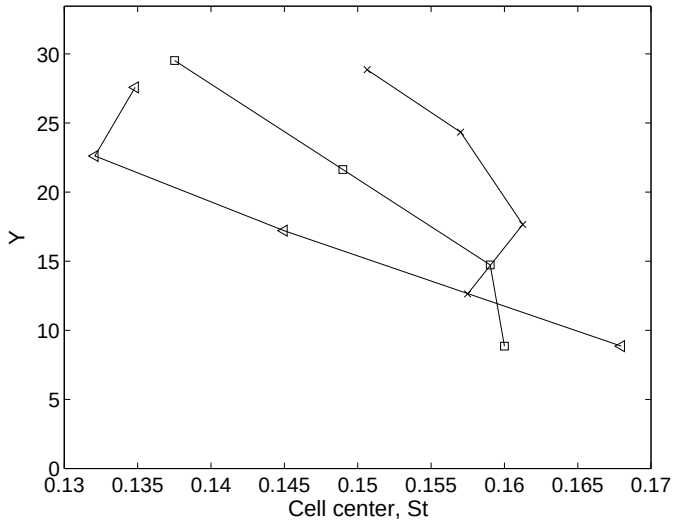

Figure 8: Shedding cell mid-point locations. Symbols are the same as in figure 7

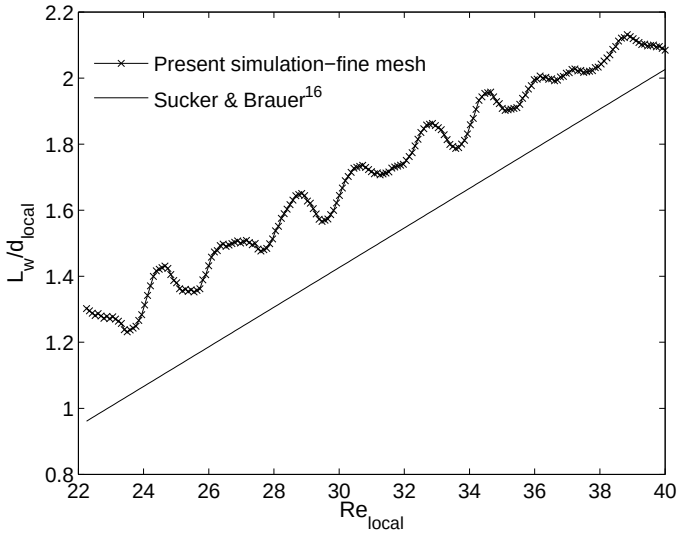

Figure 9: Non-dimensional steady wake length along the span

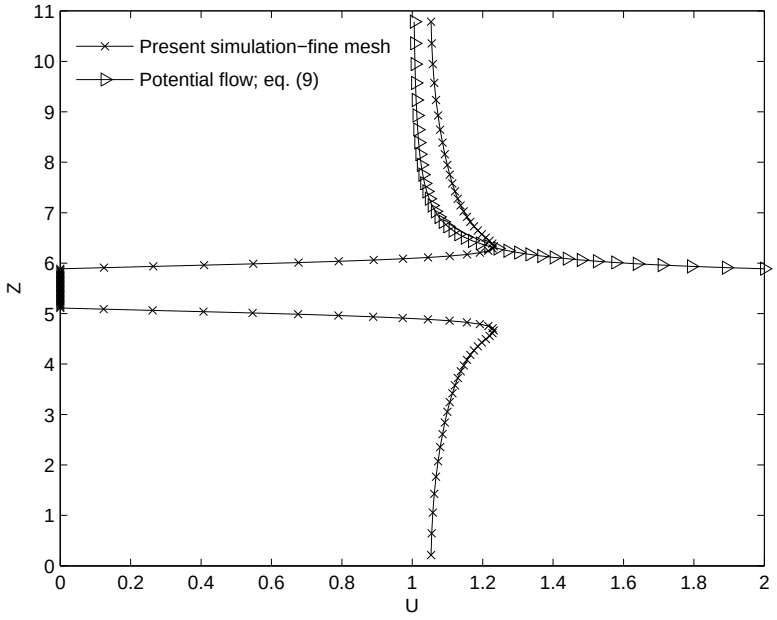

Figure 10: Variation of the streamwise velocity (U) profile in the cross-stream (Z) direction at X = 4.5 and Y = 16.7 (center-span of the cylinder)

dimensional bubble or wake length (L_w/d_{local}) for each spanwise position with Sucker & Brauer's[16] empirical curve fit for straight uniform circular cylinders. The empirical

relation was given by,

$$\frac{L_w}{d_{local}} = 0.12 Re_{local} - 0.748 \tag{7}$$

From figure 9, it is clear that small oscillations do exist in the span-wise direction even though the trend is excellent. Our initial guess was that the oscillations were due to the grid resolution close to the cylinder surface being some what too coarse. It should be noted that the difference between the two radii, $(d_2 - d_1)/2 = 0.222$, was very small compared to the length l of the cylinder. Given the grid aspect ratio restrictions, this would mean a high demand on the mesh. This demand on the mesh refinement would in turn lead to a grid-clustering around the cylinder. However this guess has to be further investigated.

In figure 10 the computed laminar boundary layer profile is compared to the potential flow calculations. From potential theory, the stream function ψ for flow past a circular cylinder without rotation was given by (see White[17]),

$$\psi = U sin\theta (r - \frac{a^2}{r}) \tag{8}$$

where a is the radius of the cylinder and r any distance from the axis of the cylinder. Here $\theta = 90^o$ corresponds to the Y-Z plane passing through the center of the cylinder. Thereby the velocity component U_θ becomes,

$$U_\theta = -\frac{\partial \psi}{\partial r} = -U sin\theta (1 + \frac{a^2}{r^2}) = -(1 + \frac{a^2}{r^2}) \tag{9}$$

The symmetry and smoothness of the flow in the boundary layer on either side of the cylinder were well captured in the simulation. However, the numerical results do not collapse with the irrotational velocity profile far from the cylinder, a reason for which could be that the potential flow assumption holds good for high Reynolds number flows. Another reason (less probable) could be that our computational box in Z-direction is slightly too narrow.

6 CONCLUSIONS

i) The computational performance of the IBM proved to be very promising when compared to the boundary fitted and unstructured grid solvers, especially the computations on the Linux PC with 1.2x10^6 grid points was surprisingly fast.

ii) Complex flow structures as observed in experiments[5], including vortex splitting and vortex dislocation, were successfully reproduced using IBM.

iii) St_{local} versus Re_{local} curve showed excellent qualitative agreement with the experiments. However, quantitative deviations exist between the two techniques. It should be

noted that end effects were negligible in our case and the boundary conditions in the numerical simulation and in the laboratory were therefore different.

iv) Numerical oscillations along the span were observed in the steady flow calculation, the reason for which has to be further investigated.

ACKNOWLEDGEMENTS

This work has received support from The Research Council of Norway (Programme for Supercomputing) through a grant of computing time. The first author was the recipient of a research fellowship offered by The Research Council of Norway.

REFERENCES

[1] D.C. Jespersen and C. Levit, "Numerical simulation of flow past a tapered cylinder", *AIAA paper*, **91-0751**, (1991).

[2] B. Vallès, H.I. Andersson and C.B. Jenssen, "Oblique vortex shedding behind tapered cylinders", *J. Fluids Struct.*, **16**, 453-463, (2002).

[3] P. Parnaudeau, D. Heitz, E. Lamballais and J.H. Silvestrini, "Direct numerical simulations of vortex shedding behind cylinders with spanwise linear nonuniformity", *Proc. TSFP4*, 111-116, (2005).

[4] P. Parnaudeau, D. Heitz, E. Lamballais and J.H. Silvestrini, "Direct numerical simulations of vortex shedding behind cylinders with spanwise linear nonuniformity", *J. Turbulence*, submitted.

[5] P.S. Piccirillo and C.W. Van Atta, "An experimental study of vortex shedding behind linearly tapered cylinders at low Reynolds number", *J. Fluid Mech.*, **246**, 163-195, (1993).

[6] N. Peller, A. Le Duc, F. Tremblay and M. Manhart, "High-order stable interpolations for immersed boundary methods", *Int. J. Numer. Meth. Fluids*, in press.

[7] F. Tremblay, M. Manhart, R. Friedrich, "DNS and LES of flow around a circular cylinder at a subcritical Reynolds number with cartesian grids", *LES of Complex Transitional and Turbulent Flows*, Kluwer Academic Publishers, 133-150, (2001).

[8] M. Manhart, F. Tremblay and R. Friedrich, "MGLET: a parallel code for efficient DNS and LES of complex geometries", *Parallel Computational Fluid Dynamics 2000*, Elsevier Science B.V., 449-456, (2001).

[9] M. Manhart, "A zonal grid algorithm for DNS of turbulent boundary layers" , *Computers & Fluids*, **33**, 435-461, (2004).

[10] J.H. Ferziger and M. Peric, *Computational Methods for Fluid Dynamics*, Springer, (1996).

[11] R. Verzicco, J. Mohd-Yusof, P. Orlandi and D. Harworth, "LES in complex geometries using boundary body forces" , *In Proc. of the Summer Program 1998*, Center for Turbulence Research, Stanford, 171-186, (1998).

[12] G. Iaccarino and R. Verzicco, "Immersed boundary technique for turbulent flow simulations" , *Appl. Mech. Rev.*, **56**, 331-347, (2003).

[13] R. Mittal and G. Iaccarino, "Immersed boundary methods" , *Annu. Rev. Fluid Mech.*, **37**, 239-261, (2005).

[14] R.L. Panton, *Incompressible Flow*, Wiley-Interscience, 2^{nd} edition, (1997).

[15] C.H.K. Williamson and G.L. Brown, "A series in $1/\sqrt{Re}$ to represent the Strouhal-Reynolds number relationship of the cylinder wake" , *J. Fluids Struct.*, **12**, 1073-1085, (1998).

[16] D. Sucker and H. Brauer, "Fluiddynamik bei der angeströmten Zylindern", *Wärme- und Stoffübertragung*, **8**, (1975).

[17] F.M. White, *Fluid Mechanics*, McGraw-Hill International Editions, 2^{nd} edition, (1988).

Article 2

Steady viscous flow past a tapered cylinder

Narasimhamurthy, V. D., Andersson, H. I. & Pettersen, B.

Accepted for publication in *Acta Mechanica*

Steady viscous flow past a tapered cylinder

Vagesh D. Narasimhamurthy[1], **Helge I. Andersson**

Fluids Engineering Division, Department of Energy and Process Engineering, Norwegian University of Science and Technology (NTNU), N-7491 Trondheim, Norway

Bjørnar Pettersen

Department of Marine Technology, Norwegian University of Science and Technology, N-7491 Trondheim, Norway

The three-dimensional nature of the viscous flow past a linearly tapered circular cylinder is examined at low Reynolds numbers. The numerical solution of the unsteady Navier-Stokes equations converges to a steady state. The primary flow in planes perpendicular to the cylinder axis is practically indistinguishable from the two-dimensional flow past a uniform cylinder. A secondary spanwise flow is observed in the stagnation zone going from the wide end towards the narrow end, whereas a secondary motion on the rear side goes in the opposite direction. In spite of this secondary flow, the length of the separation zone varies linearly with the local Reynolds number.

1 Introduction

The flow past a circular cylinder with a uniform cross-section remains two-dimensional as long as the Reynolds number Re is below the critical value ≈ 190 beyond which the intrinsic 'mode A' instability is known to occur. If the diameter varies along the cylinder span, however, the diameter variation introduces inherent three-dimensionality into the flow. At Reynolds numbers of $\bigcirc(100)$, the wake flow becomes time-dependent and the local shedding frequency turns out to vary abruptly along the span either if the diameter changes discontinuously [1],[2],[3] or linearly [4],[5],[6],[7],[8]. For Reynolds numbers below ≈ 42, however, the wake behind a uniform cylinder is steady and the length of the closed wake is known to vary linearly with the Reynolds number.

The aim of this Note is to examine the three-dimensional wake behind a linearly tapered circular cylinder at low Reynolds number. Both experiments [5] and simulations [6],[8] have shown that even very modest tapering (taper ratio 75:1) gives rise to complex non-linear wake phenomena such as vortex splitting and dislocations for Reynolds numbers slightly above 100. Nevertheless, one may speculate whether the wake flow behind a slightly tapered cylinder can be considered as quasi-two-dimensional provided that the Reynolds number is lower than the critical value at which vortex shedding occurs. One may furthermore wonder how the secondary flow field, i.e. the departure from purely 2D behaviour, will appear. These issues will be addressed for the first time in the present study where we intentionally consider the same taper ratio for which complex three-dimensional wake phenomena have been

[1]Corresponding author. Tel.: +47 73593563; fax: +47 73593491; E-mail: vagesh@ntnu.no

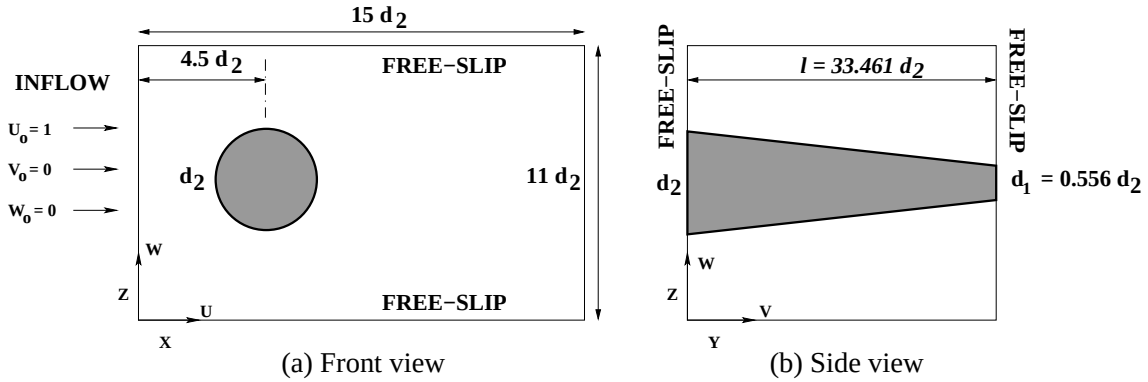

Figure 1: Computational domain (not to scale)

observed at Reynolds numbers below the critical Reynolds number ≈ 190 at which intrinsic secondary instabilities are known to occur in the wake of uniform cylinders.

2 Problem formulation and numerical method

To this end we considered a circular cylinder with taper ratio $R_T = l/(d_2 - d_1) = 75 : 1$ (where, $l = 33.461 d_2$ is the length of the cylinder, and d_2 and $d_1 = 0.556 d_2$ denote the diameter of its wide and narrow ends, respectively). The size of the computational domain in each coordinate direction was $L_X = 15 d_2$, $L_Y = 33.461 d_2$, and $L_Z = 11 d_2$, as shown in Fig. 1. The Reynolds numbers based on the uniform inflow velocity U_o and the diameters d_2 and d_1 were $Re_2 = 40$ and $Re_1 = 22.24$, respectively.

The Navier-Stokes equations in *incompressible* form were solved in 3-D space and time using the *parallel* Finite Volume code MGLET [9]. The code uses a staggered Cartesian grid arrangement and is 3^{rd} order accurate in time (explicit Runge-Kutta scheme) and 2^{nd} order accurate in space (central scheme). The number of grid points in the streamwise (X), spanwise (Y) and cross-stream (Z) directions were $[N_X, N_Y, N_Z] = [224, 200, 170]$. A uniform velocity profile $U_o = 1$ was prescribed at the inlet and a Neumann boundary condition was used for the pressure. At both the ends of the cylinder and at the top and bottom of the computational domain a *free-slip* boundary condition was used (see Fig. 1). At the outlet, a Neumann boundary condition was used for velocities and the pressure was set to zero.

A *direct forcing* Immersed Boundary Method (IBM) [10] was used to transform the *no-slip* condition at the cylinder surface into internal boundary conditions at the nodes of the Cartesian grid. The solid body (tapered cylinder) to be immersed in the Cartesian mesh was represented by a mesh consisting of triangles. The blocking of the Cartesian cells intersected by these triangles was accomplished as follows:

i)The intersection points of a triangle surface and the coordinate line passing through

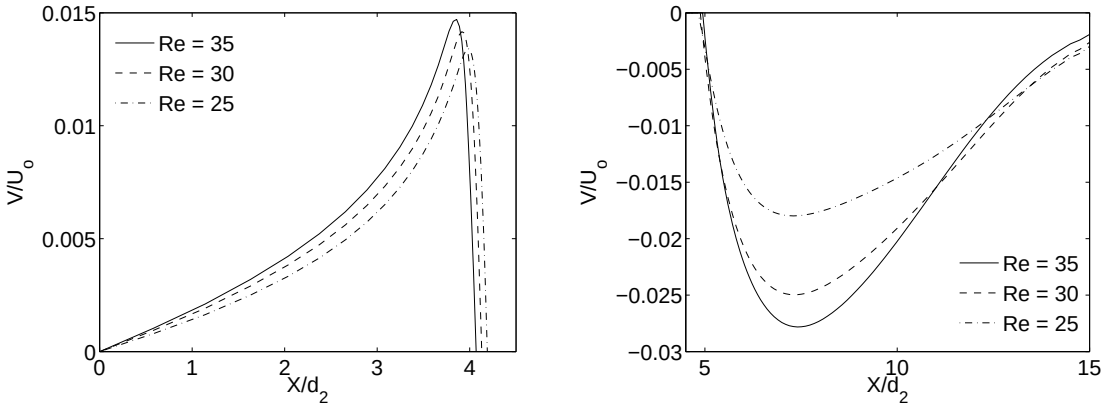

(a) Upstream the cylinder

(b) Downstream the cylinder

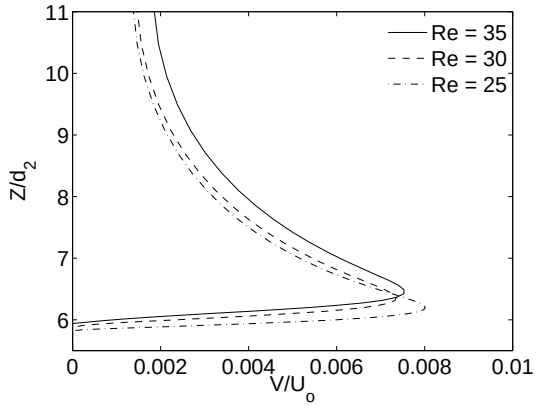

(c) 90^o from the upstream stagnation line

Figure 2: Spanwise velocity V/U_o (secondary flow) at three different spanwise locations identified by the local Reynolds number $Re = U_o d/\nu$. The position of the axis of the cylinder is at $[X/d_2, Z/d_2] = [4.5, 5.5]$.

the pressure cell center were identified. The pressure cells containing those intersection points were blocked.
ii)In a second sweep all the pressure cells within the blocked surface were blocked.
iii)Finally, all the velocity cells corresponding to blocked pressure cells were blocked.
The internal boundary condition value had to be determined by interpolation. In the present study we used *least-squares* interpolation of 3^{rd}-order accuracy. The detailed derivation, validation and implementation of this technique in the code MGLET were explained in [10].

3 Results and discussion

The numerical solution of the unsteady Navier-Stokes equations converged to a steady state. The present 3-D calculation revealed a modest secondary spanwise velocity V, both in the front stagnation zone and also in the wake of the cylinder (see

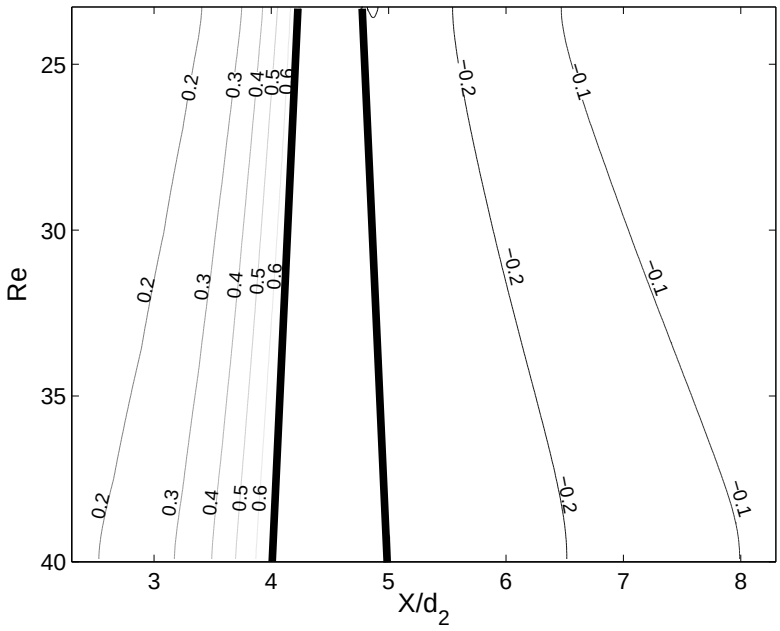

Figure 3: Pressure ($P/\rho\, U_o^2$) contours in the $X-Y$ plane through the axis of the cylinder. The cylinder walls are drawn as bold lines.

Fig. 2(a),2(b),2(c)). It can be observed from Fig. 2(a) that in the front stagnation zone the secondary flow is going from the wide end of the cylinder towards the narrow end. On the side, i.e. 90^o from the front stagnation line, the secondary flow still persist in the same direction although at a lower speed. On the contrary, the secondary motion on the rear side of the cylinder goes in the opposite direction (see Fig. 2(b)). The magnitude of this spanwise velocity is quite small, typically of the order $1-3\%$ of the inflow U_o. The secondary motion in the spanwise direction is a direct consequence of three-dimensionality of the tapered cylinder and this kind of secondary flows does not arise in the vicinity of uniform circular cylinders.

The secondary flow is driven by a spanwise pressure gradient. The front stagnation line is slightly inclined with respect to the cylinder axis and this tilt gives rise to a somewhat higher pressure near the wide end of the cylinder as compared to the narrow end. The pressure contours (isobars) in Fig. 3 show that the isobars are more inclined towards the cylinder axis than the stagnation line, thereby giving rise to a spanwise pressure gradient which drives the flow towards the narrow end. Similarly, the (negative) isobars in the cylinder wake are also tilted towards the cylinder axis, i.e. the lowest pressure is found in the wake downstream of the widest part of the cylinder. This observation indicates that also the spanwise-oriented flow in the cylinder wake is pressure-driven.

The constant length L of the closed wake behind a uniform circular cylinder is known to increase monotonically with Reynolds number in the low-Re regime. Sucker and

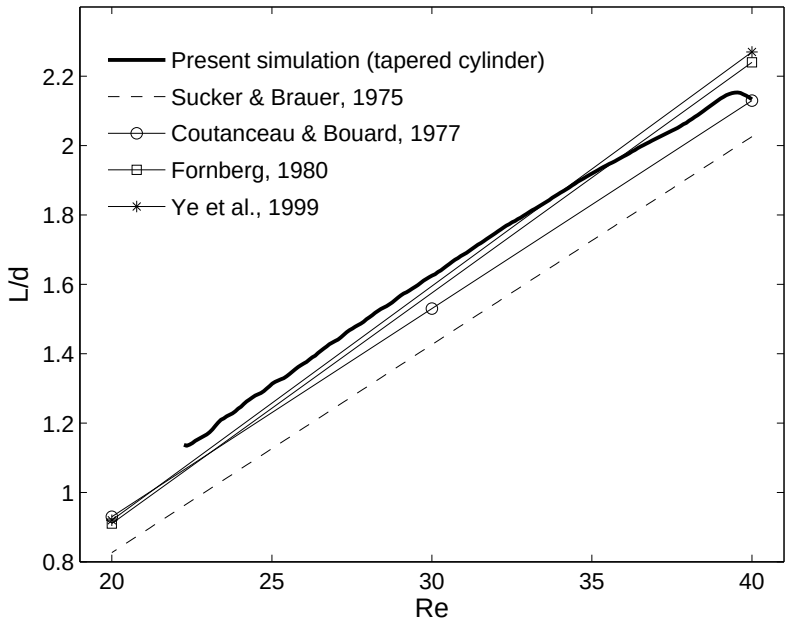

Figure 4: Non-dimensional length of the steady re-circulation zone (L/d) versus local Reynolds number $Re = U_o\ d/\nu$.

Brauer [11] deduced the empirical correlation $L/d = 0.12\ Re - 0.748$ on the basis of several experimental and numerical data available at that time. Subsequent data from more refined experiments by Coutanceau and Bouard [12] and computations by Fornberg [13] and Ye et al. [14] and others suggest that the linear correlation due to Sucker and Brauer [11] slightly underestimates the wake length. In the present 3D case, the wake length varies substantially along the cylinder span of the tapered cylinder. In the present context the local wake length L is defined as the streamwise distance from the cylinder surface to the position where the streamwise velocity U changes sign from negative to positive. The wake behind the wide end is roughly four times longer than the wake behind the narrow end of the cylinder. If the local wake length L is scaled with the local diameter d, the spanwise variation of L/d shown in Fig. 4 is surprisingly close to the results for uniform (i.e. 2D) cylinders. The deviation from 2D behaviour is largest near the wide part of the tapered cylinder where the secondary flow is most pronounced (cf. Fig. 2). The co-ordinate position of the vortex centers (a, b) were plotted against the local Reynolds number in Fig. 5. Here a is defined as the streamwise distance from the cylinder surface to the vortex center and b is defined as the cross-stream distance between the two vortex centers. The data from the present numerical study scaled with the local diameter d is in good agreement with the experimental results for uniform (i.e. 2D) cylinders.

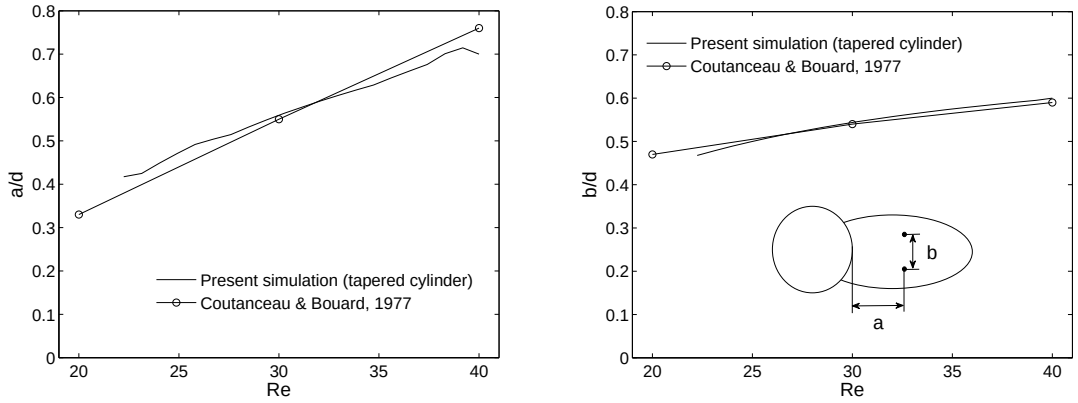

(a) (b)

Figure 5: Position of the re-circulation bubble centre $(a/d, b/d)$ plotted against Re.

4 Conclusion

We have seen that the modest tapering gives rise to a pressure-driven secondary flow along the span of the cylinder. The steady wake exhibits a substantial variation along the span. This variation is associated partly with the variation of the local diameter and partly with the local Reynolds number. The flow field in planes perpendicular to the cylinder axis can thus be considered as quasi-two-dimensional.

Acknowledgments

This work has received support from The Research Council of Norway (Programme for Supercomputing) through a grant of computing time. The first author was the recipient of a research fellowship offered by The Research Council of Norway.

References

[1] C.G. Lewis and M. Gharib, "An exploration of the wake three dimensionalities caused by a local discontinuity in cylinder diameter," Phys. Fluids A **4**, 104-117 (1992).

[2] B. Vallès, H.I. Andersson, and C.B. Jenssen, "Direct-mode interactions in the wake behind a stepped cylinder," Phys. Fluids **14**, 1548-1551 (2002).

[3] W. Dunn and S. Tavoularis, "Experimental studies of vortices shed from cylinders with a step-change in diameter," J. Fluid Mech. **555**, 409-437 (2006).

[4] M. Gaster, "Vortex shedding from slender cones at low Reynolds numbers," J. Fluid Mech. **38**, 565-576 (1969).

[5] P.S. Piccirillo, and C.W. Van Atta, "An experimental study of vortex shedding behind linearly tapered cylinders at low Reynolds number," J. Fluid Mech. **246**, 163-195 (1993).

[6] B. Vallès, H.I. Andersson, and C.B. Jenssen, "Oblique vortex shedding behind tapered cylinders," J. Fluids Struct. **16**, 453-463 (2002).

[7] P. Parnaudeau, D. Heitz, E. Lamballais, and J.H. Silvestrini, "Direct numerical simulations of vortex shedding behind cylinders with spanwise linear nonuniformity," J. Turbulence **8**, No. 13 (2007).

[8] V. D. Narasimhamurthy, H. I. Andersson, and B. Pettersen, "Direct numerical simulation of vortex shedding behind a linearly tapered circular cylinder," In Proc. IUTAM Symposium on Unsteady Separated Flows and their Control, (2007). (to be published by Springer).

[9] M. Manhart, "A zonal grid algorithm for DNS of turbulent boundary layers," Computers & Fluids **33**, 435 (2004).

[10] N. Peller, A. Le Duc, F. Tremblay and M. Manhart, "High-order stable interpolations for immersed boundary methods," Int. J. Numer. Meth. Fluids **52**, 1175-1193 (2006).

[11] D. Sucker and H. Brauer, "Fluiddynamik bei quer angeströmten Zylindern," Wärme- und Stoffübertragung, **8**, 149-158 (1975).

[12] M. Coutanceau and R. Bouard, "Experimental determination of the main features of the viscous flow in the wake of a circular cylinder in uniform translation. Part 1. Steady flow," J. Fluid Mech. **79**, 231-256 (1977).

[13] B. Fornberg, "A numerical study of steady viscous flow past a circular cylinder," J. Fluid Mech. **98**, 819-855 (1980).

[14] T. Ye, R. Mittal, H.S. Udaykumar, and W. Shyy, "An accurate Cartesian grid method for viscous incompressible flows with complex immersed boundaries," J. Comp. Phys. **156**, 209-240 (1999).

Article 3

Direct numerical simulation of vortex shedding behind a linearly tapered circular cylinder

Narasimhamurthy, V. D., Andersson, H. I. & Pettersen, B.

In *Proc. IUTAM Symposium on Unsteady Separated Flows and their Control, Corfu, Greece*, 2007 (to be published by Springer).

Direct Numerical Simulation of Vortex Shedding Behind a Linearly Tapered Circular Cylinder

Vagesh D. NARASIMHAMURTHY[†], Helge I. ANDERSSON[†] and Bjørnar PETTERSEN[§]

[†]*Norwegian University of Science and Technology (NTNU), Department of Energy and Process Engineering, 7491 Trondheim, Norway, vagesh@ntnu.no*
[§]*NTNU, Department of Marine Technology, 7491 Trondheim, Norway*

Abstract. The three-dimensional transition to turbulence in the wake of a tapered circular cylinder with the taper ratio 75:1 has been analyzed by performing direct numerical simulation. The Reynolds number based on the uniform inflow velocity and the diameters at the wide and narrow ends were 300 and 102, respectively. The same Reynolds number range was previously studied by Parnaudeau et al. (*J. Turbulence*, 2007) but with a different taper ratio 40:1. The effect of taper ratio on the transition to turbulence was investigated in the present study. It was found that the Strouhal number *versus* Reynolds number curves nearly collapse, thereby indicating that a change in the taper ratio by a factor of two has only a modest effect on the Strouhal number. However, there still exists a significant contrast in the cellular shedding pattern. Flow-visualization of instantaneous λ_2-structures and the enstrophy $\mid \omega \mid$ revealed that the mode A instability appeared around $Re \approx 200$ and mode B around $Re \approx 250$.

Key words: instability, transition, turbulence, DNS, tapered cylinder.

1. Introduction

Three-dimensional flow over circular cylinders is a common phenomenon in many engineering applications which occurs behind oil-platform legs, chimneys, cooling towers and even tapered aircraft wings. Such three-dimensionalization of the separated flow is often induced by a spanwise variation of the cylinder diameter (e.g. tapered cylinders). A distinct feature of tapered cylinder wakes is that depending on the local Reynolds number (Re_{local}) along the span, a range of flow-regimes (e.g., laminar unsteady wake (L3), transition in the wake (TrW) or shear layer (TrSL), etc) may exist side by side in the same geometry. Three-dimensional instabilities in the wake of tapered circular cylinders (L3 regime) was previously studied by Papangelou [1], Piccirillo and Van Atta [2], Vallés et al. [3] and more recently by Narasimhamurthy et al. [4]. In comparison, remarkably few investigations of the TrW regime for tapered cylinders has appeared. Recently Parnaudeau et al. [5] performed Direct Numerical Simulation (DNS) in the TrW regime with a taper ratio, $R_T = l/(d_2 - d_1) = 40 : 1$ (where l is the length of the circular cylinder and d_2 and d_1 denote the diameter of its wide and narrow ends, respectively).

In the present study $R_T = 75 : 1$, which implies a more modest tapering than considered by Parnaudeau et al. [5] and the Reynolds numbers are same in both the cases. Thereby, the effect of tapering on the transition to turbulent process is

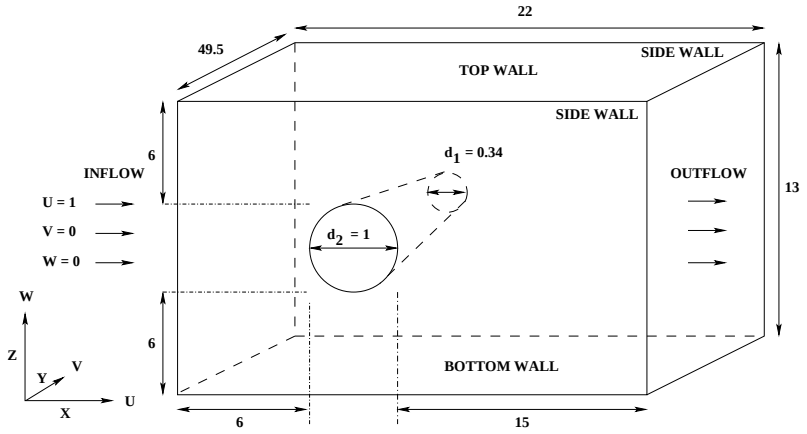

Figure 1. Computational domain (not to scale)

investigated in the present study. In this DNS study, an in-depth exploration of the frequency spectra and the instantaneous vortical structures was carried out to understand both the evolution of large-scale structures (*vortex dislocation* or *vortex splits*) and the small-scale structures (*mode A* and *mode B*). Qualitative comparisons of the present results with the earlier numerical study in L3 regime [4], and in-house PIV (Particle Image Velocimetry) measurements by Visscher et al. [6] (where they studied TrSL regime) are also made.

2. Flow configuration and numerical method

The computational domain was as shown in Figure 1. All dimensions were normalized by d_2. The mean diameter $d_m = 0.67$. The aspect ratio ($a = l/d_m$), R_T, and the Reynolds numbers Re_2, Re_1, Re_m, based on the uniform inflow velocity ($U = 1$) and the diameters d_2, d_1, d_m, respectively were as shown in Table 1.

Table 1. Flow parameters

Case	**a**	$\mathbf{R_T}$	$\mathbf{Re_2}$	$\mathbf{Re_1}$	$\mathbf{Re_m}$
Present simulation	74	75:1	300	102	201
Parnaudeau et al.[5]	40	40:1	300	100	200

The Navier-Stokes (N-S) equations in *incompressible* form were solved in 3-D space and time using a *parallel* Finite Volume code [4, 10]. The code uses staggered Cartesian grid arrangement. Time marching was carried out using a 3^{rd} order explicit Runge-Kutta scheme for the momentum equations and an iterative SIP (Strongly Implicit Procedure) solver for the Poisson equation. Spatial discretization was carried out using a 2^{nd} order central-differencing scheme. The total number of grid points used was equal to 15 x 10^6. The time step $\Delta t = 0.003 d_2/U$ and the number of Poisson iterations per time step was equal to 50.

A uniform inflow velocity profile $U = 1$ was fixed at the inlet without any free-stream perturbations. A *free-slip* boundary condition was applied on both the side walls, top wall and the bottom wall (see Figure 1). At the outlet, Neumann

boundary condition was used for velocities and pressure was set to zero. The *no-slip* boundary condition on the cylinder body was implemented by using a *direct forcing* Immersed Boundary Method (IBM) [4, 9]. The computations were performed on a *SGI Origin 3800* parallel computer. The total consumption of CPU-time was approximately equal to 12000 hours.

3. Results and discussion

3.1. FREQUENCY ANALYSIS

The time evolution of the instantaneous velocity components U, V, W and the instantaneous pressure, P, were sampled along two lines parallel to the axis of the cylinder and located $2d_m$ and $12d_m$ downstream the axis in X-direction, respectively. Both lines were offset by $1d_m$ in Z-direction. The time traces of U, V, W and P were plotted in Figure 2, 3, 4 and 5, respectively. The figures clearly indicate the oblique and cellular shedding pattern. Quantitative investigations of the frequency spectra were carried out by spectral analysis of the cross-stream velocity component (W) time trace. In Figure 6(a) the Strouhal number ($St = fd_m/U$) *versus* Re_{local} ($= Ud_{local}/\nu$; d_{local} is the local diameter) curve from Parnaudeau et al. [5] was compared against the present result. It is surprising to see that the curves nearly collapse, thereby indicating that a change in the R_T by a factor of two does not affect the Strouhal number much. However, there still exists a significant contrast in the distribution of constant-frequency cells along the span.

The vortex dislocations in the TrW state of flow behind a uniform circular cylinder typically occur at the location of mode A instability [8]. In contrast, these large-scale structures occur spontaneously along the whole span for tapered circular cylinders (see Figure 6(b)). The two discontinuities in the local Strouhal number ($St_{local} = fd_{local}/U$) *versus* Re_{local} curve in Figure 6(b) for the uniform circular cylinder correspond to change over of eddy-shedding mode from laminar-mode A and mode A-mode B, respectively [8]. However, for the tapered case it seems that the vortex dislocations depend primarily on R_T.

In Figure 7 the St_{local} curve from the present simulation (TrW regime) was plotted together with the results from Narasimhamurthy et al. [4] (L3 regime) and the PIV measurements by Visscher et al. [6] (TrSL regime). In all the three studies $R_T = 75 : 1$. The Strouhal number initially increases with Reynolds number and then decreases with the increase in Re_m, similar to the uniform circular cylinder [11]. Piccirillo and Van Atta [2] in their experimental study (L3 regime) observed that the shedding cell size increases with the local diameter. A similar observation was also reported by Parnaudeau et al. [5]. In Figure 7 it can be seen that shedding cell size clearly increases towards the large diameter for low Reynolds numbers (L3 and TrW). It seems that this observation is only valid for low Reynolds numbers as the curves for TrSL does not follow this trend.

3.2. INSTANTANEOUS VORTICAL STRUCTURES

In order to identify the topology and the geometry of the vortex cores correctly the λ_2-definition due to Jeong and Hussain [12] was used. λ_2 corresponds to the second largest eigenvalue of the symmetric tensor $S_{ij}S_{ij} + \Omega_{ij}\Omega_{ij}$, where S_{ij} and

Ω_{ij} are respectively the symmetric and antisymmetric parts of the velocity gradient tensor. Figure 8 shows the iso-surfaces of negative λ_2 at different instances in time, t. A 3-dimensionality in the form of waviness in the spanwise vortex cores (primary Karman vortices) is evident even in the L3 regime. The snapshots clearly illustrate the time-evolution of the vortex dislocations (around $Y = 25 - 40$) and the small-scale streamwise structures (mode A and mode B) along the span. However, vortex dislocations are more clearly visible in Figure 9. Negative λ_2, vorticity magnitude or enstrophy $\mid \omega \mid$ and the vorticity components evaluated at the same instant in time were plotted together. The vortex dislocations formed between spanwise cells of different frequency when the primary vortices move out of phase with each other are visible at $Y \approx 12$, 23, and 40. The development of helical twisting of vortex tubes is visible in the vicinity of the vortex dislocations. Williamson [7] concluded that these helical twistings are the fundamental cause for the rapid spanwise spreading of dislocations, and indeed for the large-scale distortion and break-up to turbulence in a natural transition wake.

In uniform circular cylinder wakes the Reynolds number will be constant along the whole span and therefore the individual modes of 3-dimensionality (either mode A or mode B) exist along the entire span of the cylinder. Barkley and Henderson [13] from their Floquet stability analysis predicted the critical Reynolds number for the uniform circular cylinder to be 188.5 ± 1.0 and the wavelength of mode A equal to 3.96 diameters. However, in the present tapered cylinder study the Re_{local} varies along the span and both mode A and mode B co-exist in the same geometry. Thereby only a small span of the cylinder is available for each of the modes to develop (especially for mode A) and it is hard to pin-point the exact Reynolds number at which these modes start to appear. Parnaudeau et al. [5] reported that the mode A behind their tapered cylinder occurred in the L3 regime. The present flow-visualizations revealed that mode A appeared around $Re_{local} \approx 200$ and mode B around $Re_{local} \approx 250$.

4. Conclusions

The effect of taper ratio on the transition to turbulence was investigated in the present study. It was found that the Strouhal number *versus* local Reynolds number curves nearly collapse, thereby indicating that a change in the taper ratio by a factor of two does not affect the Strouhal number much. However, there still exists a significant contrast in the cellular shedding pattern.

Spot-like vortex dislocations in the TrW regime of uniform circular cylinders correspond to change over of eddy-shedding mode from laminar-mode A and mode A-mode B [8], but for tapered circular cylinders dislocation primarily depends on R_T. In the present investigation, it was observed that the shedding cell size increases with the local diameter, which is in agreement with the previous studies at low Reynolds numbers [2, 4, 5]. Both mode A and mode B were found to co-exist in the same geometry but only in a small span of the cylinder. It was hard to pin-point the exact Reynolds number at which these modes develop. However, from the flow-visualization it can be concluded that the mode A appeared around $Re_{local} \approx 200$ and mode B around $Re_{local} \approx 250$.

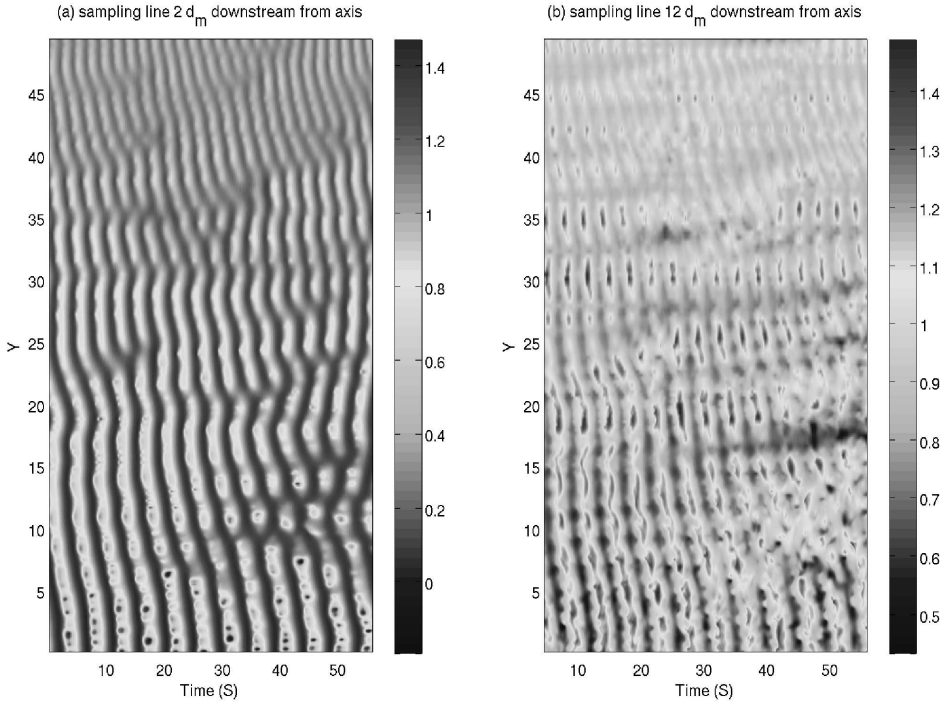

Figure 2. Time evolution of the U velocity along the entire span. Y = 0 corresponds to Re_2 and Y = 49.5 corresponds to Re_1.

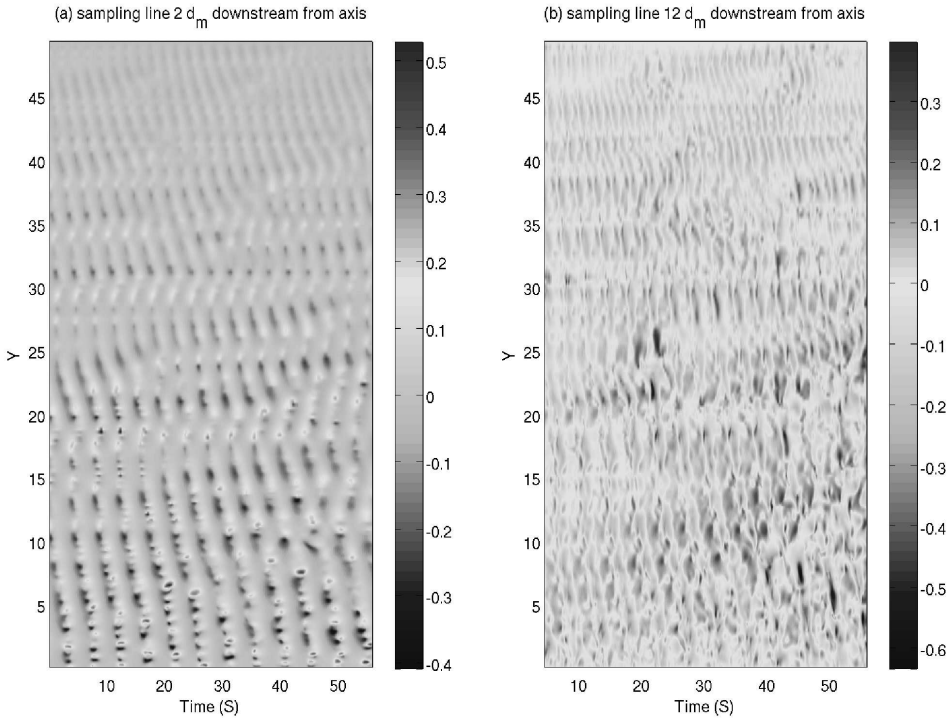

Figure 3. Time evolution of the V velocity along the entire span (see Figure 2 for details).

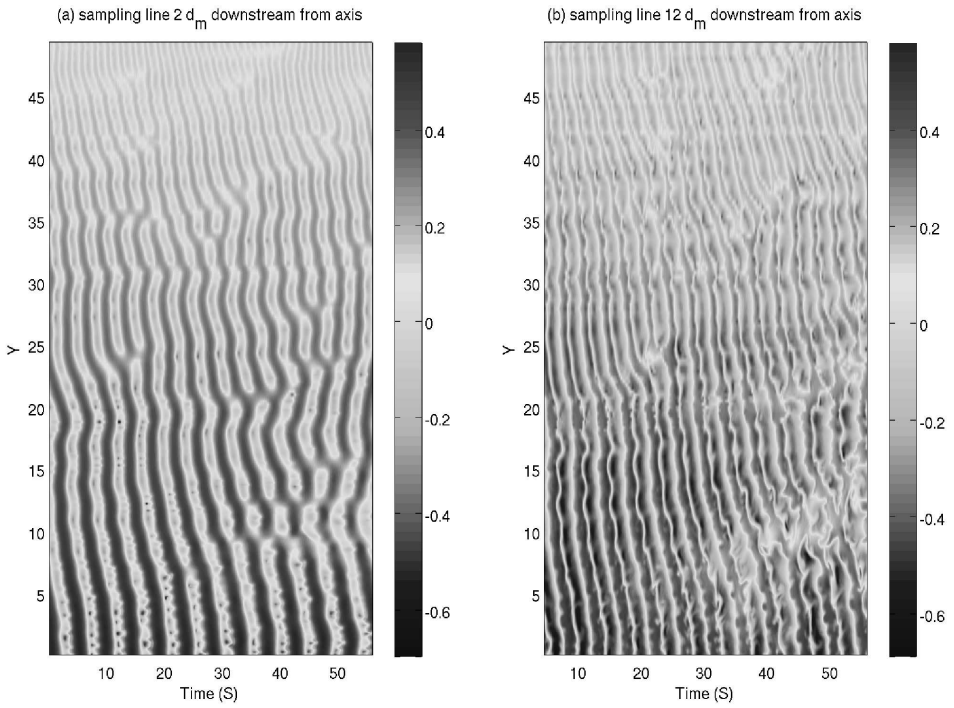

Figure 4. Time evolution of the W velocity along the entire span (see Figure 2 for details).

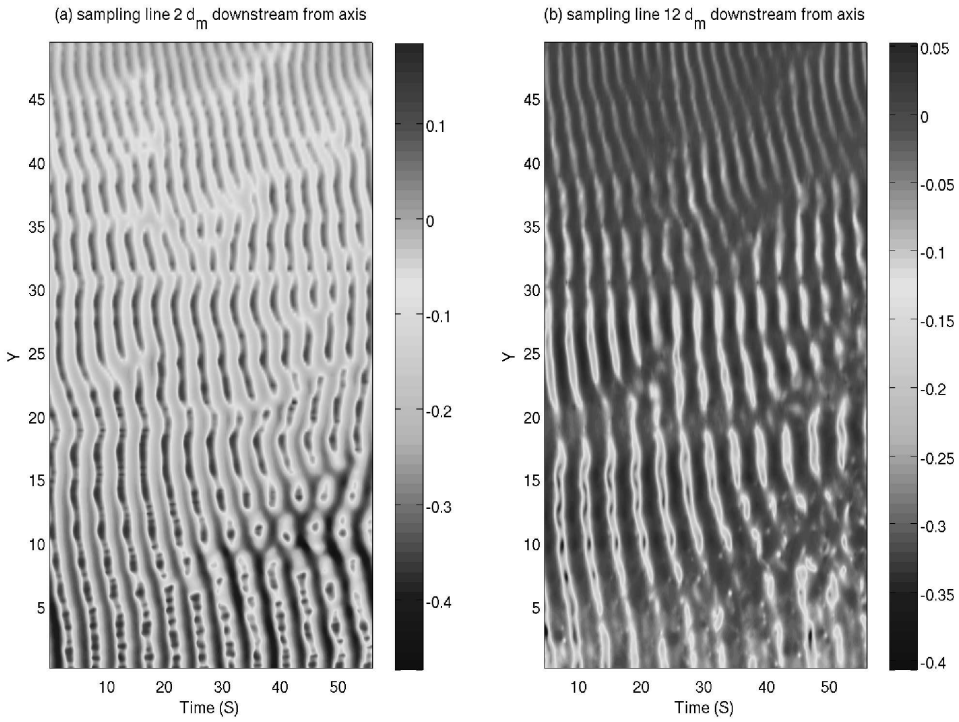

Figure 5. Time evolution of the pressure P along the entire span (see Figure 2 for details).

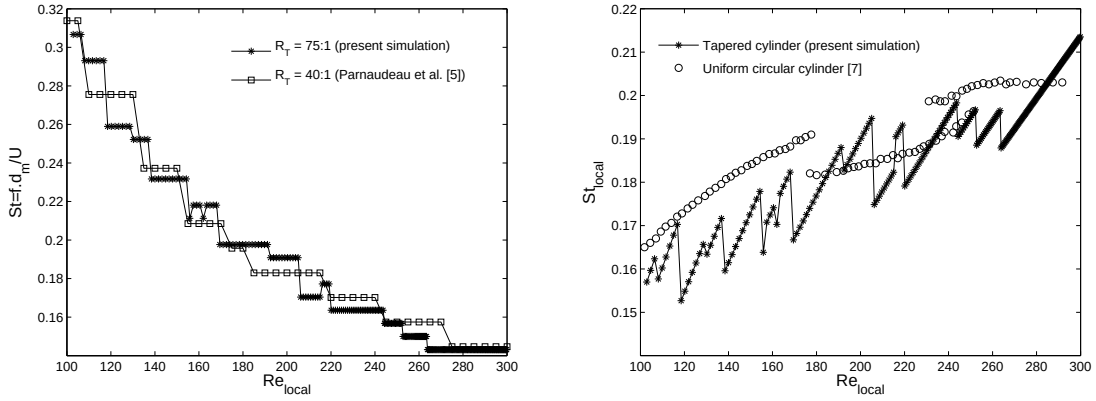

(a) Effect of taper ratio (R_T) (b) Tapered cylinder *versus* uniform circular cylinder

Figure 6. Strouhal number *versus* Reynolds number.

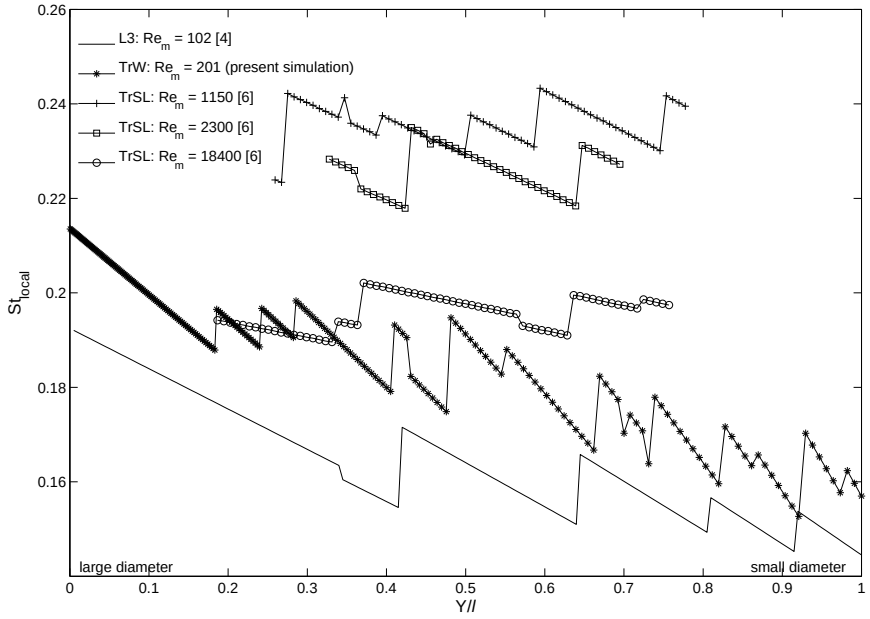

Figure 7. St_{local} along the non-dimensionalized span. $R_T = 75:1$ for all the curves.

Acknowledgments

This work has received support from The Research Council of Norway (Programme for Supercomputing) through a grant of computing time. The first author was the recipient of a research fellowship offered by The Research Council of Norway.

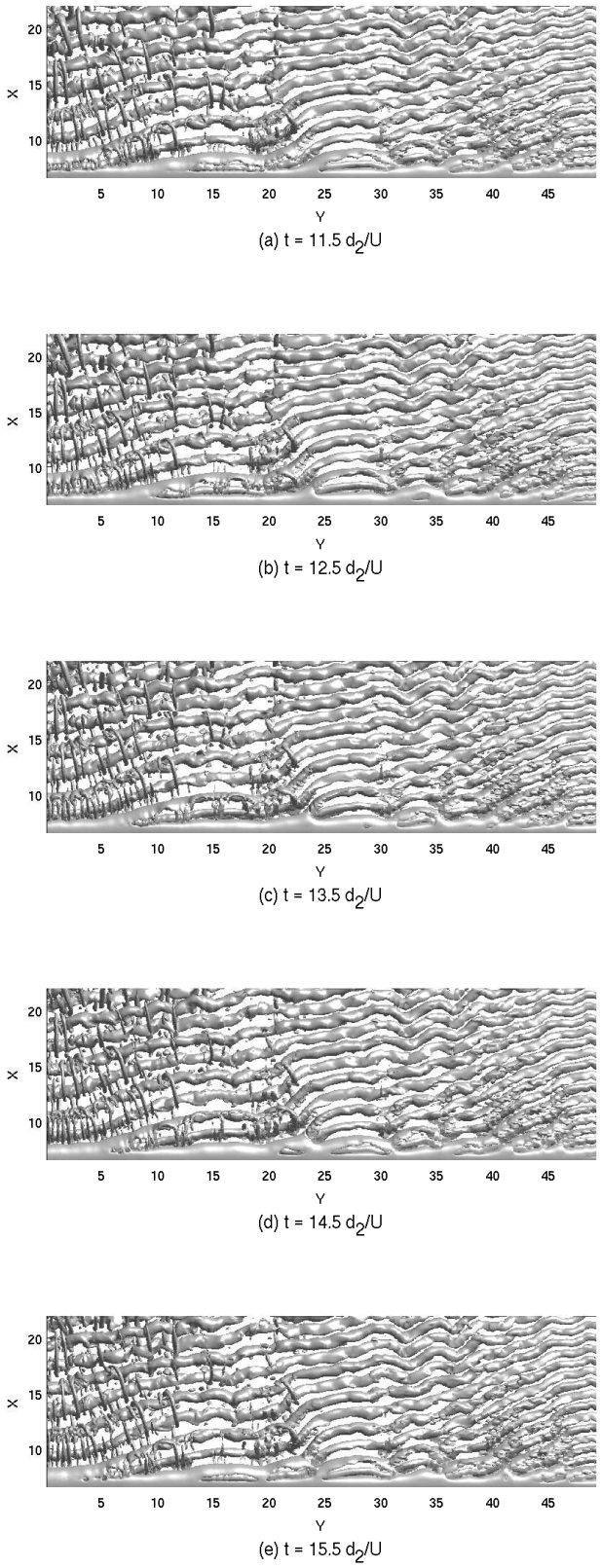

Figure 8. 3-dimensional λ_2 contours (negative λ_2) showing the topology and geometry of the vortex cores at different instances in time, t. Y-axis corresponds to the axis of the cylinder. The flow direction is from bottom to top.

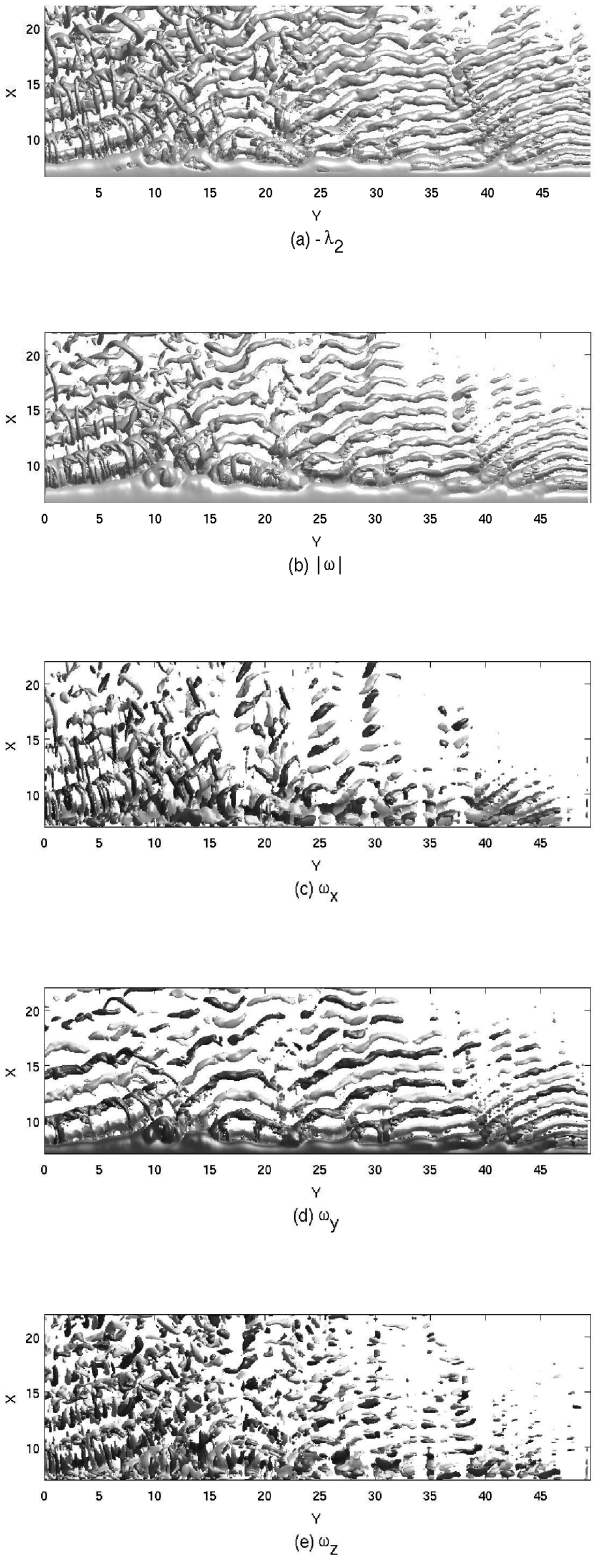

Figure 9. 3-dimensional vortical structures at the same instant in time, $t = 47d_2/U$ as vortex dislocation occurs along the span. The flow direction is from bottom to top. (a) Negative λ_2; (b) Enstrophy $\mid \omega \mid$; (c) streamwise vorticity ω_x; (d) spanwise vorticity ω_y; (e) cross-stream vorticity ω_z. The surfaces colored yellow and red mark a particular value of positive and negative vorticity, respectively.

References

[1] Papangelou, A., Vortex shedding from slender cones at low Reynolds numbers. *J. Fluid Mech.* **242**, (1992), 299-321.

[2] Piccirillo, P. S. and Van Atta, C. W., An experimental study of vortex shedding behind linearly tapered cylinders at low Reynolds number. *J. Fluid Mech.* **246**, (1993), 163-195.

[3] Vallès, B., Andersson, H. I. and Jenssen, C. B., Oblique vortex shedding behind tapered cylinders. *J. Fluids Struct.* ***16***, (2002), 453-463.

[4] Narasimhamurthy, V. D., Schwertfirm, F., Andersson, H. I. and Pettersen, B., Simulation of unsteady flow past tapered circular cylinders using an immersed boundary method. In: *Proc. ECCOMAS Computational Fluid Dynamics 06*, Eds. P. Wesseling, E. Oñate, J. Périaux, Publisher TU Delft, The Netherlands, Egmond aan Zee (2006).

[5] Parnaudeau, P., Heitz, D., Lamballais, E. and Silvestrini, J. H., Direct numerical simulations of vortex shedding behind cylinders with spanwise linear nonuniformity. *J. Turbulence* ***8***, (2007), No. 13.

[6] Visscher, J., Pettersen, B. and Andersson, H. I., PIV study on the turbulent wake behind tapered cylinders. In: *Advances in Turbulence XI*, Eds. J. M. L. M. Palma, A. Silva Lopes, Publisher Springer, Portugal, Porto (2007), 254-256.

[7] Williamson, C. H. K., The natural and forced formation of spot-like vortex dislocations in the transition of a wake. *J. Fluid Mech.* **243**, (1992), 393-441.

[8] Williamson, C. H. K., Vortex dynamics in the cylinder wake. *Annu. Rev. Fluid. Mech.* **28**, (1996), 477-539.

[9] Peller, N., Le Duc, A., Tremblay F. and Manhart M., High-order stable interpolations for immersed boundary methods. *Int. J. Numer. Meth. Fluids.* **52**, (2006), 1175-1193.

[10] Manhart M., A zonal grid algorithm for DNS of turbulent boundary layers. *Computers & Fluids.* **33**, (2004), 435-461.

[11] Zdravkovich, M. M., *Flow Around Circular Cylinders: Volume 1*, Oxford Univ. Press, (1997).

[12] Jeong, J. and Hussain, F., On the identification of a vortex. *J. Fluid Mech.* **285**, (1995), 69-94.

[13] Barkley, D. and Henderson, R. D., Three-dimensional Floquet stability analysis of the wake of a circular cylinder. *J. Fluid Mech.* **322**, (1996), 215-241.

Article 4

DNS and PIV study of the 3D wake behind tapered circular cylinders

Narasimhamurthy, V. D., Visscher, J., Andersson, H. I. & Pettersen, B.

In *Proc. Fifth International Symposium on Turbulence and Shear Flow Phenomena, Munich, Germany*, pp. 667-672, 2007.

DNS AND PIV STUDY OF THE 3D WAKE BEHIND TAPERED CIRCULAR CYLINDERS

Vagesh D. Narasimhamurthy
Dept. of Energy and Process Engineering,
Norwegian University of Science and Technology (NTNU),
NO-7491 Trondheim, Norway
vagesh@ntnu.no

Jan Visscher
Dept. of Marine Technology, NTNU
NO-7491 Trondheim, Norway
jan.h.visscher@ntnu.no

Helge I. Andersson
Dept. of Energy and Process Engineering, NTNU
NO-7491 Trondheim, Norway
helge.i.andersson@ntnu.no

Bjørnar Pettersen
Dept. of Marine Technology, NTNU
NO-7491 Trondheim, Norway
bjornar.pettersen@ntnu.no

ABSTRACT

Three-dimensional wake behind a tapered circular cylinder has been studied at low-Reynolds number (transition in the wake regime) by performing Direct Numerical Simulation (DNS) and at higher Reynolds numbers (transition in the shear-layer regime) by Particle Image Velocimetry (PIV). The taper ratio (75) was constant in both the studies. In the PIV study it was found that increase in aspect ratio increases the number of shedding cells along the span, an effect also reported by Piccirillo and Van Atta (*J. Fluid Mech.*, 1993). Both mode A and mode B were found to coexist in the same geometry (DNS) but only in a small span of the cylinder. Flow-visualization revealed that the mode A appeared around $Re \approx 200$ and mode B around $Re \approx 250$. Cross-sectional views of mode B in the DNS results revealed the smaller-scale 'mushroom' vortex pair structures, which is remarkably similar to those found by Williamson (*J. Fluid Mech.*, 1996). The wavelength of mode B was found to be $\lambda_Z/D \approx 1$, which is surprisingly close to the experimental value $\lambda_Z/D = 0.98$ found by Williamson (*J. Fluid Mech.*, 1996) in the uniform circular cylinder wake. In the present DNS study it was found that streamwise vorticity ω_x becomes large as vortex dislocation occurs, an effect also observed by Piccirillo and Van Atta (*J. Fluid Mech.*, 1993).

INTRODUCTION

The flow over cylinders involves complex interactions of three shear layers: a boundary layer, a separating free shear layer, and a wake, in the same problem. Depending on the Reynolds number transition-turbulence may occur either in the wake (TrW) or separating free shear layer (TrSL) or in the boundary layer (TrBL) of a cylinder. However, non-uniformities in the inflow or in the cylinder diameter (e.g. tapered cylinders) may produce the above mentioned regimes to exist side by side in the same geometry.

Three-dimensional instabilities in the laminar unsteady wake (L3 regime) of tapered circular cylinders were previously studied by Papangelou (1992), Piccirillo and Van Atta (1993), Vallés et al. (2002) and more recently by Narasimhamurthy et al. (2006). However, the TrW regime for tapered cylinders has had remarkably few investigations in comparison to uniform circular cylinders. Recently Parnaudeau et al. (2007) performed Direct Numerical Simulation (DNS) in the TrW regime with a taper ratio, $R_T = l/(d_2 - d_1) = 40$ (where l is the length of the circular cylinder and d_2 and d_1 denote the diameter of its wide and narrow ends, respectively). The same Reynolds number range was studied by Narasimhamurthy et al. (2007) but with a different $R_T = 75$ and they found that a change in R_T by a factor of two has only a modest effect on the Strouhal number. After a literature survey it was noted that the only available results in the TrSL regime is the hot-wire measurements by Hsiao and Chiang (1998), where they studied the tapered cylinder wake with different taper ratios and in the Reynolds number range $Re_m = 4.0 \times 10^3$ to 1.4×10^4 (based on the mean diameter d_m).

The present DNS computations is aimed at studying the wake in the low-Reynolds turbulent regime (as DNS at higher Reynolds number is beyond the reach of any modern computational facility). However, Particle Image Velocimetry (PIV) provides an opportunity to study the turbulent wake at higher Reynolds number (low Reynolds numbers could not be reached in our test facility due to practical issues). The aim of the present study is not to validate the DNS results with PIV results and vice versa but to

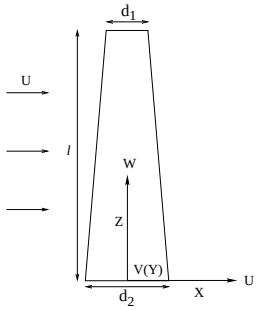

Figure 1: Tapered cylinder configuration

Table 1: Flow parameters ($R_T = 75$).

Case	a	d_1	d_m	d_2	Re_1	Re_m	Re_2
DNS	74	0.34	0.67	1	102	201	300
A_1	13	42	46	50	2100	2300	2500
A_2	13	42	46	50	4200	4600	5000
A_3	13	42	46	50	8400	9200	10000
A_4	13	42	46	50	16800	18400	20000
B_1	26	19	23	27	950	1150	1350
B_2	26	19	23	27	1900	2300	2700
B_3	26	19	23	27	3800	4600	5400

investigate the flow physics in two different Reynolds number ranges with two different techniques (DNS and PIV). It should be noted that the R_T is same in both the cases. Thereby the effect of Reynolds number alone is investigated in the present study.

NUMERICAL AND EXPERIMENTAL SETUP

The tapered cylinder configuration was as shown in figure 1. The aspect ratio ($a = l/d_m$) and the Reynolds numbers Re_2, Re_1, Re_m, based on the uniform inflow velocity ($U = 1$) and the diameters d_2, d_1, d_m, respectively were as shown in Table 1. $R_T = 75$ was constant in all the cases.

The Navier-Stokes equations in *incompressible* form were solved in 3-D space and time using a *parallel* Finite Volume code (Narasimhamurthy et al., 2006; Manhart, 2004). The code uses staggered Cartesian grid arrangement. Time marching was carried out using a 3^{rd} order explicit Runge-Kutta scheme for the momentum equations and an iterative SIP (Strongly Implicit Procedure) solver for the Poisson equation. Spatial discretization was carried out using a 2^{nd} order central-differencing scheme. The total number of grid points used was equal to $15{\times}10^6$. The time step $\Delta t = 0.003 d_2/U$ and the number of Poisson iterations per time step was equal to 50. A uniform inflow velocity profile $U = 1$ was fixed at the inlet without any free-stream perturbations[1]. *Free-slip* boundary condition was applied at the ends of the cylinder. The *no-slip* boundary condition on the cylinder body was implemented by using a *direct forcing* Immersed Boundary Method (Narasimhamurthy et al., 2006; Peller et al., 2006). The total consumption of CPU-time was approximately equal to 12000 CPU-hours on a *SGI Origin 3800* computer.

In the present experimental study stereoscopic PIV was used to measure a large area of the flow field in the cylinder wake with image rates up to 100 Hz. Two different models

[1]Note that transitional wake is still surrounded by laminar free-shear layers and thus insensitive to free stream turbulence.

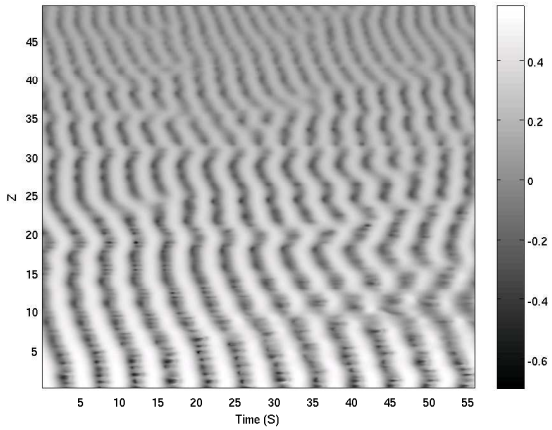

(a) Sampling line 2 d_m downstream from axis

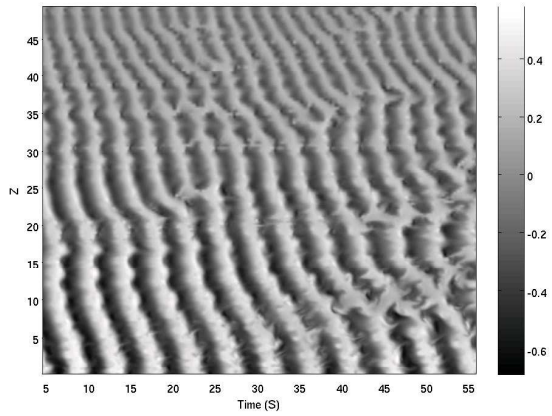

(b) Sampling line 12 d_m downstream from axis

Figure 2: Time evolution of cross-stream velocity 'V' along the span in the present DNS.

of same length 600 mm and $R_T = 75$ were used. The mean diameter of the cylinder A is set to 46 mm resulting in an aspect ratio of 13. The mean diameter of the cylinder B is 23 mm, leading to an aspect ratio of 26 (see Table 1). All models were equipped with thin circular end-plates with diameters equal to $3d_{2,A}$ to eliminate disturbances caused by free ends, an effect which has been reported by several authors. An entirely uniform inflow velocity was achieved by towing the models and the measurement system through a still water basin. Each measurement was tailored to observe the maximum number of shedding cycles by estimating the shedding frequency and adapting the image rate to match between 10 and 20 images per cycle. However, the maximum number of images is defined by the camera memory to about 1100 while the maximal experiment length is restricted by the tank length at higher towing velocities. The measurement plane is situated in line with the cylinder axis and directly at its downstream edge. It covers about 400 mm in streamwise and about 300 mm in spanwise direction, thus about half of the cylinder length. To observe the flow along the whole span, each run was repeated for the top, center and lower half. The velocity maps obtained from the images have a resolution of 84 by 72 vectors for all components U, V, and W.

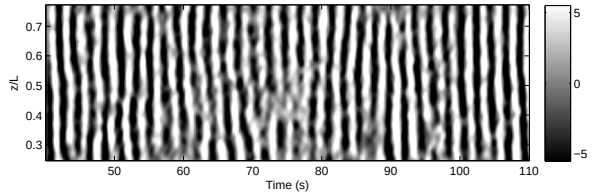

(a) model A_2

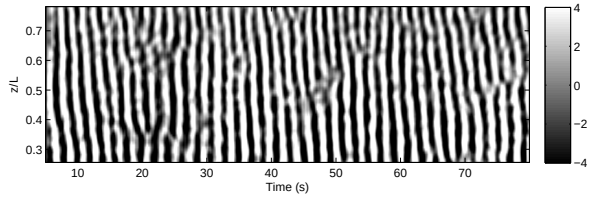

(b) model B_1

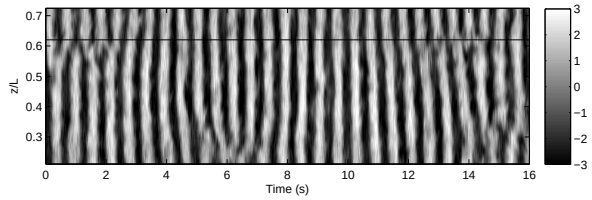

(c) model A_4

Figure 3: Time evolution of 'V' velocity along the span from PIV data (Sampling line 2 d_m downstream from axis).

RESULTS AND DISCUSSION

Figure 2(a),2(b) shows the time evolution of the instantaneous V velocity component in the present DNS sampled along two lines parallel to the axis of the cylinder and located $2d_m$ and $12d_m$ downstream the axis in X-direction, respectively. Similarly, the time evolution from the PIV measurements is shown in figure 3(a),3(b),3(c). An oblique and cellular shedding pattern is evident in both TrW (DNS) and TrSL regime (PIV).

Time traces of the cross-stream velocity (V) signal randomly picked at different Reynolds numbers from the DNS results were shown in figure 4(a),4(b). Low-frequency modulation, a typical feature of *vortex dislocations* or *vortex splits* can be seen in figure 4(a). However, random low-frequency fluctuations, a characteristic feature of TrW state of flow is only visible in figure 4(b) (for $Re > 175$). This is because the transitional eddies are formed laminar but become turbulent as they are carried downstream.

Time traces of U, V, W velocity components inside a dislocation region from the PIV data is shown in figure 5. The U component indicates a frequency modulation and decrease in amplitude similar to the DNS results (figure 4(a)) each time a dislocation occurs. Furthermore, the spanwise W component shows an increased amplitude shortly after. Figure 6 shows the instantaneous flow field of the same case under the vortex split. With the cross-stream V component plotted as background, the vortex centerlines can be found just at the boundary between dark and bright regions. It is obvious that the greatest spanwise velocity appears right in the split zone, while the parallel shedding is dominated by horizontal flow.

Qualitative investigations of the frequency spectra were carried out by the spectral analysis of cross-stream velocity component. The local Strouhal number ($St_{local} = fd_{local}/U$; d_{local} is the local diameter) *versus* local Reynolds number ($Re_{local} = Ud_{local}/\nu$) curve is shown in figure 7.

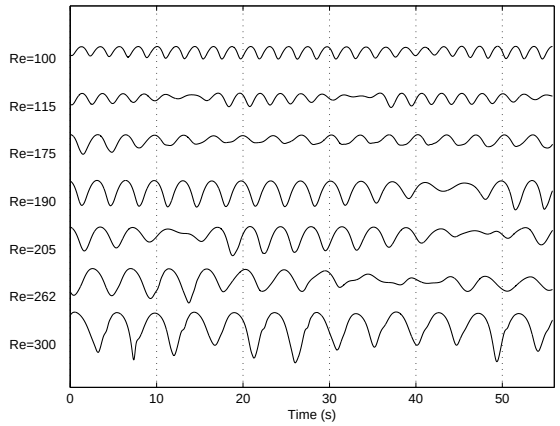

(a) Sampled 2 d_m downstream from axis

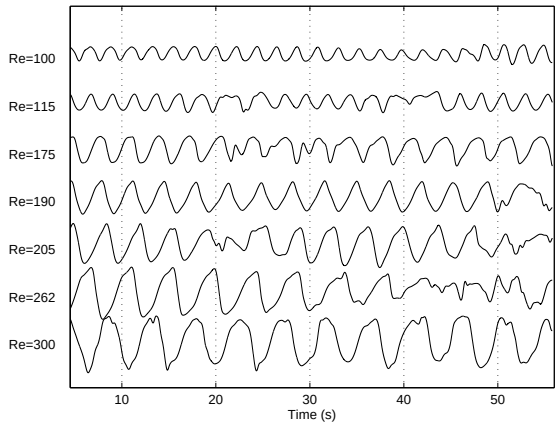

(b) Sampled 12 d_m downstream from axis

Figure 4: Time traces of 'V' velocity (DNS)

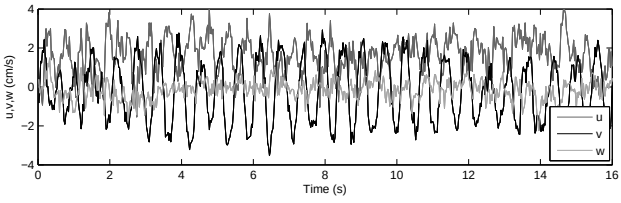

Figure 5: Time traces of U,V,W velocity components along the line marked in figure 3(c). (PIV data)

Piccirillo and Van Atta's (1993) curve-fit ($St = 0.195 - 5.0/Re$) and the numerical results by Narasimhamurthy et al.(2006) for the L3 regime together with the present DNS results (TrW) and the PIV measurements (TrSL) were plotted against the Fey et al. (1998) curve-fit for the uniform circular cylinder. The two discontinuities in the St_{local} *versus* Re_{local} curve in figure 7 for the uniform circular cylinder correspond to change over of eddy-shedding mode from laminar-mode A and mode A-mode B, respectively (Williamson, 1996). In contrast, these vortex dislocations occur spontaneously along the whole span for tapered circular cylinders. The St_{local} *versus* Re_{local} curve for $Re_m > 2300$ from the model B cylinder(PIV) matches the Fey et al. (1998) curve-fit for uniform circular cylinder.

The St_{local} distribution along the span reveals vortex

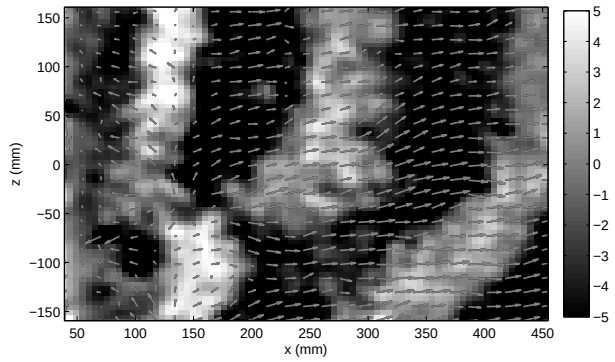

Figure 6: Instantaneous flow field at t=73s for case A_2 (PIV)

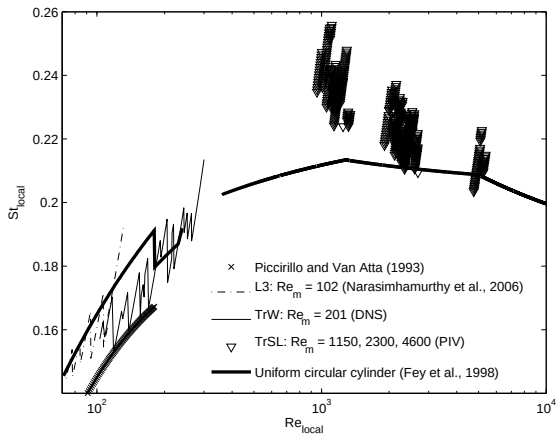

Figure 7: St_{local} *versus* Re_{local}

dislocations as changes in the local shedding frequency (figure 8(a),8(b)). Large jumps in the curve indicate a split region with a fixed spanwise position. If the shedding cell boundaries are more evenly distributed over the span, the St curve shows a greater number of small changes in the shedding frequency. The St_{local} magnitude gets smaller and smaller with increasing Re_m for all the experiments. It is generally lower for the cylinder A. Due to its low aspect ratio, the vortices were hardly dislocated in the model A case. Long time series reveal the presence of two cells with constant shedding frequency for Reynolds numbers up to 4600 (see the single dislocation in figure 3(a)). In the A_3 and A_4 models a third cell appears temporarily at $Re_m > 9200$. Figure 3(c) shows the two splits between the three cells being fixed in spanwise position for case A_4. Increasing numbers of cells with rising Re_m have been reported by Hsiao et al. (1998) as well. Piccirillo and Van Atta (1993) found that increase in aspect ratio increases the number of shedding cells along the span in L3 regime. It is interesting to see a similar effect in the TrSL regime of the present PIV study (see model B results in figure 8(b)). For the B model are the cell boundaries only in the lower half distinct and consistent over multiple experiments. The upper half shows less well defined cell boundaries which is also visible in figure 3(b). This might indicate a stronger end effect on the upper cylinder end.

In order to identify the topology and the geometry of the vortex cores correctly the λ_2-definition by Jeong and Hussain (1995) was used in the present DNS study. λ_2 corresponds to the second largest eigenvalue of the symmetric tensor $S_{ij}S_{ij} + \Omega_{ij}\Omega_{ij}$, where S_{ij} and Ω_{ij} are respectively the symmetric and antisymmetric parts of the velocity gradient tensor. Figure 9 shows the iso-surfaces of negative λ_2, vorticity magnitude or enstrophy $\mid \omega \mid$, streamwise vorticity ω_x and the spanwise vorticity ω_z evaluated at the same instant in time. The vortex dislocations at $Z \approx 12.5, 22, 40$ and the small-scale streamwise structures (mode A and mode B) along the span are clearly visible. The development of helical twisting of vortex tubes is visible in the vicinity of the vortex dislocations. Williamson concluded that these helical twistings are the fundamental cause for the rapid spanwise spreading of dislocations, and indeed for the large-scale distortion and break-up to turbulence in a natural transition wake. In uniform circular cylinder wakes the Reynolds number will be constant along the whole span and therefore the individual modes of 3-dimensionality (either mode A or mode B) exist along the entire span of the cylinder. However, in the present tapered cylinder case (DNS) the Re_{local} varies along the span and both mode A and mode B co-exists in the same geometry. Thereby, only a small span of the cylinder is available for each of the modes to develop (especially for mode A) and it is hard to pin-point the exact Reynolds number at which these modes start to appear. Flow-visualization revealed that the mode A appeared around $Re_{local} \approx 200$ and mode B around $Re_{local} \approx 250$.

In figure 10(b),10(c) cross-sectional views of mode-B

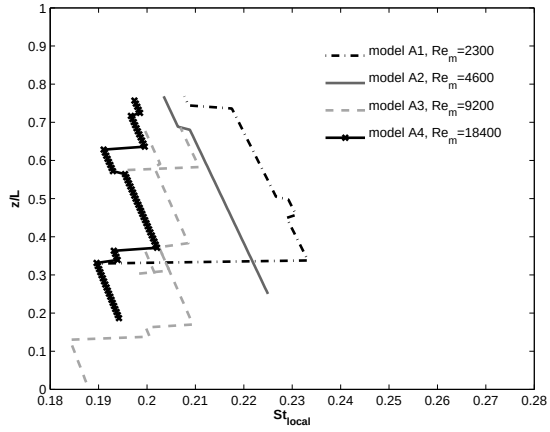

(a) model A; aspect ratio = 13

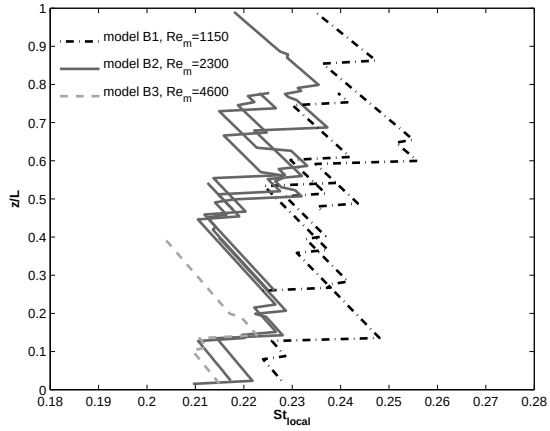

(b) model B; aspect ratio = 26

Figure 8: St_{local} along the span (PIV data)

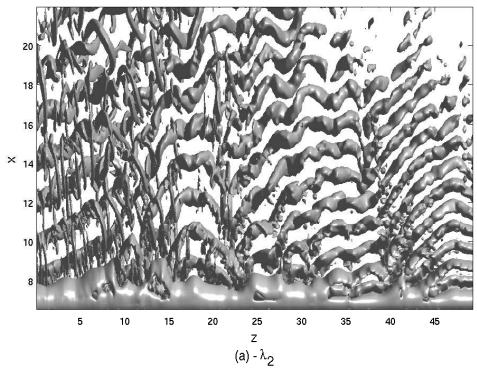

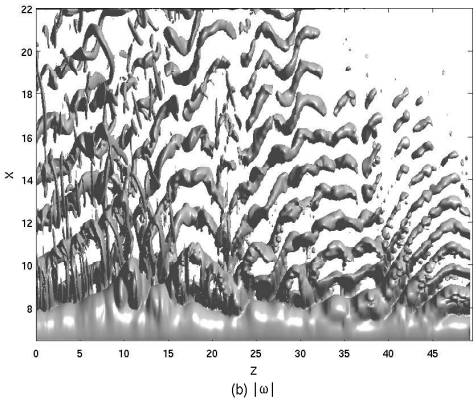

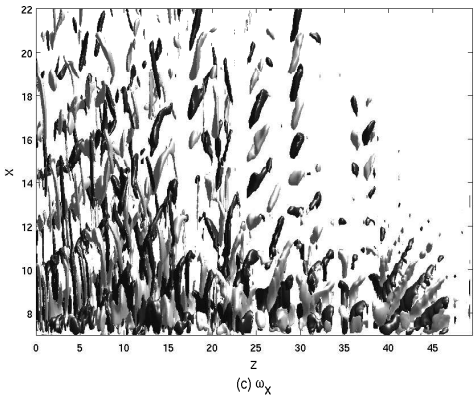

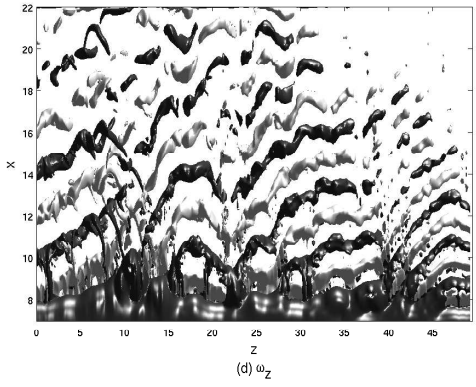

Figure 9: 3-dimensional vortical structures from the present DNS taken at the same instant in time as vortex dislocation occurs (at $Z \approx 12.5, 22, 40$) along the span. The flow direction is from bottom to top. (a)Negative λ_2; (b)Enstrophy $\mid \omega \mid$; (c)streamwise vorticity ω_x; (d)cross-stream vorticity ω_z. The surfaces colored white and black mark a particular value of positive and negative vorticity, respectively.

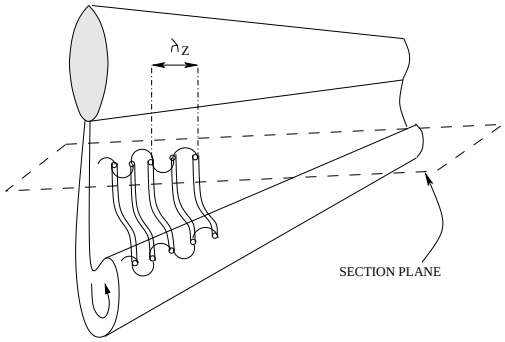

(a) $Y - Z$ section plane (dotted line)

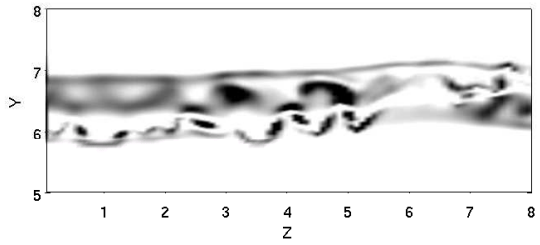

(b) mode B 'mushroom' structures at $Z \approx 3 - 6$

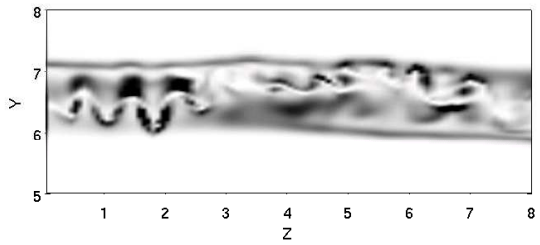

(c) mode B 'mushroom' structures at $Z \approx 0 - 3$

Figure 10: Cross-sectional views of mode B showing 'mushroom' vortex pair structures in the present DNS. (note that section plane is parallel to the axis and at an angle to the vortex lines and thereby structures are visible only in some parts of the plane)

streamwise vortex structure from the DNS results were shown. We can see clearly the smaller-scale 'mushroom' vortex pair structures of mode-B vortex shedding. There is a remarkable similarity between this vortex array and that found by Williamson (1996). However, note that the section plane is parallel to the axis and at an angle to the vortex lines (see figure 10(a)) and thereby structures are visible only in some parts of the plane. The wavelength of mode B was found to be $\lambda_Z/d_2 \approx 1$, which is surprisingly close to the experimental value $\lambda_Z/D = 0.98$ found by Williamson (1996) in the uniform circular cylinder wake.

Piccirillo and Van Atta (1993) reported that the vortex splitting in L3 regime occurs when the streamwise vorticity ω_x becomes too large. It is fascinating to see the sharp contrast between the normal vortex shedding pattern and the vortex split in figure 11(a),11(c) and 11(b),11(d), respectively. Note the increase in ω_x in figure 11(b) and 11(d) by an order of magnitude 10 as vortex splits.

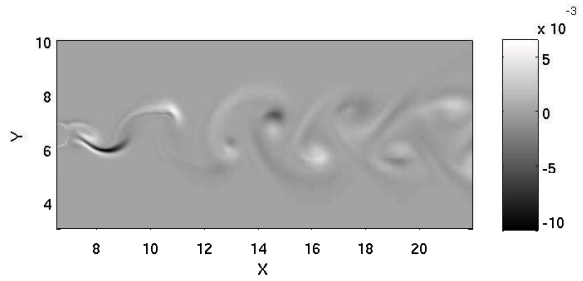

(a) Z=12.5; $Re_{local} = 250$ (before split)

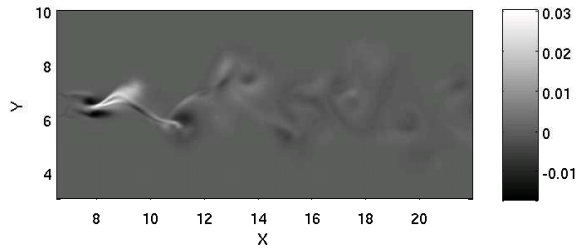

(b) Z=12.5; $Re_{local} = 250$ (vortex split)

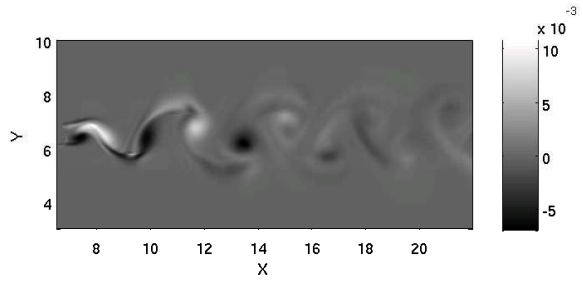

(c) Z=22; $Re_{local} = 212$ (before split)

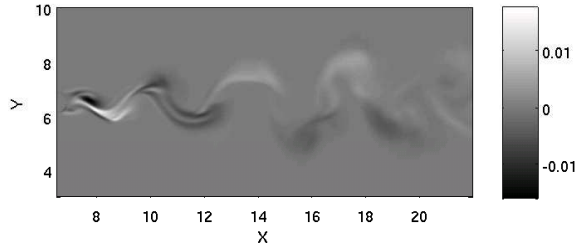

(d) Z=22; $Re_{local} = 212$ (vortex split)

Figure 11: Streamwise vorticity (ω_x) as vortex splits (DNS results). (note that (a),(b) and (c),(d) were taken at the same spanwise location, respectively)

CONCLUSIONS

Oblique and cellular shedding pattern was observed in both TrW (DNS) and TrSL regime (PIV). In the present PIV study it was found that increase in aspect ratio increases the number of shedding cells along the span, an effect also reported by Piccirillo and Van Atta (1993) in their L3 regime case. Both mode A and mode B were found to co-exist in the same geometry (DNS) but only in a small span of the cylinder. Flow-visualization revealed that the mode A appeared around $Re_{local} \approx 200$ and mode B around $Re_{local} \approx 250$. Cross-sectional views of mode B in the DNS results revealed the smaller-scale 'mushroom' vortex pair structures, which is remarkably similar to that found by Williamson (1996). The wavelength of mode B was found to be $\lambda_Z/d_2 \approx 1$, which is surprisingly close to the experimental value $\lambda_Z/D = 0.98$ found by Williamson (1996) in the uniform circular cylinder wake. In the present DNS study it was found that streamwise vorticity ω_x becomes large (increases by an order of magnitude 10) as vortex dislocation occurs, an effect also observed by Piccirillo and Van Atta (1993).

REFERENCES

Fey, U., König, M., and Eckelmann, H., 1998, "A new Strouhal-Reynolds-number relationship for the circular cylinder in the range 47<Re<2 × 10^5", *Phys. Fluids*, Vol. 10, pp. 1547-1549.

Hsiao, F., and Chiang, C., 1998, "Experimental study of cellular shedding vortices behind a tapered circular cylinder", *Exp. Thermal Fluid Sci.*, Vol. 17, pp. 179-188.

Jeong, J., and Hussain, F., 1995, "On the identification of a vortex", *J. Fluid Mech.*, Vol. 285, pp. 69-94.

Manhart M., 2004, "A zonal grid algorithm for DNS of turbulent boundary layers", *Computers & Fluids*, Vol. 33, pp. 435-461.

Narasimhamurthy, V. D., Schwertfirm, F., Andersson, H. I., and Pettersen, B., 2006, "Simulation of unsteady flow past tapered circular cylinders using an immersed boundary method", *Proceedings, ECCOMAS European Conference on Computational Fluid Dynamics*, P. Wesseling et al., ed., TU Delft, The Netherlands.

Narasimhamurthy, V. D., Andersson, H. I., and Pettersen, B., 2007, "Direct numerical simulation of vortex shedding behind a linearly tapered circular cylinder", *Proceedings, IUTAM Symposium on Unsteady Separated Flows and their Control*, Corfu, Greece.

Papangelou, A., 1992, "Vortex shedding from slender cones at low Reynolds numbers", *J. Fluid Mech.*, Vol. 242, pp. 299-321.

Parnaudeau, P., Heitz, D., Lamballais, E., and Silvestrini, J. H., 2007, "Direct numerical simulations of vortex shedding behind cylinders with spanwise linear nonuniformity", *J. Turbulence*, Vol. 8, No. 13.

Peller, N., Le Duc, A., Tremblay F., and Manhart M., 2006, "High-order stable interpolations for immersed boundary methods", *Int. J. Numer. Meth. Fluids.* Vol. 52, pp. 1175-1193.

Piccirillo, P. S., and Van Atta, C. W., 1993, "An experimental study of vortex shedding behind linearly tapered cylinders at low Reynolds number", *J. Fluid Mech.*, Vol. 246, pp. 163-195.

Vallès, B., Andersson, H. I., and Jenssen, C. B., 2002, "Oblique vortex shedding behind tapered cylinders", *J. Fluids Struct.*, Vol. 16, pp. 453-463.

Williamson, C. H. K., 1996, "Three-dimensional wake transition", *J. Fluid Mech.*, Vol. 328, pp. 345-407.

Article 5

Cellular vortex shedding behind a tapered circular cylinder

Narasimhamurthy, V. D., Andersson, H. I. & Pettersen, B.

Submitted to *Physics of Fluids*.

Cellular vortex shedding behind a tapered circular cylinder

Vagesh D. Narasimhamurthy[1], **Helge I. Andersson**

Fluids Engineering Division, Department of Energy and Process Engineering, Norwegian University of Science and Technology (NTNU), 7491 Trondheim, Norway

Bjørnar Pettersen

Department of Marine Technology, Norwegian University of Science and Technology, 7491 Trondheim, Norway

Direct numerical simulation of vortex shedding behind a tapered circular cylinder with the taper ratio 75 placed normal to the inflow has been studied. The Reynolds numbers based on the uniform inflow velocity and the diameter of the cylinder at the wide and narrow ends were 300 and 102, respectively. In the present numerical study it was observed that even with a very long time sampling discrete cellular shedding pattern prevails. This is in contrast to what Parnaudeau et al. (2007) speculated in their tapered cylinder study, where they suggested that with a longer time sampling diffused cellular pattern might appear. In the present investigation it was found that streamwise vorticity becomes large as vortex dislocation occurs, an effect also reported by Piccirillo and Van Atta (1993) in their experimental study. Flow-visualizations revealed that both mode A and mode B secondary flow structures co-exist along the span of the present tapered cylinder. The wavelength of mode B is surprisingly in good agreement with the experimental value found by Williamson (1996) for uniform circular cylinders. The present numerical calculation revealed a spanwise secondary motion, both in the front stagnation zone and also in the wake of the cylinder. In the front stagnation zone, the secondary flow was driven by a spanwise pressure gradient. The secondary flow pattern in the wake was found to be rather complex. This complex behaviour of the secondary motion was attributed to the *intrinsic* secondary-instabilities induced by the transition process itself. This is in contrast to what Parnaudeau et al. (2007) speculated in their tapered cylinder study, where they attributed this to the oblique and cellular vortex shedding. In spite of this secondary flow in the base region, the local formation length from the present tapered cylinder study is surprisingly in good agreement with the results of uniform circular cylinders.

[1]Corresponding author. Tel.: +47 73593563; fax: +47 73593491; E-mail: vagesh@ntnu.no

Key words: Oblique shedding, DNS, tapered cylinder, vortex dislocation, bluff body wake.

1 Introduction

The flow over a circular cylinder remains two-dimensional as long as the Reynolds number is below the critical value ≈ 190 [1] beyond which intrinsic secondary instabilities are known to occur. Such secondary instabilities render the flow three-dimensional and eventually to a turbulent state. These three-dimensionalities can induce significant spanwise variations in the velocity and pressure fields. In contrast, such three-dimensionalities are known to occur if the diameter of the cylinder changes discontinuously [2, 3, 4] or linearly [5, 6, 7, 8, 9, 10, 11, 12, 13, 14] even at a Reynolds number well below the critical value ≈ 190. Almost all the previous studies on the flow past linearly tapered circular cylinders are either in the laminar flow regime [5, 6, 7, 8, 9, 10, 11, 15] or in the turbulent flow regime [12, 13]. It is therefore not clear at this stage how the flow responds in the transitional flow regime.

The only exception is the numerical study by Parnaudeau et al. [14] where they provided some data of the cellular wake pattern behind their tapered circular cylinder. Their objective was limited to study and compare the flow topology of the wake behind a circular cylinder in a linear shear flow with the wake of a tapered circular cylinder. They however confess that their frequency data were obtained from a short time-series (around 10 vortex shedding cycles at the wide end of the tapered cylinder) and the number of realizations were not sufficient for the results to converge to a statistically stationary state. The time evolution of their data along the span of the cylinder revealed a more complex vortex shedding pattern than the cellular structure obtained from the Fourier analysis. They argued that with a longer time-series the Fourier analysis might perhaps produce a diffused cellular wake pattern. This however has not been verified.

In addition to the frequency data Parnaudeau et al. [14] observed wavy distribution of the spanwise secondary motion in the wake. They speculated that this oscillatory behaviour of the secondary motion along the span, where the secondary flow changed its course of direction randomly, may be due to the three-dimensionalities induced by the oblique vortex shedding and the vortex dislocations along the span. They state that this point needs further insight. Recently Narasimhamurthy et al. [15] studied steady laminar flow past a tapered circular cylinder and they observed spanwise secondary motion both in the front stagnation zone and also in the wake, driven

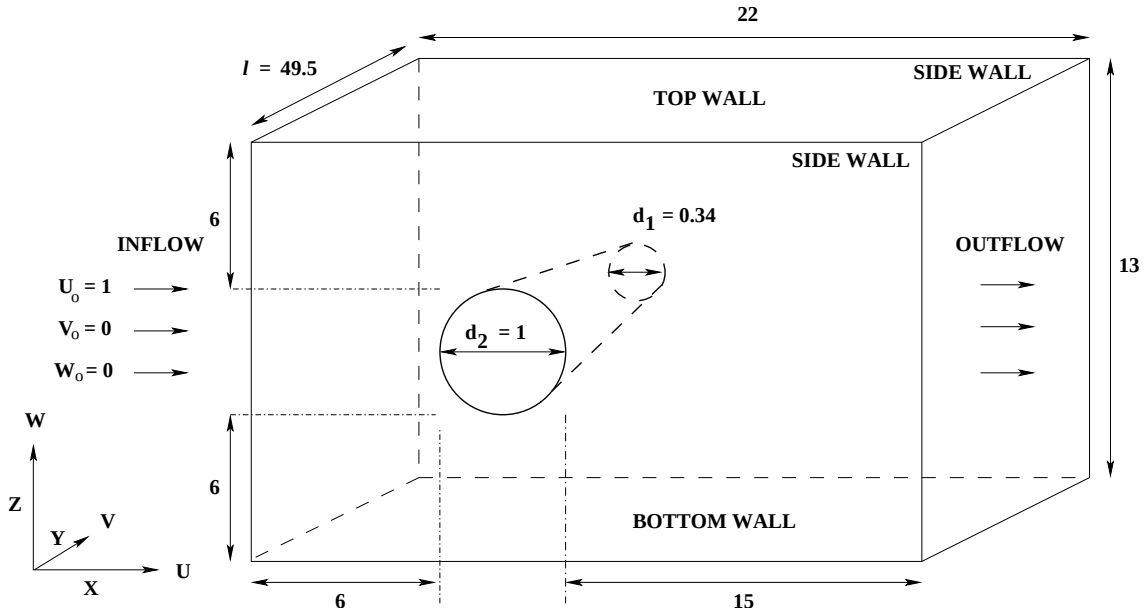

Figure 1: Computational domain (not to scale).

by the spanwise pressure-gradient alone. Similar conclusions were also drawn by Narasimhamurthy et al. [16] where they noticed pressure-driven secondary motion in the turbulent wake of a tapered flat plate, which coincidentally also exhibited cellular vortex shedding pattern. It is therefore interesting to see whether such a conclusion can be drawn even in the present study of flow past a tapered cylinder, where the wake is in the transitional flow regime.

The above issues will be addressed for the first time in the present Direct numerical simulation (DNS) study. In addition to frequency (both Fourier and Wavelet) analysis a more detailed investigation of the spanwise two-point correlations and the instantaneous vortical structures will be carried out. The spanwise variations of the velocity and the pressure fields will also be shown. Reynolds averaged statistical quantities at some sections along the span of the cylinder will be presented and the underlying physics will be highlighted.

2 Flow configuration and numerical method

Let us consider the flow past a tapered circular cylinder with the view to explore the vortex shedding at low Reynolds numbers. The taper ratio, $R_T = l/(d_2 - d_1) = 75$, where l is the length of the cylinder and d_2 and d_1 denote the diameter of its wide and narrow ends, respectively. Due to the substantial tapering, the local Reynolds number varies from 300 at the wide end to 102 at the narrow end of the cylinder. Thereby, the Reynolds number chosen in the present DNS study is such that both the

CASE	R_T	AR	Re_2	Re_m	Re_1
Present simulation	75	74	300	201	102
Piccirillo & Van Atta [8]	75	-	179	-	99
Piccirillo & Van Atta [8]	75	-	103	-	57
Vallès et al.[9]	75	53	163	-	91
Vallès et al.[9]	75	53	131	-	73
Narasimhamurthy et al.[15]	75	43	40	31	22
Hsiao & Chiang [12]	75	-	-	1.4×10^4	-
Parnaudeau et al.[14]	40	40	300	200	100

Table 1: Geometrical and flow parameters for tapered cylinder studies.

laminar and the transitional flow regimes co-exist along the span of the cylinder. The computational domain was as shown in figure 1. All spatial dimensions are normalized by d_2 and all velocities are scaled with the uniform inflow velocity U_o. The mean diameter of the cylinder, $d_m = 0.67d_2$. The aspect ratio ($AR = l/d_m$), R_T, and the Reynolds numbers Re_2, Re_1, Re_m, based on the uniform inflow velocity U_o and the diameters d_2, d_1, d_m, respectively, are as shown in Table 1.

The Navier-Stokes equations in *incompressible* form were solved in 3-D space and time using a *parallel* finite-volume code called MGLET ([18, 11]). The code uses staggered Cartesian grid arrangements. Discretization of the spatial derivatives was achieved by means of a 2^{nd}-order central-differencing scheme. The time marching was carried out using a 3^{rd}-order explicit Runge-Kutta scheme for the momentum equations in combination with an iterative SIP (Strongly Implicit Procedure) solver for the Poisson equation. The size of the computational domain in each coordinate direction was $L_x = 22d_2$, $L_y = 49.5d_2$, and $L_z = 13d_2$, as shown in figure 1. The number of grid points in each coordinate direction ($N_x \times N_y \times N_z$) was equal to $360 \times 250 \times 164$, respectively. The time step was chosen as $\Delta t = 0.003d_2/U_o$ and the number of Poisson iterations per time step was limited to 50. Parallelization was implemented using Message Passing Interface (MPI). The computations were performed on a *SGI Origin 3800* parallel computer. The total consumption of CPU-time was approximately 40000 hours.

A uniform velocity profile $U_o = 1$ was prescribed at the inlet without any free-stream perturbations and a Neumann boundary condition was used for the pressure. A free-slip boundary condition was applied on both the side walls, as well as at the top and bottom walls (cf. figure 1). At the outlet, a Neumann boundary condition was used for velocities and the pressure was set to zero. A *direct forcing* Immersed Boundary Method (IBM) ([17, 11]) was used to transform the no-slip condition at the cylinder surface into internal boundary conditions at the nodes of the Cartesian grid. The

internal boundary condition value had to be determined by interpolation. In the present DNS we used least-squares interpolation of 3^{rd}-order accuracy. The detailed derivation, validation and implementation of this technique in the code MGLET were explained in [17].

3 Results and discussion

3.1 Frequency analysis

The time evolution of the instantaneous velocity components U, V, W and the instantaneous pressure, P, were sampled along two lines parallel to the axis of the cylinder and located $2d_m$ and $12d_m$ downstream the axis in X-direction, respectively. Both lines were offset by $1d_m$ in Z-direction. It would be inappropriate to present all the data here due to space constraints. Therefore, only the time trace of the cross-stream velocity W sampled at $12d_m$ is shown in figure 2. The total sampling time was equal to 180 d_2/U_o or 530 d_1/U_o, which covers about 38 vortex shedding cycles at the wide end and about 80 shedding cycles at the narrow end of the cylinder. In contrast, the sampling length in Parnaudeau et al. [14] was about 10 vortex shedding cycles at the wide end of their tapered cylinder. Thereby, the sampling length in the present DNS is around 4 times longer than that of Parnaudeau et al. [14]. The pattern clearly indicates *oblique* and *cellular* vortex shedding with random occurance of *vortex dislocations* or *vortex splits* along the span. It is easy to see that the vortex dislocations are not occurring periodically in time at the same spanwise position. This justifies the need for such a long and expensive time sampling. Some time trace signals of the cross-stream velocity (W) at some different Reynolds numbers are shown in figure 3(a),3(b). Low-frequency modulation, a typical feature of *vortex dislocations* or *vortex splits* can be seen in figure 3(a). The signals are more distorted in figure 3(b) (for $Re > 190$) due to the appearance of random fluctuations which is a characteristic feature of transition state of flow. This is because the transitional eddies are formed laminar but become turbulent as they are carried downstream. In other words transitional eddies have laminar cores with turbulent circumference.

3.1.1 Fourier analysis

Quantitative investigations of the frequency spectra were carried out by Fourier analysis of cross-stream velocity component (W) time traces. Shedding frequencies (f) obtained from the Fast Fourier Transform (FFT) of the velocity signals are plotted against the Re_{local} ($= U_o d_{local}/\nu$; d_{local} is the local diameter) in figure 4(a).

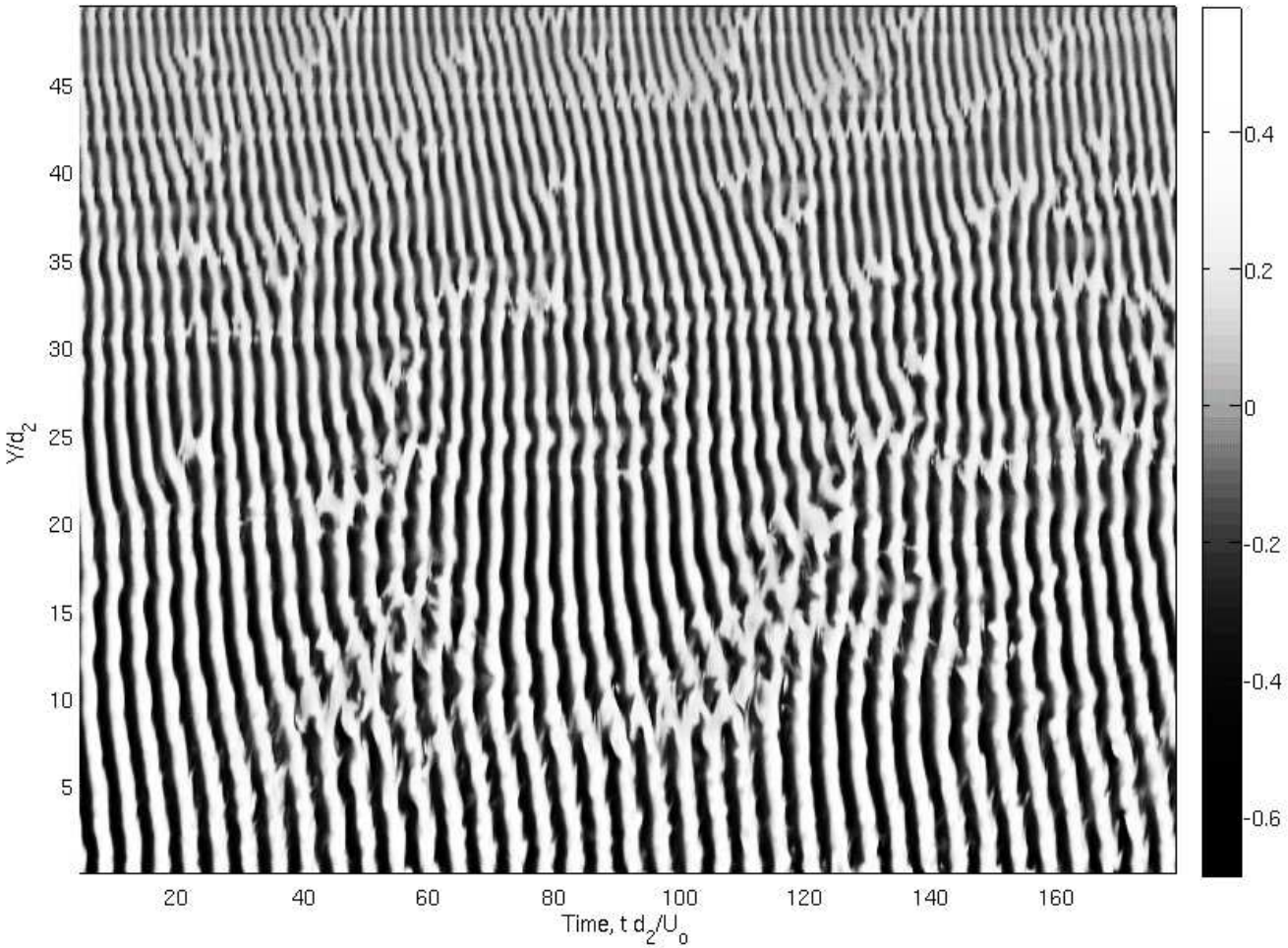

Figure 2: Time evolution of the cross-stream velocity (W) showing vortex-dislocations along the entire span. The sampling line is at $X/d_m = 12$ and $Z/d_m = -1$ (measured from the axis of the cylinder). $Y/d_2 = 0$ corresponds to $Re_2 = 300$ and $Y/d_2 = 49.5$ corresponds to $Re_1 = 102$.

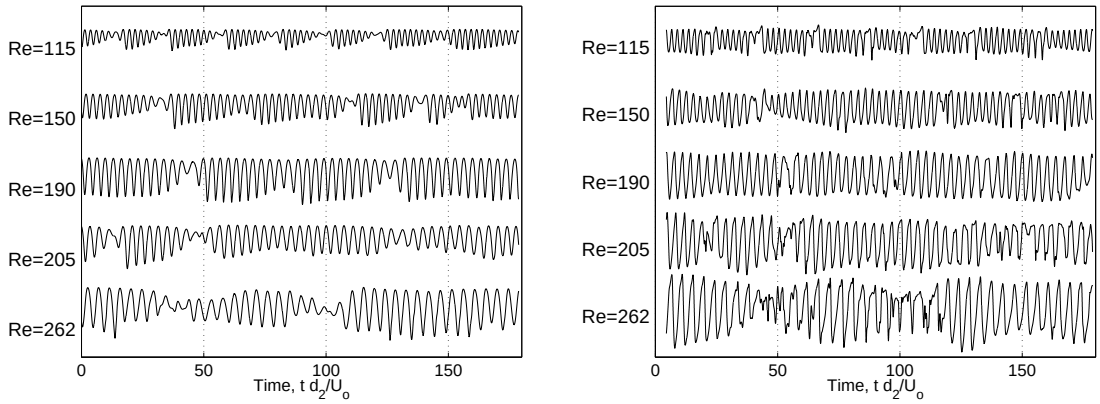

(a) Sampled 2 d_m downstream from axis

(b) Sampled 12 d_m downstream from axis

Figure 3: Time traces of 'W' velocity at different local Reynolds numbers.

Note that the shedding frequency is varying along the span in discrete steps between cells of constant shedding frequency. In order to confirm that the total sampling time in the present DNS is long enough for the results to converge to a statistically stationary state, the local Strouhal number ($St_{local} = fd_{local}/U_o$) obtained from varying lengths of time sample was plotted in figure 4(b). Even though the curves nearly collapse towards the narrow end of the cylinder distinct differences arise towards the wider end, where the length of the shedding period is longer, thereby demanding a longer sampling time for the curves to collapse. This is clearly achieved in the present case where the curves with the respective sampling times $174.0d_2/U_o$ and $130.5d_2/U_o$ nearly coincide. The present DNS data clearly demonstrates that even with a longer time series (nearly 4 times longer than Parnaudeau et al. [14]) discrete cellular shedding pattern prevails. This is in contrast to what Parnaudeau et al. [14] speculated in their tapered cylinder study, where they suggested that with a longer time sampling diffused cellular pattern might appear.

In figure 5(a), Strouhal number ($St = fd_m/U_o$) obtained from both the time series of the present DNS (sampled $2d_m$ and $12d_m$ downstream the axis, respectively) is compared against the data of Parnaudeau et al. [14]. Even though the data from both the time series nearly collapse, small differences between them exist in identifying the position of the cells along the span. The reason for which was observed in the flow visualizations, where the dislocated vortex filaments experience a modest spanwise motion as they are carried downstream. The significant contrast in the cellular shedding pattern between the present tapered cylinder and that of Parnaudeau et al. [14] should be noticed in figure 5(a). Recall that the Reynolds numbers were same in both the studies. However, it is difficult to draw any firm conclusions about this observation as their data were obtained from a very short time series. The

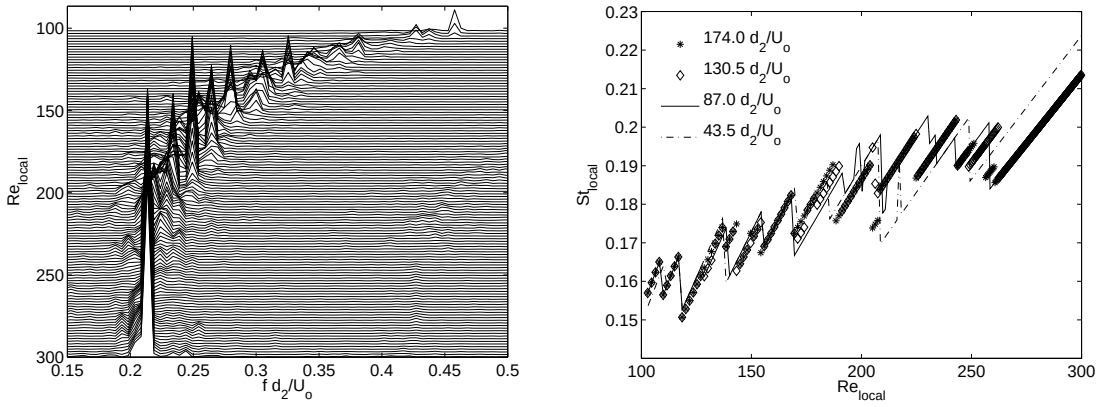

(a) Frequency spectra

(b) Effect of sampling time

Figure 4: Shedding frequencies (fd_2/U_o) from Fourier analysis of the W velocity time trace sampled $12d_m$ downstream from the axis; and the corresponding local Strouhal number (St_{local}) obtained with varying lengths of time sample.

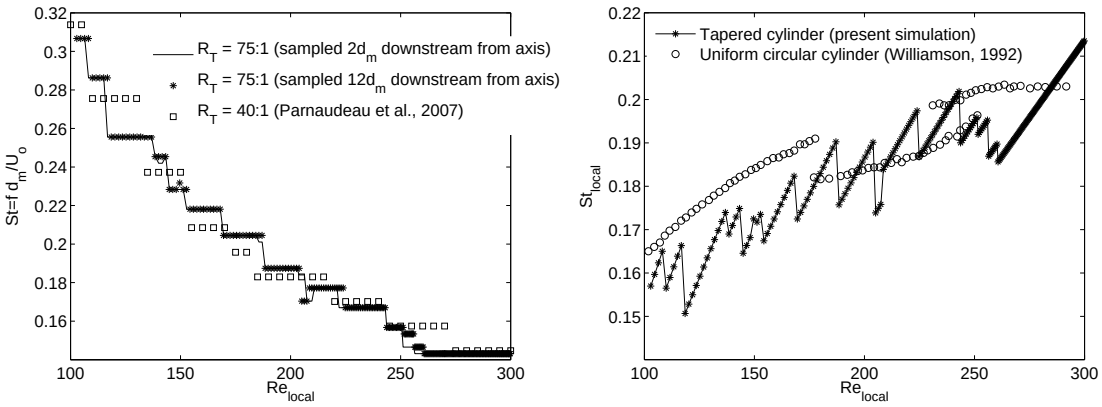

(a) Effect of taper ratio (R_T)

(b) Tapered cylinder *versus* uniform circular cylinder

Figure 5: Strouhal number *versus* Reynolds number.

vortex dislocations in the transition state of flow of a *uniform* circular cylinder typically occur at the location of mode A instability [20]. In contrast, these large-scale structures occur spontaneously along the whole span of tapered circular cylinders (see figure 5(b)). The two discontinuities in the local Strouhal number *versus* Re_{local} curve in figure 5(b) for the uniform circular cylinder correspond to change-over of eddy-shedding mode from laminar-mode A and mode A-mode B, respectively [20]. However, for tapered circular cylinders vortex dislocations depend primarily on the taper ratio R_T [8].

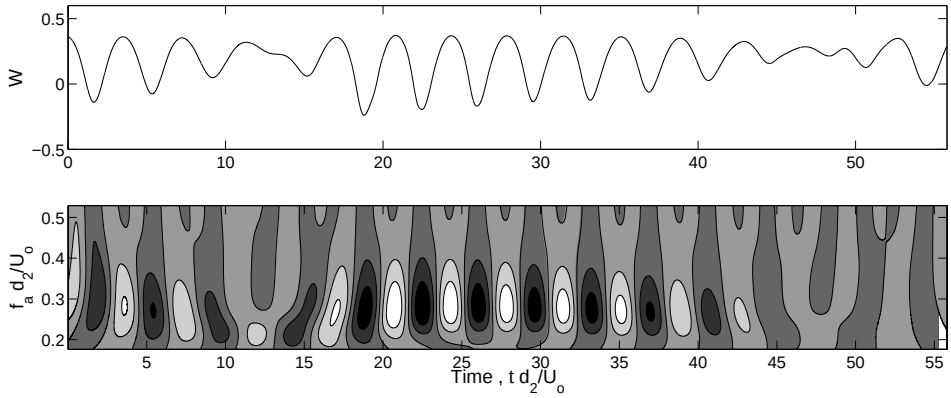

(a) Re=205; Sampled 2 d_m downstream from axis

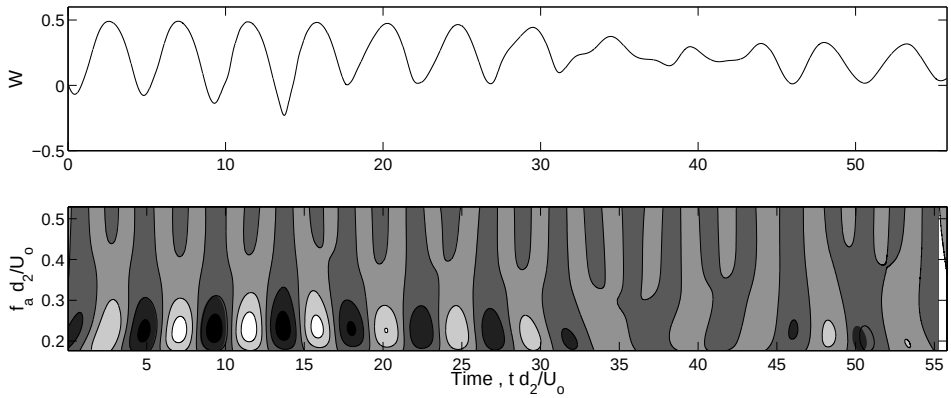

(b) Re=262; Sampled 2 d_m downstream from axis

Figure 6: Wavelet results corresponding to the pseudo-shedding frequencies (f_a). In each plot, the phase diagram is plotted below the signal which was transformed.

3.1.2 Wavelet analysis

It is essential to quantify the variations of frequency as a function of time but Fourier analysis fails to provide any time-variance distribution of the fluctuating signals. Therefore, in order to explore the time-scale or time-frequency variations of the velocity signal as vortex splits, a one-dimensional continuous wavelet transform (CWT) was applied to selected data sets. The CWT is defined as,

$$C(a,b) = \int_{-\infty}^{\infty} s(t) \frac{1}{\sqrt{a}} \Psi \left(\frac{t-b}{a} \right) dt \tag{1}$$

where *C(a,b)* is the wavelet coefficient of the data *s(t)* at any given temporal scaling factor a and the position b (see Farge [22] for an extensive review of different wavelet transforms). In the present analysis, the mother wavelet Ψ is the *Morlet* wavelet

defined as $\Psi(t) = e^{-t^2/2}\ cos(5t)$. Since *s(t)* is a discrete signal, a piecewise constant interpolation of the *s(k)* values, *k=1 to length* was used. The CWT was performed using algorithms implemented in the MATLAB software package. In wavelet analysis, the temporal scaling factor a is used rather than the frequency (f) employed in conventional Fourier analysis. In order to interpret the results of wavelet analysis in the conventional way, the scaling factor was converted into an equivalent Fourier frequency or *pseudo-shedding frequency* $f_a = f_c/(a\ \Delta t)$, where, f_c is the center frequency of the *Morlet* wavelet and Δt is the sampling period. In figure 6, the phase diagrams are shown below the corresponding transformed signals. From the phase diagrams it is clear that the primary shedding frequency undergoes a considerable and abrupt reduction during the time interval $40 - 55$ in figure 6(a) and $30 - 45$ in figure 6(b), respectively. The contours of high energy density (white) in figure 6 correspond to the parts of the signal before and after the occurance of vortex dislocations, where the primary shedding frequency is the most energetic and associated with the highest amplitude values. These harmonics, which are initially arranged in a consistent pattern correspond to the organized coherent motion. With the occurance of a vortex dislocation, the harmonics break from this pattern. In order to compensate the delay in the vortex shedding mechanism caused by the vortex dislocations, the harmonics then reorganize themselves as the flow further evolves in time. Thus wavelet analysis clearly illustrates the flow mechanism associated with the frequency and amplitude modulations, which appear during the formation and advection of a vortex dislocation.

3.2 Spanwise two-point correlation

To further explore the cellular vortex shedding phenomenon, the spanwise coupling of the vortex motion is studied by means of spanwise two-point correlations, where the correlation coefficient is defined as $\overline{\phi(Y)\ \phi(Y + \Delta Y)}\ /\ \overline{\phi(Y)^2}$. In statistically homogeneous flows, this correlation is a function only of the separation ΔY between the two points and does not depend on the position Y. In addition, the correlation is symmetric in the direction of homogeneity, i.e. independent of the sign of ΔY. However, this should not be true in the present case as the flow is inhomogeneous in all the three directions. This is indeed what we see in figure 7. The correlation coefficient of the secondary flow (V) and the cross-stream velocity (W) are plotted against the spanwise separation ΔY at the middle of the span (corresponding to $Re_{local} = 200$) in figure 7(a) and figure 7(b), respectively. The correlation is clearly asymmetric and goes to zero within about $\Delta Y/d_2 = 4 - 8$, since the spanwise vortex filaments experience vortex dislocations along the span. The negative correlation

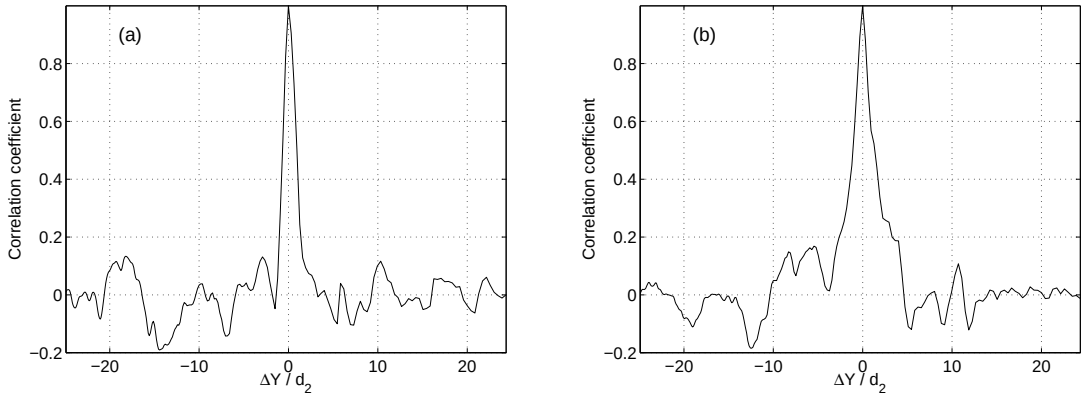

Figure 7: Spanwise correlation of (a) the secondary motion V; (b) cross-stream velocity W; at the middle of the span corresponding to $Re_{local} = 200$. ΔY corresponds to spanwise separation length.

implies that the secondary motion is oppositely directed at that position.

3.3 Instantaneous vortical structures

In order to identify the topology of the vortex cores correctly the λ_2-definition by Jeong and Hussain [23] was used. λ_2 corresponds to the second largest eigenvalue of the symmetric tensor $S_{ij}S_{ij} + \Omega_{ij}\Omega_{ij}$, where S_{ij} and Ω_{ij} are respectively the symmetric and antisymmetric parts of the velocity gradient tensor. In figure 8, the iso-surfaces of negative λ_2, spanwise vorticity ω_y and streamwise vorticity ω_x evaluated at the same instant in time, $t = 47d_2/U_o$ were plotted together. Three-dimensionality in the form of waviness in the spanwise vortex cores (primary Karman vortices) is evident even in the laminar part of the wake. The vortex dislocations formed between spanwise cells of different frequency when the primary vortices move out of phase with each other are visible at $Y \approx 12.5, 22$, and 37. The snap shots show the appearance of small-scale streamwise structures (mode A and mode B) along the span in the lower parts of figure 8(a),8(c). The development of helical twisting of vortex tubes is visible in the vicinity of the vortex dislocations. Williamson [19] concluded that these helical twistings are the fundamental cause for the rapid spanwise spreading of dislocations, and indeed for the large-scale distortion and break-up to turbulence in a natural transitional wake behind a uniform cylinder. Increase in streamwise vorticity ω_x in the vicinity of vortex dislocations should be observed in figure 8(c). It is fascinating to see the distinct contrast between the normal vortex shedding pattern (before the dislocation) and as the vortex dislocation occurs in figure 9(a),9(c) and 9(b),9(d), respectively. The ten-fold increase in ω_x in

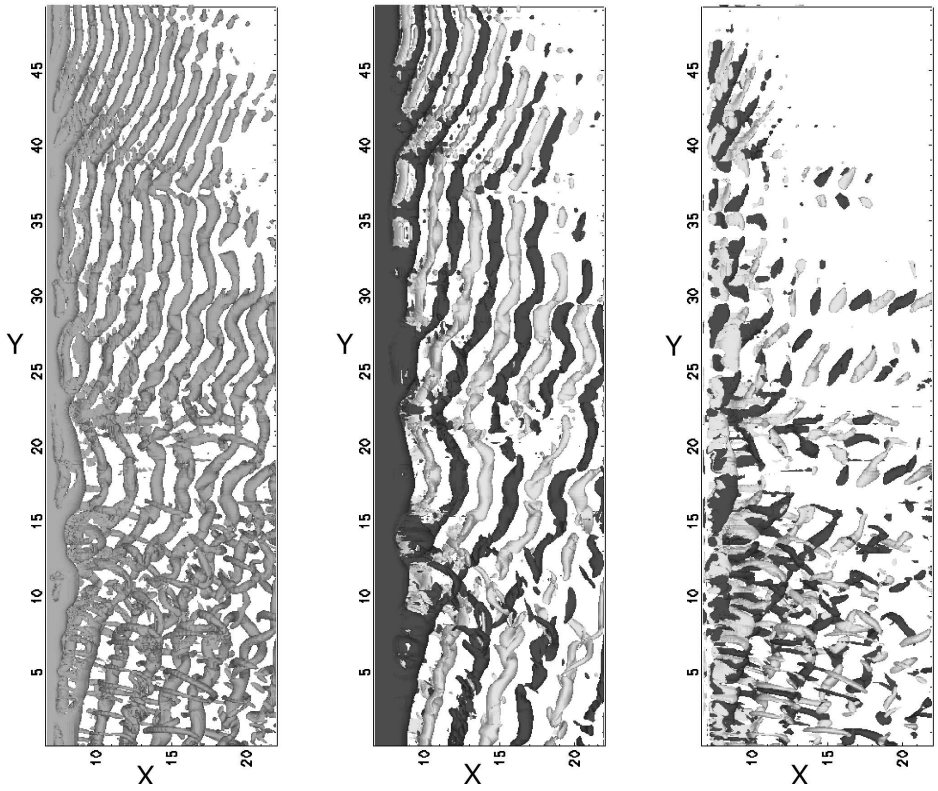

(a) negative λ_2 (b) spanwise vorticity ω_y (c) streamwise vorticity ω_x

Figure 8: 3-dimensional vortical structures at the same instant in time, $t = 47d_2/U_o$ as vortex dislocation occurs along the span. The surfaces colored white and black in (b),(c) mark $+0.003\ \omega\nu/U_o^2$ and $-0.003\ \omega\nu/U_o^2$, respectively.

figure 9(b) and 9(d) as the vortex dislocation occurs is note-worthy. Piccirillo and Van Atta [8] reported that the vortex dislocations in the laminar regime occurred when the streamwise vorticity ω_x became too large or in other words when the angle of shedding became too large.

In uniform circular cylinder wakes the Reynolds number is constant along the whole span and therefore the individual modes of three-dimensionality (either mode A or mode B) exist along the entire span of the cylinder. Barkley and Henderson [1] from their Floquet stability analysis predicted the critical Reynolds number for the uniform circular cylinder to be 188.5 ± 1.0 and the wavelength of mode A equal to 3.96 diameters. However, in the present tapered cylinder study Re_{local} varies along the span and both mode A and mode B co-exist in the same flow. Thereby, only a short span of the cylinder is available for each of the modes to develop (especially for mode A) and it is difficult to pin-point the exact Reynolds number at which these modes start to appear. Flow-visualizations revealed that the mode A appeared around $Re_{local} \approx 200$ and mode B around $Re_{local} \approx 250$ in the present study. In

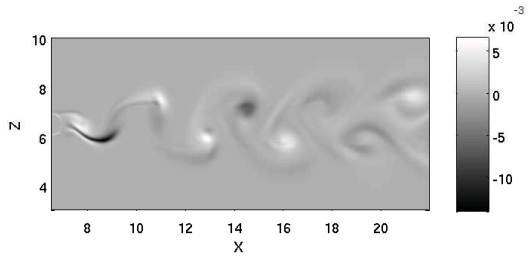

(a) Y=12.5; $Re_{local} = 250$ (before split)

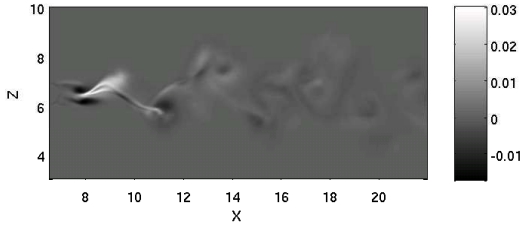

(b) Y=12.5; $Re_{local} = 250$ (vortex split)

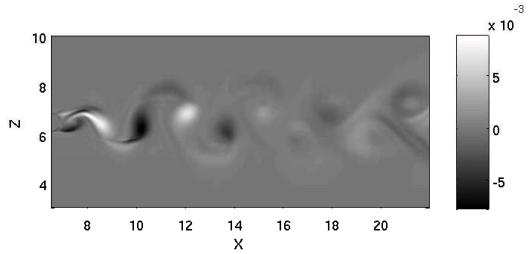

(c) Y=22; $Re_{local} = 212$ (before split)

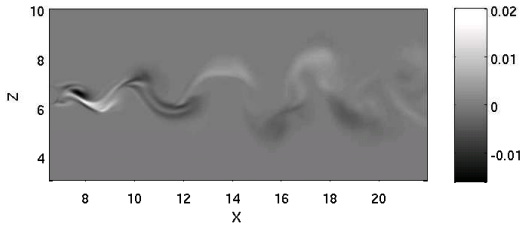

(d) Y=22; $Re_{local} = 212$ (vortex split)

Figure 9: Non-dimensionalized streamwise vorticity component ($\omega_x\ \nu/U_o^2$) as vortex splits. (note that (a),(b) and (c),(d) were taken at the same spanwise location, respectively)

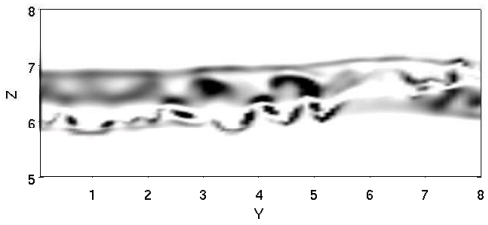

(a) mode B 'mushroom' structures at $Y \approx 3-6$

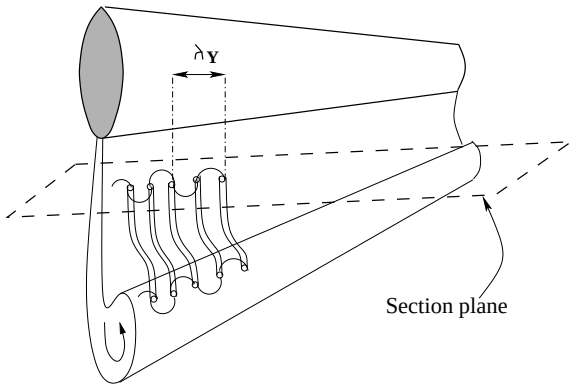

(b) $Y-Z$ section plane (dotted line)

Figure 10: Cross-sectional view of mode B showing 'mushroom' vortex pair structures.

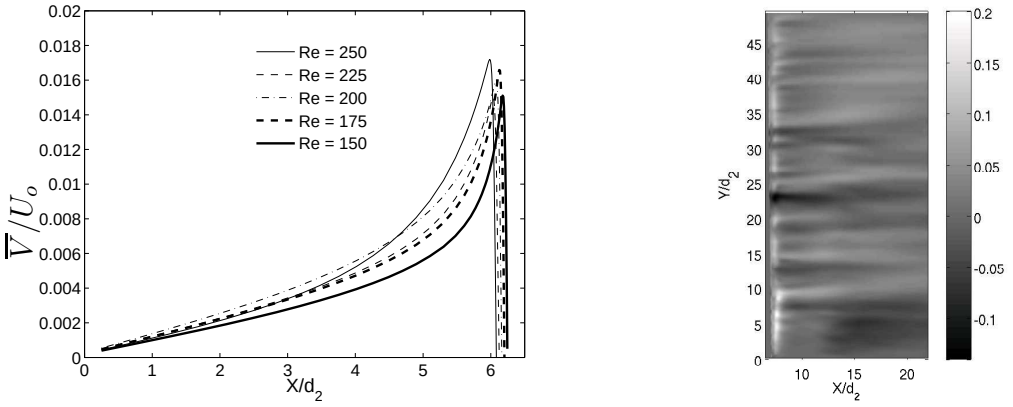

(a) Upstream the cylinder (b) Downstream the cylinder

Figure 11: Time-mean spanwise velocity $\overline{V}/U_o$ (secondary flow) along the span: (a) at some different spanwise locations identified by the local Reynolds number; (b) velocity contours in the $X-Y$ section plane through the axis of the cylider.

figure 10(a) a cross-sectional view of mode-B streamwise vortex structures is shown. We can see clearly the smaller-scale 'mushroom' vortex pair structures of mode-B vortex shedding. There is a remarkable similarity between this vortex array and that found by Williamson [21] in the uniform circular cylinder wake. However, note that the section plane is parallel to the axis and at an angle to the vortex lines (see figure 10(b)) and thereby structures are visible only in some parts of the plane. The wavelength of mode B was found to be $\lambda_Y/d_2 \approx 1$, which is very close to the experimental value $\lambda_Y/D = 0.98$ found by Williamson [21] for uniform cylinders.

3.4 Secondary motion

Time-averaged statistical quantities were evaluated by sampling for 123 d_2/U_o or 360 d_1/U_o time units. This sampling period corresponds to about 40 mean shedding cycles. The present simulation revealed a mean spanwise velocity $\overline{V}$, both in the front stagnation zone and also in the wake of the cylinder (see figure 11). It can be observed from figure 11(a) that in the front stagnation zone the secondary flow is going from the wide end of the cylinder towards the narrow end. The magnitude of this spanwise velocity is quite small, around 2% of the inflow U_o. The direction and magnitude of this secondary motion is surprisingly similar to what was observed in the steady laminar regime [15]. This flow is driven by a spanwise pressure gradient. The front stagnation line is slightly inclined with respect to the cylinder axis and this tilt gives rise to a somewhat higher pressure near the wide end of the cylinder as compared to the narrow end. The pressure contours (isobars) in figure 12(a) show

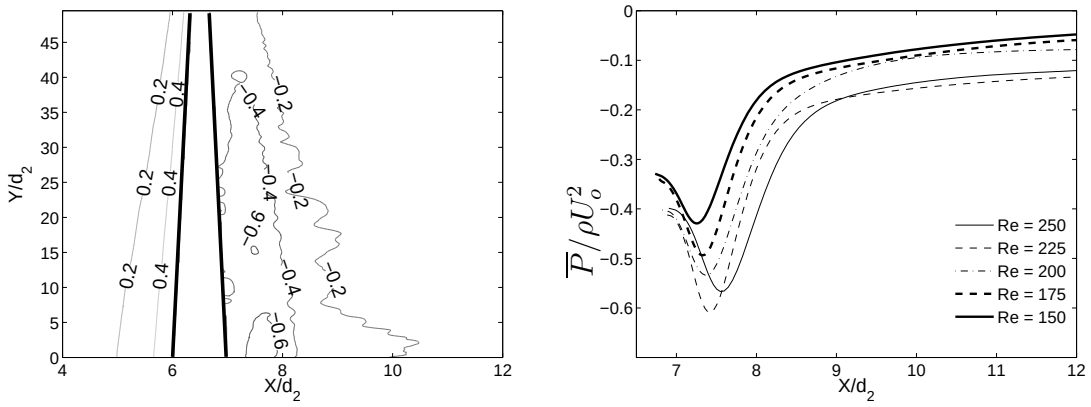

(a) (b)

Figure 12: (a) Pressure ($\overline{P}/\rho U_o^2$) contours in the $X-Y$ section plane through the axis of the cylinder. The cylinder is drawn as a bold line. (b) Mean pressure ($\overline{P}/\rho U_o^2$) in the wake at different spanwise locations identified by the local Reynolds number.

that the isobars are more inclined to the cylinder axis than the stagnation line, thereby giving rise to a spanwise pressure gradient which drives the flow towards the narrow end.

On the contrary, the secondary motion on the rear side of the cylinder in figure 11(b) is complex. The flow, both in the near vicinity of the cylinder and in the wake has no preference for a specific direction of motion, i.e. it changes its course of direction randomly along the span. This is in contrast to what was observed in the steady laminar regime [15], where the secondary motion was found to go from the narrow end of the cylinder towards the wide end. The magnitude of this spanwise velocity is typically of the order $15-20\%$ of the inflow U_o, i.e., about ten times larger than what was observed in the steady laminar regime [15], but similar to the results of Parnaudeau et al. [14]. It is worth mentioning here that the secondary flow in the steady laminar regime [15] was driven by the spanwise pressure gradient alone. Even though a significant spanwise pressure gradient exists in the wake of the present tapered cylinder (see figure 12(a), 12(b)), it is clear that pressure is not the only driving mechanism here. Parnaudeau et al. [14] speculated that this 'wavy secondary motion along the span' was due to the three-dimensionalities induced by the oblique vortex shedding and the vortex dislocations. Recently Narasimhamurthy et al. [16] studied the turbulent wake behind a tapered flat plate and they observed oblique and cellular vortex shedding. In spite of this the secondary motion they noticed was driven by the spanwise pressure gradient alone. Therefore attributing the waviness in the secondary motion to the oblique and cellular vortex shedding might not be appropriate. On the other hand, this 'wavy secondary motion along

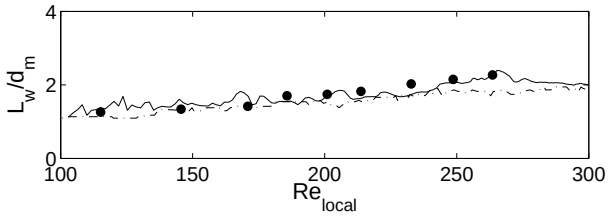

Figure 13: Non-dimensional length of the re-circulation zone *versus* Re_{local}: $-$, tapered cylinder (present simulation) ; $-.-$, tapered cylinder (Parnaudeau et al. [14]) ; $\bullet$, uniform cylinder (Williamson [21]).

the span' was observed only in the transitional wake of a tapered cylinder, i.e. both in the present study and in Parnaudeau et al. [14]. Therefore effect of transition process itself on the direction of secondary motion cannot be ruled out. Recall that spanwise velocity V is directly linked to the streamwise vorticity ω_x; and streamwise vortical structures occur along the span (cf. figure 8(c)). Therefore at this stage we suggest that the 'wavy secondary motion' in the wake of the present tapered cylinder is a direct consequence of the *intrinsic* secondary-instabilities induced by the transition process itself. In spite of the secondary flow in the base region, the local length of the re-circulation zone from the present computations is nearly in good agreement with the results of uniform circular cylinder (see figure 13). In the present context the local formation length L_w is defined as the streamwise distance from the axis of the cylinder to the position where the mean streamwise velocity $\overline{U}$ changes sign from negative to positive.

3.5 Reynolds averaged statistics

It is important to quantify the growth and decay of different properties of the fluctuating motion, especially in the near wake region where the similarity laws cannot be applied. Therefore in the present section Reynolds averaged statistical quantities at some sections along the span of the cylinder will be presented and the underlying physics will be discussed. The variation of the mean streamwise velocity $\overline{U}$ in the very near wake at two different Reynolds numbers corresponding to the laminar regime ($Re_{local} = 150$) and the transitional regime ($Re_{local} = 250$) are shown in figure 14(a) and 14(b), respectively. Note that $\overline{U}$ profiles in figure 14(a) and 14(b) are qualitatively similar. However, owing to the production of turbulence, magnitude of $\overline{U}$ drastically reduces as the flow evolves downstream in figure 14(b). Similar conclusions can also be drawn from figure 15(a) and 15(b), where the mean cross-stream velocity $\overline{W}$ profiles are plotted. The anti-symmetric configuration of $\overline{W}$ represents the effects of the mean re-circulation zone.

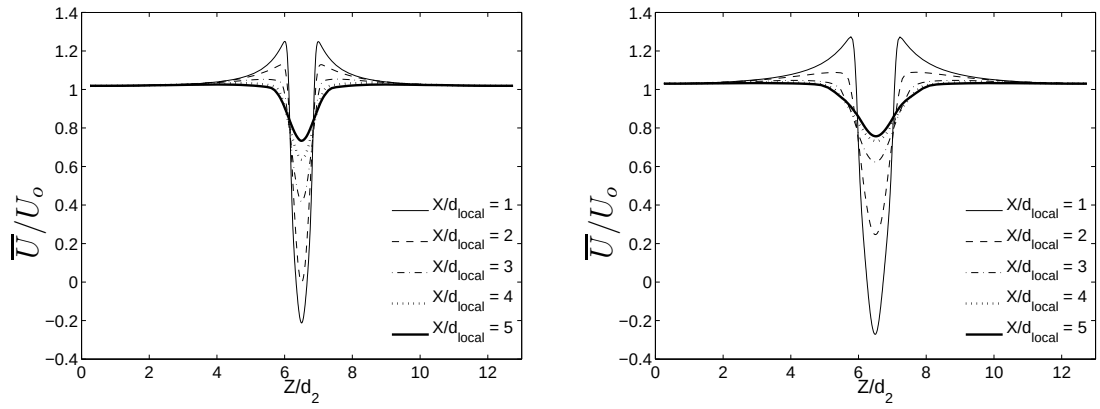

(a) $Re_{local} = 150$ (b) $Re_{local} = 250$

Figure 14: Mean streamwise velocity ($\overline{U}/U_o$) profiles at fixed X/d_{local} positions (measured from the axis of the cylinder).

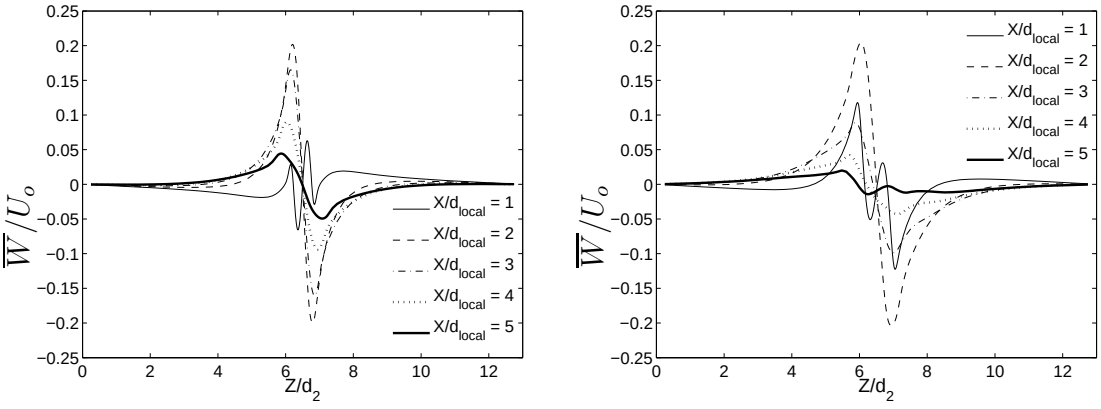

(a) $Re_{local} = 150$ (b) $Re_{local} = 250$

Figure 15: Mean cross-stream velocity ($\overline{W}/U_o$) profiles at fixed X/d_{local} positions (measured from the axis of the cylinder).

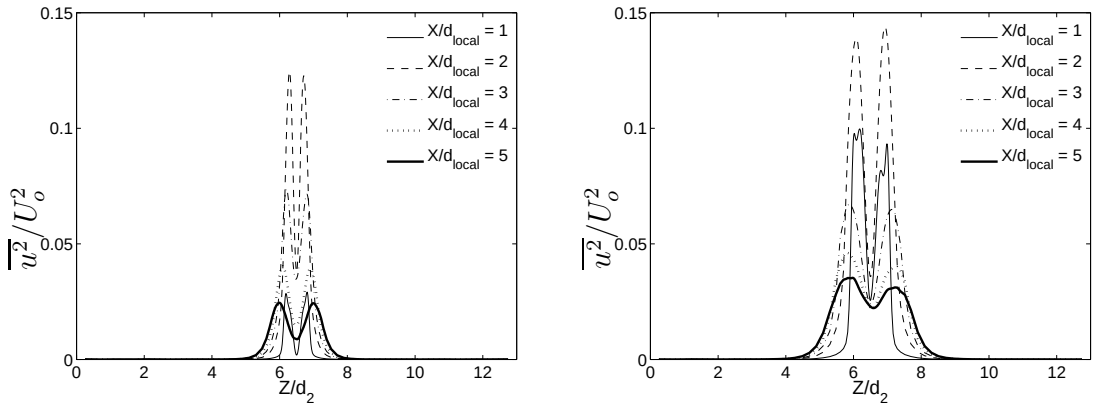

(a) $Re_{local} = 150$ (b) $Re_{local} = 250$

Figure 16: Reynolds stress ($\overline{u^2}/U_o^2$) profiles at fixed X/d_{local} positions (measured from the axis of the cylinder).

Reynolds stresses $\overline{u^2}$, $\overline{w^2}$ and $\overline{uw}$ are shown in figures 16, 17 and 18, respectively. Note that due to the Reynolds-averaging stress components have contributions from both the unsteady fluctuations and the turbulent fluctuations. Increase in the magnitude of Reynolds stresses at the higher Reynolds number ($Re_{local} = 250$) is apparent in all the three figures. A bi-modal $\overline{u^2}$ profile similar to the uniform circular cylinder data by Persillon & Braza [24] can be observed in all the present cases in figure 16. The highest level of streamwise velocity fluctuations occur in the shear layers shed from the cylinder surface and hence the two peaks in figure 16 are offset from the wake centerline. In contrast the maximum values of $\overline{w^2}$ stress component appear along the wake centerline (see figure 17). This is because at the wake centerline the flow is subjected to an equally weighted influence of both the alternating vortices shed from either side of the cylinder. Except at the most upstream location $X/d_{local} = 1$ (which lies inside the recirculation zone), the transverse velocity fluctuations are more energetic than the streamwise velocity fluctuations, hence the magnitude of $\overline{w^2}$ stress component is much larger than the $\overline{u^2}$ stress component. The peak amplitudes of the shear stress in figure 18 indicates the position where the two fluctuating components are in phase; and the regions where this correlation goes to zero indicates that they are out of phase by 180^o in those positions. At $X/d_{local} = 1$, two more peaks appear near the wake centerline. This pattern, however, disappears downstream, i.e. beyond the recirculation zone.

The mean fluctuating kinetic energy, $k = (\overline{u^2} + \overline{v^2} + \overline{w^2})/2$, profiles are shown in figure 19. From $X/d_{local} = 2$ and further downstream, the highest energy level is observed along the wake centerline and the actual peak level decays monotonically with X. This is because the transverse velocity fluctuations are more energetic than

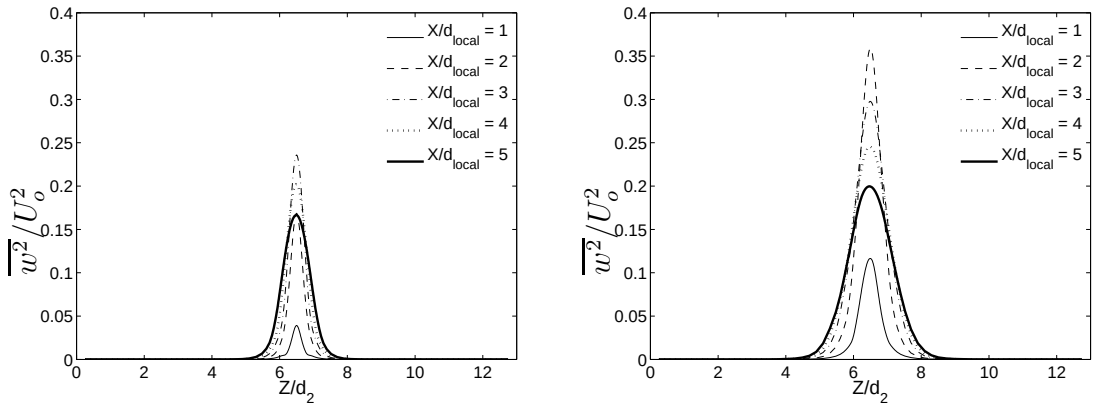

(a) $Re_{local} = 150$ (b) $Re_{local} = 250$

Figure 17: Reynolds stress ($\overline{w^2}/U_o^2$) profiles at fixed X/d_{local} positions (measured from the axis of the cylinder).

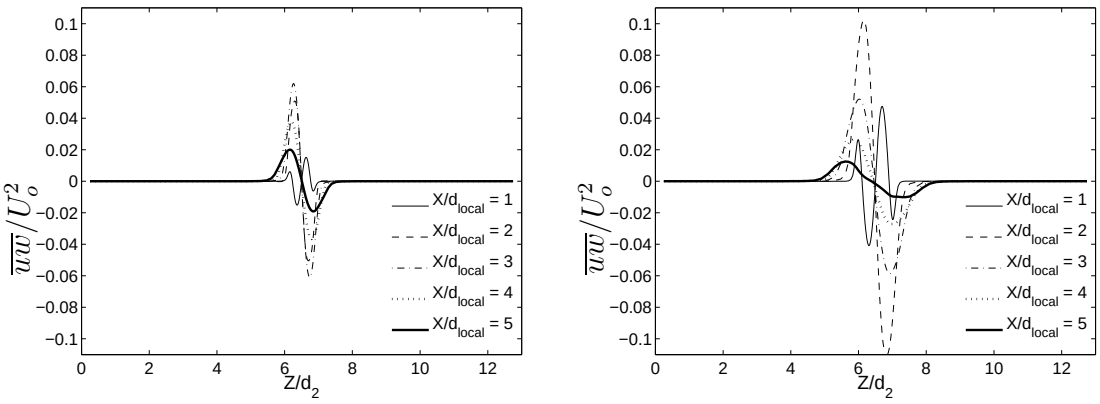

(a) $Re_{local} = 150$ (b) $Re_{local} = 250$

Figure 18: Reynolds shear stress ($\overline{uw}/U_o^2$) profiles at fixed X/d_{local} positions (measured from the axis of the cylinder).

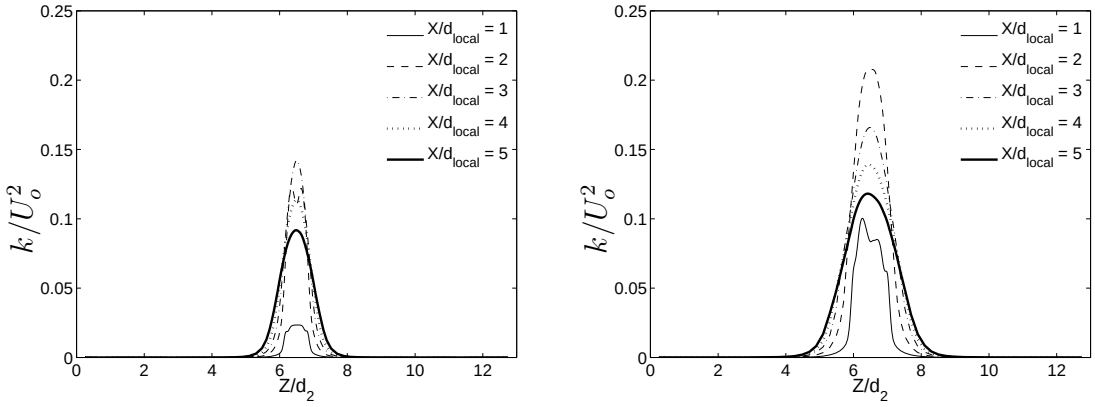

(a) $Re_{local} = 150$ (b) $Re_{local} = 250$

Figure 19: Fluctuating kinetic energy (k/U_o^2) profiles at fixed X/d_{local} positions (measured from the axis of the cylinder).

the streamwise velocity fluctuations in those regions and therefore $\overline{w^2}$ represent the major contribution to k. Close to the cylinder, however, the highest energy levels are offset from the wake centerline since $\overline{w^2}$ is relatively modest and roughly comparable to $\overline{u^2}$ in those regions. It can thus be concluded that the bi-modal $k-$profile at this location stems from the streamwise velocity fluctuations. Mean fluctuating kinetic energy profiles from the present tapered cylinder was compared against the uniform circular cylinder data by Persillon & Braza [24] at $Re = 200$ in figure 20. In spite of the different wake patterns behind the two bluff-bodies, qualitative agreement between the two results is surprising. There is also a remarkable similarity (qualitatively) between the present tapered cylinder wake statistics and that of uniform circular cylinder wake statistics by Persillon & Braza [24], even though the underlying flow physics in the wake of tapered cylinders and the uniform cylinders are completely different from each other.

4 Conclusions

Frequency analysis, two-point correlations and the three-dimensional flow visualizations collectively confirm that multiple cells of constant shedding frequency exist along the span of the present tapered cylinder. The present DNS data clearly demonstrated that even with a longer sampling time (nearly 4 times longer than Parnaudeau et al. [14]) discrete cellular shedding pattern prevails. This is in contrast to what Parnaudeau et al. [14] speculated in their tapered cylinder study, where they suggested that with a longer time sampling diffused cellular pattern might appear. In the present study it was found that streamwise vorticity becomes large as vortex

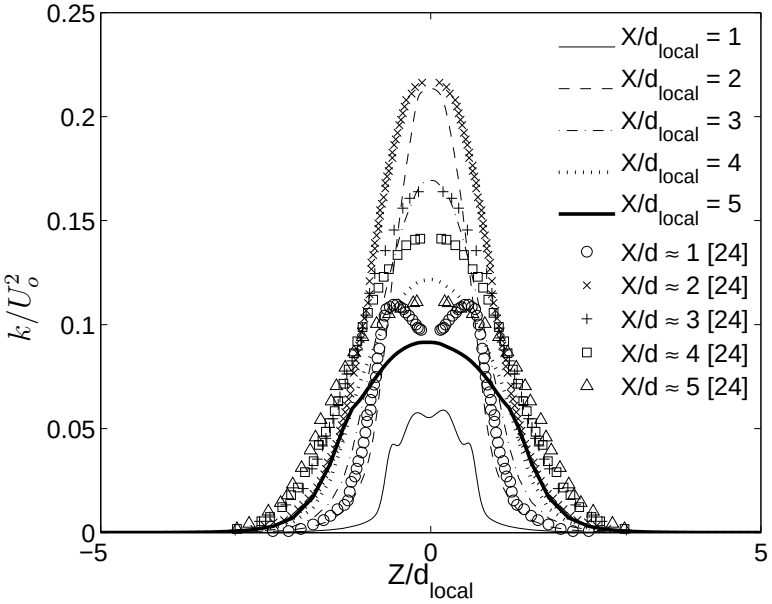

Figure 20: Fluctuating kinetic energy (k/U_o^2) from the present tapered cylinder at $Re_{local} = 200$ compared against the uniform circular cylinder data by Persillon & Braza [24] at $Re = 200$. X/d positions are measured from the axis of the cylinder.

dislocation occurs, an effect also observed experimentally by Piccirillo & Van Atta [8] in the laminar flow regime. Flow-visualizations revealed that the mode A appeared around $Re_{local} \approx 200$ and mode B around $Re_{local} \approx 250$ in the present study. The wavelength of mode B was found to be $\lambda_Y/d_2 \approx 1$, which is surprisingly very close to the experimental value $\lambda_Y/D = 0.98$ found by Williamson [21] for uniform circular cylinders.

The present three-dimensional calculation revealed a spanwise secondary motion, both in the front stagnation zone and also in the wake of the cylinder. It was observed that in the front stagnation zone the secondary flow was driven by a spanwise pressure gradient, driving the flow from the wide end of the cylinder towards the narrow end. This is surprisingly similar to what was observed in the steady laminar regime [15]. On the contrary, the secondary flow pattern on the rear side of the cylinder is rather complex. The flow, both in the near wake and further downstream has no preference for a specific direction of motion, i.e. it changes its course of direction randomly along the span. This is in contrast to what was observed in the steady laminar regime [15], where the secondary motion was found to go from the narrow end of the cylinder towards the wide end. The spanwise secondary motion in the wake was found to be more pronounced in the present transitional flow case than in the steady laminar case [15]. Even though significant spanwise pressure gradient was noticed in the wake of the present tapered cylinder, it was observed that pressure

is not the only driving mechanism here. It was suggested that the 'waviness in the secondary motion' in the wake of the present tapered cylinder is due to the *intrinsic* secondary-instabilities induced by the transition process itself. This is in contrast to what Parnaudeau et al. [14] speculated in their tapered cylinder study, where they attributed this 'waviness in the secondary motion' to the oblique and cellular vortex shedding.

In spite of the secondary flow in the base region, the local formation length from the present tapered cylinder study is nearly in good agreement with the results of uniform circular cylinder [21]. On comparing the Reynolds averaged statistical quantities it was observed that there is a remarkable similarity (qualitatively) between the present tapered cylinder wake statistics and the uniform circular cylinder wake statistics by Persillon & Braza [24]. This, in spite of the underlying flow physics in the wake of tapered cylinders and the uniform cylinders being completely different from each other, is surprising.

Acknowledgments

This work has received support from The Research Council of Norway (Programme for Supercomputing) through a grant of computing time. The first author was the recipient of a research fellowship offered by The Research Council of Norway.

References

[1] Barkley, D. and Henderson, R. D., 1996. Three-dimensional Floquet stability analysis of the wake of a circular cylinder. *J. Fluid Mech.* **322**, 215-241.

[2] C.G. Lewis and M. Gharib, "An exploration of the wake three dimensionalities caused by a local discontinuity in cylinder diameter," Phys. Fluids A **4**, 104- 117 (1992).

[3] B. Vallès, H.I. Andersson, and C.B. Jenssen, "Direct-mode interactions in the wake behind a stepped cylinder," Phys. Fluids **14**, 1548-1551 (2002).

[4] W. Dunn and S. Tavoularis, "Experimental studies of vortices shed from cylinders with a step-change in diameter," J. Fluid Mech. **555**, 409-437 (2006).

[5] Gaster, M., 1969. Vortex shedding from slender cones at low Reynolds numbers. *J. Fluid Mech.* ***38***, 565-576.

[6] Jespersen, D. C. and Levit, C., 1991. Numerical simulation of flow past a tapered cylinder. *AIAA paper.* ***91-0751***.

[7] Papangelou, A., 1992. Vortex shedding from slender cones at low Reynolds numbers. *J. Fluid Mech.* **242**, 299-321.

[8] Piccirillo, P. S. and Van Atta, C. W., 1993. An experimental study of vortex shedding behind linearly tapered cylinders at low Reynolds number. *J. Fluid Mech.* **246**, 163-195.

[9] Vallès, B., Andersson, H. I. and Jenssen, C. B., 2002. Oblique vortex shedding behind tapered cylinders. *J. Fluids Struct.* ***16***, 453-463.

[10] Monkewitz, P. and Provansal, M., 2005. Vortex shedding dynamics in the wake of slender cones at low Reynolds numbers. *Bull. Am. Phys. Soc.*, A.P.S. Meeting DFD.

[11] Narasimhamurthy, V. D., Schwertfirm, F., Andersson, H. I. and Pettersen, B., 2006. Simulation of unsteady flow past tapered circular cylinders using an immersed boundary method. In: *Proc. ECCOMAS Computational Fluid Dynamics*, Eds. P. Wesseling, E. Oñate, J. Périaux, Publisher TU Delft, The Netherlands, Egmond aan Zee.

[12] Hsiao, F., and Chiang, C., 1998. Experimental study of cellular shedding vortices behind a tapered circular cylinder, *Exp. Thermal Fluid Sci.*, ***17***, 179-188.

[13] Visscher, J., Pettersen, B. and Andersson, H. I., 2007. PIV study on the turbulent wake behind tapered cylinders. In: *Advances in Turbulence XI*, Eds. J. M. L. M. Palma, A. Silva Lopes, Publisher Springer, Portugal, Porto, pp.254-256.

[14] Parnaudeau, P., Heitz, D., Lamballais, E. and Silvestrini, J. H., 2007. Direct numerical simulations of vortex shedding behind cylinders with spanwise linear nonuniformity. *J. Turbulence*, ***8***, No. 13.

[15] Narasimhamurthy, V. D., Andersson, H. I. and Pettersen, B., 2008. Steady viscous flow past a tapered cylinder. *Acta Mechanica* (accepted).

[16] Narasimhamurthy, V. D., Andersson, H. I. and Pettersen, B., 2007. Cellular vortex shedding in the wake of a tapered plate. *J. Fluid Mech.* (accepted).

[17] Peller, N., Le Duc, A., Tremblay F. and Manhart M., 2006. High-order stable interpolations for immersed boundary methods. *Int. J. Numer. Meth. Fluids.* **52**, 1175-1193.

[18] Manhart M., 2004. A zonal grid algorithm for DNS of turbulent boundary layers. *Computers & Fluids.* **33**, 435-461.

[19] Williamson, C. H. K., 1992 The natural and forced formation of spot-like vortex dislocations in the transition of a wake. *J. Fluid Mech.* **243**, 393-441.

[20] Williamson, C. H. K., 1996. Vortex dynamics in the cylinder wake. *Annu. Rev. Fluid Mech.* **28**, 477-539.

[21] Williamson, C. H. K., 1996. Three-dimensional wake transition. *J. Fluid. Mech.* **328**, 345-407.

[22] Farge, M., 1992. Wavelet transforms and their applications to turbulence. *Annu. Rev. Fluid Mech.* **24**, 395-457.

[23] Jeong, J. and Hussain, F., 1995. On the identification of a vortex. *J. Fluid Mech.* **285**, 69-94.

[24] Persillon, H. and Braza, M., 1998. Physical analysis of the transition to turbulence in the wake of a circular cylinder by three-dimensional Navier-Stokes simulation. *J. Fluid Mech.* **365**, 23-88.

Article 6

Asymmetries in the wake behind a circular cylinder in planar shear flow

Huang, Z., Narasimhamurthy, V. D., Andersson, H. I. & Cui, W.

Manuscript to be submitted.

Asymmetries in the wake behind a circular cylinder in planar shear flow

Zhiyong Huang[a,b] , Vagesh D. Narasimhamurthy[b], Helge I. Andersson [b]*, Weicheng Cui[a]

[a] State Key Laboratory of Ocean Engineering, Shanghai Jiao Tong University, Shanghai 200030, China
[b] Department of Energy and Process Engineering, Norwegian University of Science and Technology, 7491 Trondheim, Norway

Abstract

Non-linear flow phenomena in the wake of a circular cylinder in planar shear flow are studied at Reynolds number 300 and a uniform shear rate $0.1U_c/D$ where U_c is the inflow velocity at the level of the cylinder axis. Direct numerical simulations are performed and the results compared with data obtained for the same configuration but with uniform inflow. Mean velocity components and Reynolds stresses are compared and reveal modest asymmetries in the boundary layer development and the pressure coefficient along the cylinder surface and in the wake. This is in contrast with the observation that the Strouhal number as well as the location at which the laminar boundary layer separates from the cylinder is unaffected by the presence of inflow shear. The mode B instability in the cylinder wake is not suppressed by the sheared inflow. The primary Karman vortices shed from the low-velocity side of the cylinder are distorted and substantially weakened as compared with the vortices shed from the high-velocity side. Moreover, vortical cells of opposite vorticity cluster in the near wake, in contrast with the regularly spaced cells in the presence of uniform inflow conditions.

Key words: Planar shear inflow; Circular cylinder; Direct numerical simulation; Vortex shedding; Wake phenomena.

1. Introduction

Three-dimensional vortex shedding occurs naturally in several engineering fields, such as behind bridges, chimneys and marine risers. Due to its geometrical simplicity, the uniform circular cylinder has become the prototype structure for investigations aimed to enhance our understanding

* Corresponding author. Tel.: +47-73-59-35-56; fax: +47-73-59-34-91.
E-mail address: helge.i.andersson@ntnu.no (Prof. H.I. Andersson)

of the complex flow physics that may occur in the wake of two-dimensional bluff bodies. Substantial progress has been made during the last two decades in the understanding of the wake instabilities, transition and vortex shedding behind a circular cylinder placed in a uniform incoming flow. The articles by Williamson [1] and Persillon and Braza [2] provide an excellent account of the present understanding of this particular flow. In practice, however, the oncoming flow is rarely uniform. In nature, the atmospheric boundary layer and the sea-bed boundary layer exhibit a substantial mean shear. The local topography may also give rise to other asymmetries of the approaching flow. Similarly, asymmetries of the bluff body itself also give rise to intricate wake-flow phenomena, notably the cell structure analysed by Noack et al. [3]. Ozono [4] recently studied the vortex shedding behind a circular cylinder by arranging a short splitter plate asymmetrically downstream. It was found that the asymmetry severely affected the wake flow and tended to suppress the vortex shedding. The oblique vortex shedding and vortex splitting which occurs behind a tapered cylinder were studied by Vallès et al. [5], Parnaudeau et al. [6] and Narasimhamurthy et al. [7]. Parnaudeau et al. [6] considered both uniform flow past a tapered cylinder and spanwise shear flow past a uniform cylinder. Their computer simulations demonstrated the close relationships between these two different flow configurations.

The orientation of the oncoming shear with respect to the cylinder gives rise to rather different flow phenomena; see e.g. Zdravkovich [8]. When the incoming velocity varies in the spanwise direction, i.e. the shear vector is perpendicular to the axis of the cylinder, the resulting wake flow exhibits striking similarities with the uniform flow past a tapered cylinder. If, on the other hand, the incoming velocity varies in the transverse direction, i.e. the shear vector is aligned with the cylinder axis, an asymmetric vortex shedding results. The latter situation, so-called planar shear inflow, has received rather modest attention in spite of its obvious practical relevance.

Kwon et al. [9] considered the flow past a circular cylinder in the presence of uniform planar shear in the Reynolds number range $\mathrm{Re} \in [600, 1600]$ where the Reynolds number is defined as $\mathrm{Re} \equiv U_c D / \nu$. Here, U_c is the incoming velocity at the level of the cylinder axis, D denotes the cylinder diameter and ν is the kinematic viscosity of the fluid. Kwon et al. [9] performed their experiments over the relatively wide range of sheared inflows $K \in [0.05 - 0.25]$ where the shear parameter K is the velocity gradient of the uniform incoming shear normalized by D/U_c. In this parameter range they interestingly observed that the Strouhal number increased with increasing shear parameter K. This observation conflicts with more recent experimental studies by Sumner et al. [10] and Cao et al. [11]. They both arrived at the conclusion that the Strouhal number remained unchanged with increasing shear parameter as long as the flow was at sub-critical Reynolds numbers $1 \cdot 10^4$ - $9 \cdot 10^4$. On the other hand, both Sumner et al. [10] and Cao et

al. [11] observed a reduction in the drag force on the circular cylinder with increasing shear rates. Lei et al. [12] performed two-dimensional flow simulations of planar shear flow over a circular cylinder in the Reynolds number range from 80 to 1000 and with dimensionless shear parameter up to K = 0.25. It is found that Strouhal number slightly decreases as the shear parameter increases from zero to 0.25.

The primary characteristics of the earlier studies of planar shear flow over circular cylinders are summarized in Table 1. Unfortunately, no three-dimensional simulation studies have been devoted to vortex shedding behind cylinders in planar shear flows. This is rather surprising since fully three-dimensional simulations are required in order to explore the three-dimensional flow physics which may give rise to secondary instabilities and complex three-dimensional vorticity fields.

Table 1 Experimental and numerical studies of planar shear flow over a circular cylinder

Authors	Approach	Shear ratio K	Reynolds number	Aspect ratio	Blockage (%)
Cao et al. [11]	Exp.	0 - 0.27	10^4 - 5.5×10^4	2.22 - 8.0	5.0 - 9.0
Sumner et al. [10]	Exp.	0.02 - 0.27	4×10^4 - 9×10^4	12.3 - 18.4	1.8 - 2.7
Kiya et al. [13]	Exp.	0 - 0.25	35 - 1500	2 - 12.5	2.7 - 17
Kwon et al. [9]	Exp.	0.05 - 0.25	600 - 1600	5.2 - 13	6.7 - 17
Lei et al. [12]	2D Num.	0 - 0.25	80 - 1000		3.3 - 20
Present	DNS	0 - 0.1	300	6.0	6.25

The aim of the investigation reported in the present paper is to perform three-dimensional simulations of flow past a circular cylinder in the presence of an upstream planar shear at Reynolds number Re = 300. The full Navier-Stokes equations will be solved in time and three-dimensional space. The simulations to be reported are thus the first direct numerical simulations (DNS) addressing this important flow problem. The asymmetric vortex shedding which results from the shear effect will be explored in some detail, together with the viscous boundary layer development along the cylinder surface. The peripheral variation of the pressure coefficient will also be reported.

2. Flow configuration and computational approach

We consider the flow past a circular cylinder with constant diameter D. The uniform cylinder is immersed in a planar shear flow, as shown in Figure 1. The incoming velocity U(z) varies linearly with the z-coordinate which is measured in the direction perpendicular both to the inflow direction (x) and the cylinder axis which is aligned with the y-direction. The dimensionless shear

parameter K is defined as $K = AD/U_c$, where $A = dU/dz$ is the velocity gradient of the incoming flow and U_c denotes the incoming velocity in the (x, y) – plane through the center of the cylinder. Results from a simulation with K = 0.1 and Re = 300 will be compared with data from a simulation with uniform inflow conditions (i.e. K = 0) at the same Reynolds number.

The simulations are performed with the well-documented finite-volume solver MGLET (see e.g. Manhart [14]). The three-dimensional Navier-Stokes equations for an incompressible fluid are approximated on a staggered Cartesian grid by means of second-order central-differences and integrated in time by an explicit 3rd-order Runge-Kutta scheme. In order to accommodate a cylindrical body in the structured Cartesian mesh, an immersed boundary method (IBM) is employed. A review of different IBM schemes was recently provided by Mittal and Iaccarino [15]. The direct-forcing IBM implemented in MGLET is described by Peller et al. [16].

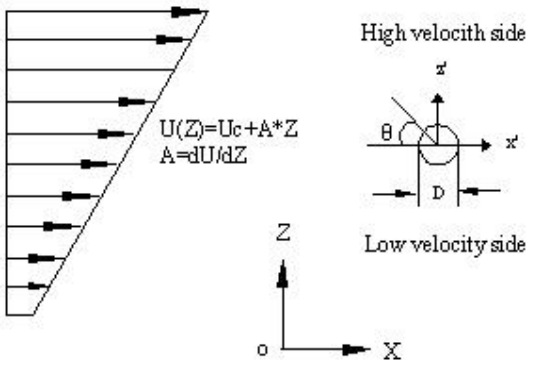

Figure 1. Circular cylinder immersed in a planar shear flow. The Cartesian coordinate system is right-handed and the y-axis is therefore pointing into the figure plane.

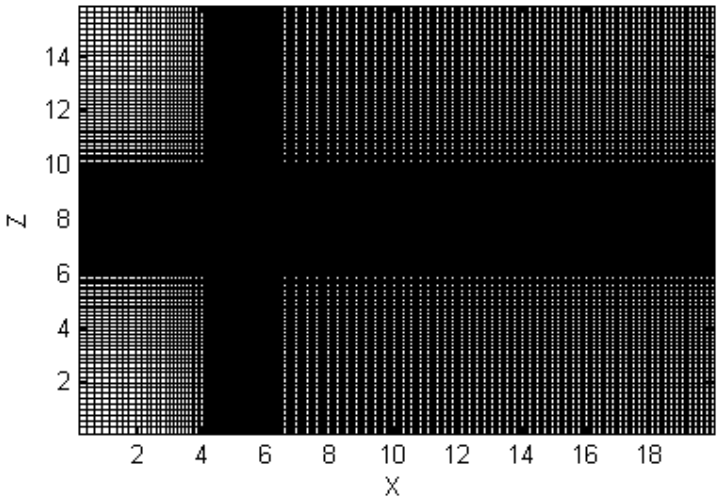

Figure 2. The computational domain and grid distribution in the (x-z)-plane. The circular cylinder center is located at (5.0, 8.0). The coordinates are scaled with the cylinder diameter D.

We used a rectangular 20D x 6D x 16D computational domain with the cylinder axis located at x = x_c = 5D and z = z_c = 8D (x and z being measured from the lower-left corner of the domain). The total number of grid points was 292×60×200 in the x, y, and z-directions, respectively. A constant grid spacing $\Delta y = 0.1D$ was used in the spanwise direction, whereas non-uniform mesh cells were used in the (x, z)-plane. Figure 2 gives an impression of the grid clustering (dark areas) in the vicinity of the cylinder surface. The time step Δt was $0.003D/U_c$.

A unidirectional inflow $U(z) = U_c + A(z - z_c)$ and V = W = 0 is prescribed at the inlet boundary plane at x = 0. At the outlet plane at x = 20D, Neumann boundary conditions are used for all three velocity components and the pressure is set to zero. Free-slip boundary conditions are applied at the top and bottom planes at z = 0 and z = 16D, respectively. Periodic boundary conditions are imposed in the spanwise direction, i.e. at the (x, z)-planes at y = 0 and y = 6D. Although the present cylinder aspect ratio 6.0, i.e. length-to-diameter ratio, is smaller than in some of the experimental studies (cf Table 1), the use of periodic boundary conditions tends to mimic an infinitely long cylinder.

3. Results and discussions

The focus of the present study is on the wake asymmetries which might arise due to planar shear inflow. In order to investigate these flow phenomena, comparisons between DNS data for K = 0.1 will be made with data from a simulation with uniform inflow (K = 0) in an otherwise identical configuration. In order to assess the reliability of the latter, some primary mean flow characteristics will be compared with DNS data reported by Persillon and Braza [2] also at Re = 300. The two-componential mean flow is homogeneous in the spanwise direction and in time. The streamwise and transverse velocity components U_{mean} and W_{mean} and the mean pressure P, as well as the Reynolds stresses, are obtained by averaging the instantaneous 3D field in the spanwise direction and in time. The time averaging is achieved by sampling every $0.03D/U_c$ during a time interval $75D/U_c$. This sampling period corresponds to roughly 15 shedding cycles.

3.1 Wake statistics and Strouhal number

The variation of the streamwise and transverse velocity components U_{mean} and W_{mean} in the wake are shown in Figure 3 and Figure 4. Figure 3 shows the variation from the rear of the cylinder at z = 8D, whereas Figure 4 shows velocity profiles across the wake at three different streamwise locations x/D. The results of the present simulation with uniform inflow (K = 0) show the same overall features as the DNS results reported by Persillon and Braza [2], except that length of the wake bubble is substantially longer in the present simulation. Here, the wake length

is identified as the streamwise extent of the region in Figure 3a where $U_{mean} < 0$ and thus signifies backflow. This somewhat surprising observation is believed to be due to the different computational domains used rather than to differences in numerical resolution. While the cylinder axis was located 5D downstream of the inlet in the present case, the cylinder was positioned almost 20D downstream of the uniform inflow in the study by Persillon and Braza [2]. On the other hand, the grid was finer in the present study.

In spite of the difference in the predicted bubble length, the oscillatory nature of the transverse velocity component W_{mean} in Figure 3b show the same behaviour in the two simulations. Persillon & Braza [2] ascribed the oscillatory variation of W_{mean} in Figure 3b (their Fig. 30a, b) to the traveling of the alternating eddies. However, the (x, y)-plane through the cylinder axis is a symmetry plane and W_{mean} should tend to zero provided the sampling time is sufficiently long. In case of sheared inflow, on the other hand, the symmetry is broken and W_{mean} will remain finite in the (x, y)-plane. The transverse velocity profiles in Figure 4 show the same near-wake behaviour as already reported by Persillon & Braza [2] with a symmetric variation of the streamwise velocity component U_{mean} and an anti-symmetric distribution of the transverse component W_{mean}.

The Strouhal number $St = fD/U_c$ was found to be 0.214 in the present case with uniform inflow. The shedding frequency f was obtained from a Fourier spectrum of the instantaneous velocity over a time interval $75D/U_c$. This value of the Strouhal number is consistent with earlier experimental and computational studies at the same Reynolds number; see the data in Table 2. The angle $\theta = 110^{\circ}$ at which the mean flow separates from the cylinder surface is slightly larger than the corresponding angle $\theta = 106.5^{\circ}$ reported by Persillon and Braza [2]. The present time-averaged recirculation bubble is therefore longer and slightly narrower than that observed by Persillon and Braza [2].

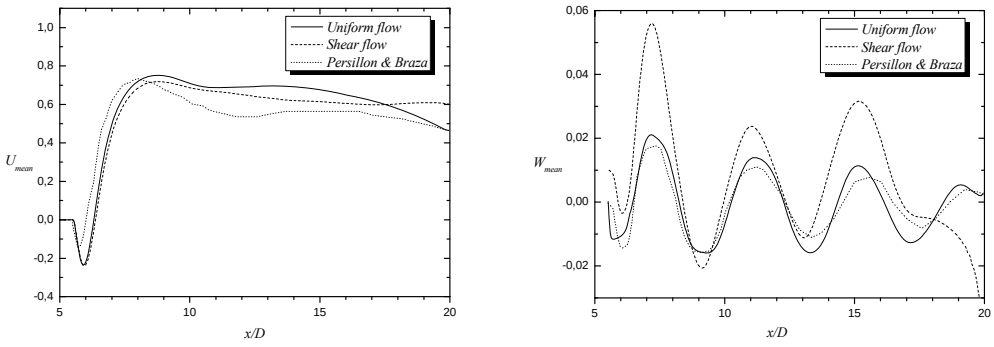

(a) (b)

Figure 3 Streamwise variation of the mean velocity components scaled with U_c in the cylinder wake for K = 0 compared with DNS data of Persillon and Braza [2]; (a) U_{mean} ; (b) W_{mean} .

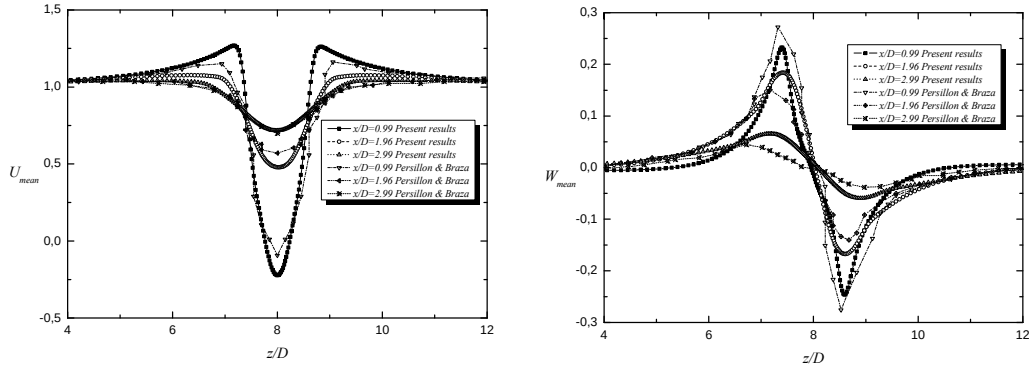

(a) (b)

Figure 4. Near-wake profiles of the mean velocity components at three different streamwise locations x/D. x is measured from the cylinder axis. Present uniform inflow case K = 0 compared with data from Persillon and Braza [2]. (a) U_{mean} ; (b) W_{mean} .

The Strouhal number St = fD/U_c was found to be 0.214 in the present case with uniform inflow. The shedding frequency f was obtained from a power spectrum of the instantaneous velocity sampled over a time interval $75D/U_c$. This value of the Strouhal number is consistent with earlier experimental and computational studies at the same Reynolds number; see the data in Table 2. The angle $\theta = 110^\circ$ at which the mean flow separates from the cylinder surface is slightly larger than the corresponding angle $\theta = 106.5^\circ$ reported by Persillon and Braza [2]. The present time-averaged recirculation bubble is therefore longer and slightly narrower than that observed by Persillon and Braza [2] while the base pressure coefficient is higher.

Table 2. Flow characteristics compared with data from other sources for uniform inflow (K = 0) at Re = 300. θ is the angle measured from the front stagnation point (see Figure 1) and λ denotes the spanwise wavelength of the streamwise vorticity (Mode B).

Author(s)	St	$\theta_{separation}$	$C_p\,(\theta = 180^o)$	λ/D
Norberg [17]	0.202			
Persillon and Braza [2]	0.206	106.5°	-1.378	0.7
Zhang et al. [18]	0.212			≈ 1.0
Barkley and Henderson [19]				0.82
Kwon et al. [9] K = 0	0.216			
Present; uniform inflow K = 0	0.214	110°	-1.20	0.75
Present; shear inflow K = 0.1	0.214	110°	-1.15	0.75

Let us now focus our attention on the case with planar shear inflow (K = 0.1). First of all, it is noteworthy that the Strouhal number and the separation angle remain the same as in the case with uniform inflow conditions (K = 0); see Table 2. As far as the Strouhal number is concerned, the same observation was made in the high-Reynolds number experiments by Sumner et al. [10] and

Cao et al. [11]. Cao et al. [11] concluded that the shear parameter K had no significant influence on the Strouhal number at sub-critical Reynolds numbers as long as K < 0.27. Kwon et al. [9], on the other hand, found that the Strouhal number increased as the shear parameter increased, especially for 0.19 < K < 0.25 in the Reynolds number range from 600 to 1600. On the basis of the present results and earlier findings we are inclined to conclude that a modestly sheared inflow, i.e. K ≤ 0.1, has only negligible influence on the Strouhal number.

Transverse profiles of the mean velocity components are shown in Figure 5a and 5b. Besides the imposed mean shear, the wake profiles resemble at first sight the velocity profiles in Fig. 4a for K = 0. However, the excess velocity just outside the wake on the lower side is higher than on the upper side. This observation is consistent with the hot-wire measurements by Cao et al. [11], which showed that the flow on the low-velocity side accelerated more than that on the high-velocity side. The largest velocity deficit is still at z/D ≈ 8.0 and the maximum velocity deficit remains about the same as for uniform inflow. The profiles of the transverse velocity component W_{mean} in Figure 5b resemble the profiles in Fig 4b for K = 0. However, the strict anti-symmetry is broken and the positive values of W_{mean} in the lower part of the flow are more pronounced than the negative values in the upper part.

Profiles of the kinetic energy of the mean flow (E_{mean}) and the turbulence (k)

$$E_{mean} = \frac{1}{2}\left(U_{mean}^2 + V_{mean}^2 + W_{mean}^2\right) \quad ; \quad k = \frac{1}{2}\left(\overline{u^2} + \overline{v^2} + \overline{w^2}\right) \tag{1}$$

are shown in Figure 5c and 5d, respectively. The mean flow energy variations resemble the profiles of the streamwise mean velocity component in Figure 5a. This is rather obvious since the major contribution to E_{mean} comes from $U_{mean.}$. The kinetic energy associated with the transverse velocity W_{mean} tends to broaden the energy deficit in the near-wake. V_{mean} = 0 due to the spanwise homogenerity! The distribution of the turbulent kinetic energy across wake is surprisingly symmetric at the five different streamwise locations shown in Figure 5d, in spite of the asymmetric inflow conditions. From x/D = 1.96 and further downstream, the highest energy level is observed along the midplane and the actual peak level decays monotonically with x. Close to the cylinder, however, the highest energy levels are offset from the midplane. The two peaks seen at x/D = 0.99 occur in the shear layers shed from the cylinder surface.

Finally, profiles of the streamwise and transverse Reynolds stress components $\overline{uu}$ and $\overline{ww}$ and the shear stress component $\overline{uw}$ are shown in Figures 5e – 5g. Except at the most upstream location x/D = 0.99, the transverse velocity fluctuations are more energetic than the

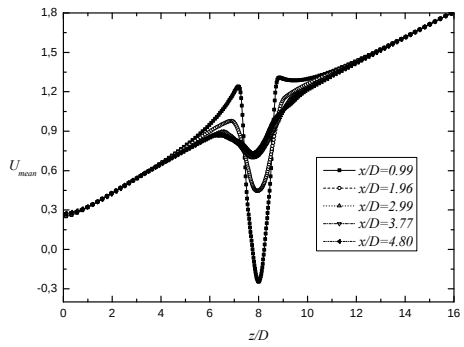

(a)

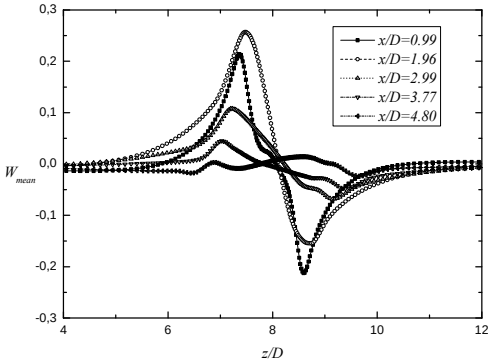

(b)

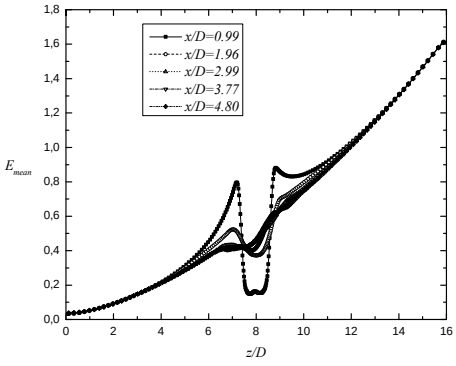

(c)

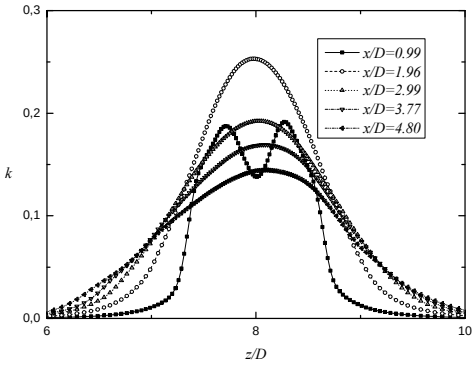

(d)

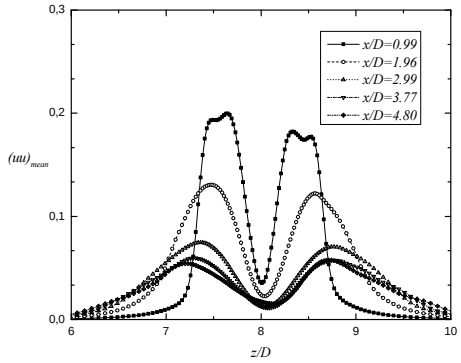

(e)

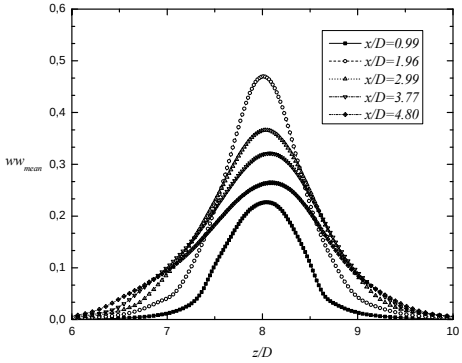

(f)

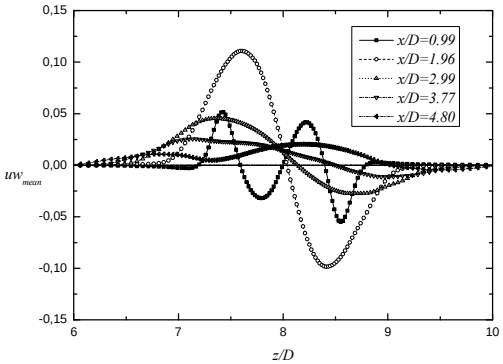

(g)

Figure 5. Near-wake profiles of the mean flow and turbulent statistics at five different streamwise locations x/D. x is measured from the axis of the cylinder. Planar shear inflow case K = 0.1.

(a) U_{mean}; (b) W_{mean}; (c) Mean flow kinetic energy E_{mean}; (d) Turbulent kinetic energy k; (e) Reynolds stress $\overline{uu}$; (f) Reynolds stress $\overline{ww}$; (g) Reynolds shear stress $\overline{uw}$.

streamwise fluctuations and therefore represent the major contribution to k. Next to the cylinder surface, on the other hand, $\overline{ww}$ is relatively modest and roughly comparable to $\overline{uu}$. It can thus be concluded that the bi-modal k-profile at this particular location stems from the streamwise velocity fluctuations. It is noteworthy that the profiles of $\overline{uu}$ in Figure 5e reveal a significant asymmetry with the highest peak located at the low-velocity side where the mean-flow acceleration is largest. The shear stress distributions would be anti-symmetric in the uniform-inflow case. The presence of mean shear tends to break the anti-symmetry of the profiles from x/D = 2.99 and further downstream. The highest shear stress levels are observed at x/D = 1.96, with $\overline{uw} > 0$ at the low-velocity side where the mean strain-rate $\partial U / \partial z < 0$ and $\overline{uw} < 0$ above the mid-plane where $\partial U / \partial z$ is positive. This is consistent with the production of the shear stress:

$$P_{xz} = -\overline{w^2}\frac{\partial U}{\partial z} - \overline{u^2}\frac{\partial W}{\partial x} - \overline{uw}\frac{\partial U}{\partial x} - \overline{uw}\frac{\partial W}{\partial z} \qquad (2)$$

For simplicity purely two-dimensional mean flow in (x, z)-plane has been assumed. The various production terms are organized in order of receding influence. In particular, the last two terms sum up to zero due to the continuity of the mean flow. The secondary production term $-\overline{u^2}\partial W / \partial x$ is responsible for the additional peaks in the shear stress profile at x/D = 0.99. The extra contribution $\partial W / \partial x$ to the mean strain rate is positive in the upstream part of the recirculation bubble at the high-velocity side and correspondingly negative at the low-speed side.

3.2 Boundary layers and pressure distribution

In order to examine any differences between the two different cases in the vicinity of the cylinder surface, we consider the boundary layer development in the front part of the cylinder as well as the pressure coefficient along the entire periphery. The component of the mean velocity vector in the direction tangential to the surface is related to the Cartesian velocity components as:

$$V_\theta = U_{mean}\sin\theta + W_{mean}\cos\theta \qquad (3)$$

See also the sketch in Figure 6 where the polar coordinate θ is defined as positive in the clockwise direction.

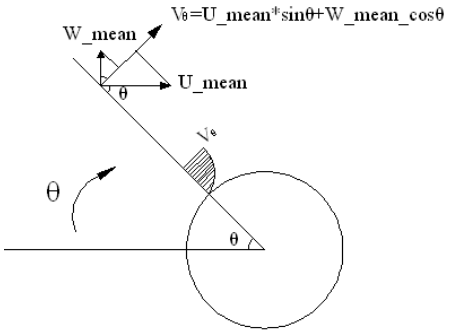

Figure 6. Relationship between mean velocity components in Cartesian and polar coordinates. θ is defined as positive in the clockwise direction. The shaded area is a schematic of the local velocity profile $V_\theta(r)$.

Velocity profiles $V_\theta(r)$ at different locations along the cylinder surface are shown in Figure 7 with the view to compare the case with planar shear inflow to that with uniform inflow conditions. The mean flow field is symmetric about the (x, z) – plane in the case of uniform inflow (K = 0). The laminar boundary layer along the front side becomes gradually thicker with increasing θ–values. At the apex θ = ± 90º the mean velocity just outside the boundary layer exceeds the inflow by about 20% due to the displacement effect of the cylindrical body. The mean velocity profiles at the rear show a substantial region of backflow (i.e. $V_\theta < 0$) since the boundary layer

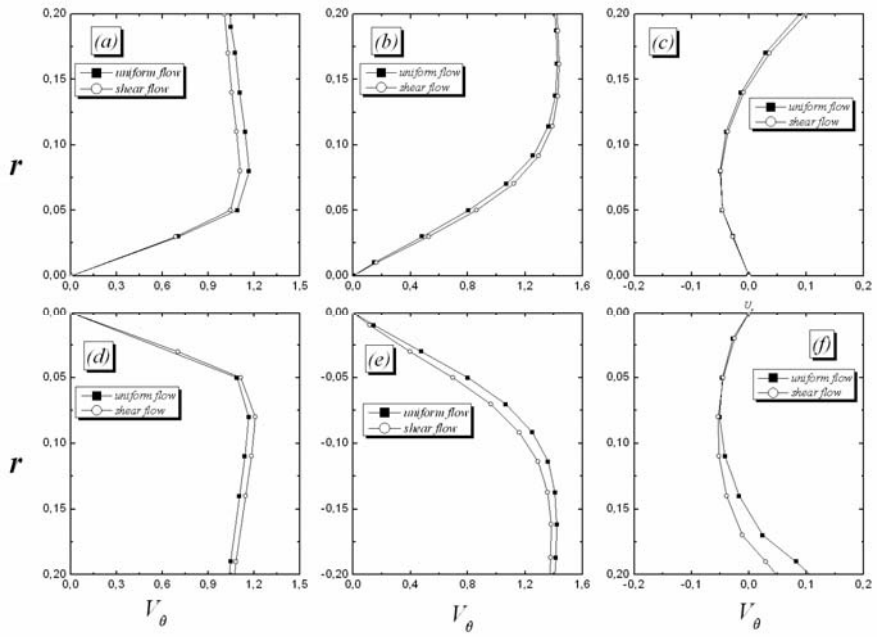

Figure 7. Profiles of V_θ at different surface locations at the high-velocity side (upper row) and the low-velocity side (lower row). The filled symbols are for K = 0 and the open symbols for K = 0.1.

(a) $\theta = 45^\circ$; (b) $\theta = 90^\circ$; (c) $\theta = 135^\circ$; (d) $\theta = -45^\circ$; (e) $\theta = -90^\circ$; (f) $\theta = -135^\circ$.

separated from the surface at θ = 110º, i.e. closely in accordance with the separation angle reported by Persillon and Braza [2]; cf Table 2. It is noteworthy that the same separation angle is obtained also in the sheared inflow case K = 0.1 and that the separation angle is the same at low-velocity and the high-velocity sides.

The symmetry of the mean velocity field is broken in the sheared inflow case. It is somewhat surprising to observe that V_θ with sheared inflow is lower than with uniform inflow at θ = + 45º and correspondingly exceeds V_θ for K = 0 at θ = – 45º. Further along the high-velocity surface the shear inflow case and the uniform inflow case are nearly indistinguishable, both at the apex and in the separated flow region. At the apex on the low-speed side, on the other hand, the tangential velocity V_θ is lower for K = 0.1 than for K = 0, as one should expect. The deviation between the two solutions is particularly pronounced in the backflow region.

The pressure coefficient C_p is defined as $C_p = (P - P_\infty)/(\frac{1}{2}\rho U_c^2)$, where P is the local mean pressure on the surface of the cylinder, P_∞ is the pressure at infinity upstream of the cylinder, and ρ is the density of the fluid. The mean pressure coefficient C_p averaged along the spanwise is plotted in Figure 8.

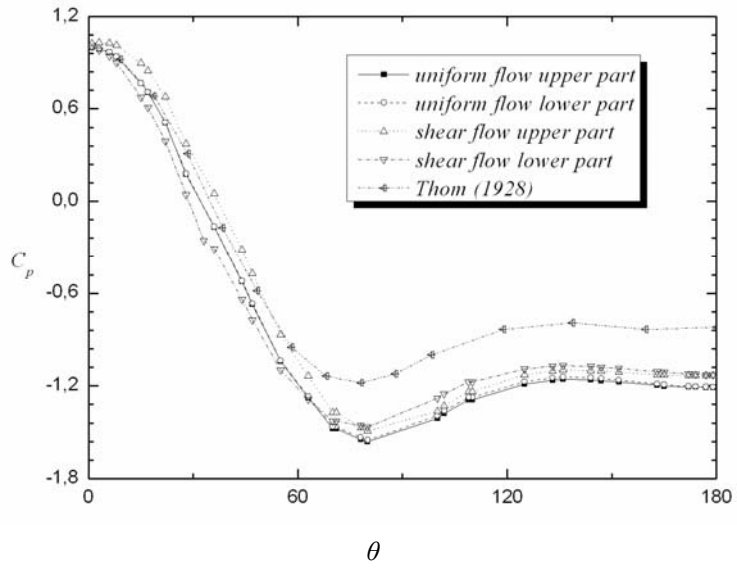

Figure 8. The mean pressure coefficient C_p along the upper and lower cylinder surface. Uniform (K = 0) and planar shear (K = 0.1) inflow compared with 2D simulations by Thom [19].

The current results for the uniform inflow case agree well with results by Thom [20] along the front side ($\theta \leq 60^{\circ}$) of the cylinder, but the predictions deviate all the way further downstream. These deviations are most likely due to insufficient accuracy of the two-dimensional calculations by Thom [20]. The base pressure coefficient at the rearmost location (θ = 180º) is substantially lower than that of Thom [20], but on the other hand higher than that found by Persillon and Braza [2] in their 3D simulations (see Table 2). They argued, however, that 3D simulations with too short span give rise to even more negative base-pressure coefficients. The present base-pressure coefficient C_p = -1.2 is in excellent agreement with the curve-fit provided by Henderson [21]. This observation suggests that the present cylinder span 6.0D is adequate, whereas the spanwise length 2.2 used in the study by Persillon and Braza [2] is somewhat insufficient and gives rise to overprediction of the magnitude of C_p.

As far as the present results are concerned, the pressure coefficient C_p in the planar inflow case straddles that of the uniform inflow case in the front of the cylinder. C_p is higher than for K = 0 along the high-speed side and lower along the low-speed side up to θ about 60º. This is probably associated with the shifting of the front stagnation point towards the high-velocity side; as discussed by Lei et al. [12] and Cao et al. [11]. Sumner et al. [10], however, found that C_p in the planar shear flow case is slightly greater than C_p in the uniform flow case along both sides of the cylinder. It should be recalled, however, that the Reynolds number were substantially higher than in the present study (see Table 1) and the shear parameter slightly lower (K = 0.07). It is likely that the effect of the planar shear inflow differs between high and low Reynolds number flows. Nevertheless, the present findings compare qualitatively with those of Cao et al. [11]. For a flow with Re = 3 640 and K = 0.124 their pressure measurements on the two sides collapsed along the after-body, i.e. downstream of the separation point, and the base-pressure coefficient was significantly smaller in magnitude than in the corresponding case with uniform inflow.

3.3 Vortex structures

The transition from a strictly two-dimensional flow to a three-dimensional state in the wake behind uniform cylinders has been extensively studied during the past two decades. Two different modes of three-dimensional vortex shedding, involving vortex loops and streamwise vortex pairs, were demonstrated by Williamson [22] and subsequently studied by many others; see e.g. Zhang et al. [18], Barkley and Henderson [19] and Thompson et al. [23] for additional references. The mode A instability occurs at Reynolds number about 190, below which the vortex flow remains two-dimensional as long as sidewall effects are excluded. The spanwise wavelength of this ‘long-wavelength’ instability is from 3 to 4.5 cylinder diameters. The next instability, named mode B, appears for Re above about 240 and is characterized by ‘short-wavelength’ instabilities with a

spanwise wavelength ≤ 1D. It is likely that the two modes co-exist over a certain Reynolds number interval and mode B will gradually become the most dominant one whereas mode A vanishes when the Reynolds number exceeds 260.

The flows considered in the present study is for a Reynolds number Re = 300, irrespective of the inflow conditions, i.e. beyond the Re-range in which mode A instabilities prevail. Instantaneous top views of the spanwise and streamwise vorticity components are displayed in Figure 9, both for the case with uniform inflow (top row) and for the case with sheared inflow (bottow row). In addition to the primary von Karman cells, which consist of regions of concentrated spanwise vorticity shed from the cylinder surface, characteristic streamwise vortex pairs are observed. The spanwise wave length λ of these mode B structures is about 0.75D, i.e. consistent with earlier observations. Although the overall appearance of the vortex patterns in Figure 9 is the same for K = 0 and K = 0.1, the regularity of the vortex structures is reduced in the presence of planar shear inflow (bottom row).

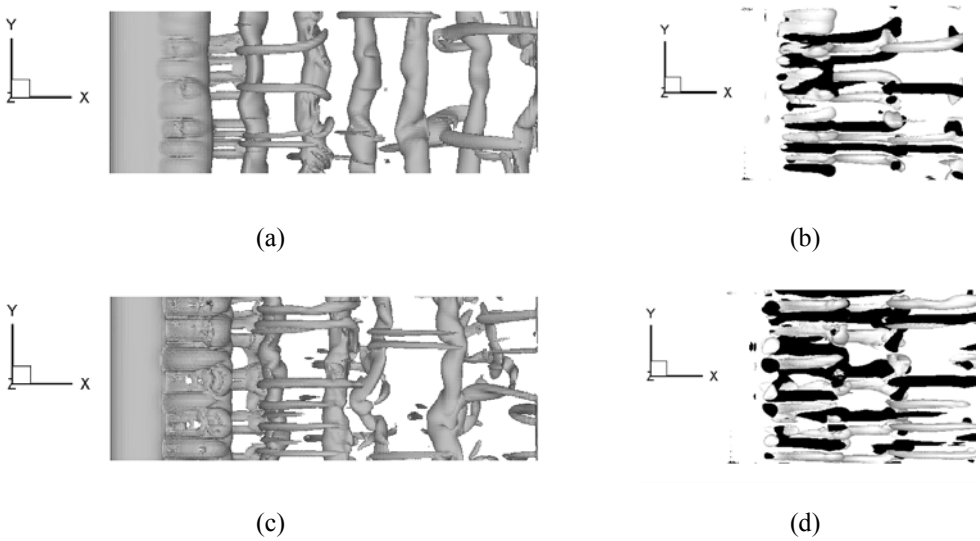

Figure 9. Intantaneous vorticity in the near wake. (a) Enstrophy pattern for uniform inflow K = 0; (b) Streamwise vorticity ω_x for uniform inflow K = 0; (c) Enstrophy pattern for planar-shear inflow K = 0.1; (d) Streamwise vorticity ω_x for planar-shear inflow K = 0.1.

Figure 10 shows plots of the instantaneous spanwise vorticity as seen from the side and from above. The side-views (Figure 10a and 10c) reveal a distinct tilting of the wake in the presence of shear. While the wake is symmetric about the x-axis in the case with uniform inflow (Fig. 10a), the vortex street is shifted towards the low-velocity side in the planar-shear inflow case

in Fig. 11c. This tilting of the vortex street is partly a direct consequence of the gradually increasing inflow velocity with z. The planar shear inflow is equivalent with a uniform spanwise vorticity $\Omega_y = \partial U / \partial z > 0$, which corresponds to a clockwise rotation of the fluid elements in Figure 1. The imposed vorticity interacts differently with the spanwise vorticity generated along the upper and lower cylinder surfaces.

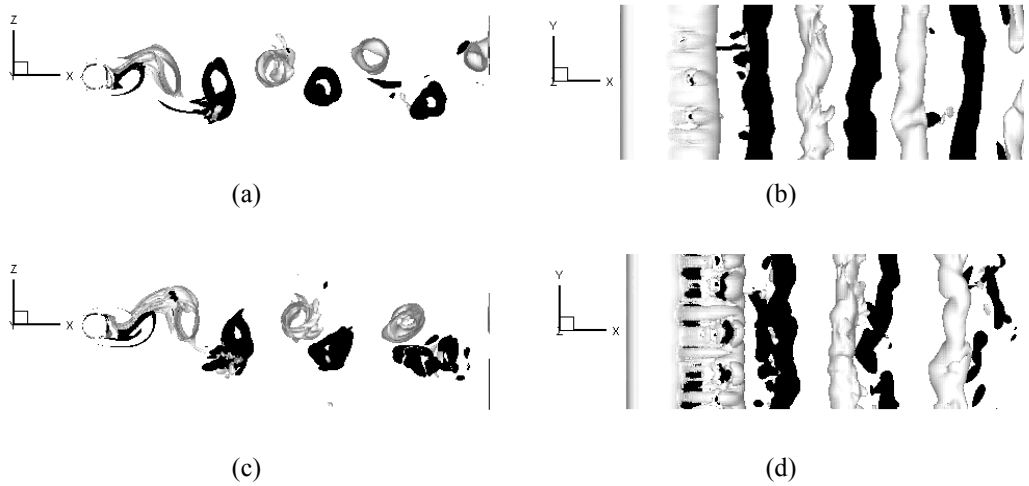

(a) (b)

(c) (d)

Figure 10. Instantaneous spanwise vorticity ω_y in the near wake. Uniform inflow case K = 0: (a) side view; (b) top view; Planar shear inflow case K = 0.1: (c) side view; (d) top view.

In contrast with a case with spanwise shear inflow, in which the vortex lines are bent and stretched around the cylinder, the vortex filaments in the presence of planar shear inflow remain parallel to the cylinder axis. The planar sheared inflow does thus not provide any explicit mechanism for generation of streamwise vorticity and the streamwise vortex pairs are therefore a result of the same mode B instability as for uniform inflow. It is evident, however, that the anti-clockwise Karman vortices shed from the low-speed side of the cylinder is weak and more irregular than the clockwise vortices shed from the high-speed side. Since the vorticity generated in the boundary layer along the low-speed side of the cylinder is of opposite sign of the uniform vorticity Ω_y associated with the inflow, the planar shear inflow tends to weaken the Karman cells shed from the lower side. The Karman vortices shed from the high-velocity side are shed into a mean vorticity field of the same sign and the shed cells are not adversely affected. A final observation which readily can be made from Figures 9 and 10 is that the distance between Karman vortices of opposite sense of rotation is different in the planer shear inflow case from the uniform inflow case. In the latter case, the vortical cells are equally spaced along the streamwise direction,

whereas a distinct pairing of two cells of opposite signs occurs for K = 0.1. This pairing phenomenon is particularly evident from the plots of the spanwise vorticity in Figure 10. One may speculate that the Karman cells shed from the low-velocity side will vanish further downstream (i.e. outside of the computational domain), possibly as these cells merge with a cell shed from the high-velocity side. If so, this could be the first stage of the complete suppression of the vortex shedding observed by Kiya et al. [13] at somewhat higher K-values.

4 Concluding remarks

Direct numerical simulations of planar shear flow past a circular have been performed and compared with results obtained with uniform inflow. Neither the Strouhal number nor the position where the flow separates from the surface are affected by the inflow shear. Other time-averaged statistics turn out be asymmetric, apparently because of the excess flow acceleration observed adjacent to the laminar boundary layer at the low-velocity side of the cylinder. These asymmetries are also reflected in the asymmetry of the surface pressure coefficient along the front on the cylinder.

The data reported herein are deduced from the first three-dimensional computer simulation of vortex shedding from a cylinder embedded in planar shear flow. The present DNS reveals that the mode B or 'short-wavelength' instability exists also in the presence of mean shear. This issue could not be addressed in the 2D simulations reported by Lei et al. [12]. The DNS furthermore enabled detailed visualizations of the complex vortex topology in the near-wake. We observed for the first time the tendency of the Karman cells shed from the low-velocity side to be severely deteriorated by the opposing inflow vorticity. Moreover, Karman cells having opposite vorticity tended to cluster, in contrast with the regularly spaced cells in the presence of uniform inflow conditions.

Acknowledgements

The first author is grateful to The Research Council of Norway for their financial support. This work has also been supported by The Research Council of Norway (Programme for Supercomputing) through a grant of computing time.

References

[1]. C.H.K. Williamson, Vortex dynamics in the cylinder wake, Annu. Rev. Fluid Mech. 24 (1996) 477 - 539.

[2]. H. Persillon, M. Braza, Physical analysis of the transition to turbulence in the wake of a circular cylinder by three-dimensional Navier-Stokes simulation, J. Fluid Mech. 365 (1998) 23 - 88.

[3]. B.R. Noack, F. Ohle, H. Eckelmann, On cell formation in vortex streets. J. Fluid Mech. 227 (1991) 293 – 308.

[4]. S. Ozono, Flow control of vortex shedding by a short splitter plate asymmetrically arranged downstream of a circular cylinder, Phys. Fluids 11 (1999) 2928 – 2934.

[5]. B. Vallès, H.I. Andersson, C.B. Jenssen, Oblique vortex shedding behind tapered cylinders, J. Fluids Struct. 16 (2002) 453 - 463.

[6]. P. Parnaudeau, D. Heitz, E. Lamballais, J.-H. Silvestrini, Direct numerical simulations of vortex shedding behind cylinders with spanwise linear nonuniformitiy, J. Turbulence 8 (2007), no. 13.

[7]. V.D. Narasimhamurthy, H.I. Andersson, B. Pettersen, Direct numerical simulation of vortex shedding behind a linearly tapered circular cylinder, in: Proc. IUTAM Symposium on Unsteady Separated Flows and their Control (2008) Springer-Verlag (in print).

[8]. M.M. Zdravkovich, Flow Around Circular Cylinders, Vol. 1, Oxford university Press, Oxford, 1997.

[9]. T.S. Kwon, H.J. Sung, J.M. Hyun, Experimental investigation of uniform-shear flow past a circular cylinder, ASME J. Fluids Eng. 114 (1992) 457 – 460.

[10]. D. Sumner, O.O. Akosile, On uniform planar shear flow around a circular cylinder at subcritical Reynolds number, J. Fluids Structs. 18 (2003) 441 - 454.

[11]. S. Cao, S. Ozono, K. Hirano, Y., Tamura, Y., Vortex shedding and aerodynamic forces on a circular cylinder in linear shear flow at subcritical Reynolds number, J. Fluids Struct. 23 (2007) 703 - 714.

[12]. C. Lei, L. Cheng, K. Kavanagh, A finite difference solution of the shear flow over a circular cylinder, Ocean Eng. 27 (2000) 271 - 290.

[13]. M. Kiya, H. Tamura, M. Arie, Vortex shedding from a circular cylinder in moderate-Reynolds-number shear flow. J. Fluid Mech. 141 (1980) 721 - 735.

[14]. M. Manhart, A zonal grid algorithm for DNS of turbulent boundary layers, Comput. Fluids 33 (2004) 435-461.

[15]. R. Mittall, G. Iaccarino,G., Immersed boundary methods, Annu. Rev. Fluid Mech. 37 (2005) 239 – 261.

[16]. N. Peller, A.L. Duc, F. Tremblay, M. Manhart, High-order stable interpolations for immersed boundary methods, Int. J. Num. Meth. Fluids 52 (2006) 1175 - 1193.

[17]. C. Norberg, Fluctuating lift on a circular cylinder: review and new measurements, J. Fluids Struct. 17 (2003) 57 - 96.

[18]. H.Q. Zhang, U. Fey, B.R. Noack, H. Eckelmann, On the transition of the cylinder wake, Phys. Fluids 7 (1995) 779 - 794.

[19]. D. Barkley, R.D. Henderson, Three-dimensional Floquet stability analysis of the wake of a circular cylinder, J. Fluid Mech. 322 (1996) 215 - 241.

[20]. A. Thom, The flow past circular cylinders at low speed, Proc. Roy. Soc. (London), A141 (1933) 651 – 669.

[21]. R. Henderson, Details of the drag curve near the onset of vortex shedding, Phys. Fluids 7 (1995) 2102 - 2104.

[22]. C.H.K. Williamson, Oblique and parallel modes of vortex shedding in the wake of a circular cylinder at low Reynolds numbers, J. Fluid Mech. 206 (1989) 579 - 627.

[23]. M. Thompson, K. Hourigan, J. Sheridan, Three-dimensional instabilities in the wake of a circular cylinder, Expr. Therm. Fluid Sci. 12 (1996) 190 - 196.

Article 7

Cellular vortex shedding in the wake of a tapered plate

Narasimhamurthy, V. D., Andersson, H. I. & Pettersen, B.

Accepted for publication in *Journal of Fluid Mechanics*.

Cellular vortex shedding in the wake of a tapered plate

VAGESH D. NARASIMHAMURTHY[1], HELGE I. ANDERSSON[1], BJØRNAR PETTERSEN[2]

[1]Fluids Engineering Division, Department of Energy and Process Engineering, Norwegian University of Science and Technology (NTNU), 7491 Trondheim, Norway

[2]Department of Marine Technology, NTNU, 7491 Trondheim, Norway

(Received 18 December 2007 and in revised form 30 July 2008)

Direct numerical simulation of vortex shedding behind a tapered plate with the taper ratio 20 placed normal to the inflow has been studied. The Reynolds numbers based on the uniform inflow velocity and the width of the plate at the wide and narrow ends were 1000 and 250, respectively. For the first time ever *cellular* vortex shedding was observed behind a tapered plate in a numerical experiment (DNS). Multiple cells of constant shedding frequency were found along the span of the plate. This is in contrast to apparent lack of cellular vortex shedding found in the high Reynolds number experiments by Gaster & Ponsford (1984). However, the present DNS data is in good qualitative agreement with similar high Reynolds number experimental data produced by Castro & Watson (2004). It was observed that a tapered plate creates longer formation length coupled with higher base pressure than compared to non-tapered (i.e. uniform) plates. The three-dimensional re-circulation bubble was nearly conical in shape. A significant base pressure reduction towards the narrow end of the plate, which results in a corresponding increase in Strouhal number, was noticed. This observation is consistent with Castro & Rogers (2002) experimental data. Pressure-driven spanwise secondary motion was observed, both in the front stagnation zone and also in the wake, thereby reflecting the three-dimensionality induced by the tapering.

Key words: turbulence, laminar, DNS, vortex dislocation, vortex split.

1. Introduction

It is a well known fact that *intrinsic* three-dimensionalities arise in an initially two-dimensional flow when secondary instabilities are generated. This

is the case for wakes of two-dimensional bluff-bodies above a certain critical Reynolds number (Williamson (1996); Najjar & Vanka (1995); Najjar & Balachandar (1998)). These three-dimensionalities can induce significant spanwise variations in the velocity and pressure fields. In contrast, such three-dimensionalities may also occur due to *extrinsic* factors, such as the variation of the body shape (Gaster (1969); Piccirillo & Van Atta (1993); Vallès *et al.* (2002*a*); Vallès *et al.* (2002*b*); Narasimhamurthy *et al.* (2007)) or the boundary conditions (Maull & Young (1973); Parnaudeau *et al.* (2007)). In his famous experimental study on slender cones Gaster (1969) found that even a small linear variation of the diameter along the span could induce complex three-dimensionalities in the wake. Such linear variations of the local diameter imply a linear variation of the local Reynolds number along the span. Wakes of two-dimensional bluff bodies are inclined to maintain a surprisingly constant Strouhal number. On this basis one may envisage two different scenarios for how the local shedding frequency f will vary with the local diameter. Either f can vary continously along the span so that the vortex filament is continuous and inclined with respect to the axis of the cylinder (the so called "oblique" vortex shedding), or f can be constant only over a finite span so that the vortex filament is discontinuous (the so called "cellular" vortex shedding). In fact, cellular vortex shedding was reported in both the experiments (Gaster (1969); Piccirillo & Van Atta (1993)) and the computations (Vallès *et al.* (2002*b*); Narasimhamurthy *et al.* (2007); Parnaudeau *et al.* (2007)).

Following the successful findings of *vortex dislocations* or *vortex splits* in the wake of cones, Gaster & Ponsford (1984) went on to investigate the wakes of tapered and triangular plates at high Reynolds numbers ($Re = \bigcirc(10^4)$) and over a range of taper ratios ($R_T = l/(d_2 - d_1)$; where l is the length of the plate and d_2 and d_1 denote the width at the wide and narrow ends, respectively). They noticed that the pressure coefficient over the plate sections was not strictly two-dimensional and they therefore anticipated a weak secondary flow along the front stagnation line to be the most likely cause of this. In addition, they found a significant base pressure gradient along the span, driving the secondary flow from the wide end of the plate towards the narrow end. In spite of the strong three-dimensionalities observed, their hot-wire measurements failed to show any cellular vortex shedding. They concluded that the base Strouhal number was constant along

the span in all their tapered models. The constancy of the Strouhal number implies that the shedding frequency varies inversely with the distance from the narrow end of the plate. In contrast, Maull & Young (1973) observed cellular shedding in the wake of a uniform (i.e. parallel-sided) plate with uniform shear as inflow. This motivated Castro & Rogers (2002) and Castro & Watson (2004) to carry out extensive hot-wire measurements in the wake of tapered and triangular plates of different taper and aspect ratios and with different end boundary conditions. The Reynolds numbers were still high ($Re = \bigcirc(10^4)$). Surprisingly, they found *end cells* in those cases where the tip of the triangular plate was lying within the flow domain (free ends), and multiple cells of constant shedding frequency when the free ends were sealed with an end plate.

The laboratory experiments on tapered plates by Gaster & Ponsford (1984) and Castro & Watson (2004) were both at high Reynolds numbers and there is no evidence that cellular vortex shedding also occurs at low Reynolds numbers. It should be noted that turbulence at high Reynolds numbers has direct consequences on the vortex dynamics in the wake. Even though Castro & Rogers (2002) and Castro & Watson (2004) provided extensive spectral data, the detailed dynamics of the wake has not been explored so far. An in-depth and comprehensive study of the wake behind a tapered plate in general and at low Reynolds numbers in particular is therefore awaited. Direct numerical simulation (DNS) as a tool is the natural choice to explore such a complex wake structure, as it gives complete access to the instantaneous three-dimensional data. The above issues will be addressed for the first time in the present DNS study, where in addition to frequency analysis a more detailed investigation of the spanwise two-point correlations and the instantaneous vortical structures will be carried out. The spanwise variations of the velocity and the pressure fields will also be shown. First, however, results from a three-dimensional simulation of the steady flow past a tapered plate at very low Reynolds numbers are presented.

2. Formulation of the problem

Let us consider the flow past a tapered flat plate with the view to explore for the first time ever the vortex shedding at moderately high Reynolds

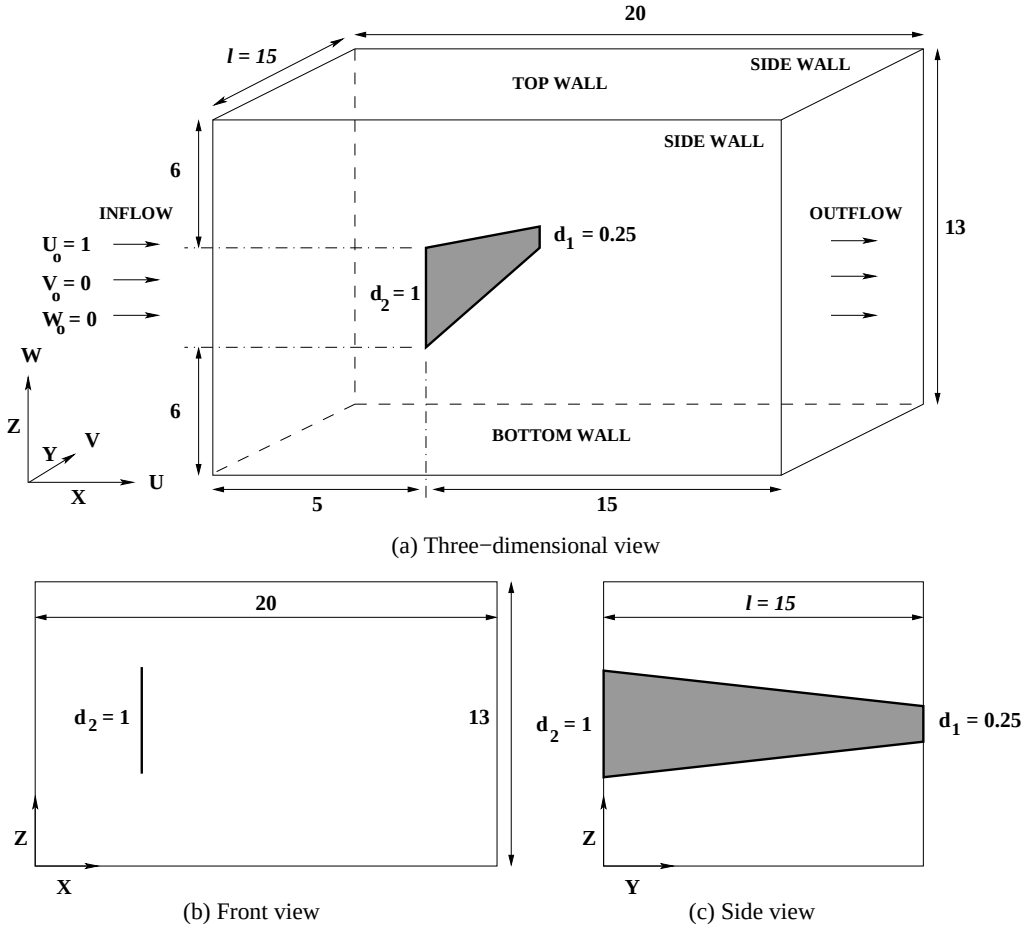

FIGURE 1. Computational domain (not to scale)

numbers, i.e. lower than in the otherwise equivalent laboratory experiments but yet sufficiently high to make even the near-wake turbulent. The taper ratio is intentionally chosen to match one of the configurations studied by Castro & Watson (2004), whereas the Reynolds number is about two orders of magnitude lower than in their experiment. Due to the substantial tapering, the local Reynolds number varies from 1000 at the wide end to 250 at the narrow end of the plate. It is evident from the existing literature that the first and second instability modes of three-dimensionality in the wake of uniform flat plates occur already at Re = 105-110 and Re = 125, respectively (Thompson *et al.* (2001, 2006); Julien *et al.* (2003, 2004)). Thereby, the Reynolds number chosen in the present study is well above the transitional regime and the wake flow is expected to be turbulent over the entire span.

CASE	R_T	AR	Re_2	Re_m	Re_1
Steady laminar flow	20	24	20	12.5	5
Turbulent flow	20	24	1000	625	250
Castro & Watson (2004)	20	20	-	$> 10^4$	-
Castro & Watson (2004)	20	15.4	-	$> 10^4$	-
Castro & Watson (2004)	20	10	-	$> 10^4$	-
Castro & Watson (2004)	20	5.8	-	$> 10^4$	-
Gaster & Ponsford (1984)	18	-	-	$> 10^4$	-

TABLE 1. Geometrical and flow parameters

2.1. *Flow configuration and numerical method*

The computational domain was as shown in figure 1. All spatial dimensions are normalized by d_2 and all velocities are scaled with the uniform inflow velocity U_o. The mean width of the plate, $d_m = 0.625\ d_2$. The thickness of the plate was very small and equal to $0.02d_2$. The aspect ratio ($AR = l/d_m$), R_T, and the Reynolds numbers Re_2, Re_1, Re_m, based on the uniform inflow velocity U_o and the widths d_2, d_1, d_m, respectively, are given in Table 1.

The Navier-Stokes (N-S) equations in *incompressible* form were solved in 3-D space and time using a *parallel* finite-volume code called MGLET (Manhart (2004); Narasimhamurthy *et al.* (2006)). The code uses staggered Cartesian grid arrangements. Discretization of the spatial derivatives was achieved by means of a 2^{nd}-order central-differencing scheme. The time marching was carried out using a 3^{rd}-order explicit Runge-Kutta scheme for the momentum equations in combination with an iterative SIP (Strongly Implicit Procedure) solver (Ferziger & Peric (1996)) for the Poisson equation. The time step was chosen as $\Delta t = 0.001 d_2/U_o$ and the number of Poisson iterations per time step was limited to 30. Parallelization was implemented using Message Passing Interface (MPI). The computations were performed on an *IBM P575+* parallel computer.

The size of the computational domain in each coordinate direction was $L_x = 20d_2$, $L_y = 15d_2$, and $L_z = 13d_2$, as shown in figure 1. All three-dimensional simulations reported in this paper are for the same flow configuration and computational domain. The number of grid points in each

$X/d_{local} =$	**1**	**3**	**5**	**8**	**12**
Present DNS: $Re_{local} = 1000$	3.84	4.03	4.96	3.44	2.94
Present DNS: $Re_{local} = 750$	2.18	2.86	4.51	3.82	3.05
Present DNS: $Re_{local} = 500$	1.31	3.80	4.90	3.68	2.99
Yao et al. (2001)	6.88	5.07	3.42	2.76	2.44
Moser et al. (1998)			≈ 15		

TABLE 2. Grid resolution $\Delta\overline{X} = \Delta X/\eta$ values at various X/d_{local} positions measured from the axis of the plate.

coordinate direction ($N_x \times N_y \times N_z$) for the steady laminar flow case and the turbulent flow case was equal to $160 \times 150 \times 180$ and $320 \times 200 \times 200$, respectively. Non-equidistant grid spacings were used in the $X - Z$ plane while an equidistant grid was used along the span (Y-direction). The ratio of grid size ΔZ near the plate's wide end to the local width of the plate $\Delta Z/d2 = 0.01$. This implies that the ratio of grid size near the plate's narrow end to the local width of the plate $\Delta Z/d1 = 0.04$. In order to justify that the present simulation is a fully resolved DNS, i.e. that all essential turbulent scales are captured, the grid size can be compared with Kolmogorov's microscale $\eta = (\nu^3/\varepsilon)^{1/4}$. Here, ε is the time-mean dissipation rate of fluctuating kinetic energy defined as

$$\varepsilon = \nu \left(\overline{\frac{\partial u_i}{\partial X_j}\frac{\partial u_i}{\partial X_j} + \frac{\partial u_i}{\partial X_j}\frac{\partial u_j}{\partial X_i}} \right) \approx \nu \left(\overline{\frac{\partial u_i}{\partial X_j}\frac{\partial u_i}{\partial X_j}} \right) \tag{2.1}$$

where u_i is the fluctuating part of the instantaneous velocity component which comprises both the unsteady fluctuations and the turbulent fluctuations. The contribution from the second term in the above definition of the total dissipation rate ε is negligible (Bradshaw & Perot (1993)) and hence neglected in the present analysis. The grid size relative to the Kolmogorov microscale at some different spanwise locations at five different downstream positions are given in Table 2 and compared with corresponding data for the plane wake DNS by Moser *et al.* (1998) and the trailing-edge wake DNS of Yao *et al.* (2001). The data in Table 2 shows that the grid size in the present study is of the same order of magnitude as the local Kolmogorov

Face	**Boundary condition**
Inflow	$U_o = 1; V_o = W_o = 0; \partial P/\partial X = 0$
Side walls	$V = 0; \partial U/\partial Y = \partial W/\partial Y = \partial P/\partial Y = 0$
Top and Bottom walls	$W = 0; \partial U/\partial Z = \partial V/\partial Z = \partial P/\partial Z = 0$
Outflow	$\partial U/\partial X = \partial V/\partial X = \partial W/\partial X = 0; P = 0$

TABLE 3. Boundary conditions

length scale. The present grid resolution compares favorably with that used in other wake flow simulations.

The boundary conditions used are as shown in Table 3. A uniform velocity profile $U_o = 1$ was prescribed at the inlet without any free-stream perturbations and a Neumann boundary condition was used for the pressure. A free-slip boundary condition was applied on both the side walls, as well as at the top and bottom walls (cf. figure 1). At the outlet, a Neumann boundary condition was used for velocities and the pressure was set to zero. A *direct forcing* Immersed Boundary Method (IBM) (Peller *et al.* (2006); Narasimhamurthy *et al.* (2006)) was used to transform the no-slip condition at the plate surface into internal boundary conditions at the nodes of the Cartesian grid (see Iaccarino & Verzicco (2003) and Mittal & Iaccarino (2005) for extensive reviews of different IBMs). The solid body (tapered plate) to be immersed in the Cartesian mesh was represented by a mesh consisting of triangles. The blocking of the Cartesian cells intersected by these triangles was accomplished as follows:

i) The intersection points of a triangle surface and the coordinate line passing through the pressure cell center were identified. The pressure cells containing those intersection points were blocked, as shown in figure 2.

ii) In a second sweep all the pressure cells within the blocked surface were blocked.

iii) Finally, all the velocity cells corresponding to blocked pressure cells were blocked.

In figure 2, ϕ_o is the internal boundary condition value to be determined by interpolation. X_r is the intersection point between the triangle and the coordinate line. ϕ_r is the value at X_r which is known (the value on the wall).

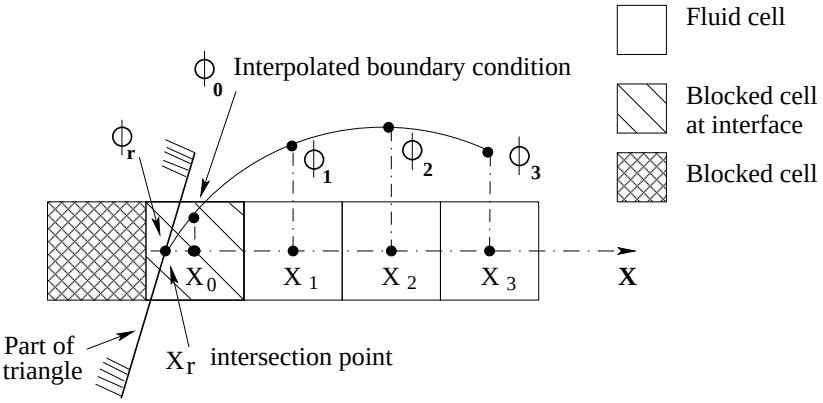

FIGURE 2. 1-Dimensional stencil configuration for interpolation in X-direction

By considering the neighboring variables ϕ_i (ϕ_1, ϕ_2, ϕ_3, etc) the stencils are formed. A general stencil formulation for ϕ_o looks like

$$\phi_o = (\sum_{i=1}^{N} \alpha_i.\phi_i) + \alpha_r.\phi_r \tag{2.2}$$

where N is the number of neighboring cells involved in the interpolation. The interpolation coefficients α_i and α_r depend on the interpolation technique and geometry only and were therefore computed in a pre-processing step. In the present DNS we used least-squares interpolation of 3^{rd}-order accuracy. The detailed derivation, validation and implementation of this technique in the code MGLET were explained in Peller *et al.* (2006). Using matrix stability analysis they studied the numerical stability of higher-order Lagrange and least-squares interpolations and concluded that the least-squares interpolation of 3^{rd}-order is very robust and numerically stable. The stencil in each direction is one-dimensional. Weighting to account for three-dimensionality was employed by Tremblay *et al.* (2001).

2.2. *A 2D case: the uniform plate*

Before undertaking the three-dimensional numerical simulations, benchmark two-dimensional calculations of the steady flow past a non-tapered plate placed normal to the free-stream were carried out. Two different simulations were performed with Reynolds number $Re = U_o d/\nu$ based on the uniform width d equal to 20 and 10. In both the simulations the domain size in X and Z directions was the same as that in the 3-D simulations (see figure 1). The number of grid points in each direction $N_x \times N_z$ were

CASE	BLOCKAGE RATIO	Re = 10	Re = 20
Present 2D case	0.077	1.12	2.12
Smith (1985)		1.00	2.00
Hudson & Dennis (1985)		1.20	2.32
Ingham et al. (1991)		1.15	2.30
Dennis et al. (1993)	0.00	1.16	2.43
Dennis et al. (1993)	0.05	1.07	-
Dennis et al. (1993)	0.10	1.02	1.98
Dennis et al. (1993)	0.15	0.92	1.76
In et al. (1995)		1.24	2.60
Koumoutsakos & Shiels (1996)		-	2.10

TABLE 4. Non-dimensional length of the steady re-circulation zone (L_w/d)

140×100. The non-dimensional length of the steady re-circulation zone (L_w/d) from the present simulations is in good agreement with the available experimental and numerical data (see Table 4). Note the scatter among the earlier results, with differences of up to 30% in estimating the length of the recirculating bubble. Koumoutsakos & Shiels (1996) attributed the differences between the existing simulations to the treatment of the boundary and far-field conditions. From their experiments Dennis *et al.* (1993) reported a strong dependence of the recirculation zone on the blockage ratio (see Table 4). They performed experiments for different blockage ratios and obtained the bubble length for zero blockage by extrapolation. The substantial increase of L_w/d with decreasing blockage ratio is indeed noteworthy. It should be noted that small differences in the thickness of the plate might also have some influence on the steady separation bubble.

3. Results and discussion

3.1. *Steady laminar flow*

There is no doubt that random turbulence and quasi-organized vortex shedding will add complexities to the wake of a three-dimensional body. This motivates a need to first study the wake of a tapered plate in the absence of these two factors. One may speculate at this stage whether the wake flow

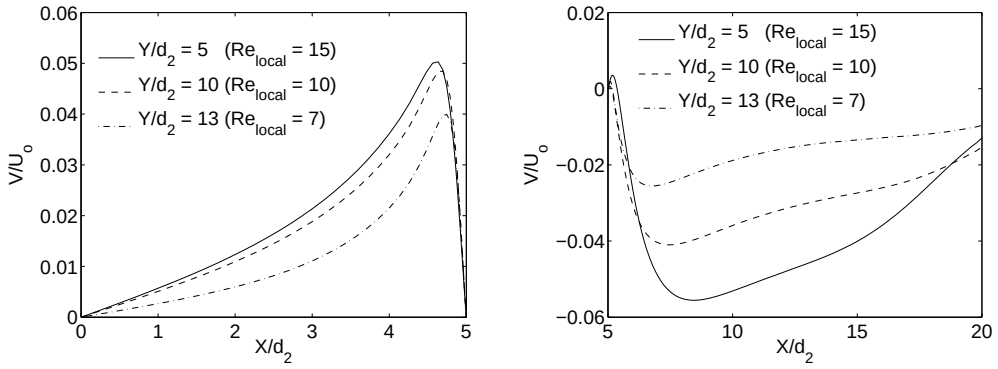

(a) Upstream the plate (b) Downstream the plate

FIGURE 3. Spanwise velocity V/U_o (secondary flow) at three different spanwise locations identified by the local Reynolds number $Re_{local} = U_o\ d/\nu$.

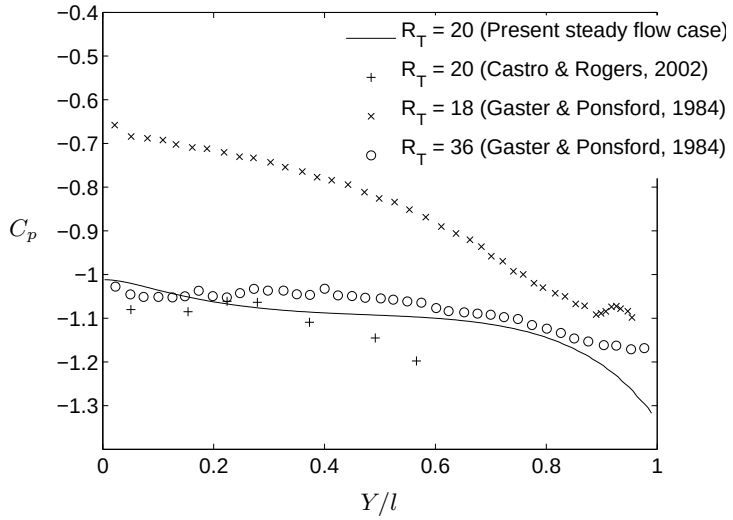

FIGURE 4. Base pressure coefficient variations along the span from the present steady laminar flow case and the previous experimental results at high Reynolds numbers.

behind a tapered plate can be considered as quasi-two-dimensional provided that the Reynolds number is lower than the critical value at which vortex shedding occurs. One may furthermore wonder how the secondary flow field, i.e. the departure from purely 2D behavior, will appear. In order to address these issues a steady laminar flow past a tapered plate was investigated; see Table 1 for details. The numerical solution of the unsteady Navier-Stokes equations converged to a steady state. The present 3-D calculation revealed a secondary spanwise velocity V, both in the front stagnation zone and also in the wake of the plate (see figure 3). It can be observed from figure

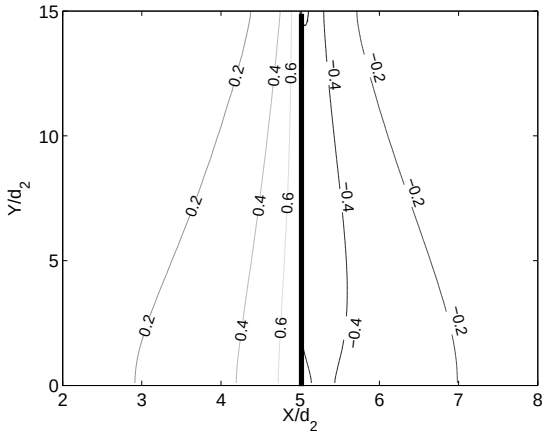

FIGURE 5. Pressure ($P/\rho\ U_o^2$) contours in the $X-Y$ section plane through the axis of the plate in the steady laminar flow case. The plate is drawn as a bold line.

3(a) that in the front stagnation zone the secondary flow is going from the wide end of the plate towards the narrow end, surprisingly as speculated by Gaster & Ponsford (1984) in their high Reynolds number study. On the contrary, the secondary motion on the rear side of the plate is rather complex. The flow in the immediate vicinity of the plate is going from the wide end towards the narrow end (see figure 3(b)). The variation of the base pressure coefficient ($C_p = 2(P-P_\infty)/(\rho U_o^2)$, where the reference pressure P_∞ is taken from the pressure at the inflow) along the span in figure 4 confirms the above observation. This is also in perfect agreement with the findings of Gaster & Ponsford (1984) at higher Reynolds number. The magnitude of this secondary flow is negligibly small, i.e. less than 0.5% of the inflow velocity U_o. However, the direction of the secondary motion is reversed somewhat away from the plate where the flow goes from the narrow end of the plate towards the wide end. The magnitude of this spanwise velocity is typically of the order 5% of the inflow U_o. The secondary motion in the spanwise direction is a direct consequence of three-dimensionality of the tapered plate and this kind of secondary flows does not arise in the vicinity of a uniform plate.

The secondary flow is driven by a spanwise pressure gradient. The tapered plate introduces a variable blockage to the inflow along the span and this gives rise to a somewhat higher pressure near the wide end of the plate as compared to the narrow end. The pressure contours (isobars) in figure 5 show that the isobars are inclined to the stagnation line, thereby giving rise

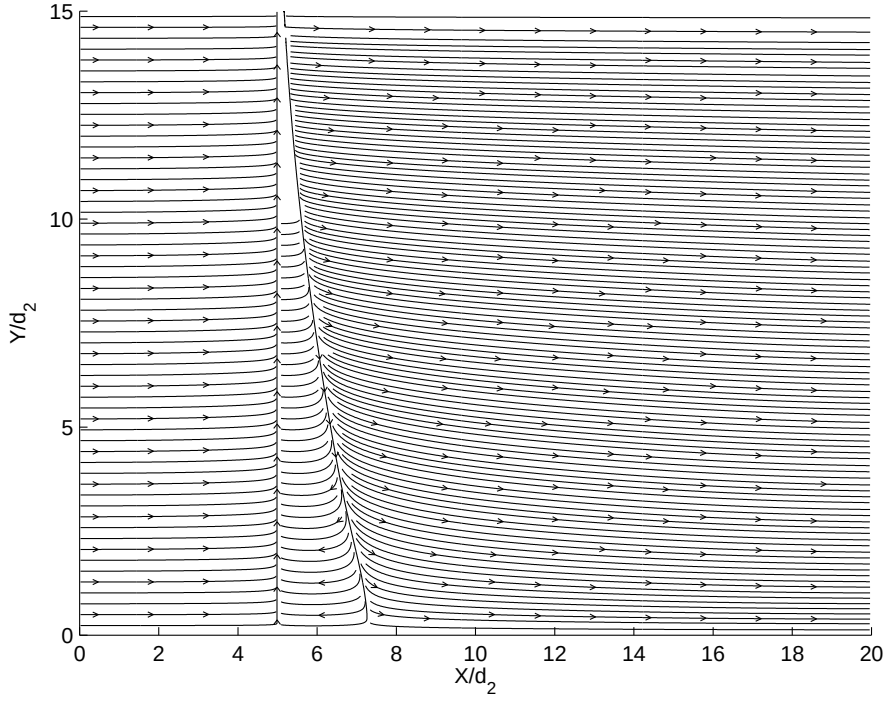

FIGURE 6. Streamlines in the $X-Y$ section plane through the axis of the plate illustrating the secondary flow direction and the re-circulation zone in the steady laminar flow case. $Y/d_2 = 0$ corresponds to $Re_2 = 20$ and $Y/d_2 = 15$ corresponds to $Re_1 = 5$.

to a spanwise pressure gradient which drives the flow towards the narrow end. Similarly, the (negative) isobars in the wake are also tilted from the rear stagnation line, i.e. the lowest pressure is found in the wake downstream of the widest part of the plate. This observation indicates that also the spanwise-oriented flow in the wake is pressure-driven. The streamlines in a $X-Y$ plane cutting through the axis of the plate in figure 6 confirms the above observations.

The constant length L_w of the closed wake behind a uniform plate is known to increase monotonically with the Reynolds number as long as the flow is in the steady laminar regime. Both the data from experiments by Dennis *et al.* (1993), Ingham *et al.* (1991) and computations by Hudson & Dennis (1985), In *et al.* (1995) and others suggest this linear variation of L_w with the Re. In the present 3D case, the wake length varies substantially along the span of the tapered plate. The wake behind the wide end is roughly 16 times longer than the wake behind the narrow end of the plate (see figure

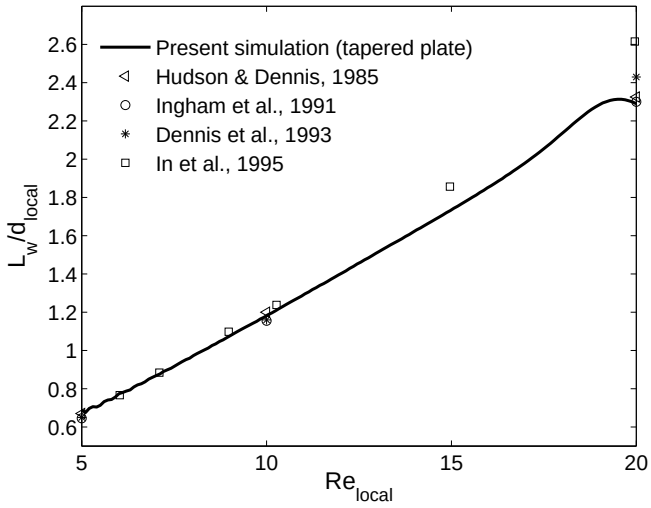

FIGURE 7. Non-dimensional length of the steady re-circulation zone (L_w/d_{local}) versus local Reynolds number $Re_{local} = U_o\ d_{local}/\nu$. The symbols denote data for non-tapered plates with uniform width d.

6). If the local wake length L_w is scaled with the local plate width d_{local}, the spanwise variation of L_w/d_{local} shown in figure 7 is surprisingly close to the results for uniform or non-tapered (i.e. 2D) plates. The deviation from 2D behavior is largest near the wide part of the tapered plate where the secondary flow is most pronounced (cf. figure 3). The results from the present simulation compares excellently with the data for uniform plates in the low-Re regime, i.e. along the narrow half of the plate.

3.2. *Turbulent flow*

3.2.1. *Wake pattern and frequency analysis*

The time evolution of the instantaneous velocity components U, V, W and the instantaneous pressure, P, were sampled along four lines parallel to the axis of the plate and located $4d_m$, $8d_m$, $11d_m$ and $14d_m$ downstream the axis in X-direction, respectively. All lines were offset by $1d_m$ in Z-direction. It would be inappropriate to present all the data here due to space constraints. Therefore, only the time trace of the cross-stream velocity W sampled at $11d_m$ is shown in figure 8. The total sampling time was equal to 260 d_2/U_o or 1040 d_1/U_o, which covers about 35 shedding cycles at the wide end and about 150 cycles at the narrow end of the plate. Note that only half of the sampled data (130 d_2/U_o) is shown in figure 8 for the purpose of clarity.

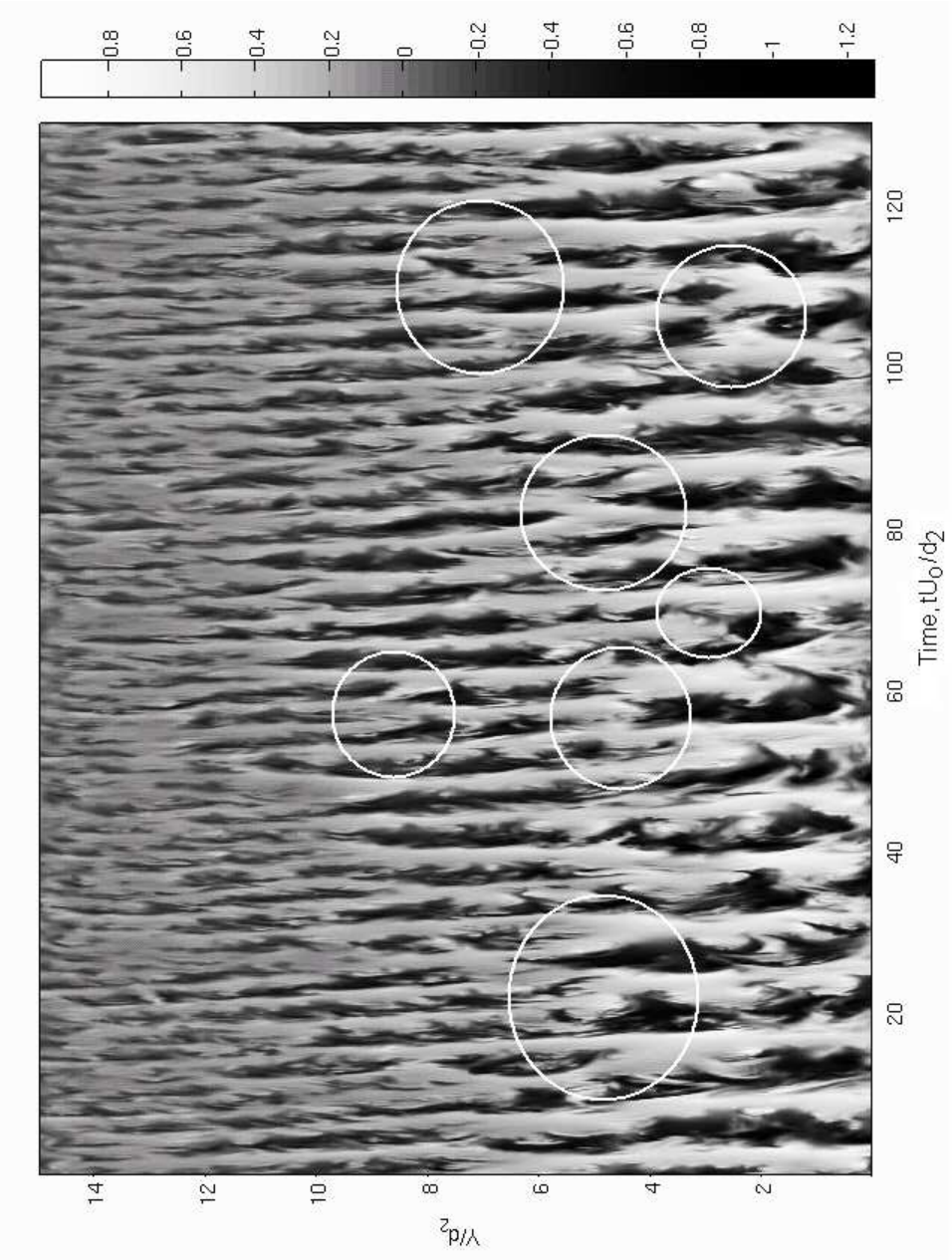

Figure 8: Time evolution of the cross-stream velocity (W) showing vortex-dislocations along the entire span (some marked by circles). The sampling line is at $X/d_m = 11$ and $Z/d_m = -1$ (measured from the axis of the plate). $Y/d_2 = 0$ corresponds to $Re_2 = 1000$ and $Y/d_2 = 15$ corresponds to $Re_1 = 250$.

The pattern clearly indicates *oblique* and *cellular* vortex shedding with random occurance of *vortex dislocations* or *vortex splits* along the span. It is easy to see that the vortex dislocations are not occurring periodically in time at the same spanwise position. This justifies the need for such a long and expensive time sampling. Some time trace signals of the cross-stream

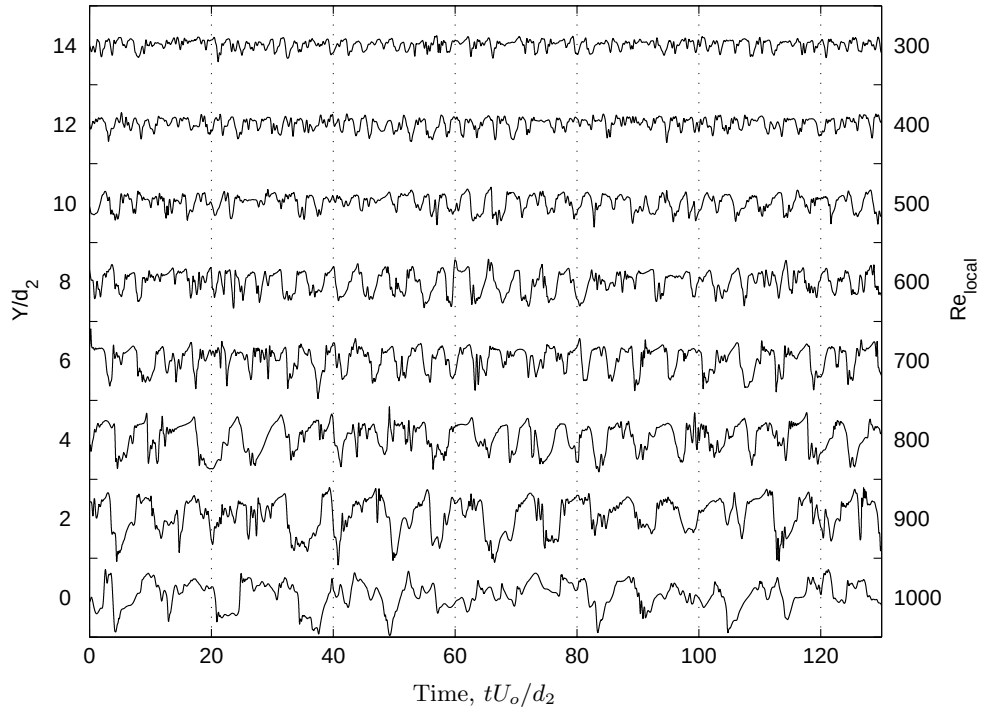

FIGURE 9. Time traces of the cross-stream velocity (W) at different spanwise locations.

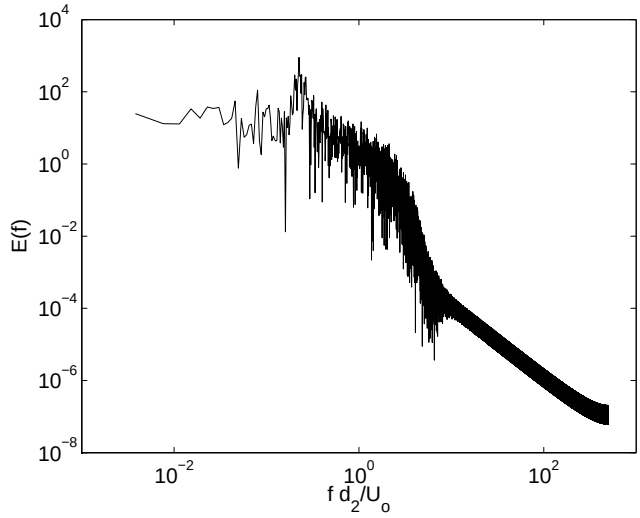

FIGURE 10. Spectrum for the mid-span location $Y/d_2 = 7.5$ ($Re_{local} = 625$).

velocity (W) at some different spanwise locations are shown in figure 9. Even though the turbulence signatures are chaotic, a low-frequency modulation, a typical feature of *vortex dislocations*, is visible in certain signals. The signal at $Y/d_2 = 4$ in figure 9, for instance, shows a low-frequency signature at time $tU_o/d_2 \approx 17$, which corresponds to the vortex dislocation at $Y/d_2 \approx 4$ in figure 8. Such low-frequency fluctuations were also observed in the wake of uniform circular cylinders, first by Roshko (1954) in the transition regime, and later Bloor (1964) suggested that these low-frequency irregularities reflect the presence of three-dimensionalities that would render the flow turbulent as it travels downstream. Williamson (1992) attributed these low-frequency irregularities in the transition regime to the presence of large-scale spot-like vortex dislocations. The dislocations were found to be generated during the change-over of eddy shedding mode from laminar-mode A (Williamson (1996)). Thereby there exists some firm evidence that low-frequency signatures can be associated with vortex-dislocations even for parallel-sided bluff bodies. However, this is not always true. The low-frequency signatures observed in the wake of uniform flat plates by Najjar & Vanka (1995), Najjar & Balachandar (1998), and Wu *et al.* (2005) were rather differently interpreted. While Najjar & Vanka (1995) speculated the low-frequency behavior to be due to a low-frequency flapping of the shear layer, Najjar & Balachandar (1998) attributed the phenomenon to the gradual variation of the flow between two regimes: a regime of short formation region and a regime of long formation region. They observed that in the short formation regime the shear layer rolls up closer to the plate to form coherent spanwise vortices, while in the long formation regime the shear layer extends farther downstream and the rolled-up Karman vortices are less coherent. Similar regimes leading to low-frequency modulations were also noticed at higher Reynolds numbers by Wu *et al.* (2005).

To enable quantitative comparisons the frequency spectra were obtained by Fourier analysis of cross-stream velocity (W) time traces. A sample spectrum is shown in figure 10, which is taken at the mid-span of the plate ($Re_{local} = 625$) and is provided in a double-logarithmic plot. The primary shedding frequency corresponds to the most energetic frequency which is found at $fd_2/U_o = 0.2257$. This gives the local Strouhal number, defined as $St_{local} = fd_{local}/U_o = 0.1411$. Shedding frequencies ($f$) obtained from the Fast Fourier Transform (FFT) of the velocity signals are plotted against

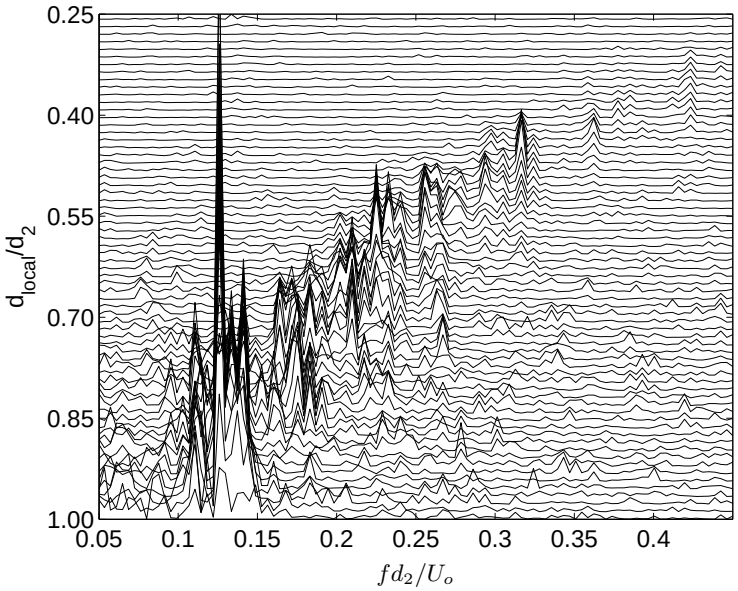

FIGURE 11. Shedding frequencies (fd_2/U_o) from Fourier analysis *versus* d_{local}

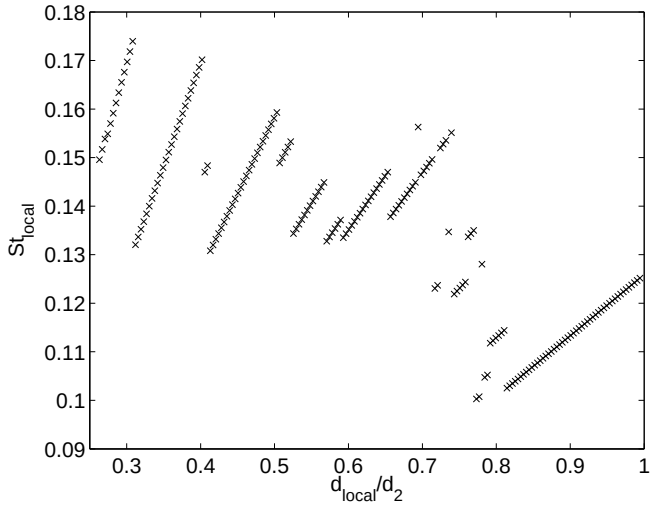

FIGURE 12. Local Strouhal number St_{local} *versus* local width of the plate d_{local}

the local widths of the plate in figure 11. Note that the shedding frequency is not varying continously along the span but in discrete steps between cells of constant shedding frequency. This is in contrast to what Gaster & Ponsford (1984) found at high Reynolds numbers, where they reported an almost constant value of base Strouhal number fd_2/U_o along the span. The local Strouhal number St_{local} is plotted against d_{local} in figure 12. It seems

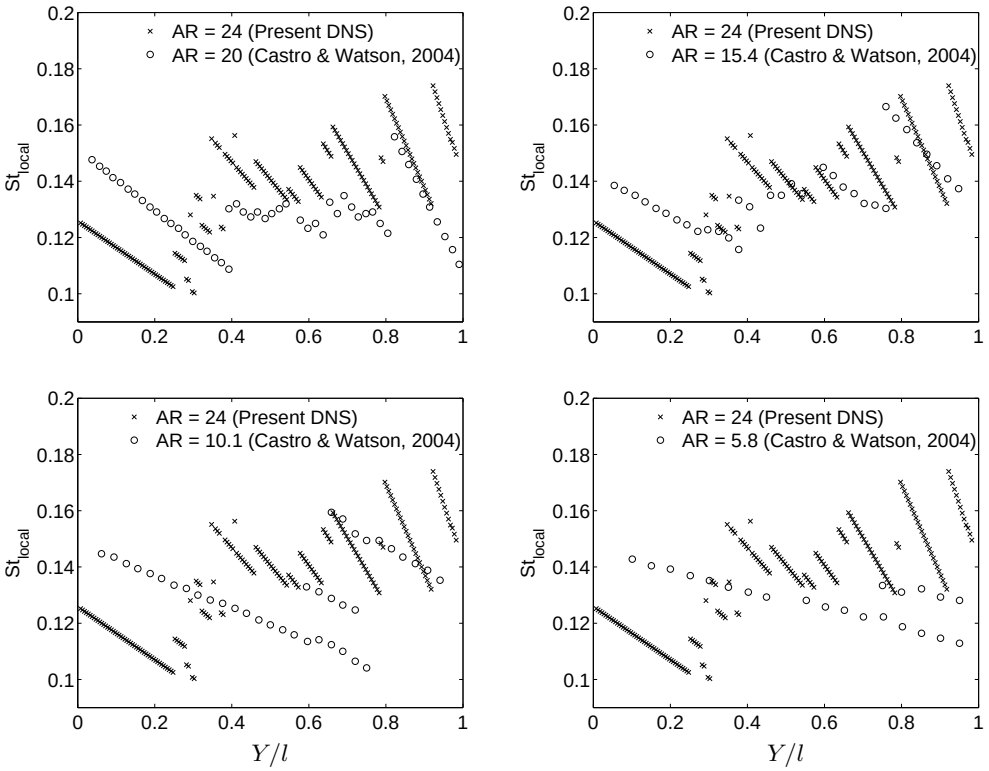

FIGURE 13. Local Strouhal number St_{local} from the present DNS calculation plotted against the hot-wire measurements data by Castro & Watson (2004) along the entire span. Taper ratio $R_T = 20$ is same in both the cases. $Y/l = 0$ corresponds to $Re_2 = 1000$ and $Y/l = 1$ corresponds to $Re_1 = 250$.

like the width of the constant shedding frequency cells increases with the d_{local}, an effect also observed in the wake of tapered cylinders (Piccirillo & Van Atta (1993); Narasimhamurthy *et al.* (2007); Parnaudeau *et al.* (2007); Narasimhamurthy *et al.* (2006)). The same observation can also be made from the results of Castro & Watson (2004) in figure 13. Here, the variation of the St_{local} from the present DNS is compared against their experimental data. Note that the taper ratio is same in both the cases (see Table 1). In spite of the different Reynolds numbers the qualitative agreement is striking. The structure of the vortex shedding is strongly dependent on the aspect ratio for low aspect ratios. The local Strouhal number behaviour deduced from the hot-wire measurements of Castro & Watson (2004) shows only minor difference between their $AR = 15.4$ and $AR = 20$. We are therefore inclined to infer that the impact of the aspect ratio difference between the

present DNS ($AR = 24$) and the Castro & Watson (2004) data for $AR = 20$ is negligibly small.

3.2.2. *Spanwise two-point correlation*

It is clear from the preceding section that cellular vortex shedding exists in the wake of a tapered plate even at low Reynolds numbers. To further explore this cellular vortex shedding phenomenon, the spanwise coupling of the vortex motion is studied by means of spanwise two-point correlation, where the correlation coefficient is defined as $\overline{\phi(Y)\ \phi(Y+\Delta Y)}\ /\ \overline{\phi(Y)^2}$. In statistically homogeneous flows, this correlation is a function only of the separation ΔY between the two points and does not depend on the position Y. In addition, the correlation is symmetric in the direction of homogeneity, i.e., independent of the sign of ΔY. However, this should not be true in the present case as the flow is inhomogeneous in all the three directions. This is indeed what we see in figure 14 and 15. The correlation coefficient of the secondary flow (V) is plotted against the spanwise separation ΔY at three different positions, $Y/d_2 = 5, 7.5$ and 10 in figure 14(a),14(b), and 14(c), respectively. The correlation is clearly asymmetric and the secondary motion remains surprisingly correlated almost for the entire span. However, it is interesting to see that the correlation reduces to $\approx 20\%$ within about $\Delta Y = 1d_2$. The negative correlation towards the narrow end of the plate implies that the secondary motion is oppositely directed at that position. This is clearly an end effect as it appears only over $1d_2$ at the narrow end. The correlation coefficient is also computed for the cross-stream velocity (W) component (see figure 15). This coefficient is again asymmetric. However, it is not surprising that the correlation goes to zero within about $\Delta Y = 3d_2$, since the cross-stream velocity is directly linked to the spanwise vorticity and the spanwise vortex filaments experience random vortex dislocations along the span.

3.2.3. *Instantaneous vortical structures*

In order to identify the topology of the vortex cores correctly the λ_2-definition by Jeong & Hussain (1995) was used. λ_2 corresponds to the second largest eigenvalue of the symmetric tensor $S_{ij}S_{ij} + \Omega_{ij}\Omega_{ij}$, where S_{ij} and Ω_{ij} are respectively the symmetric and antisymmetric parts of the velocity gradient tensor. Iso-surfaces of negative λ_2 and pressure ($P/\rho\ U_o^2$) at

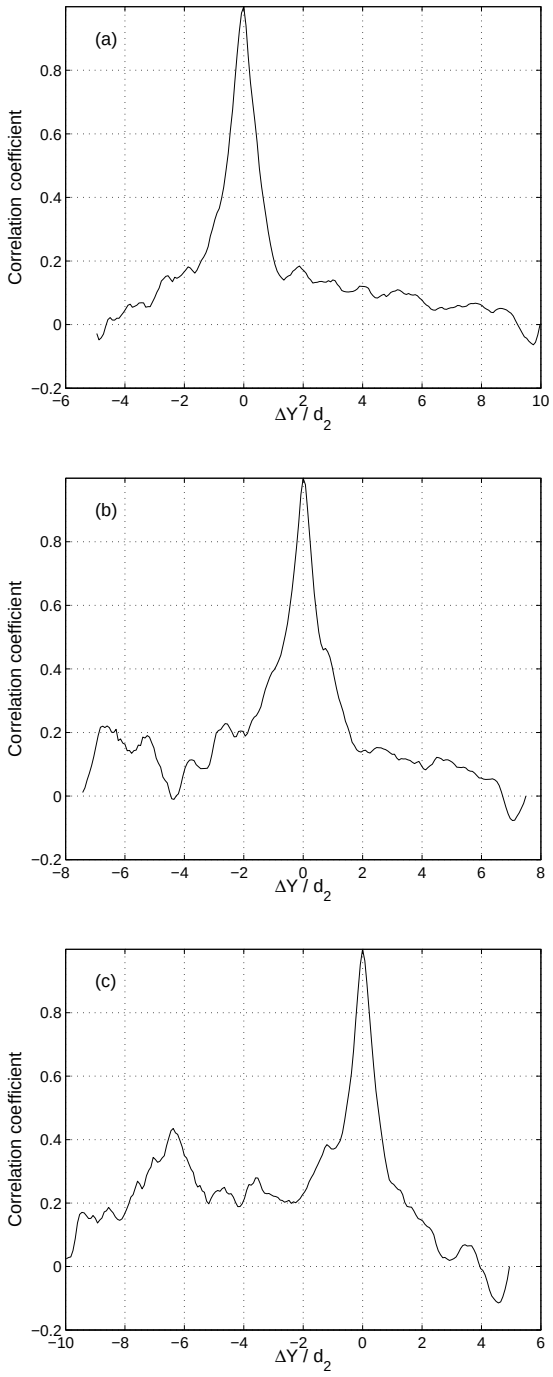

FIGURE 14. Spanwise correlation of the secondary flow (V) at three different positions along the span corresponding to the Re_{local}: (a)750; (b)625; (c)500. ΔY corresponds to spanwise separation length.

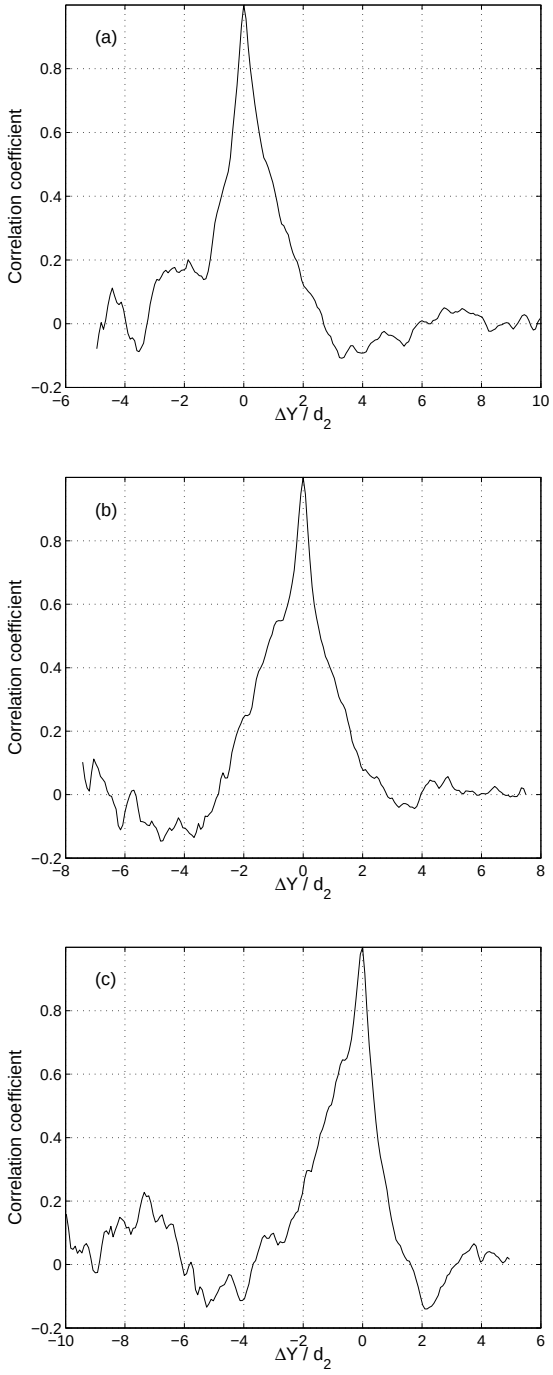

FIGURE 15. Spanwise correlation of the cross-stream (W) velocity at three different positions along the span corresponding to the Re_{local}: (a)750; (b)625; (c)500. ΔY corresponds to spanwise separation length.

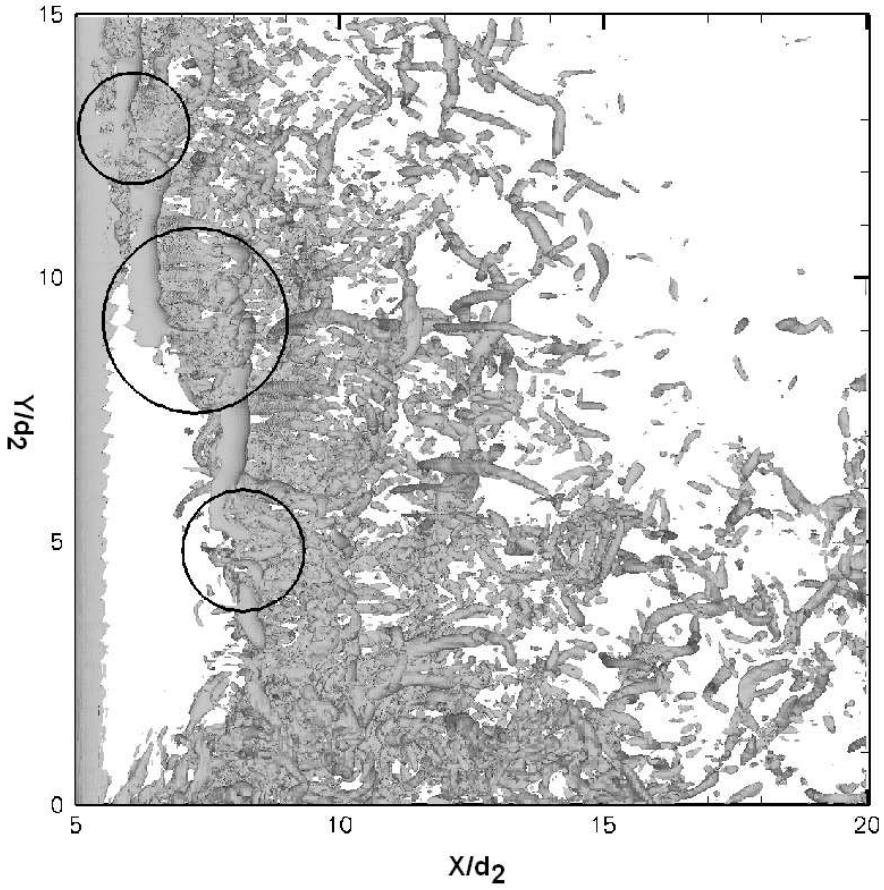

FIGURE 16. $-\lambda_2$ vortical structures at time, $t = 130\ d_2/U_o$ showing vortex-dislocations along the span at $Y/d_2 \approx 5, 9, 12.5$ (marked by circles). The flow direction is from left to right and the Y-axis corresponds to the axis of the plate.

the same instant in time are shown in figures 16 and 17, respectively. The snapshots clearly demonstrate the discontinuity in the spanwise vortex filament at $Y/d_2 \approx 5, 9$, and 12.5. As seen in figure 17, the three-dimensional re-circulation bubble is nearly conical in shape. This observation is consistent with the finding of Gaster & Ponsford (1984) reported from their high-Reynolds-number experiments. Figure 18(a) and 18(b) shows the iso-surfaces of instantaneous streamwise and cross-stream vorticity components at the same instant in time. Vortices rotating in opposite directions are distinguished by colour (white and black). The vortices towards the narrow part of the plate ($Y \rightarrow 15$) appear to be organized but highly irregular in the very near wake and rapidly break up into incoherent motion downstream. Towards the wider part of the plate ($Y \rightarrow 0$) there is chaos even in

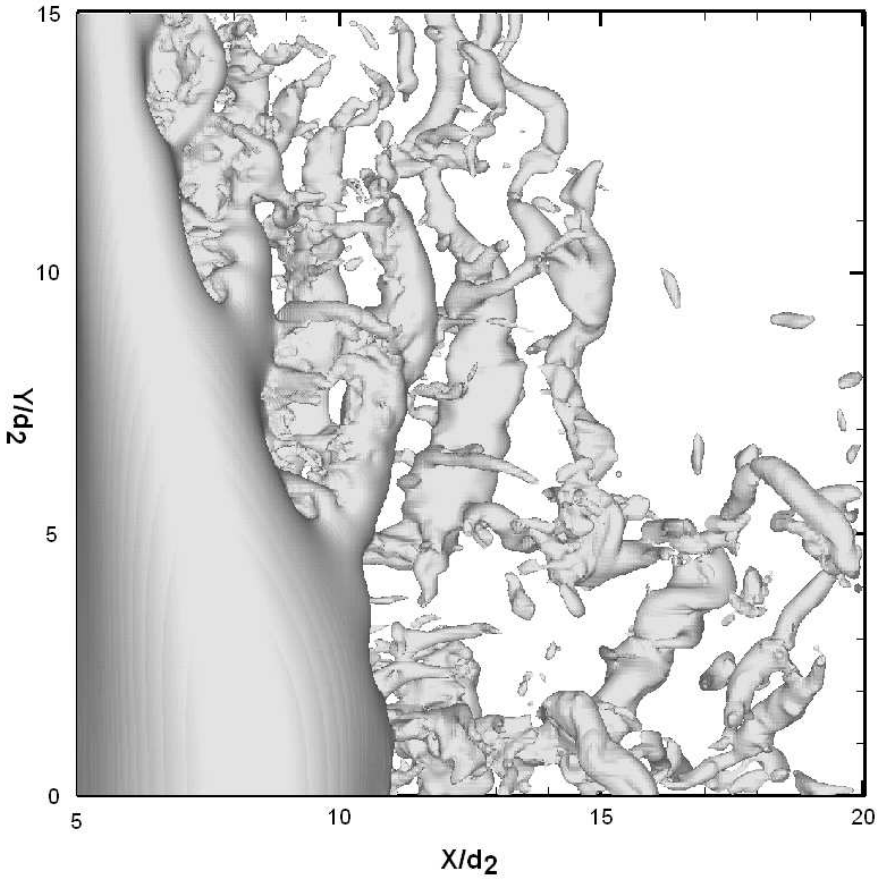

FIGURE 17. 3-dimensional iso-pressure ($P/\rho\ U_o^2 = -0.07$) contours at time, $t = 130\ d_2/U_o$ showing vortex-dislocations along the span at $Y/d_2 \approx 5, 9, 12.5$. The flow direction is from left to right and the Y-axis corresponds to the axis of the plate.

the near wake. This is obviously a Reynolds number effect. The above observation is clearly illustrated in figure 19, where $-\lambda_2$ at two different spanwise positions were plotted in the $X - Z$ plane perpendicular to the plate. Note that the shear layer extends farther downstream of the plate before rolling-up than in the case of parallel-sided plates; e.g. Najjar & Vanka (1995) and Najjar & Balachandar (1998). This is consistent with a conclusion drawn by Gaster & Ponsford (1984), where they noticed that tapered plates have longer formation length than their corresponding uniform plates.

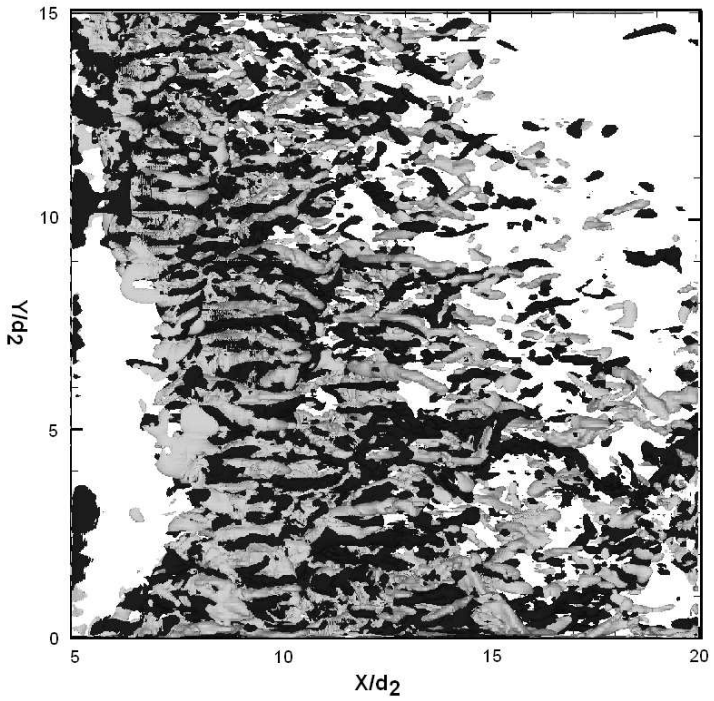

(a) Streamwise vorticity, ω_x

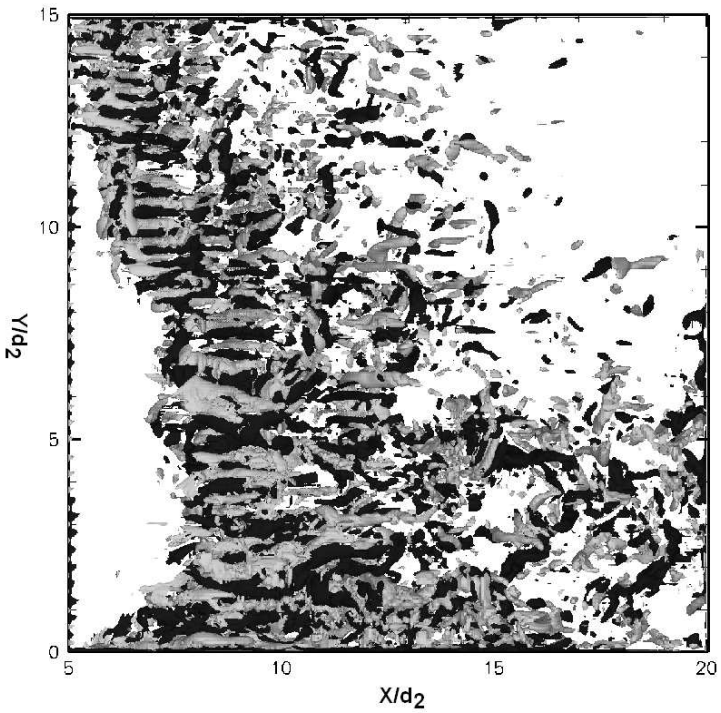

(b) Cross-stream vorticity, ω_z

FIGURE 18. 3-dimensional iso-surfaces at the same instant in time, $t = 130\ d_2/U_o$. The flow direction is from left to right and the Y-axis corresponds to the axis of the plate. The surfaces colored white and black mark $\omega\nu/U_o^2 = -0.002$ and $\omega\nu/U_o^2 = +0.002$, respectively.

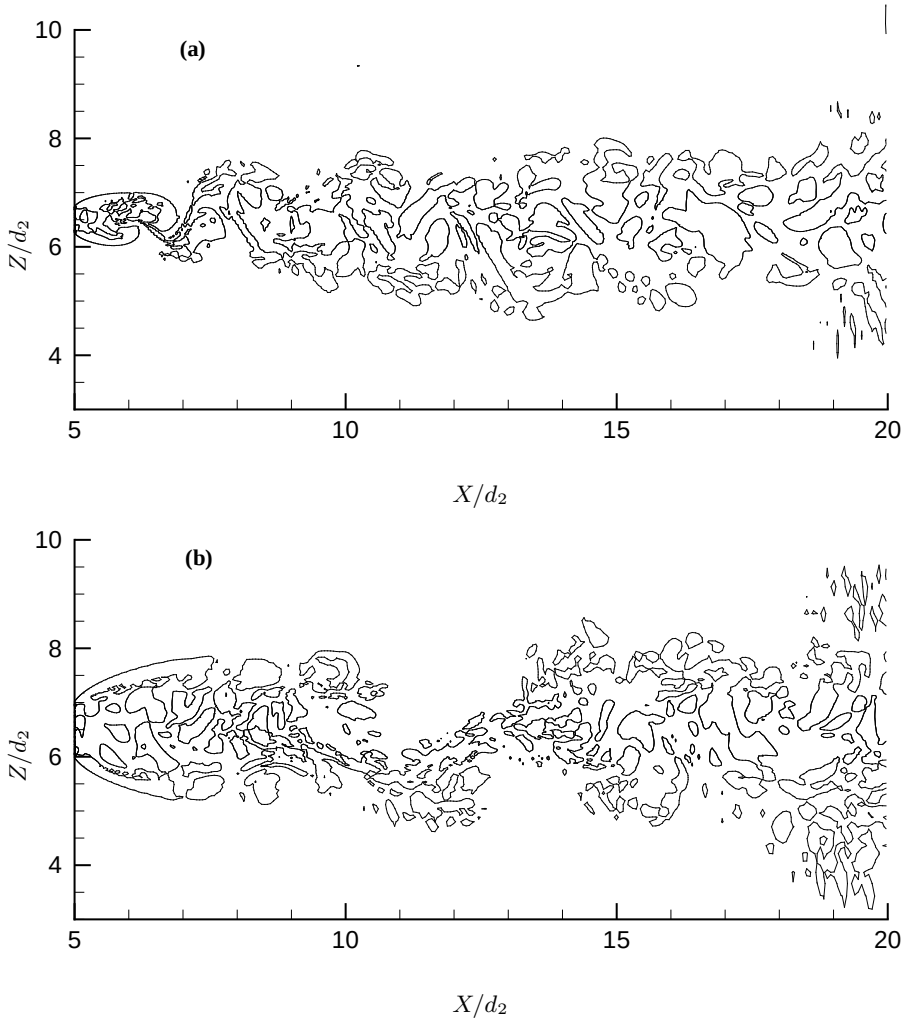

FIGURE 19. Contour plots of $-\lambda_2$ at two different spanwise positions: (a) $Y/d_2 = 12$; (b) $Y/d_2 = 2$.

3.2.4. *Mean pressure and base suction coefficients*

Time-averaged statistical quantities were evaluated by sampling for 170 d_2/U_o or 680 d_1/U_o time units. This sampling period corresponds to about 60 mean shedding cycles. One sample is taken every tenth time step for averaging.

The mean pressure coefficient is defined as, $\overline{C}_p = 2(\overline{P} - P_\infty)/(\rho U_o^2)$, where the reference pressure P_∞ is taken from the pressure at the inflow. The distribution of $\overline{C}_p$ on the surface of the tapered plate at different spanwise positions is compared against uniform plate results in figure 20. The pressure on the upstream surface of the tapered plate compares well with the uniform plate experimental data by Fage & Johansen (1927) and the nu-

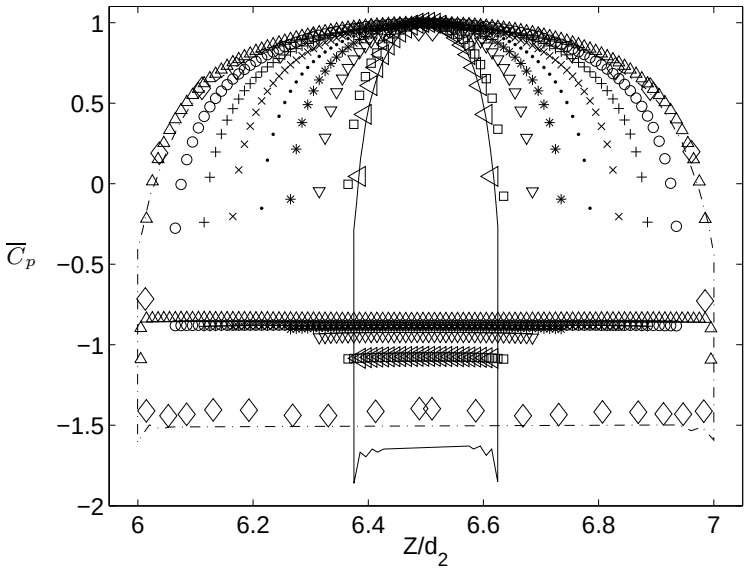

FIGURE 20. Distribution of the mean pressure coefficient, $\overline{C}_p$, on the surface of the plate from the present DNS (tapered plate): $\triangle, Y/d_2 = 0$; $\circ, Y/d_2 = 2$; $+, Y/d_2 = 4$; $\times, Y/d_2 = 6$; $\cdot, Y/d_2 = 8$; $*, Y/d_2 = 10$; $\nabla, Y/d_2 = 12$; $\square, Y/d_2 = 14$; $\triangleleft, Y/d_2 = 15$; and the experimental data (uniform plate) of Fage & Johansen (1927): $\diamond, Re = 1.5 \times 10^5$; and the DNS results (uniform plate) of Najjar & Vanka (1995): $-.-, Re = 1000$; Najjar & Balachandar (1998): $-, Re = 250$.

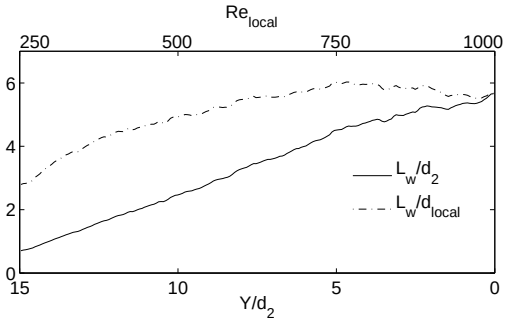

FIGURE 21. Non-dimensional length of the mean re-circulation zone *versus* Re_{local}. L_w is the streamwise distance from the axis of the plate to the position where the mean streamwise velocity $\overline{U}$ changes sign from negative to positive.

merical data by Najjar & Vanka (1995), Najjar & Balachandar (1998). It should be noticed that the front face pressures collapse if plotted versus Z/d_{local} rather than versus Z/d_2. The constancy of the pressure in the base region is well captured in the present DNS. However, the pressure in the base region is significantly higher compared to the uniform plate data. The

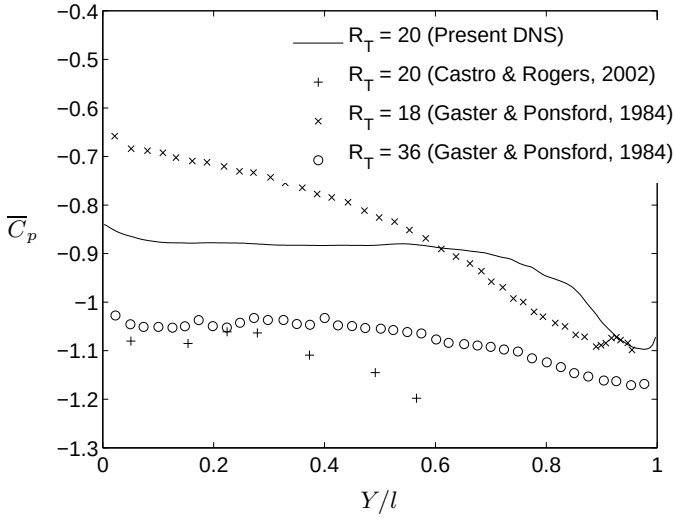

FIGURE 22. Mean base pressure coefficient variations along the span for different taper ratios from the present turbulent flow case and experiments.

reason for this lies in the wake formation length, which is closely coupled to the local base pressure. As discussed already in the previous section, Gaster & Ponsford (1984) reported very strong and periodic vortex shedding behind the uniform plates, which gives rise to significantly shorter formation lengths compared to tapered plates. Najjar & Vanka (1995) noted that the wake formation length in their uniform plate case at $Re = 1000$ was about two plate widths. The mean wake formation length in the present case in figure 21 clearly shows that at $Re_{local} = 1000$ the bubble is 6 times the local plate width, i.e., 3 times larger than in the corresponding uniform plate case. This suggests a coupling between the local base pressure and the vortex formation process (Bearman (1965, 1967)).

The mean base pressure coefficient along the span of the plate is shown in figure 22. Even though Gaster & Ponsford (1984) observed base pressure variations for all their tapered models with a significant reduction towards the narrow end of the plate, they did not give any explanation to this phenomenon. They noticed however, that this base pressure gradient was driving the secondary flow from the wide end of the plate towards the narrow end. Castro & Rogers (2002) made a similar observation in their experiments and they attributed this reduction in base pressure towards the narrow end to the corresponding increase in Strouhal number. By comparing the $\overline{C}_p$

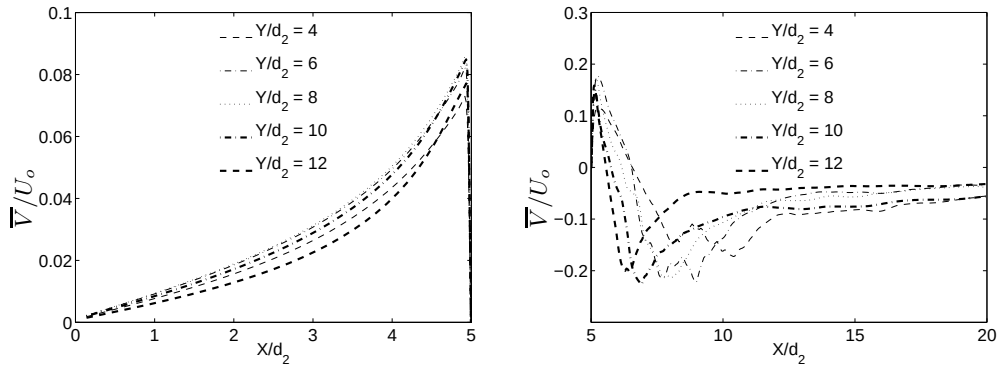

(a) Upstream the plate (b) Downstream the plate

FIGURE 23. Time-mean spanwise velocity (secondary flow) at different spanwise locations.

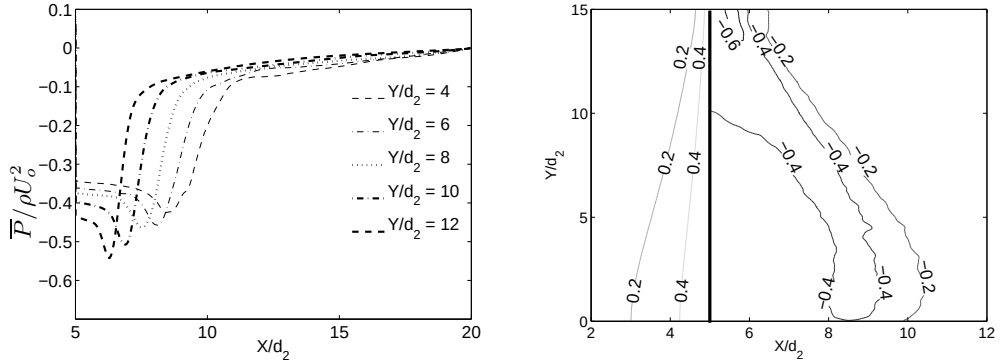

(a) (b)

FIGURE 24. (a) Mean pressure ($\overline{P}/\rho U_o^2$) in the wake at different spanwise locations. (b) Iso-bars in the $X-Y$ section plane through the axis of the plate. The plate is drawn as a bold line.

variations in figure 22 to the St_{local} variation in figure 13, the present DNS data confirms Castro & Rogers (2002) conclusion.

3.2.5. *Secondary motion*

The pressure-driven secondary motion in the steady laminar flow regime has been discussed in section 3.1. There is also some evidence in the experiments (Gaster & Ponsford (1984); Castro & Rogers (2002)) that such pressure-driven secondary flow may exist even at high Reynolds numbers, i.e., in the turbulent flow regime. This issue has not yet been thoroughly addressed. The present turbulent flow simulation revealed a mean spanwise velocity $\overline{V}$, both in the front stagnation zone and also in the wake of the plate (see figure 23). It can be observed from figure 23(a) that in the front

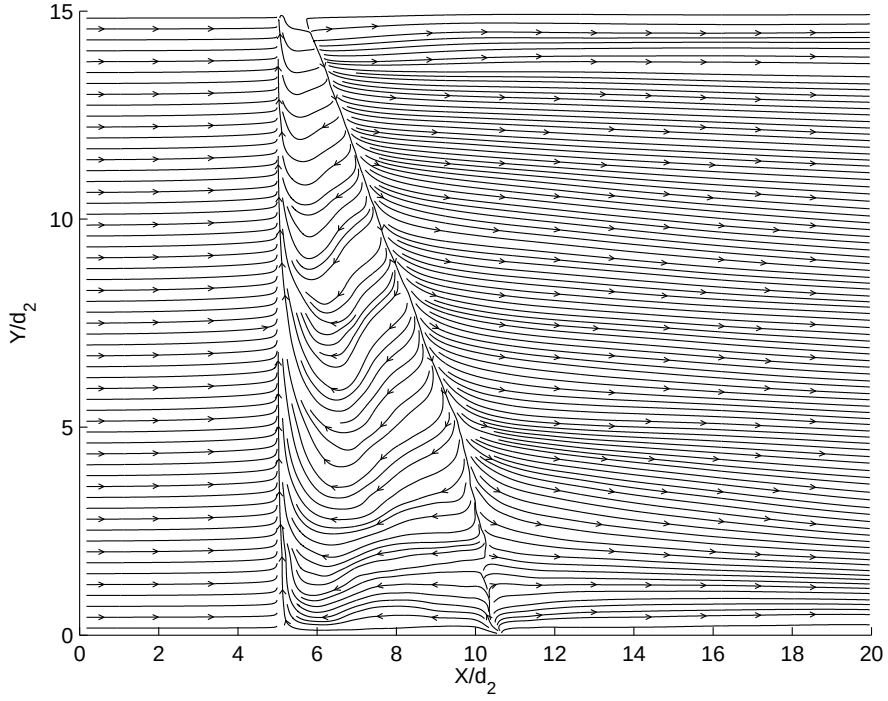

FIGURE 25. Streamlines in the $X-Y$ section plane through the axis of the plate illustrating the mean secondary flow ($\overline{V}$) direction and the mean re-circulation zone.

stagnation zone the secondary flow is still going from the wide end of the plate towards the narrow end, similar to what we saw in the steady laminar regime (cf. figure 3(a)) and also as speculated by Gaster & Ponsford (1984). The magnitude of this spanwise velocity is around 10% of the inflow U_o, i.e., twice larger than what we observed in the steady laminar regime. On the contrary, the secondary motion on the rear side of the plate in figure 23(b) is more complex and similar to what we observed in the steady laminar wake (see figure 3(b)). The flow in the near vicinity of the plate is going from the wide end towards the narrow end. This is in perfect agreement to what Gaster & Ponsford (1984) claimed in their experimental study. However, the direction of this secondary motion is surprisingly reversed somewhat away from the plate, so that the flow goes from the narrow end of the plate towards the wide end. The magnitude of this spanwise velocity is around 20% of the inflow U_o, i.e., about four times larger than what was observed in the steady laminar regime (cf. figure 3(b)). The secondary motion discussed above is driven by local pressure gradients. Mean pressure profiles at differ-

ent spanwise locations in figure 24(a) and the isobars in figure 24(b) justify the above claim. The streamlines in a $X-Y$ plane through the axis of the plate in figure 25 confirm the above observations. The streamlines within the separation bubble are distinctly different from those in the steady laminar case (figure 6). The shape of the -0.4 mean-pressure contour in figure 24(b) resembles the topology of the instantaneous iso-pressure surface in figure 17.

4. Conclusions

For the first time ever *cellular* vortex shedding has been observed behind a tapered plate in a numerical experiment (DNS). Frequency analysis, two-point correlations and the three-dimensional visualizations collectively confirm that multiple cells of constant shedding frequency exist along the span of the plate. This is in contrast to apparent lack of cellular vortex shedding found in the high-Reynolds-number experiments by Gaster & Ponsford (1984). However, the present DNS data is in good qualitative agreement with similar high-Reynolds-number experimental data produced by Castro & Rogers (2002) and Castro & Watson (2004). A possible reason for the failure of Gaster & Ponsford (1984) experiments to show cellular vortex shedding was suggested by Castro & Rogers (2002). They argued that tracking of the variation in shedding frequency across the span certainly requires closely spaced measurements, whereas only a modest number of spectral measurements were made by Gaster & Ponsford (1984).

In the present DNS, it has been observed that tapering tends to decorrelate the vortex shedding both in time and also along the span. The decorrelated vortex shedding results in a longer formation length of the separation bubble and higher base pressure than compared to the non-tapered (i.e. uniform) plates. This is consistent with a conclusion drawn by Gaster & Ponsford (1984). Base pressure variations were noted in the present tapered configuration with a significant reduction towards the narrow end of the plate. This reduction in base pressure towards the narrow end results in a corresponding increase in Strouhal number. This observation is consistent with Castro & Watson (2004) findings.

The three-dimensional re-circulation bubble was found to be nearly conical in shape in both the steady laminar case and the turbulent flow case.

This observation is similar to what Gaster & Ponsford (1984) reported in their high-Reynolds-number experiment. In addition it was observed that the length of the closed wake in the steady laminar case is in good agreement with non-tapered (i.e. uniform) plate data. Thus the flow field in planes perpendicular to the plate axis can be considered as quasi-two-dimensional in the steady laminar flow regime.

The present three-dimensional calculations revealed a pressure-driven spanwise secondary motion, both in the steady laminar flow regime and also in the turbulent flow regime. It was observed that in the front stagnation zone the secondary flow is going from the wide end of the plate towards the narrow end. This is in accordance with the speculations by Gaster & Ponsford (1984) in their high Reynolds number study. On the contrary, the secondary flow pattern on the rear side of the plate is rather complex. The flow in the immediate vicinity of the plate is going from the wide end towards the narrow end. This is in perfect agreement to what Gaster & Ponsford (1984) claimed. However, the direction of this secondary motion is surprisingly reversed somewhat away from the plate, so that the flow goes from the narrow end of the plate towards the wide end. The spanwise secondary motion was found to be more pronounced in the turbulent flow case than in the steady laminar case.

The present computer simulations of flow past a linearly tapered plate facilitated detailed study of three-dimensional wake flow phenomena in the laminar and low-Reynolds-number turbulent flow regime, which thereby supplement earlier experimental investigations at substantially higher Reynolds numbers. Similarities and differences between the two distinctly different cases herein and the earlier high-Re studies are pointed out. The cellular shedding observed at relatively low Re in the present study supports and complements the findings of Castro & Watson (2004) at a significantly higher Reynolds number.

Acknowledgments. The authors are grateful for the constructive comments from the anonymous reviewers and to Prof. I. P. Castro (Southampton, UK) who encouraged us to undertake this study and also provided some helpful suggestions. This work has received support from The Research Council of Norway (Programme for Supercomputing) through a grant of

computing time. The first author was the recipient of a research fellowship offered by The Research Council of Norway.

REFERENCES

Bearman, P. W. 1965 Investigation of the flow behind a two-dimensional model with a blunt trailing edge and fitted with splitter plates. *J. Fluid Mech.* **21**, 241–255.

Bearman, P. W. 1967 The effect of base bleed on the flow behind a two-dimensional model with a blunt trailing edge. *Aero. Q.* **18**, 207.

Bloor, M. S. 1964 The transition to turbulence in the wake of a circular cylinder. *J. Fluid Mech.* **19**, 290–304.

Bradshaw, P. & Perot, J. B. 1993 A note on turbulent energy dissipation in the viscous wall region. *Phys. Fluids A* **5**, 3305–3306.

Castro, I. P. & Rogers, P. 2002 Vortex shedding from tapered plates. *Exp. Fluids* **33**, 66–74.

Castro, I. P. & Watson, L. 2004 Vortex shedding from tapered, triangular plates: taper and aspect ratio effects. *Exp. Fluids* **37**, 159–167.

Dennis, S. C. R., Wang Qiang, Coutanceau, M. & Launay, J. L. 1993 Viscous flow normal to a flat plate at moderate reynolds numbers. *J. Fluid Mech.* **248**, 605–635.

Fage, A. & Johansen, F. C. 1927 On the flow of air behind an inclined flat plate of infinite span. *British Aero. Res. Coun. Rep. Memo* **1104**, 81–106.

Ferziger, J. H. & Peric, M. 1996 *Computational Methods for Fluid Dynamics*. Springer.

Gaster, M. 1969 Vortex shedding from slender cones at low reynolds numbers. *J. Fluid Mech.* **38**, 565–576.

Gaster, M. & Ponsford, P. J. 1984 The flows over tapered flat plates normal to the stream. *Aeronautical J.* **88**, 206–212.

Hudson, J. D. & Dennis, S. C. R. 1985 The flow of a viscous incompressible fluid past a normal flat plate at low and intermediate reynolds numbers: the wake. *J. Fluid Mech.* **160**, 369–383.

Iaccarino, G. & Verzicco, R. 2003 Immersed boundary technique for turbulent flow simulations. *Appl. Mech. Rev.* **56**, 331–347.

In, K. M., Choi, D. H. & Kim, M.-U. 1995 Two-dimensional viscous flow past a flat plate. *Fluid Dyn. Res.* **15**, 13–24.

Ingham, D. B., Tang, T. & Morton, B. R. 1991 Steady two-dimensional flow past a normal flat plate. *J. Appl. Math. Phys. (ZAMP)* **42**, 584–604.

Jeong, J. & Hussain, F. 1995 On the identification of a vortex. *J. Fluid Mech.* **285**, 69–94.

Julien, S., Lasheras, J. & Chomaz, J.-M. 2003 Three-dimensional instability and vorticity patterns in the wake of a flat plate. *J. Fluid Mech.* **479**, 155–189.

Julien, S., Ortiz, S. & Chomaz, J.-M. 2004 Secondary instability mechanisms in the wake of a flat plate. *European J. Mech. B/Fluids* **23(1)**, 157–165.

Koumoutsakos, P. & Shiels, D. 1996 Simulations of the viscous flow normal to an impulsively started and uniformly accelerated flat plate. *J. Fluid Mech.* **328**, 177–227.

Manhart, M. 2004 A zonal grid algorithm for dns of turbulent boundary layers. *Computers & Fluids* **33**, 435–461.

Maull, D. J. & Young, R. A. 1973 Vortex shedding from bluff bodies in a shear flow. *J. Fluid Mech.* **60**, 401–409.

Mittal, R. & Iaccarino, G. 2005 Immersed boundary methods. *Annu. Rev. Fluid Mech.* **37**, 239–261.

Moser, R. D., Rogers, M. M. & Ewing, D. W. 1998 Self-similarity of time-evolving plane wakes. *J. Fluid Mech.* **367**, 255–289.

Najjar, F. M. & Balachandar, S. 1998 Low-frequency unsteadiness in the wake of a normal flat plate. *J. Fluid Mech.* **370**, 101–147.

Najjar, F. M. & Vanka, S. P. 1995 Effects of intrinsic three-dimensionality on the drag characteristics of a normal flat plate. *Phys. Fluids* **7**, 2516–2518.

Narasimhamurthy, V. D., Andersson, H. I. & Pettersen, B. 2007 Direct numerical simulation of vortex shedding behind a linearly tapered circular cylinder. In *Proc. IUTAM Symposium on Unsteady Separated Flows and their Control*. (to be published by Springer).

Narasimhamurthy, V. D., Schwertfirm, F., Andersson, H. I. & Pettersen, B. 2006 Simulation of unsteady flow past tapered circular cylinders using an immersed boundary method. In *Proc. ECCOMAS Computational Fluid Dynamics* (ed. J. Périaux P. Wesseling, E. Oñate). TU Delft.

Parnaudeau, P., Heitz, D., Lamballais, E. & Silvestrini, J. H. 2007 Direct numerical simulations of vortex shedding behind cylinders with spanwise linear nonuniformity. *J. Turbulence* **8**, No. 13.

Peller, N., Le Duc, A., Tremblay, F. & Manhart, M. 2006 High-order stable interpolations for immersed boundary methods. *Int. J. Numer. Meth. Fluids* **52**, 1175–1193.

Piccirillo, P. S. & Van Atta, C. W. 1993 An experimental study of vortex shedding behind linearly tapered cylinders at low reynolds number. *J. Fluid Mech.* **246**, 163–195.

Roshko, A. 1954 On the development of turbulent wakes from vortex streets. *Tech. Rep.* 1191. NACA.

Thompson, M. C., Hourigan, K., Ryan, K. & Sheard, G. J. 2006 Wake transition of two-dimensional cylinders and axisymmetric bluff bodies. *J. Fluids Struct.* **22**, 793–806.

Thompson, M. C., Leweke, T. & Williamson, C. H. K. 2001 The physical mechanism of transition in bluff body wakes. *J. Fluids Struct.* **15**, 607–616.

Tremblay, F., Manhart, M. & Friedrich, R. 2001 DNS and LES of flow around a circular cylinder at a subcritical reynolds number with cartesian grids. In *LES of Complex Transitional and Turbulent Flows*, pp. 133–150. Kluwer Academic Publishers.

Vallès, B., Andersson, H. I. & Jenssen, C. B. 2002*a* Direct-mode interactions in the wake behind a stepped cylinder. *Phys. Fluids* **14**, 1548–1551.

Vallès, B., Andersson, H. I. & Jenssen, C. B. 2002*b* Oblique vortex shedding behind tapered cylinders. *J. Fluids Struct.* **16**, 453–463.

Williamson, C. H. K. 1992 The natural and forced formation of spot-like dislocations in the transition of a wake. *J. Fluid Mech.* **243**, 393–441.

Williamson, C. H. K. 1996 Vortex dynamics in the cylinder wake. *Annu. Rev. Fluid Mech.* **28**, 477–539.

Wu, S. J., Miau, J. J., Hu, C. C. & Chou, J. H. 2005 On low-frequency modulations and three-dimensionality in vortex shedding behind a normal plate. *J. Fluid Mech.* **526**, 117–146.

Yao, Y. F., Thomas, T. G., Sandham, N. D. & Williams, J. J. R. 2001 Direct numerical simulation of turbulent flow over a rectangular trailing edge. *Theoret. Comput. Fluid Dynamics* **14**, 337–358.

Article 8

Turbulent wake behind a normal flat plate

Narasimhamurthy, V. D. & Andersson, H. I.

Submitted to *International Journal of Heat and Fluid Flow*.

Turbulent wake behind a normal flat plate

Vagesh D. Narasimhamurthy[1], **Helge I. Andersson**

Fluids Engineering Division, Department of Energy and Process Engineering, Norwegian University of Science and Technology (NTNU), 7491 Trondheim, Norway

The vortex shedding in the wake behind a flat plate perpendicular to an oncoming stream have been examined. The Reynolds number Re based on the uniform inflow velocity and the width of the plate was 750. The wake flow was turbulent and direct numerical simulations have been performed to achieve a complete representation of the unsteady wake. The Strouhal number 0.1678 turned out to match that in the laminar flow regime reported by others. The impact of the base pressure on the shedding frequency and the vortex formation process was elaborated. A steady 2D mean flow and the accompanying Reynolds stress components were obtained by averaging in time and along the span. It was concluded that the kinetic energy of the wake unsteadiness was not only dissipated locally.

Key words: Uniform plate, Parallel-sided plate, DNS, Turbulence, Wake flow.

1 Introduction

Vortex shedding from bluff bodies, and particularly from two-dimensional bluff bodies, is one of the most studied research topics in fluid mechanics. Among such two-dimensional bluff bodies, the normal flat plate, i.e. a uniform flat plate placed normal to the free-stream, is the simplest configuration that can yield complex wake flow phenomena. Unlike the case of circular or elliptic cylinders, the flow past a normal flat plate is characterized by fixed separation points and the separated near-wake is known to remain symmetrical and steady in the Reynolds number range $Re = 5 - 20$ [1]. Recently, Saha [2] reported that the separated near-wake of a normal flat plate undergoes a Hopf bifurcation, i.e. transition from a steady state to an unsteady state, at a Reynolds number that lies in between 30 and 35. It is also known from the existing literature that a second transition, which renders the flow three-dimensional (and eventually turbulent) occurs already at $Re = 105 - 110$ [3].

If we now focus our attention on turbulent wakes, it is surprising to see that almost all the turbulent flow cases are either studied by experiments or by means

[1]Corresponding author. Tel.: +47 73593563; fax: +47 73593491; E-mail: vagesh@ntnu.no

CASE	Re	Flow regime	Method
Present study	750	Turbulence	3D-Numerical
Fage & Johansen [4]	1.5×10^5	Turbulence	Experiments
Mazharoğlu & Hac1şevki [5]	3.3×10^4	Turbulence	Experiments
Kiya & Matsumura [6]	2.3×10^4	Turbulence	Experiments
Wu et al. [7]	$1.8 \times 10^3 - 2.7 \times 10^4$	Turbulence	Experiments
Najjar & Vanka [8]	$100 - 1000$	Turbulence	2D-Numerical
Tamaddon-Jahromi et al. [9]	$126 - 500$	Turbulence	2D-Numerical
Najjar & Vanka [10]	1000	Turbulence	3D-Numerical
Najjar & Balachandar [11]	250	Transition	3D-Numerical
Julien et al. [12]	$200 - 220$	Transition	Experiments
Julien et al. [13]	220	Transition	2D-Numerical
Saha [2]	$30 - 175$	Laminar	2D-Numerical
Dennis et al. [1]	$5 - 20$	Laminar	Experiments

Table 1: Various studies on flow past normal flat plates.

of two-dimensional (2D) simulations (see Table 1). The only exception is the Direct Numerical Simulation (DNS) carried out by Najjar & Vanka [10] where they provided some data of the mean integral parameters such as the drag coefficient and the base pressure coefficient. Their objective, however, was limited to study and compare the drag characteristics obtained from a three-dimensional simulation with those obtained from an equally resolved 2D simulation. Even though some of the previous experimental studies [5, 6] documented the turbulence statistical quantities, they were nevertheless carried out at high Reynolds numbers. Moreover, experimental methods cannot capture the complete three-dimensional data. In contrast, the 2D numerical simulations are known to overpredict the drag and base pressure coefficients and underpredict the formation length [10, 14]. An in-depth and comprehensive study of the turbulent wake behind a normal flat plate is therefore awaited. DNS as a tool is the natural choice in the present investigation, as it gives complete access to the instantaneous three-dimensional flow field. In addition to frequency analysis and vortical structure information, a detailed analysis of Reynolds averaged statistical quantities will be presented.

2 Flow configuration and numerical method

We considered the flow past a normal flat plate with the view to explore the vortex shedding at moderately high Reynolds numbers, i.e. sufficiently high to make even the near-wake turbulent. The Reynolds number Re based on the uniform inflow velocity U_o and the width of the plate d was equal to 750. The size of the compu-

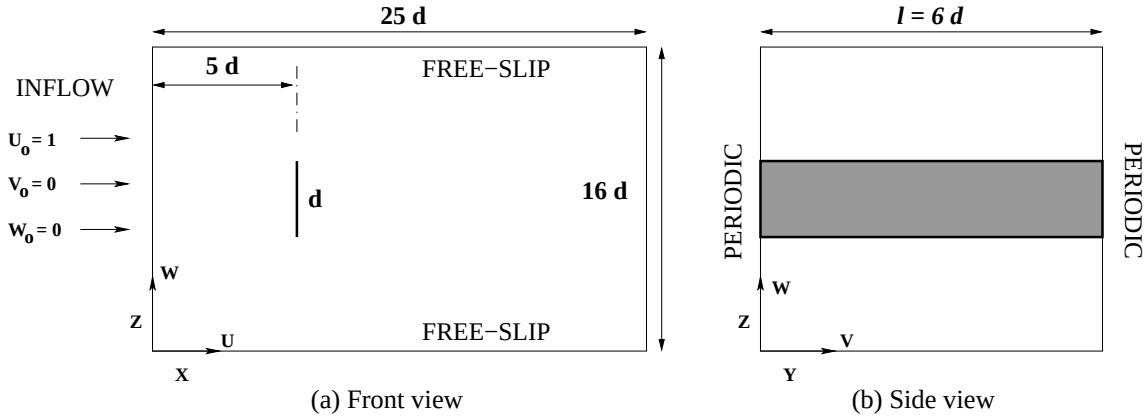

Figure 1: Computational domain (not to scale).

CASE	N_x	N_y	N_z	L_x	L_y	L_z	Re
Present DNS	512	60	384	25	6	16	750
Najjar & Vanka [10]	256	32	256	28	2π	16	1000
Najjar & Balachandar [11]	192	48	128	25	2π	16	250

Table 2: Geometrical and grid parameters.

tational domain in each coordinate direction was $L_x = 25d$, $L_y = 6d$, and $L_z = 16d$, as shown in figure 1. All spatial dimensions are normalized by d and all velocities are scaled with the uniform inflow velocity U_o. The thickness of the plate was very small and equal to $0.02d$.

The Navier-Stokes equations in *incompressible* form were solved in 3-D space and time using a *parallel* finite-volume code called MGLET [15, 16]. The code uses staggered Cartesian grid arrangements. Discretization of the spatial derivatives was achieved by means of a 2^{nd}-order central-differencing scheme. The time marching was carried out using a 3^{rd}-order explicit Runge-Kutta scheme for the momentum equations in combination with an iterative SIP (Strongly Implicit Procedure) solver for the Poisson equation. The number of grid points in each coordinate direction ($N_x \times N_y \times N_z$) is shown in Table 2 and compared with the previous DNS studies on normal flat plates [10, 11]. The time step was chosen as $\Delta t = 0.001d/U_o$ and the number of Poisson iterations per time step was limited to 60. The computations were performed on an *IBM P575+* parallel computer.

In order to justify that the present simulation is a fully resolved DNS, i.e. that all essential turbulent scales are captured, the grid size can be compared with Kolmogorov's microscale $\eta = (\nu^3/\varepsilon)^{1/4}$. Here, ε is the time-mean dissipation rate of fluctuating kinetic energy defined as

$X/d =$	**1**	**3**	**5**	**8**	**12**
Present DNS	3.48	2.69	2.19	1.87	1.65
Yao et al. [19]	6.88	5.07	3.42	2.76	2.44
Moser et al. [18]			≈ 15		

Table 3: Grid resolution $\Delta\overline{X} = \Delta X/\eta$ values at various X/d positions measured from the axis of the plate.

$$\varepsilon = \nu \left(\overline{\frac{\partial u_i}{\partial X_j}\frac{\partial u_i}{\partial X_j} + \frac{\partial u_i}{\partial X_j}\frac{\partial u_j}{\partial X_i}} \right) \approx \nu \left(\overline{\frac{\partial u_i}{\partial X_j}\frac{\partial u_i}{\partial X_j}} \right) \tag{1}$$

where u_i is the fluctuating part of the instantaneous velocity component which comprises both the unsteady fluctuations and the turbulent fluctuations. The contribution from the second term in the above definition of the total dissipation rate ε is negligible [17] and hence neglected in the present analysis. The grid size relative to the Kolmogorov microscale at five different downstream positions are given in Table 3 and compared with corresponding data for the plane wake DNS by Moser et al. [18] and the trailing-edge wake DNS of Yao et al. [19]. The data in Table 3 shows that the grid size in the present study is of the same order of magnitude as the Kolmogorov length scale. The present grid resolution compares favorably with that used in other wake flow simulations.

A uniform velocity profile $U_o = 1$ was prescribed at the inlet without any free-stream perturbations and a Neumann boundary condition was used for the pressure. A free-slip boundary condition was applied on both the top and the bottom wall and a periodic boundary condition was used for the side walls (cf. figure 1). At the outlet, a Neumann boundary condition was used for velocities and the pressure was set to zero. A *direct forcing* Immersed Boundary Method [20, 16] was used to transform the no-slip condition at the plate surface into internal boundary conditions at the nodes of the Cartesian grid. The internal boundary condition value had to be determined by interpolation. In the present DNS we used least-squares interpolation of 3^{rd}-order accuracy. The detailed derivation, validation and implementation of this technique in the code MGLET were explained in [20].

3 Results and discussion

3.1 Wake pattern and frequency analysis

In order to identify the topology of the vortex cores correctly the λ_2-definition by Jeong & Hussain [21] was used. λ_2 corresponds to the second largest eigenvalue of the symmetric tensor $S_{ij}S_{ij} + \Omega_{ij}\Omega_{ij}$, where S_{ij} and Ω_{ij} are respectively the symmetric and antisymmetric parts of the velocity gradient tensor. Iso-surfaces of negative λ_2 at time $t = 120d/U_o$ is shown in figure 2(a). Note that the shear layer extends downstream of the plate by about two plate widths before rolling-up. The top view or the spanwise view of the same flow field is shown in figure 2(b) and the corresponding iso-pressure ($P/\rho U_o^2$) contours are plotted in figure 2(c). The spanwise vortex filaments are shed parallel to the axis of the plate but experience vortex stretching and twisting. The vortices appear to be highly irregular in the near wake and rapidly break up into incoherent motion further downstream.

The time evolution of the instantaneous velocity components U, V, W and the instantaneous pressure, P, were sampled along two lines parallel to the axis of the plate and located $3d$ and $6d$ downstream the axis in X-direction, respectively. Both lines were offset by $0.5d$ in Z-direction. It would be inappropriate to present all the data here due to space constraints. Therefore, only the time trace of the cross-stream velocity W sampled at $3d$ is shown in figure 3(a). The total sampling time was equal to 120 d/U_o, which covers about 20 vortex shedding cycles. The present sampling length was found to be long enough for the results to converge to a statistically stationary state. The spatio-temporal variations of W in figure 3(a) clearly demonstrate the parallel-shedding feature of the wake. To enable quantitative comparisons the frequency spectra were obtained from the Fast Fourier Transform (FFT) of the cross-stream velocity (W) time traces. A sample spectrum is shown in figure 3(b), which is taken at the mid-span of the plate and is provided in a double-logarithmic plot. The primary shedding frequency corresponds to the most energetic frequency which is found at $fd/U_o = 0.1678$. In Table 4 the Strouhal number (fd/U_o) from the present DNS is compared with earlier studies on normal flat plates. It can be observed that the present value is in close agreement with the previous low-Re studies carried out at $Re \leq 250$ [2, 11]. In contrast, the Strouhal number from Najjar & Vanka [10] at $Re = 1000$ is in close agreement with the higher Reynolds number case [6]. The exceptionally low Strouhal number reported by Najjar & Vanka [10] is perhaps due to the shear-layer instabilities, which are known to occur at higher Reynolds numbers. Another possible reason could be the lower grid resolution used in their DNS study (cf. Table 2).

(a) $-\lambda_2$ contours (streamwise view)

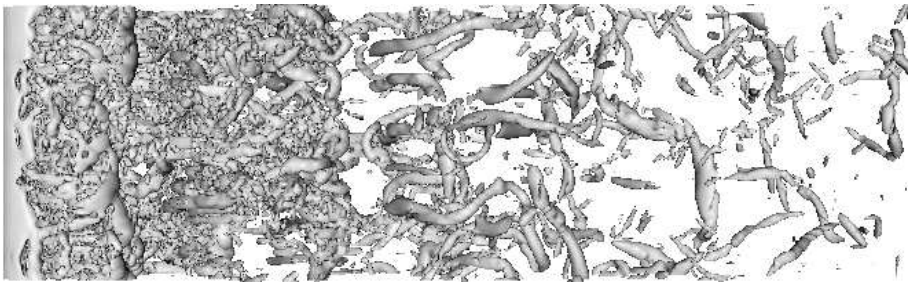

(b) $-\lambda_2$ contours (spanwise view)

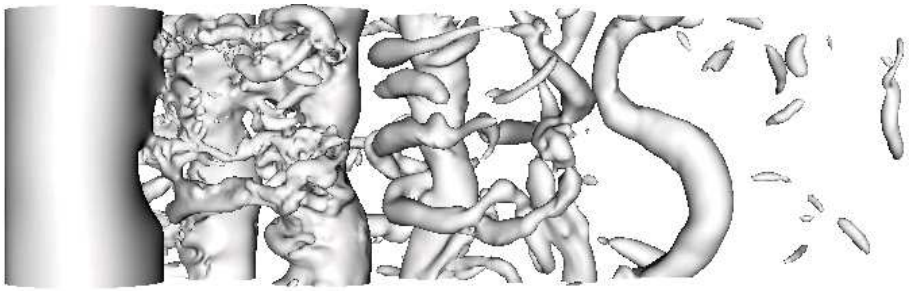

(c) Iso-pressure ($P/\rho U_o^2 = -0.1$) contours (spanwise view)

Figure 2: 3-dimensional vortical structures at the same instant in time, $t = 120\, d/U_o$. The plate is located on the left side and the flow direction is from left to right.

CASE	$\mathbf{St = fd/U_o}$	$\mathbf{L_w/d}$	**Re**
Present study	0.1678	1.96	750
Saha [2]	0.1665		150
Saha [2]	0.1640		175
Najjar & Balachandar [11]	0.1613	2.35	250
Najjar & Vanka [10]	≈ 0.1428	2.55	1000
Kiya & Matsumura [6]	0.1460		2.3×10^4

Table 4: Strouhal number (St) and formation length (L_w) data from various studies.

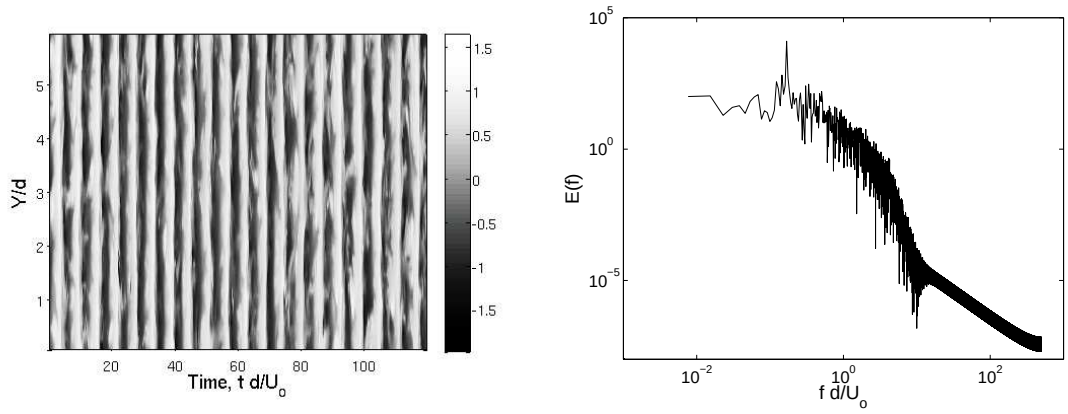

(a) (b)

Figure 3: (a) Time traces of the cross-stream velocity (W) component along the entire span. The sampling line is at $X/d = 3$ and $Z/d = -0.5$ (measured from the axis of the plate). (b) Power spectrum indicating the dominant frequency at $fd/U_o = 0.1678$.

3.2 Mean pressure coefficient and formation length

Time-averaged statistical quantities were evaluated by sampling for 120 d/U_o time units. One sample is taken every tenth time step for averaging. The three-dimensional data is then averaged in the spanwise $Y-$direction, i.e. in the direction of homogeneity. The mean pressure coefficient is defined as, $\overline{C}_p = 2(\overline{P} - P_\infty)/(\rho U_o^2)$, where the reference pressure P_∞ is taken from the pressure at the inflow and the overbar signifies averaging in time and spanwise direction. The distribution of $\overline{C}_p$ on the surface of the plate from the present DNS is compared against the earlier experimental [4] and numerical [10, 11] data in figure 4. The pressure on the upstream surface of the plate compares well with the previous data. The constancy of the pressure in the base region is well captured in the present DNS. However, the pressure in the base region is relatively lower compared to the prediction of Najjar & Vanka [10] but is in good agreement with the low-Reynolds number case of Najjar & Balachandar [11]. This could again be a pure Reynolds number effect as discussed in the previous section or perhaps due to the modest grid resolution used in Najjar & Vanka [10].

The coupling suggested by Bearman [22, 23] and others between the base pressure and the vortex formation process can be explored in the present study. If we compare the base pressure values in figure 4 with the corresponding Strouhal numbers in Table 4, it is apparent that the reduction in base pressure causes an increase in St, i.e. gives rise to a stronger vortex shedding. A very strong and periodic vortex shedding eventually produces shorter formation lengths. It can be observed from Table 4 that the formation length L_w decreases with an increase in St and vice versa.

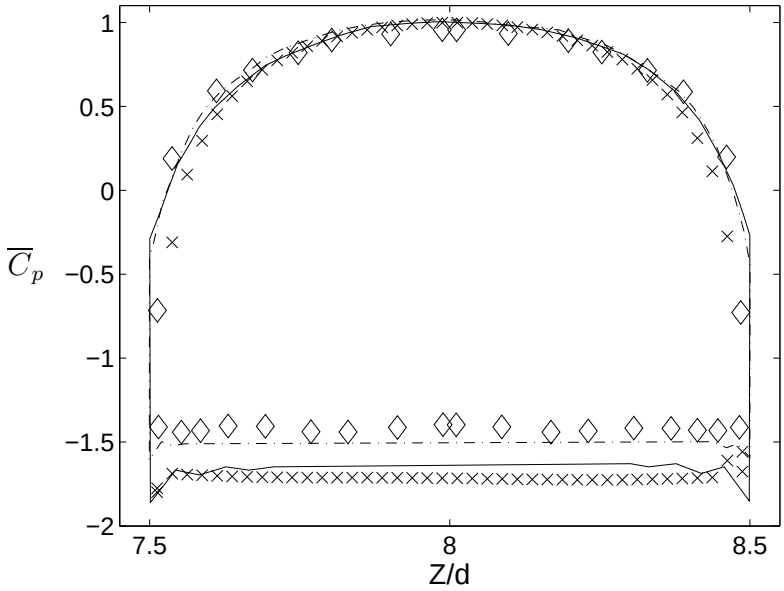

Figure 4: Distribution of the mean pressure coefficient, $\overline{C}_p$, on the surface of the plate from the present DNS: $\times, Re = 750$; compared with the experimental data of Fage & Johansen [4]: $\diamond, Re = 1.5 \times 10^5$; and the DNS results of Najjar & Vanka [10]: $-.-, Re = 1000$; Najjar & Balachandar [11]: $-, Re = 250$.

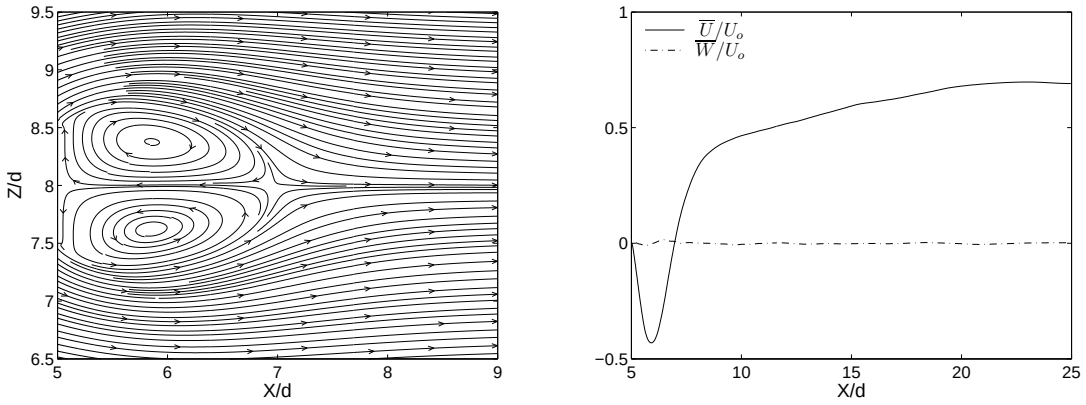

(a) (b)

Figure 5: (a) Streamlines showing the mean recirculation bubble. (b) Time-mean velocity profiles along the wake centerline.

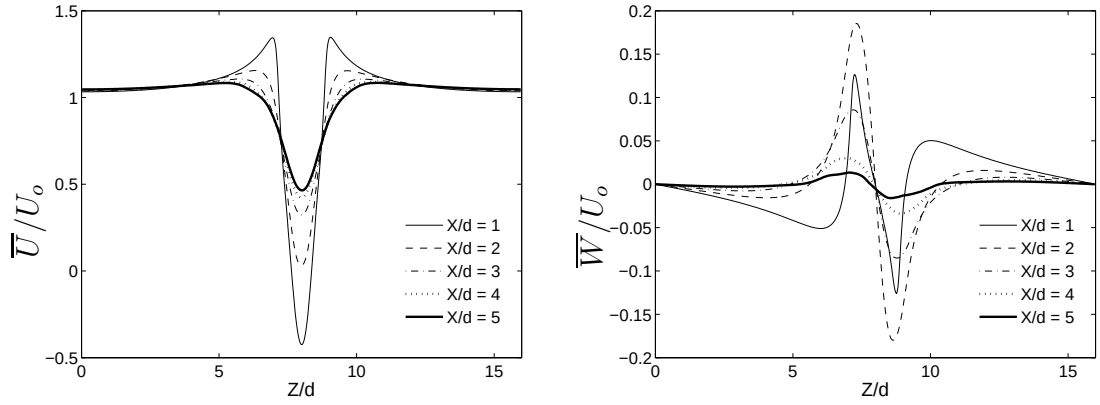

(a) Mean streamwise velocity ($\overline{U}/U_o$) (b) Mean cross-stream velocity ($\overline{W}/U_o$)

Figure 6: Mean velocity profiles at fixed X/d positions (measured from the axis of the plate).

Thereby, the coupling between the wake formation length L_w and the base pressure is explained. In the present context the formation length L_w, i.e. the length of the mean recirculation bubble (see figure 5(a)), is defined as the streamwise distance from the axis of the plate to the position where the mean streamwise velocity $\overline{U}$ changes sign from negative to positive (see figure 5(b)).

3.3 Reynolds-averaged statistics

It is important to quantify the growth and decay of different properties of the fluctuating motion, especially in the near wake region where the similarity laws are not valid. Therefore in the present section Reynolds-averaged statistical quantities at some sections downstream the plate will be presented and the underlying physics will be discussed. It can be observed from figure 5(b) that the mean cross-stream velocity $\overline{W}$ is zero along the wake centerline. Note that the wake centerline is subjected to an equally weighted influence of both the alternating vortices shed from either side of the plate. The observation that $\overline{W} \approx 0$ along the wake centerline reconfirms that the present statistics are fully converged to a stationary state. The variation of the mean streamwise velocity $\overline{U}$ in the near wake at five different positions downstream the plate is shown in figure 6(a). The negative velocity at the location $X/d = 1$ stems from the recirculation zone. Along the wake centerline at $X/d = 2$, $\overline{U}$ is nearly zero since this position is very close to the re-attachment point. The mean cross-stream velocity ($\overline{W}$) profiles are shown in figure 6(b). The anti-symmetric variation of $\overline{W}$ is consistent with the symmetry of $\overline{U}$.

Reynolds stresses $\overline{u^2}$, $\overline{v^2}$, $\overline{w^2}$ and $\overline{uw}$ are plotted in figures 7(a), 7(b), 7(c) and 7(d),

respectively. Note that due to the Reynolds-averaging, the stress components have contributions from both the unsteady fluctuations and the turbulent fluctuations. A bi-modal $\overline{u^2}$ profile can be observed in all the curves in figure 7(a). The highest level of streamwise velocity fluctuations occurs in the shear layers shed from the plate and hence the two peaks in figure 7(a) are offset from the wake centerline. A similar bi-modal trend can also be seen in the spanwise normal stress ($\overline{v^2}$) profiles (see figure 7(b)). The origin of this bi-modal trend can again be traced to the shear layer, which constitutes regions of concentrated secondary flow structures, popularly termed as "braid regions". The magnitude of $\overline{v^2}$, however, is substantially smaller than $\overline{u^2}$. In contrast, the maximum values of the $\overline{w^2}$ stress component appear along the wake centerline (see figure 7(c)). This is because the flow at the wake centerline is subjected to an equally weighted influence of both the alternating vortices shed from either side of the plate. The transverse velocity fluctuations are more energetic than the streamwise velocity fluctuations, hence the magnitude of the $\overline{w^2}$ stress component is much larger than the $\overline{u^2}$ stress component. The peak amplitudes of the shear stress $\overline{uw}$ in figure 7(d) indicate the position where the two fluctuating components are in phase.

The variation of the mean fluctuating kinetic energy, $k = (\overline{u^2}+\overline{v^2}+\overline{w^2})/2$, is shown in figure 8(a). From $X/d = 2$ and further downstream, the highest energy level is observed along the wake centerline and the actual peak level decays monotonically with X. This is because the transverse velocity fluctuations are more energetic than the streamwise velocity fluctuations in those regions and therefore $\overline{w^2}$ represents the major contribution to k. Close to the plate, however, the highest energy levels are offset from the wake centerline since $\overline{w^2}$ is roughly comparable to $\overline{u^2}$ in those regions. It can thus be concluded that the bi-modal $k-$profile at this location ($X/d = 1$) stems from the streamwise velocity fluctuations. The contribution of each normal stress component to the fluctuating kinetic energy along the wake centerline can be explored in figure 8(b). The magnitude of $\overline{u^2}$ and $\overline{v^2}$ are comparable along the wake centerline, while the magnitude of $\overline{w^2}$ is several times larger than $\overline{u^2}$ and $\overline{v^2}$ and hence represents the major contribution to k. The normalized dissipation rate of the fluctuating kinetic energy ($\varepsilon\ \nu/U_o^4$) is plotted in figure 9. The bi-modal pattern clearly indicates that the maximum dissipation levels are offset from the wake centerline and are occurring in the shear layers. It is interesting to observe that the spatial variation of ε does not match the distribution of k. This implies that the kinetic energy is only partially dissipated locally.

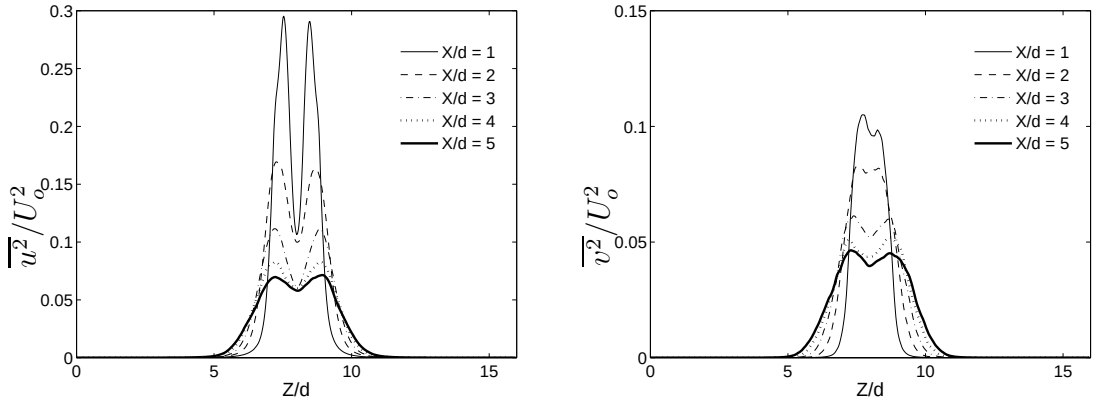

(a) Reynolds normal stress, $\overline{u^2}$

(b) Reynolds normal stress, $\overline{v^2}$

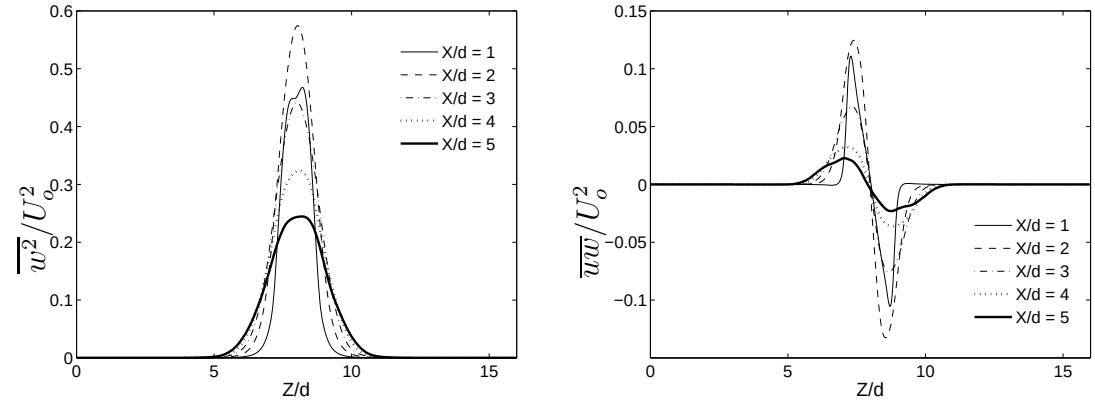

(c) Reynolds normal stress, $\overline{w^2}$

(d) Reynolds shear stress, $\overline{uw}$

Figure 7: Reynolds stress profiles at fixed X/d positions (measured from the axis of the plate).

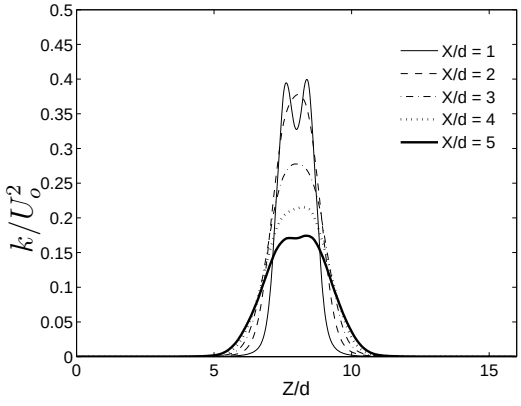

(a)

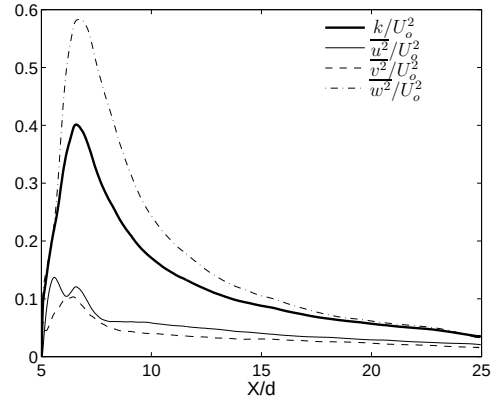

(b)

Figure 8: (a) Mean fluctuating kinetic energy (k/U_o^2) profiles at fixed X/d positions (measured from the axis of the plate). (b) Mean fluctuating kinetic energy and Reynolds stress distribution along the wake centerline.

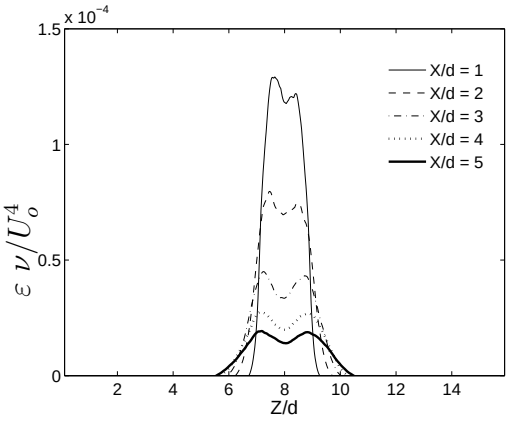

Figure 9: Dissipation rate of fluctuating kinetic energy ($\varepsilon\ \nu/U_o^4$) at fixed X/d positions (measured from the axis of the plate).

4 Conclusions

The parallel-shedding characteristics of the wake behind a normal flat plate was well captured in the present DNS study. Both flow visualizations and spectral analysis together confirm this feature. The Strouhal number in the present turbulent flow case was found to be in excellent agreement with the previous studies on normal flat plates carried out at low Reynolds numbers [2, 11]. In contrast the Strouhal number predicted by Najjar & Vanka [10] was found to be significantly lower. In addition, the predicted base pressure in Najjar & Vanka [10] was relatively higher than in the present case. The reason for this discrepancy was suggested to be due to the different Reynolds numbers used in the present study and in Najjar & Vanka [10]. Another possible reason could be the coarse grid resolution adopted by Najjar & Vanka [10]. The coupling between the base pressure and the vortex formation process was explored in the present study. It was observed that the reduction in base pressure causes a surge in the shedding frequency and hence produces a shorter recirculation bubble. A detailed analysis of the Reynolds-averaged statistical quantities were presented. It was noticed that the transverse velocity fluctuations were more energetic than the streamwise and spanwise velocity fluctuations and hence represented the major contribution to the fluctuating kinetic energy.

Acknowledgments

This work has received support from The Research Council of Norway (Programme for Supercomputing) through a grant of computing time. The first author was the recipient of a research fellowship offered by The Research Council of Norway.

References

[1] Dennis, S. C. R., Wang Qiang, Coutanceau, M. and Launay, J.-L., 1993. Viscous flow normal to a flat plate at moderate reynolds numbers. *J. Fluid Mech.* **248**, 605-635.

[2] Saha, A.K., 2007. Far-wake characteristics of two-dimensional flow past a normal flat plate. *Phys. Fluids* **19**, 128110.

[3] Thompson, M.C., Hourigan, K., Ryan, K. and Sheard, G.J., 2006. Wake transition of two-dimensional cylinders and axisymmetric bluff bodies. *J. Fluids Struct.* **22**, 793-806.

[4] Fage, A. and Johansen, F. C., 1927. On the flow of air behind an inclined flat plate of infinite span. *British Aero. Res. Coun. Rep. Memo* **1104**, 81-106.

[5] Mazharoğlu, Ç. and Hac1şevki, H., 1999. Coherent and incoherent flow structures behind a normal flat plate. *Exp. Thermal Fluid Sci.* **19**, 160-167.

[6] Kiya, M. and Matsumura, M., 1988. Incoherent turbulence structure in the near wake of a normal plate. *J. Fluid Mech.* **190**, 343-356.

[7] Wu, S.J., Miau, J.J., Hu, C.C. and Chou, J.H., 2005. On low-frequency modulations and three-dimensionality in vortex shedding behind a normal plate. *J. Fluid Mech.* **526**, 117-146.

[8] Najjar, F.M. and Vanka, S.P., 1995. Simulations of the unsteady separated flow past a normal flat plate. *Int. J. Numer. Meth. Fluids* **21**, 525-547.

[9] Tamaddon-Jahromi, H.R., Townsend, P. and Webster, M.F., 1994. Unsteady viscous flow past a flat plate orthogonal to the flow. *Computers & Fluids* **23**, 433-446.

[10] Najjar, F.M. and Vanka, S.P., 1995. Effects of intrinsic three-dimensionality on the drag characteristics of a normal flat plate. *Phys. Fluids* **7**, 2516-2518.

[11] Najjar, F.M. and Balachandar, S., 1998. Low-frequency unsteadiness in the wake of a normal flat plate. *J. Fluid Mech.* **370**, 101-147.

[12] Julien, S., Lasheras, J. and Chomaz, J.-M., 2003. Three-dimensional instability and vorticity patterns in the wake of a flat plate. *J. Fluid Mech.* **479**, 155-189.

[13] Julien, S., Ortiz, S. and Chomaz, J.-M., 2004. Secondary instability mechanisms in the wake of a flat plate. *European J. Mech. B/Fluids* **23**, 157-165.

[14] Mittal, R. and Balachandar, S., 1995. Effect of three-dimensionality on the lift and drag of nominally two-dimensional cylinders. *Phys. Fluids* **7**, 1841-1865.

[15] Manhart M., 2004. A zonal grid algorithm for DNS of turbulent boundary layers. *Computers & Fluids*. **33**, 435-461.

[16] Narasimhamurthy, V. D., Schwertfirm, F., Andersson, H. I. and Pettersen, B., 2006. Simulation of unsteady flow past tapered circular cylinders using an immersed boundary method. In: *Proc. ECCOMAS Computational Fluid Dynamics*, Eds. P. Wesseling, E. Oñate, J. Périaux, Publisher TU Delft, The Netherlands, Egmond aan Zee.

[17] Bradshaw, P. and Perot, J.B., 1993. A note on turbulent energy dissipation in the viscous wall region. *Phys. Fluids A* **5**, 3305-3306.

[18] Moser, R.D., Rogers, M.M. and Ewing, D.W., 1998. Self-similarity of time-evolving plane wakes. *J. Fluid Mech.* **367**, 255-289.

[19] Yao, Y.F., Thomas, T.G., Sandham, N.D. and Williams, J. J.R., 2001. Direct numerical simulation of turbulent flow over a rectangular trailing edge. *Theoret. Comput. Fluid Dynamics* **14**, 337-358.

[20] Peller, N., Le Duc, A., Tremblay F. and Manhart M., 2006. High-order stable interpolations for immersed boundary methods. *Int. J. Numer. Meth. Fluids.* **52**, 1175-1193.

[21] Jeong, J. and Hussain, F., 1995. On the identification of a vortex. *J. Fluid Mech.* **285**, 69-94.

[22] Bearman, P.W., 1965. Investigation of the flow behind a two-dimensional model with a blunt trailing edge and fitted with splitter plates. *J. Fluid Mech.* **21**, 241-255.

[23] Bearman, P.W., 1967. The effect of base bleed on the flow behind a two-dimensional model with a blunt trailing edge. *Aero. Q.* **18**, 207.

Article 9

Cellular vortex shedding in the wake of a tapered plate at low Reynolds numbers

Khaledi, H. A., Narasimhamurthy, V. D., & Andersson, H. I.

Submitted to *Physics of Fluids*.

Cellular vortex shedding in the wake of a tapered plate at low Reynolds number

Hatef A.Khaledi, Vagesh D.Narasimhamurthy, Helge I.Andersson

Department of Energy and Process Engineering, Norwegian University of Science and Technology, 7491 Trondheim, Norway

Abstract:

The unsteady near-wake behind a linearly tapered plate has been investigated numerically. The tapering made the Reynolds number based on the inflow velocity and the local width of the plate vary from 25 to 100. The wake flow comprised three different flow regimes co-existing side-by-side. The wake flow was steady behind the narrow end of the plate. Periodic vortex shedding occurred downstream from where the local Reynolds number exceeded 32. Vortex dislocations enabled a cellular shedding pattern with shedding frequency decreasing towards the wide end of the plate. The regular oblique vortex shedding near mid-span was subjected to three-dimensional scrambling towards the wide end of the plate which gave rise to streamwise-oriented vortex structures. The Strouhal number was distinctly lower than in the wake of a uniform plate whereas the base pressure coefficient was substantially higher.

Key words: taper plate, oblique vortex shedding, unsteady laminar flow, wake phenomenon

1. Introduction

Wakes of bluff bodies and their vortex structure have been broadly investigated because of their practical importance with respect to integral quantities such as drag and lift forces. The flow structure around bluff bodies like plates, circular cylinders, toruses and so on have been pondered more frequently due to their geometrical simplicity. Among all, the flat plate has

been the center of attention, either numerically or experimentally, to explore the physics of the flow and its fundamental aspect of wake instabilities and transition.

The secondary instability has been dubbed the main argument for occurrence of three dimensionalities. This phenomenon happens intrinsically for wakes of two dimensional bluff body structures at a critical Reynolds number which effectuates momentous spanwise variations in the flow field [Williamson (1996), Najjar & Vanka (1995a)]. Furthermore, these three dimensionalities can arise extrinsically by introducing an asymmetry or tapering in bluff body geometry [Gaster (1969) Piccirillo & Van Atta (1993), Narasimhamurthy et al. (2008)] or by manipulation of the boundary conditions [Maull & Young (1973), Parnaudeau et al. (2007)]. The inherent three-dimensionality extrinsically was considered firstly by Gaster (1969) in study of vortex shedding behind a very slender cone. He conceived that the fluctuating velocity in the wake is not singly periodic in time but rather exhibits two different frequencies with one an order of magnitude lower than the other. It was revealed that this modulation frequency was a constant all along the span. However, he in another heuristic study [Gaster (1971)] divulged a "cellular structure" of vortex shedding behind a mild tapered cylinder in a low Reynolds number flow. Cellular vortex shedding structure corresponds to cells of different frequency coexisting along the span. In case of a tapered geometry where the diameter changes linearly, the observation of cellular vortex structures eventuates to "oblique" vortex shedding. Nonetheless several investigations have reported that cellular vortex structure is not the only stimulation of onset of oblique shedding and the particular boundary conditions at the spanwise end may lead to angulation of vortex structure [Williamson (1989), Gerich & Eckelmann (1982)]. It is very conceivable in the case of different coexisting cells that vortices move out of phase with each other in the boundary of each cell and spanwise vortex filaments split apart. Although vortex dislocations were first

introduced as a main feature of three dimensional transition of wake, this phenomenon has been reportedly observed, even more coherently, in the laminar regime.

Ensuing the observation of vortex dislocation and cellular pattern in the wake of cones, Gaster & Ponsford (1984) settled up a new experiment for flow over a tapered plate at Reynolds numbers of order of 10^4. They provided limited data for the taper ratio of 8<TR<240 ($TR = l/(d_2 - d_1)$ where l is the length of plate and d_2 and d_1 are widths at wide and narrow end, respectively). In spite of the fact that they found an evidential base pressure gradient along the span which induced a spanwise secondary flow, they failed to detect any cellular vortex structure for any range of taper ratio. This in fact was in contrast with the preceding investigation of Maull & Young (1973) who beheld the cellular vortex structure of incoming shear flow behind a parallel-sided plate. This contradiction stimulated Castro & Rogers (2002) and Castro & Watson (2004) to canvass in extensive experimental data of the wake of tapered and triangular plates with different taper ratios and different boundary conditions. However they kept the Reynolds number at an order of 10^4 and they observed cells of constant shedding frequency throughout the taper ratio range of 20<TR<60. Very recently Narasimhamurthy et al (2008) performed a direct numerical simulation of turbulent flow around a tapered plate with 250<Re<1000. The wake exhibited a cellular vortex structure once again.

The parallel-sided plate, placed perpendicular to the flow, has been the eye-catcher case for several experimentalists during decades. Almost all the experiments have been carried out in the turbulent regime. Fage & Johansen (1927) measured the pressure downstream and upstream of the flat plate at various angles of attack for a Reynolds number 1.5×10^5. Hotwire anemometry was recruited by Perry & Steiner (1987) to study the flow past a flat and inclined plate at Reynolds number 2×10^4. Castro and Jones (1987) performed a 2-D simulation of steady state flow at 100<Re<800, the steady state assumption overpredicted the wake length

though. Joshi (1993) performed 2D and 3D numerical simulations using second-order accurate finite-volume time-splitting scheme at Reynolds number varying from 40 to 1000. Najjar and Vanka (1995b) carried through a 2D unsteady simulation with high-order accurate scheme in the Reynolds number range of 80-1000 and apperceived parallel shedding below Re=250. Nonetheless at higher Reynolds numbers complex interactions such as vortex paring and tearing were observed in the far-wake region. More recently Najjar (1994) conducted 3D simulations to resolve the overprediction of the drag coefficient due to inherent three-dimensionality of flows above Re = 200.

Compared to the number of experimental surveys, relatively few numerical studies have been performed for flows past a tapered or flat plate. Though capturing the whole range of small scales down to the Kolmogorov microscale seems computationally unattainable at very high Reynolds number turbulent flows, direct numerical simulation is an effectual tool to study the complex nature of the phenomenon in comparably lower Reynolds number turbulent or unsteady laminar regimes. The present study has been devoted to investigate the presumably complex structure of the vortex shedding behind the tapered plate in Reynolds number range of 25 to 100. Besides pondering on the intricate structure of cellular vortex shedding behind the tapered plate, simulation of the flow around a parallel-sided plate at Reynolds number 62.5 (based on $d_m = (d_1+d_2)/2$) was performed for comparative purposes.

This paper is organized as follows. In section 2 the flow configuration and computational approach is outlined. The results of simulation are discussed in section 3 and concluding remarks are summarized at the end.

2. Flow field and computational approach

The flow past a tapered plate is considered. The computational domain is shown in Figure 1. Unless otherwise explicitly mentioned, all spatial dimensions are non-dimensionalized by d_2 and velocities are normalized with the uniform inflow velocity U_0. The mean width of the

plate is $d_m = 0.625$ and the thickness of the plate is only $0.02d_2$. The aspect ratio ($AR = l/d_m$) is 24 and taper ratio (TR) equals 20. The Reynolds numbers at the wide and narrow end of the plate are 100 and 25, respectively. Table 1 gives an overview of the boundary conditions. A uniform velocity profile $U_0 = 1$ has been prescribed as inlet boundary condition. A Neumann boundary condition is recruited for pressure at the inflow. A free-slip boundary condition was applied at side walls, top wall and bottom wall. The choice of slip condition averts end effects. At the outlet, the Neumann and Dirichlet boundary conditions were set for velocities and pressure, respectively.

For comparative purpose the flow over a parallel-sided plate with width equal to the mean width d_m of the tapered plate has also been simulated. Periodic boundary conditions were recruited at each spanwise end of the plate. Moreover, the spanwise length of the plate was reduced to 6 and the cross-stream height of the domain increased to 16; see also Table 2.

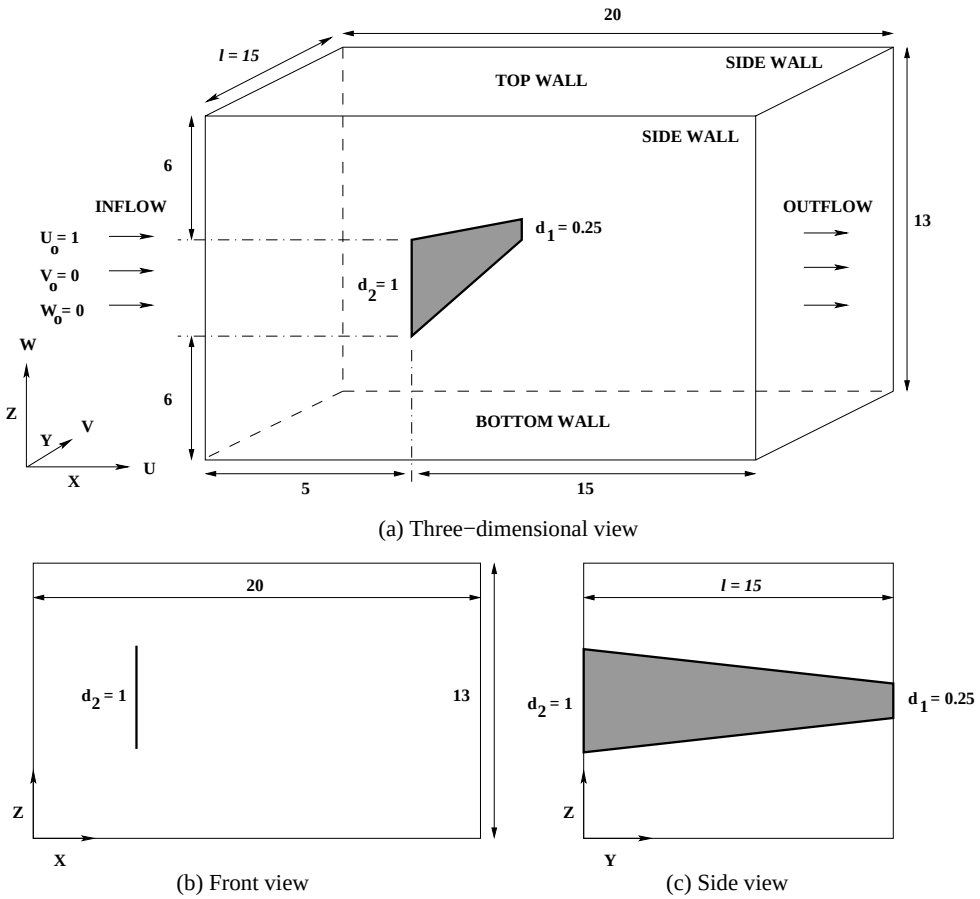

Figure 1 Flow domain and coordinate system. All length are scaled with d_2

The simulation has been carried out with the well-documented finite-volume solver MGLET [Manhart (2004)]. The three-dimensional Navier-Stokes equations for an incompressible fluid are approximated on a staggered Cartesian grid system. A 3rd-order explicit Runge-Kutta scheme in time and a 2nd-order accurate central-differencing scheme in combination with an iterative SIP (Strongly Implicit Procedure) for solving the Poisson equation are employed.

The time step $\Delta t = 0.003 d_2 / U_0$ and number of Poisson iterations per time step was limited to 30. To accommodate the tapered plate in the Cartesian mesh, a direct forcing immersed boundary method (IBM) is used. A review of different IBM schemes is provided by Mittal and Iaccarino (2005). A full description of direct forcing method which is implemented in MGLET can be found in the article by Peller et al. (2006).

Face	Boundary Condition
Inflow	$U_0 = 1\,;\ V_0 = W_0 = 0\,;\ \partial P/\partial x = 0$
Side walls	$V = 0\,;\ \partial U/\partial Y = \partial W/\partial Y = \partial P/\partial Y = 0$
Top & Bottom wall	$W = 0\,;\ \partial U/\partial Z = \partial V/\partial Z = \partial P/\partial Z = 0$
Outflow	$P = 0\,;\ \partial U/\partial X = \partial V/\partial X = \partial W/\partial X = 0$

Table 1 Boundary conditions

In order to be assured of obtaining a grid independent solution, two different grid resolutions were utilized. The number of grid points in each grid for the tapered plate case and also the parallel-sided plate is shown in Table 2. Note has to be taken that the grid refinement is in spanwise direction and in the near body wake. All discussed results in section 3 are taken from grid B which is fine enough to present a grid independent solution for such a laminar case. The grid independency analysis is brought in section 3.1.

		Dimension $L_x \times L_y \times L_z$	Grid Points $N_x \times N_y \times N_z$	AR	TR	Re_1	Re_2
Tapered	**A**	20×15×13	224×125×150	24	20	25	100
Plate	**B**	20×15×13	254×154×184	24	20	25	100
Parallel sided plate		20×6×16	192×60×192	9.6	∞	62.5	62.5

Table 2: Geometrical and computational parameters

3. Results and discussions

3.1. Frequency analysis and wake pattern

The instantaneous velocity components U, V, W, and also the instantaneous pressure, p, were sampled along two lines parallel to the axis of the plate which were located 4 d_m and 7 d_m

downstream of the plate axis in the x-direction. In addition the lines were offset $1d_m$ in the z-direction from the (x-y) - plane through the axis of the plate. The total sampling time was $360\,d_2/U_0$. It attributes to 120,000 samples which encompass nearly 55 shedding cycles at wide end of the plate.

The time trace of the instantaneous cross-stream velocity (W) along the first sampling line is shown in Figure 2. The aslant pattern of time traces is clearly demonstrating the oblique-like vortex shedding along the span. Moreover the vortex splitting or vortex dislocation is intelligibly notable along the span. Some of these dislocations are marked in the figure by circles. The picture also envisions the periodic occurrence of vortex dislocation at certain spanwise locations. This regularity is probably an intrinsic feature of laminar vortex shedding. This in fact is in contrast to the observation of Narasimhamurthy et al. (2008) who discovered the random and chaotic occurrence of dislocations and vortex splitting in the turbulent flow regime with respect to time and spanwise direction.

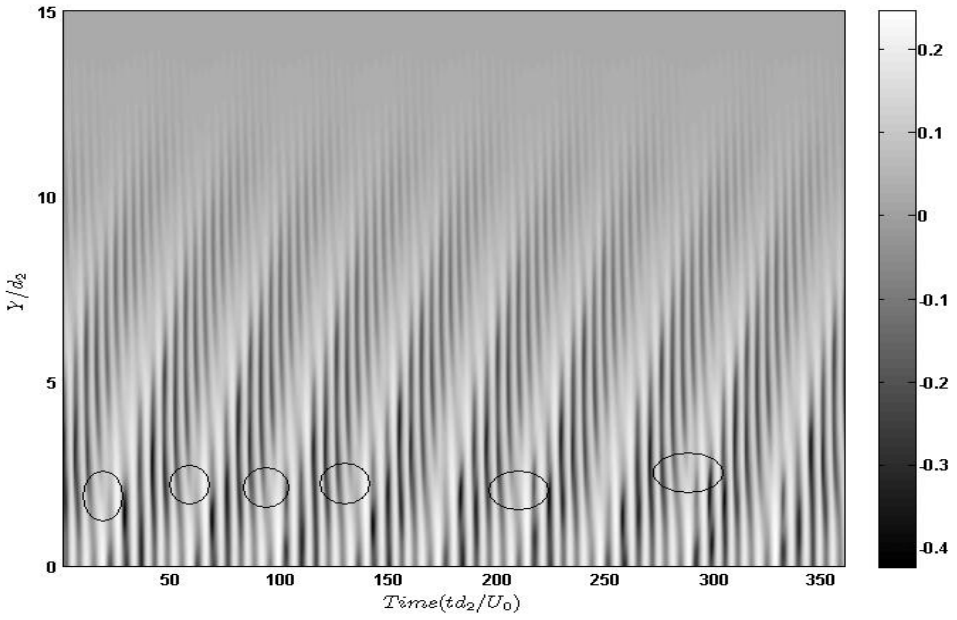

Figure 2 : Time evolution of cross-stream velocity (W) along the span. The sampling line is located at $x=4d_m$ and $z=-1\ d_m$ from the axis of the plate. Some vortex dislocations are encircled.

Time traces of some signals at different local Reynolds numbers are shown in Figure 3. The low frequency, low amplitude signals that are apparent in between the high frequency flapping signals can be attributed to the presence of large-scale spot-like vortex dislocations that was first observed by Williamson (1992) in the wake of the uniform circular cylinder. For instance in Figure 3 the time record for Reynolds number 90 reveals a very apparent low-frequency signature. The period of the low-frequency modulation for Re=90 is about $35d_2/U_0$ which is fully consistent with the separation between the circles (at about $y/d_2 \approx 2$) in Figure 2. This is in fact a strong endorsement to the claim that these low-frequency irregularities attribute to the vortex splitting phenomenon. However this is not always the case. Najjar & Vanka (1995a) conjectured that these low frequency signals are due to oscillations of the shear layer itself. Several other interpretations of this low frequency modulation can be found in Najjar & Balachandar (1998) and Wu et al. (2005).

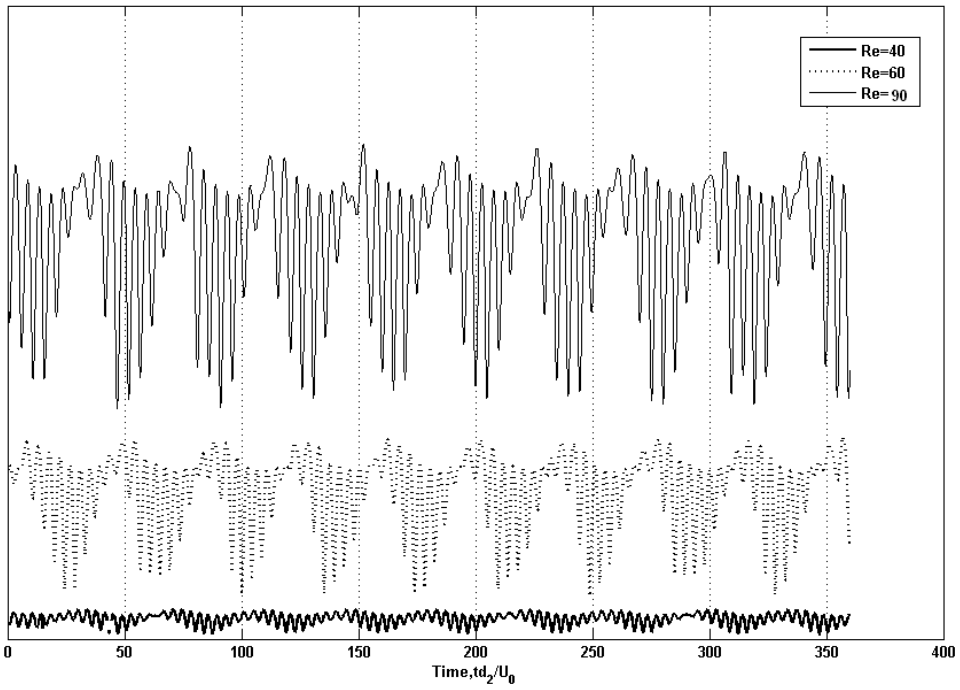

Figure 3 : Time trace of cross-stream velocity (W) at three different local Reynolds numbers, i.e. at different spanwise locations

Figure 4 shows one-dimensional energy spectrums for the parallel-sided plate and the tapered plate. By taking advantage of the Fourier transform of the cross-stream velocity (W), the spectral estimator for a finite length of time record is:

$$E(f) = \frac{\hat{W} \times \hat{W}^*}{T} \tag{1}$$

In equation (1) the superscript * denotes the conjugate of Fourier transformed velocity of W. In the parallel-sided plate the most dominant frequency which is associated with the primary vortex shedding is found at $St \equiv fd/U_0 = 0.1704$. The two-dimensional calculation of Joshi (1993) gave the Strouhal number 0.175 for Re=100. Tamaddon-Jahromi et al (1994) obtained the Strouhal number 0.173 at Re=126 and Najjar & Vanka (1995b) reached the value of 0.166 at Re=100 in their computation. On the right side of Figure 4 where the spectrum for the tapered plate at $\mathrm{Re}_{\mathrm{local}}$=62.5 ($\mathrm{Re}_{local} = Ud_{local}/\upsilon$) is depicted, the most dominant frequency is $fd_2/U_0 = 0.2263$. This corresponds to a local Strouhal number ($St_{local} = fd_{local}/U_0$) of 0.1414, which is distinctly lower than the Strouhal number obtained fro the parallel-sided plate; see Table 3.

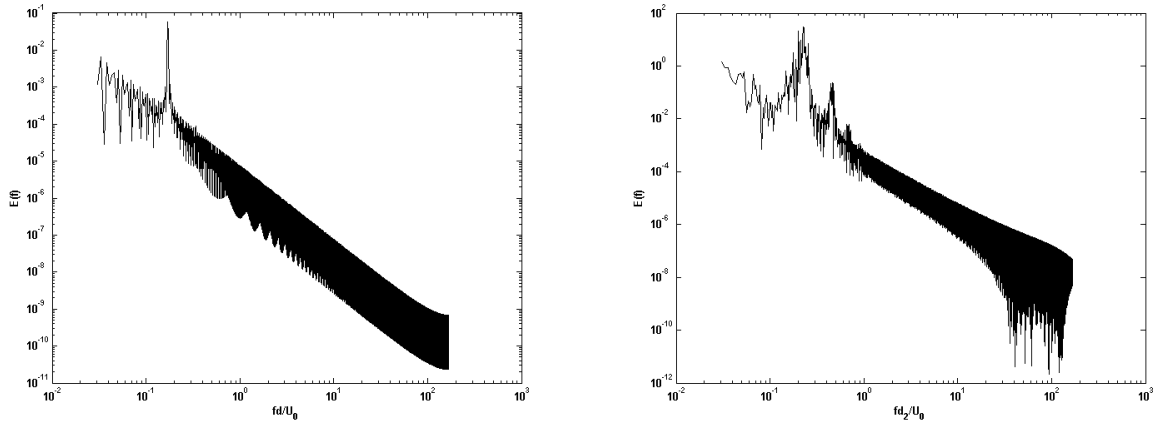

(a) (b)

Figure 4 : One dimensional energy spectrum, (a): parallel-sided plate (Re=62.5), (b): tapered plate at local Re=62.5; i.e. at mid-section.

	Reynolds Number	Strouhal Number
Tapered Plate, Current simulation	62.5	0.1414
Parallel sided Plate, Current simulation	62.5	0.1704
Parallel sided Plate, Joshi (1993)	100	0.175
Parallel sided Plate, Tamaddon –Jahromi et al. (1994)	126	0.173
Parallel sided Plate, Najjar & Vanka (1995b)	100	0.166

Table 3 : Comparison of Strouhal numbers cited in different literatures

The spanwise variation of the frequency spectra of cross-stream velocity (W) is shown in Figure 5(a). Different dominant shedding frequencies are observed along the span and reflect the cellular pattern of vortex structure. This has been shown more distinctly in Figure 5(b) where the local Strouhal number along the span of the tapered plate is pictured. It should be noted that the Strouhal number does not vary continuously but rather in discrete linear parts which mimic constant shedding frequency cells. This fact can be more easily seen in Figure 5(c). The spectral analysis shows that no regular vortex shedding occurs at the narrow end of the tapered plate where $\mathrm{Re}_{local} \leq 32$, whereas distinct cellular shedding takes place along the remainder of the plate.

Besides the discrete pattern of Strouhal number revealed in Figure 5(b), the grid independency has also been investigated. For this purpose two different grids are compared. The overall matching of Strouhal number as shown in Figure 5(b) along the span is convincing. Nonetheless all presented results in this paper are extracted from the simulation on the finest grid B. In the same figure it is proved that the sampling time is sufficient. The agreement between the result of 80000 and 120000 samples is clear.

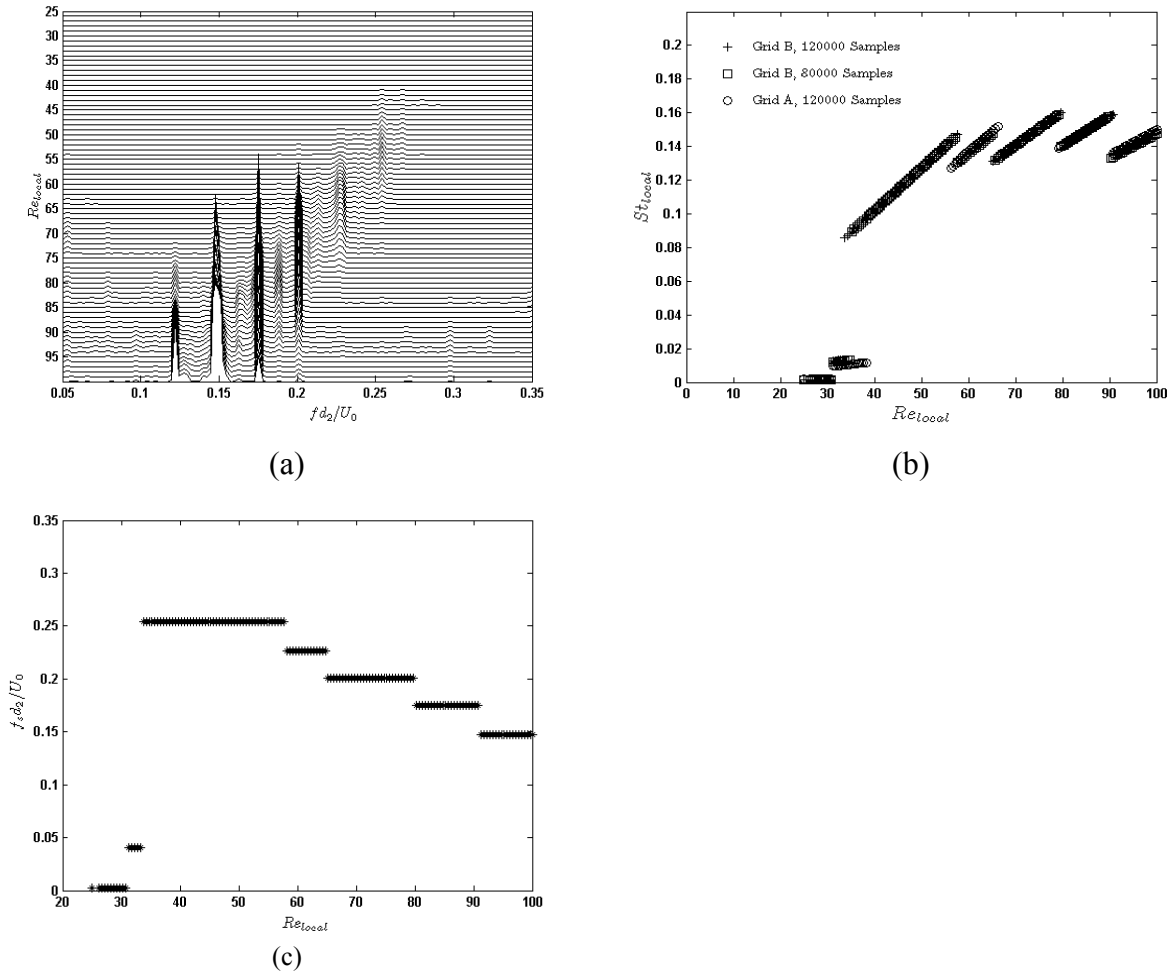

Figure 5 : (a) Spanwise variation of frequency spectra of cross-stream velocity, (b) The spanwise distribution of local Strouhal number corresponding to the maxima of spectra in three different cases, (c) Shedding frequency versus local Reynolds number. Results from different grids (see Table 2) and different sampling times are compared in (b).

The onset of vortex shedding as it can be seen in Figure 5(b) occurs somewhere around Re_{local}=32 where very a shedding frequency below 0.05 is detectable in Figure 5(c). This fact can also be verified by observing the occurrence of asymmetry in the wake of the tapered plate at Re_{local}=32 at Figure 6(b). The more periodic and frequent shedding of vortices at Re_{local}=35 shown in Figure 5(c) is endorsed by depicting the wake in Figure 6(c). The bigger periodicity and higher frequency of shedding is absolutely detectable. This can be compared with the claim of Saha (2007) that the near wake of a parallel-sided plate becomes unsteady at Reynolds numbers which lies between 30 and 35.

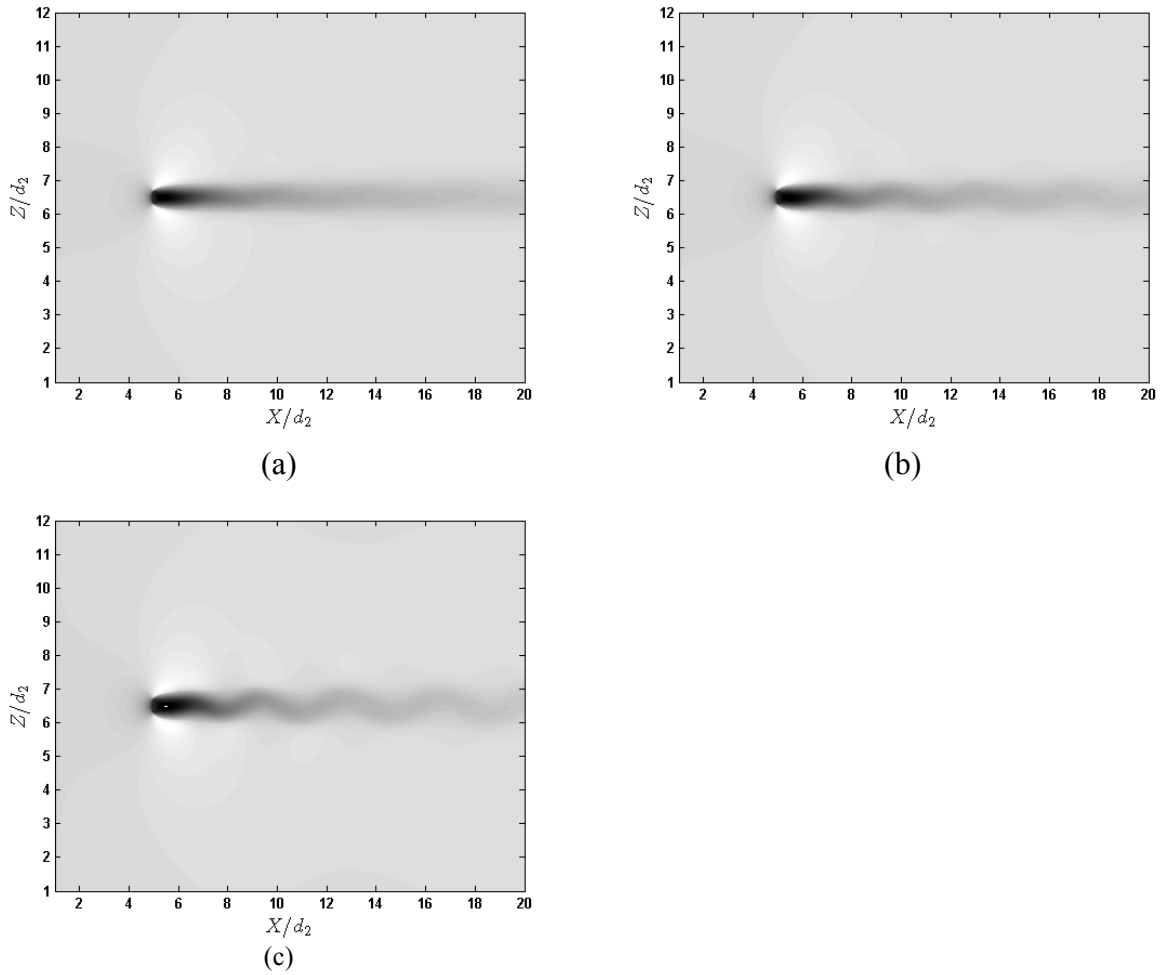

Figure 6 : Wake of the tapered plate at (a) Re_{local}=30 (b)Re_{local}=32 (c) Re_{local}=35

3.2. Secondary motion and formation length

The secondary motion in the unsteady laminar wake and in the front stagnation zone of tapered plate is of great interest since it can be accountable for many complexities in fluid flow. In the front stagnation zone of the plate, it is obvious in Figure 7(a) that the flow is going from wide end of the plate towards the narrow end since the time-averaged spanwise velocity has positive sign. By looking at the isobar Figure 8(a) it can be easily understood that the pressure is the driving force of the secondary motion towards the narrow end upstream the plate. The magnitude of this secondary flow in stagnation region is of the order 0.01. Gaster & Ponsford (1984) and Narasimhamurthy et al. (2008) observed a more complex pattern in the near-wake vicinity of the plate. Gaster & Ponsford in their high Reynolds number turbulent

flow noticed a stream from the wide end of the plate towards the narrow end in the downstream vicinity of plate. This stream was also detected by Narasimhamurthy et al. (2008) near the plate. However, they discovered a reversed direction of the flow from the narrow end toward the wide end, away from the plate. They affirmed that the pressure is accountable for such a driven secondary motion in their turbulent flow downstream the plate.

In the current simulation of unsteady laminar flow over a tapered plate, the secondary motion downstream of the plate divulged somehow a different feature from what was detected by previous observers. As it can be seen in Figure 7(b) and Figure 7(c), in the immediate vicinity of the plate the flow goes from the wide end towards the middle of span. The positive spanwise velocity at the higher local Reynolds numbers, i.e. near the wide end of the plate, supports this claim. At the other side of the plate where negative spanwise velocity is detectable, the flow moves from the narrow part toward somewhere at the midspan. However it should be noted that very near to the plate, i.e. x=5.025 or x=5.10, at the narrow end of the plate where there is no vortex shedding, a small positive value of spanwise velocity is observable. This suggests the secondary flow toward the narrowest end in the non-shedding part of the plate. Figure 7(c) gives a different view of the secondary flow along the span at different distances from the plate. In order to grasp a better impression of secondary flow, the streamline of the time-averaged velocity is visualized in Figure 7(d).

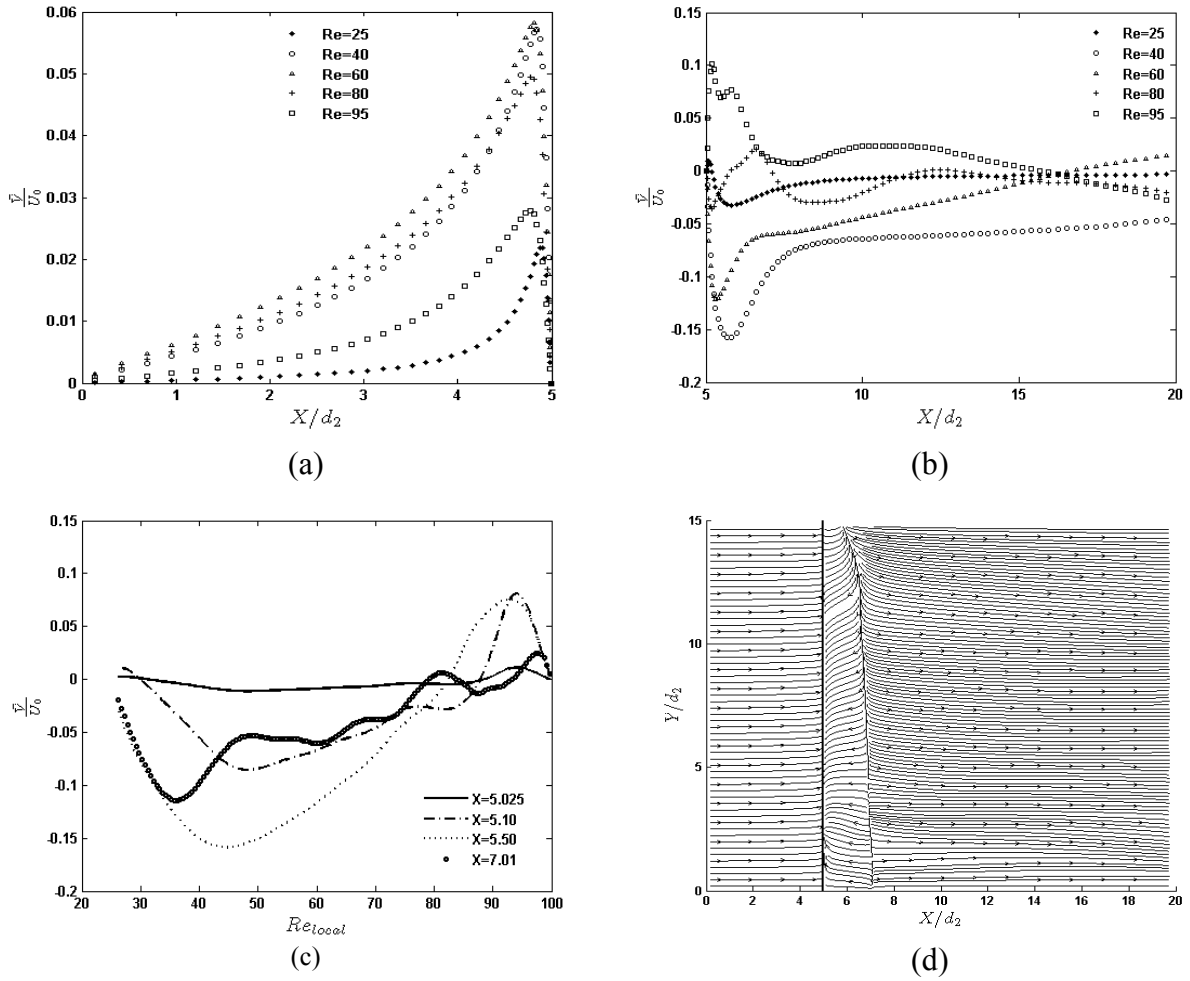

Figure 7 : Time-averaged spanwise velocity (secondary flow) at different spanwise location identified by local Reynolds number, (a) upstream the plate, (b) downstream the plate, (c) downstream the plate versus local Reynolds number for different x-positions, (d) Stream-trace of time averaged velocity

As noted earlier it has been shown by Narasimhamurthy et al. (2008) in the turbulent flow regime that the pressure is the main driving force of the secondary motion after the plate. In the present case, a closer observation of the pressure field in the downstream vicinity of the plate conceals somehow a similar conclusion. Figure 8(b) demonstrates the normalized time averaged pressure after the plate for different local Reynolds number. Figure 8(c), however, gives a more accurate impression of the mean pressure along the span at downstream of the plate. As it can be observed easily there are two extreme points, one maximum, and one minimum, along the span which clearly describes the secondary flow in the very near wake of the plate. The local pressure maximum at about Re_{local} = 35 tends to drive the flow towards both ends in the immediate vicinity of the plate. Nonetheless the potential effect of secondary

instabilities shall not be dismissed. The three-dimensional finite-amplitude quasi-steady state instability that results from the two-dimensional primary instability of the wake, namely secondary instability can also be conjectured as a driving mechanism of the complex spanwise flow. Either high strain-rate in regions between so-called braid regions, separating two consecutive primary vortices, or the instability of primary vortices due to destabilization of waves in the vortex core can lead to a three-dimensional secondary instability.

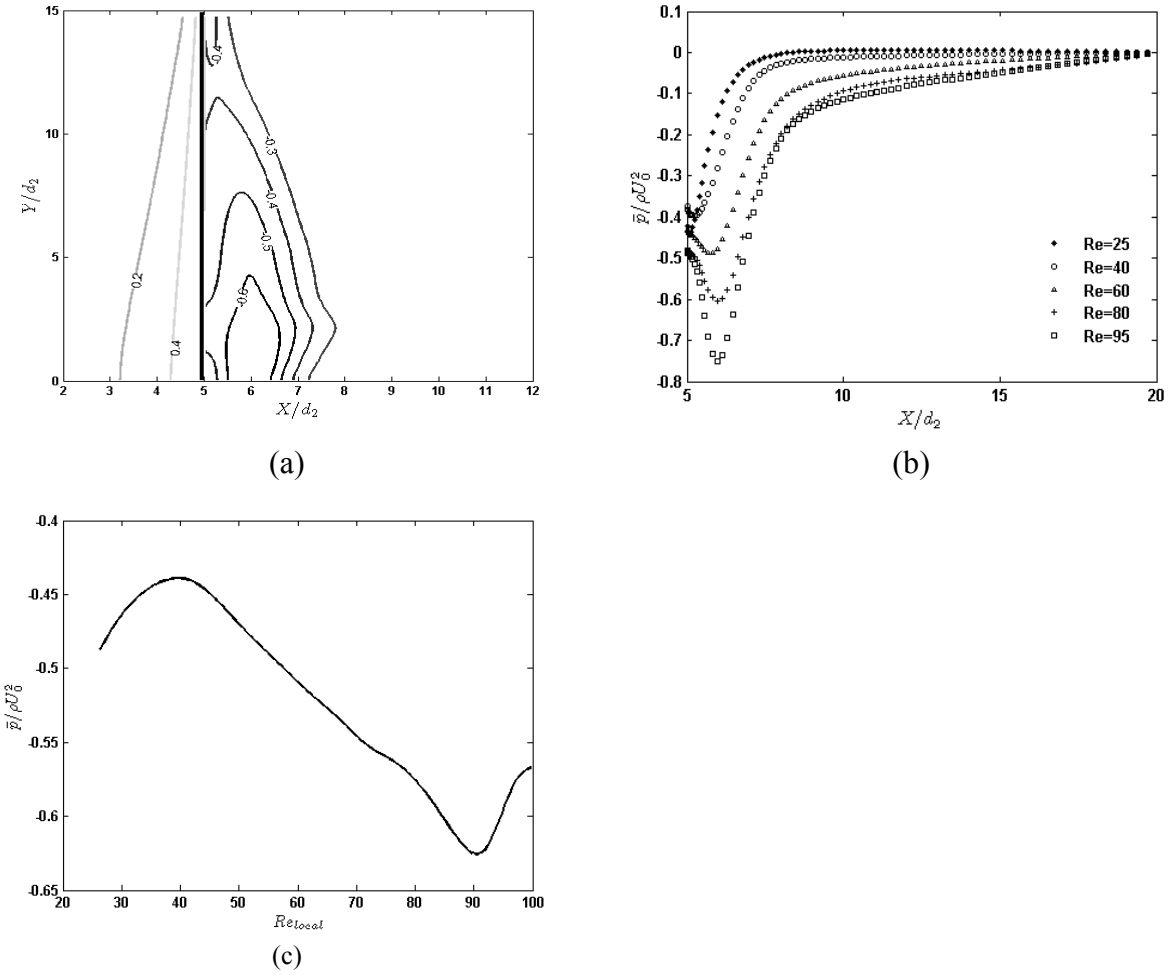

(a) (b)

(c)

Figure 8 : (a) Iso-contours of mean pressure ($\bar{p}/\rho U_0^2$) in X-Y section through the axis of the plate, (b) Normalized mean pressure after the plate versus x-position for different local Reynolds numbers, (c) Normalized mean pressure after the plate (base pressure) versus local Reynolds number

The non-dimensional length of the mean recirculation zone versus local Reynolds number is shown in Figure 9. The length is normalized by either local width (d_{local}) or widest width (d_2)

of the plate. The formation length L_w is the streamwise extent of the closed wake which results after time averaging of the velocity field. Figure 10 shows the iso-contour plot of time averaged streamwise velocity which clearly depicts the recirculation zone at downstream the plate. The length of formation length in this figure can be compared with the one which is normalized by d_2 in Figure 9.

There is in fact a coupling between the formation length and vortex shedding strength. In the case of turbulent flow in the wake of a tapered plate studied by Narasimhamurthy et al. (2008), the formation length was significantly bigger than the formation length in parallel-sided case of Najjar & Vanka (1995a). In the latter at the Reynolds number 1000 the formation length equals only two plate widths whereas in the former at the same local Reynolds number the formation length was 6 times the local plate width. This suggests a coupling between the formation length and vortex shedding strength. The more coherent and stronger vortex shedding in the parallel-sided plate turbulent flow, leads to a smaller formation length. This is in concord with the observation of Gaster & Ponsford (1984) who also reported stronger vortex shedding and shorter formation length compared to tapered plate. This trend does also exist in current simulation. The formation length in the case of the present parallel sided plate equals to 1.527d where at local Reynolds number of 62.5 in tapered plate case the formation length when normalized by local width of the plate is around 2.6 (see Figure 9). Recalling the local Strouhal number 0.1414 for the case of tapered plate and comparing this value with the Strouhal number 0.1704 in parallel-sided plate case, the same conclusion is arrived at to the present laminar wake. The stronger and more coherent vortex shedding behind the parallel-sided plate eventuates to smaller formation length as compared with the tapered plate at the same local Reynolds number.

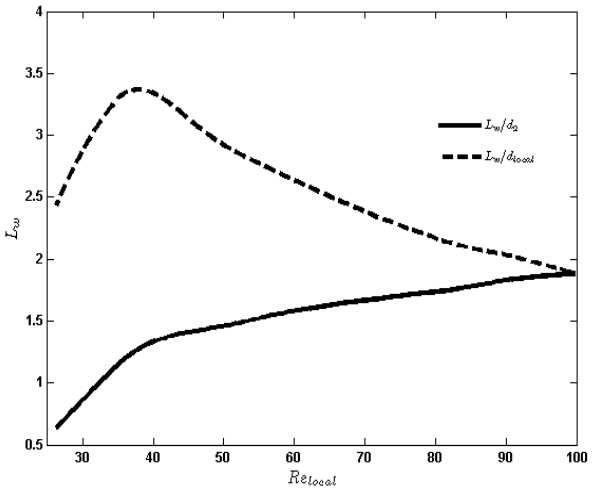

Figure 9 : Formation lengths of the wake of the tapered plate normalized by d_2 and d_{local}, respectively.

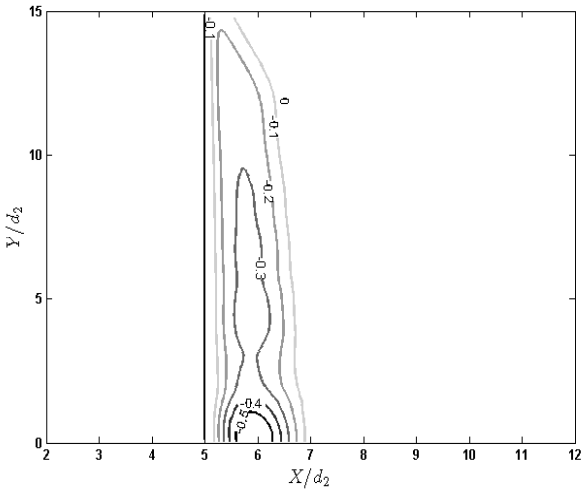

Figure 10 : Iso-contour plot of time averaged normalized streamwise velocity depicting the region of recirculation in spanwise direction, data are from midsection.

3.3. Mean pressure coefficient

In Figure 11 the mean pressure coefficient taken from time averaged pressure is depicted. The mean pressure coefficient is defined as $\overline{C}_p = 2(\overline{p} - p_0)/(\rho U_0^2)$ where the reference pressure p_0 is taken as the inflow pressure. The mean pressure coefficient for the case of the tapered plate at different local Reynolds numbers is shown. When the local coordinate on the surface of plate is being normalized by local width of the plate, the pressure coefficients for

different local Reynolds numbers in the tapered plate case are quite close together. In the same figure the pressure coefficient for the present parallel-sided plate at Re=62.5 is compared with the result of Najjar & Vanka (1995b) at Re=100. The pressure coefficient of Najjar & Vanka (1995b) at upstream of the plate compares well with the simulated uniform plate at Re=62.5. The downstream pressure is comparably lower though. However, one should not expect a complete matching of the pressure coefficients at the downstream of the plate in these two cases since the Reynolds numbers are different.

It is noteworthy that irrespective of the local Reynolds number, the base pressure coefficient is consistently higher for the tapered plate case than behind a parallel-sided plate.

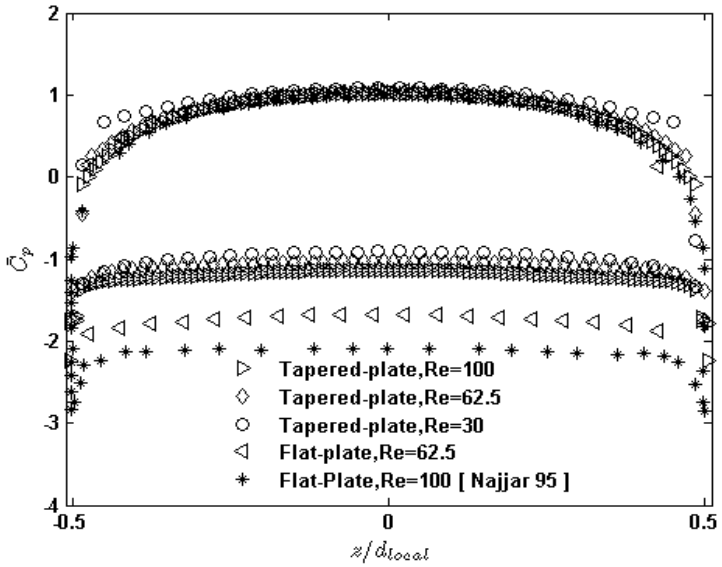

Figure 11 : Mean pressure coefficient for different cases at different Reynolds number. Here z denotes the position on the plate measured from centerline ($z=z-z_{middle}$)

3.4. Instantaneous vortical structure

In an attempt to better understand the evolution of the vortex structures in the complex wake of a tapered plate, it is important to determine and identify the relation between the various vortical structures. It is also of great interest from the perspective of macroscopic quantities such as drag and heat transfer coefficient to quantify the relative strength and orientation of

the vorticity vector in each class of vortices. Presenting 3 dimensional iso-surfaces of vorticity components in Figure 12, the complex and intricate three-dimensional features of the field is being revealed. In Figure 12(a) and 12(b) 3-D perspectives of the surface of instantaneous streamwise vorticity ($\omega_x = \partial w/\partial y - \partial v/\partial z$) and spanwise vorticity ($\omega_y = \partial u/\partial z - \partial w/\partial x$) at $t=360d_2/U_0$ is depicted. The plate is laid at the bottom of the figure and flow is from bottom to top. The Reynolds number is 25 to the right and 100 to the left of the figure. In Figure 12(c) the instantaneous vorticity magnitude ($|\omega| = 1/2(\omega_x^2 + \omega_y^2 + \omega_z^2)$) oblivious to any coordinate direction is shown. It is quite newsworthy that three different flow regimes simultaneously exist in the flow. At the narrow end of the plate where a big conical separation bubble is especially clear in iso-surface plot of the vorticity magnitude, the vortex has not started shedding. Further to the left of the plate another distinct regime is distinctive. Periodic and regular patterns of angulated vortices which diminish in streamwise direction are a feature which is being observed in a particular range of Reynolds number in the wake of tapered plate. Proceeding further to the left, bewildering structures of vortices emerge. Wriggling patterns of streamwise vorticity with twisted and squirmed longitudinal filaments and "slingshot"-like structures are observed downstream of the wide end of the plate. The complexity of the vortex pattern does not suggest any pre-distinguished modes (mode A or B) of transition. The irregularity of the vortex shedding, and the early breakdown of Karman vortices to distorted longitudinal structures at the wide end of the plate is due to secondary instabilities which first produce region of highly concentrated streamwise vorticity. When the spanwise Karman roller is shed from the plate, the vorticity becomes distorted and takes the shape of elongated longitudinal structures which fork into two branches resembling the slingshot shape.

A side-view of the spanwise vorticity can be seen in Figure 13. Note that the observer is looking towards the wide end of the plate in this view.

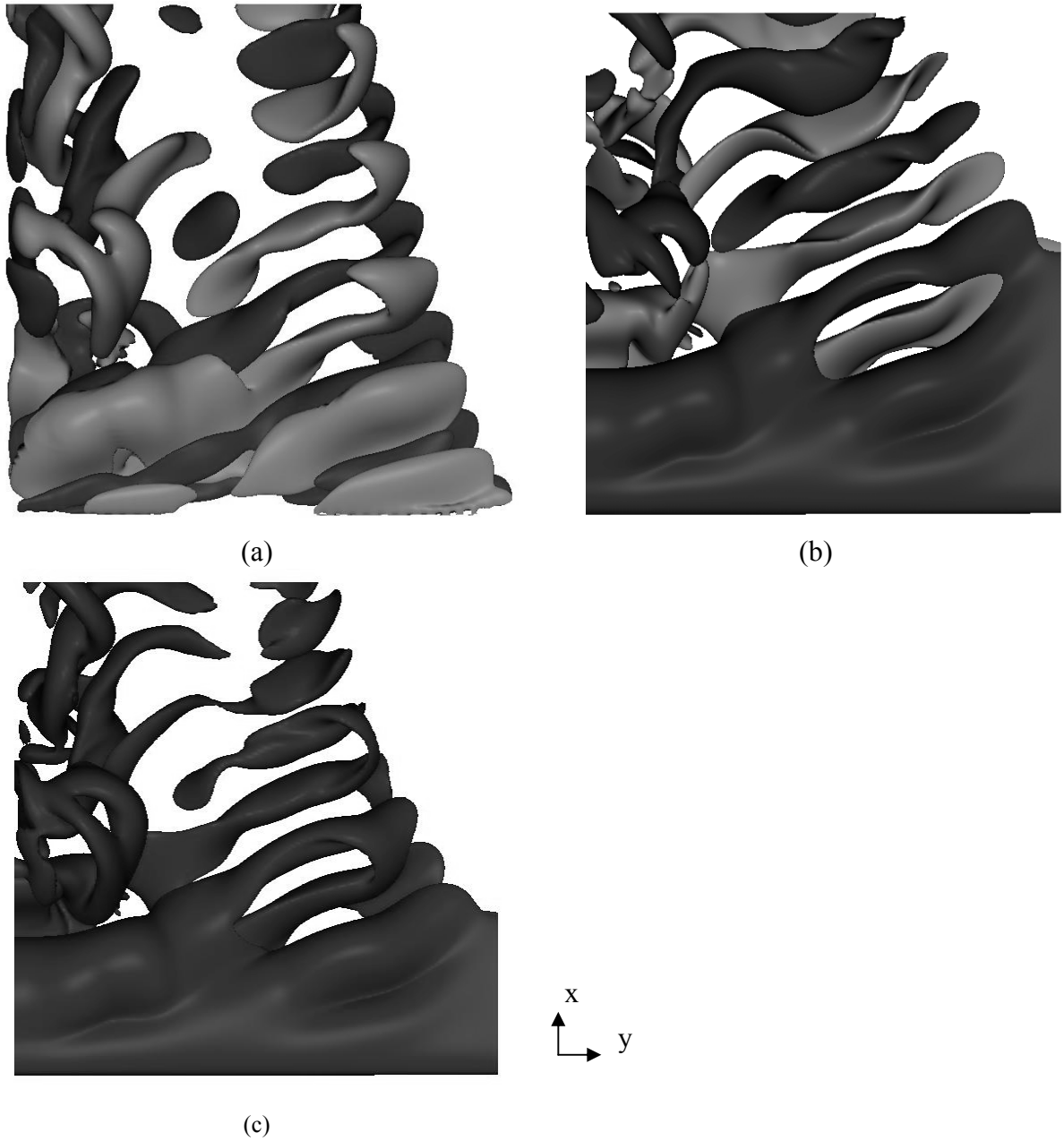

Figure 12 : (a) 3-dimensional iso-surface plot of streamwise vorticity at time, $t=360d_2/U_0$. Flow direction is from bottom to top and plate is laid at the bottom, white: $\omega_x \nu / U_0^2$ = -0.004, Black: $\omega_x \nu / U_0^2$ = +0.004, (b) 3-dimensional iso-surface plot of spanwise vorticity at same time instant, white: $\omega_y \nu / U_0^2$ = -0.004, Black: $\omega_y \nu / U_0^2$ = +0.004. (c) Iso-surface plot of vorticity magnitude at the same time instant, $|\omega| \nu^2 / U_0^4$ =5e-5

Figure 13 : Side-view of 3-dimensional Iso-surface of spanwise vorticity. The flow is from left to right. Details are the same as caption of Figure 11(b)

In order to visualize the topology of vortex cores the λ_2 definition proposed by Jeong & Hussain (1995) is used. λ_2 corresponds to the second largest eigenvalue of the symmetric tensor $S_{ij}S_{ij}+\Omega_{ij}\Omega_{ij}$ where S_{ij} and Ω_{ij} represent the symmetric and anti-symmetric part of velocity gradient tensor. It should be noted that this definition is equivalent to the requirement that $\lambda_2 < 0$ within the vortex core. In other words, only the negative value of λ_2 can be interpreted as a vortex core. Figure 14 presents an iso-contour plot of λ_2 in the midsection of domain. Only negative values which represent vortex cores have been depicted. Oblique vortex shedding which dies out downstream of the plate at mid-span, and also strong vortical structures which break down to smaller longitudinal vortex elements at the wide end of the plate are characteristics of this flow. The three-dimensional iso-surface of λ_2 in Figure 15 reveals a very similar pattern to what is observed in the iso-surface of vorticity magnitude in Figure 12(c). Again three distinct regimes are observed. A steady state at the narrow end, regular oblique vortex shedding in the middle of span and very irregular and chaotic breakdown of Karman shedding into longitudinal filaments at the wide end can be seen clearly.

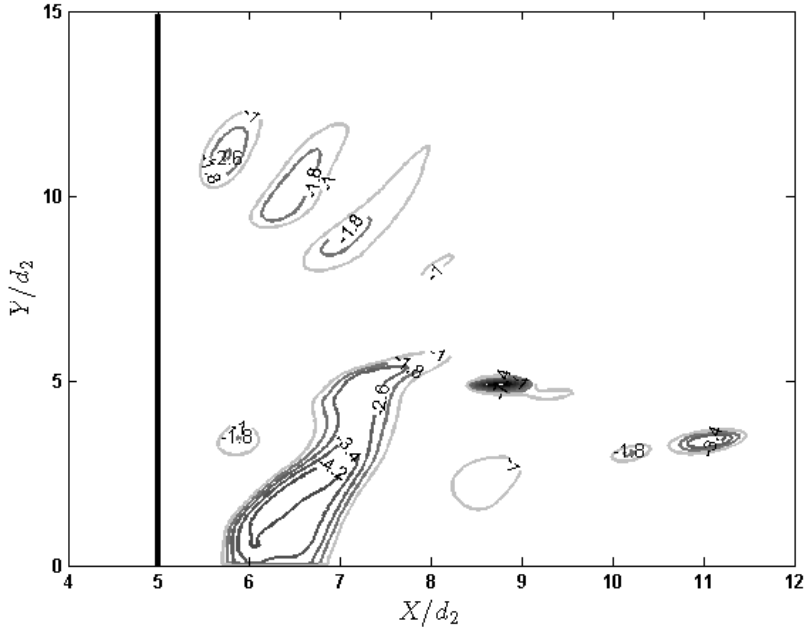

Figure 14 : Iso-contour plot of λ_2 in the midsection of domain, the thick line identifies the tapered plate.

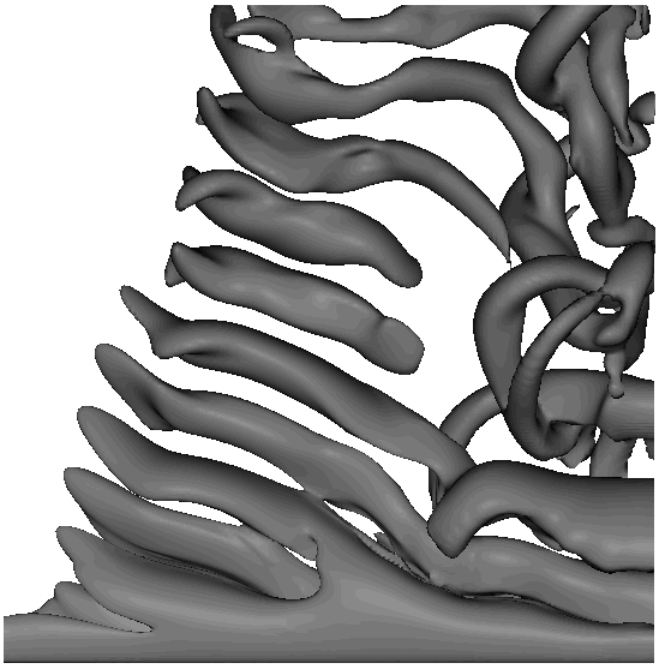

Figure 15 : Iso-surface plot of - λ_2 , the tapered plate is laid at the bottom of figure, the flow is from bottom to top, and local Reynolds number increases toward the right of figure.

4. Concluding remarks

The present study has been concerned with the unsteady laminar wake behind a tapered plate. This flow configuration has been studied rather extensively before, but only for other Reynolds number ranges. The wake topology in the present low-Reynolds-number range

exhibited a surprising complexity downstream of the wide end of the plate where streamwise-oriented vortex structures occurred as the result of an unexpected three-dimensionalization of the regular oblique shedding pattern at mid-span. A particularly fascinating feature of this special wake flow is the co-existence of three different flow regimes literally side by side in the same configuration. In addition, the cellular vortex shedding and oblique vortex structures were observed behind a tapered plate in this numerical experiment. Frequency analysis and three-dimensional visualization collectively confirmed that multiple cells of constant shedding frequency exist along the span of the plate.

The present three-dimensional calculation revealed a pressure-driven spanwise secondary motion. It was shown that in front stagnation zone the secondary flow is going from the wide end of the plate towards the narrow end. The secondary flow in downstream of the plate is more complex though.

Comparisons with results for wake flow behind a uniform plate at the same Reynolds number showed that the tapering gave rise to a lower Strouhal number and a significantly higher base pressure. The latter finding implies that the pressure drag is reduced due to the tapering.

Acknowledgments

The first author is grateful to the Research Council of Norway for the grant of computation time (Programme for Supercomputing). The first and second authors are thankful to the Research Council of Norway for their financial support.

REFERENCES

Castro, I. P. & Jones, J. M. (1987). "Studies in numerical computations of recirculating flows." Int. J. for Numerical Methods in Fluids **7:** 793-823.

Castro, I. P. & Rogers, P. (2002). "Vortex shedding from tapered plate." Experiments in Fluids **33**: 66-74.

Castro, I. P. & Watson, L. (2004). "Vortex shedding from tapered, triangular plates: taper and aspect ratio effect." Experiments in Fluids **37**: 159-167.

Fage, A. & Johanesn, F. C. (1927). "On the flow of air behind an inclined flat plate of infinite span." British Aero. Res. Coun. Rep. Memo **1104**: 81-106.

Gaster, M. (1969). "Vortex shedding from slender cones at low Reynolds numbers." J.Fluid Mech. **38**: 565-576.

Gaster, M. (1971). "Vortex shedding from circular cylinders at low Reynolds numbers " J.Fluid Mech. **46**: 749-756

Gaster, M. & Ponsford, P. J. (1984). "The flow over tapered plate normal to the stream." Aeronautical J. **88**: 206-212.

Gerich, D. & Eckelmann, H. (1982). "Influence of end plates and free ends on the shedding frequency of circular cylinders." J.Fluid Mech **122**(109).

Iaccarino, G. & Verzicco, R. (2003). "immersed boundary technique for turbulent flow simulations." Applied Mech. rev. **56**: 331-347.

Jeong, J. & Hussain, F. (1995). "On the identification of a vortex." J.Fluid Mech. **285**: 69-94.

Joshi, D. S. (1993). "Numerical studies of the wake of a plate normal to a free stream." PhD thesis, University of Illinois at Urbana-Champaign.

Manhart, M. (2004). "A zonal grid algorithm for DNS of turbulent boundary layers." Computer & Fluids **33**: 435-461.

Maull, D. J. & Young, R. A. (1973). "Vortex shedding from bluff bodies in shear flow." J.Fluid Mech. **60**: 401-409.

Mittal, R. & Iaccarino, G. (2005). "Immersed boundary methods." Annu.Rev.Fluid Mech **37**: 239-261.

Najjar, F. M. (1994). "Direct numerical simulations of separated and separeated-reattcahnig flows on massively parallel processing computers." PhD thesis, University of Illinois at Urbana-Champaign.

Najjar, F. M. & Balachandar, S. (1998). "Low frequency unsteadiness in the wake of a normal flat plate." J.Fluid Mech **370**: 101-147.

Najjar, F. M. & Vanka, S. P. (1995a). "Effects of intrinsic three-dimensionality on the drag characteristics of normal flat plate." Phys.Fluids **7**: 2516-2518.

Najjar, F. M. & Vanka, S. P. (1995b). "Simulation of the unsteady separated flow past a normal flat plate." Int. J. for Numerical Methods in Fluids **21**: 525-547.

Narasimhamurthy, V. D., Andersson, H. I., Pettersen, B. (2008). "Cellular vortex shedding in the wake of a tapered plate." J.Fluid mech.

Parnaudeau, P., Heitz, D., Lamballais,E. , Silvestrini,J.H. (2007). "Direct numerical simulation of vortex shedding behind cylinder with spanwise linear nonuniformity " J. Turbulence **8**(13).

Peller, N., Le duc, A., Tremblay,F., Manhart,M. (2006). "High-order stable interpolations for immersed boundary methods." Int. J. for Numerical Methods inFluids **52**: 1175-1193.

Perry, A. E. & Steiner, T. R. (1987). "Large scale vortex structures in turbulent wake behind bluff bodies." J.Fluid Mech. **174**: 233-270.

Piccirillo, P. S. & Van Atta, C. W. (1993). "An experimental study of vortex shedding behind linearly tapered cylinder at low Reynolds number " J.Fluid Mech. **246**: 163-195.

Roshko, A. (1954). "On the development of turbulent wakes of vortex streets." Tech.Rep.NACA **1191**.

Saha, A. K. (2007). "Far-Wake characteristics of two-dimensional flow past a normal flat plate." Phys.Fluids **19**: 128110-128110-4.

Tammadon-Jahromi, H. R., Townsend, P., Webster, M.F. (1994). "Unsteady viscous flow past a flat plate orthogonal to the flow." Comput. Fluids **23**: 433-446.

Williamson, C. H. K. (1992). "The natural and forced formation of spot-like dislocations in the transition of a wake." J.Fluid Mech. **243**: 393-441.

Williamson, C. H. K. (1996). "Vortex dynamics in the cylinder wake." Annu.Rev.Fluid Mech **28**: 477-539.

Wu, S. J., Miau, J. J., Hu,C.C., Chou,J.H. (2005). "On low frequency modulations and three-dimensionality in vortex shedding behind normal plate." J.Fluid Mech **526**: 117-146.